Title
Nanoparticle Enabled Phase Control in Solidification Processing

Author
Cao, Chezheng

Publication Date
2018

Peer reviewed|Thesis/dissertation

UNIVERSITY OF CALIFORNIA

Los Angeles

Nanoparticle Enabled Phase Control in Solidification Processing

A dissertation submitted in partial satisfaction of the

requirements for the degree Doctor of Philosophy

in Materials Science and Engineering

by

Chezheng Cao

2018

ABSTRACT OF THE DISSERTATION

Nanoparticle Enabled Phase Control in Solidification Processing

by

Chezheng Cao

Doctor of Philosophy in Materials Science and Engineering

University of California, Los Angeles, 2018

Professor Xiaochun Li, Chair

Solidification processing such as casting is of paramount significance for the mass production of complex materials and components throughout human history. Phase control during solidification processing is vital to achieve desired structures and properties for numerous applications. However, it is a long-standing challenge to achieve effective phase control during solidification processing of materials. Conventional phase control approaches have gradually encountered certain technical and/or fundamental limits. The emerging nanotechnology could provide a new pathway to control the phase evolution during solidification to break these limits. The objective of this study is to significantly advance the fundamental understanding of nanoparticles enabled phase control during solidification processing of materials and to overcome

the limits of the current methods by the incorporation of nanoparticles. More specifically, fundamental studies were conducted to understand how nanoparticles interact with liquid-liquid phase in immiscible alloys, solid-liquid phase during solidification of pure metals for unprecedented grain refinement and solid-solid phase for the grain structure stability at high temperatures.

To investigate the nanoparticle enabled phase control in solidification processing, key issues of nanoparticles incorporation and dispersion should be tackled first. In this study, a novel salt-assisted incorporation method was developed to fabricate metals containing uniformly distributed and dispersed nanoparticles. Molten salt such as $KAlF_4$ can effectively remove the oxide layer at the top of the metal melt and readily assist the incorporation of nanoparticles into molten metal. This new salt-assisted incorporation paves a new pathway for mass production of metal matrix nanocomposites. In this thesis, metal matrix nanocomposites of Al-TiC, Al-TiB_2 and Cu-WC were successfully fabricated by this method through solidification process.

In addition, to enhance the Orowan strengthening and study the phase control effect from nanoparticles of smaller diameter, a novel and facile molten salt reaction method was developed to synthesis small TiC nanoparticles with a diameter about 10 nm, which is not commercially available. The size of the TiC nanoparticles can be well controlled by the reaction template made of diamond nanoparticles in this study. To further improve and simplify the processing of Al nanocomposites reinforced by TiC (10 nm) nanoparticles, a novel in-situ reaction and incorporation method was explored, which enable one-step synthesis and incorporation. Al-TiC nanocomposites with 10 nm TiC nanoparticles show significantly improved mechanical properties.

Cu-WC nanocomposites with various volume fractions of nanoparticles were also successfully fabricated by this molten salt method after different salts were tested for optimized processing. $KAlF_4$, borax and NaCl were all effective for the incorporation of WC nanoparticles into the molten Cu. WC nanoparticles can be uniformly distributed and dispersed in Cu matrix by this method and provide much enhanced mechanical properties (strength, hardness and Young's modulus) without significant deterioration of the electrical conductivity, which suggests that the new Cu-WC nanocomposites could serve as high strength and high electrical conductivity materials for a widespread range of applications. .

The nanoparticles enabled phase control for liquid-liquid phase were studied in immiscible alloys both experimentally and theoretically to advance the fundamental understanding and to solve the long-standing challenges in solidification processing of immiscible alloys. It is shown that nanoparticles can move to the interface between the primary phase and secondary phase forming a coating and slowing down the diffusional growth of the secondary phase, which result in a significantly refined microstructure. TiC and $TiC_{0.7}N_{0.3}$ nanoparticles were successfully utilized in Al-Bi immiscible alloy for scalable manufacturing of high performance self-lubrication bearing materials. It was also found that the addition of Cu element can significantly enhance the mechanical properties without microstructure deterioration. Tungsten (W) nanoparticle is also demonstrated to be effective for the processing Zn-Bi immiscible alloys. In addition, our study show that nanoparticles not only worked for processing of metallic immiscible alloys, but also function well in organic immiscible systems such as B_4C nanoparticles in the organic SCN-CTB immiscible system.

The solid-liquid phase control by nanoparticles were investigated by studying the grain refinement effect during solidification. The grain refinement by nanoparticles for pure metals is

studied in different model material systems such as Cu-WC, Al-TiB_2 and Zn-WC. In this study, a new discovery that nanoparticles can refine metal grains down to ultrafine or even nanoscale by instilling a continuous nucleation and grain growth restriction mechanism during slow cooling (< 100 K/s) is reported for the first time. When casting pure Cu with WC nanoparticles, the grain sizes of Cu are refined substantially ultrafine and even nanoscale, which is approximate to the inter-particle spacing. Differential scanning calorimetry (DSC) studies showed that Cu-WC samples need significantly longer time (by 83%) to complete the solidification than pure Cu, indicating nanoparticles can substantially slow down the solidification process. It is proposed that nanoparticles can restrict the grain growth by the Gibbs-Thompson effect, thus allowing a continuous nucleation throughout the solidification process. Furthermore, this newly revealed grain control mechanism is successfully applied in other materials systems such as Al-TiB_2 and Zn-WC for ultrafine grains via slow cooling. This revolutionary method paves a pathway for the mass production of bulk stable ultrafine-grained (UFG)/nanocrystalline materials. This method may be readily extended to any other processes that involve cooling, nucleation and phase growth for widespread applications.

The solid-solid phase control by nanoparticles was investigated by studying the thermal stability of UFG/nanocrystalline Cu-WC nanocomposites. It is shown that the as-solidified bulk ultrafine/nanocrystalline Cu reveals an unprecedented thermal stability up to 1023 K (0.75 melting point of Cu) by the Zener pinning effect from WC nanoparticles.

In summary, this dissertation presents experimental methods and a theoretical framework to understand and utilize the newly discovered nanoparticles enabled phase control mechanisms during solidification processing. Cases studies of liquid-liquid phase (e.g. immiscible alloys), solid-liquid phase (e.g. grain refinement) and solid-solid phase (grain structure thermal stability)

of pure metals show that nanoparticle is extremely effective to control phase evolution. This approach breaks the fundamental and/or technical limits for solidification processing of numerous metals with unusual properties for broad applications.

The dissertation of Chezheng Cao is approved.

Jenn-Ming Yang

Nasr M. Ghoniem

Jaime Marian

Yongjie Hu

Xiaochun Li, Committee Chair

University of California, Los Angeles

2018

TABLE OF CONTENTS

NOMENCLATURE

Al	Aluminum
Al_2O_3	Alumina
B_4C	Boron Carbide
Bi	Bismuth
CTB	Carbontetrabromide
Cu	Copper
EBSD	Electron Backscatter Diffraction
EDS	Energy Dispersive X-ray Spectroscopy
FSP	Friction Stir Processing
$KAlF_4$	Potassium Aluminum Fluoride
KCl	Potassium Chloride
Mg	Magnesium
MMNC	Metal Matrix Nanocomposites
$Na_2B_4O_7$	Sodium Tetraborate (Borax)
NaCl	Sodium Chloride
Ni	Nickel
SCN	Succinonitrile

SEM	Scanning Electron Microscopy
SiC	Silicon Carbide
TEM	Transmission Electron Microscopy
TiB_2	Titanium Diboride
TiC	Titanium Carbide
$TiC_{0.7}N_{0.3}$	Titanium Carbonitride
WC	Tungsten Carbide
Zn	Zinc

ACKNOWLEDGEMENTS

Firstly, I would like to express my sincere gratitude to my advisor Professor Xiaochun Li for the continuous support of my PhD study, for his patience, motivation, and immense knowledge. His guidance helped me in all the time of research and life. In addition, I would like thank him for the opportunities he granted me to study in his group, without which this would not be possible.

I would also like to acknowledge Professors Jenn-Ming Yang, Nasr M. Ghoniem, Jaime Marian and Yongjie Hu for serving in my doctoral committee. I sincerely appreciate their valuable inputs for my research.

I am also very grateful to all of my colleagues in the research group, for the five years collaboration, life-time friendships and long-standing inspirations.

The last but not the least, I would like to thank my parents and wife for their unconditional support throughout this journey.

VITA

2013, B.S., Materials Science and Engineering, University of Science and Technology Beijing, China

JOURNAL PAPERS

- **Cao, C.**, Liu, W., Liu, Z., Xu, J., Hwang, I., De Rosa, I., & Li, X. (2018). Scalable manufacturing of immiscible Al Bi alloy by self-assembled nanoparticles. *Materials & Design*.
- **Cao, C.**, Liu, W., Javadi, A., Ling, H., & Li, X. (2017). Scalable manufacturing of 10 nm TiC nanoparticles through molten salt reaction. *Procedia Manufacturing*, *10*, 634-640.
- **Cao, C.**, Chen, L., Xu, J., Zhao, J., Pozuelo, M., & Li, X. (2016). Phase control in immiscible Zn-Bi alloy by tungsten nanoparticles. *Materials Letters*, *174*, 213-216.
- **Cao, C.**, Chen, L., Xu, J., Choi, H., & Li, X. (2016). Strengthening Al–Bi–TiC0. 7N0. 3 nanocomposites by Cu addition and grain refinement. *Materials Science and Engineering: A*, *651*, 332-335.
- Yao, G., **Cao, C.**, Pan, S., Lin, T. C., Sokoluk, M., & Li, X. (2018). High-performance copper reinforced with dispersed nanoparticles. *Journal of Materials Science*, 1-10.
- Javadi, A., Pan, S., **Cao, C.**, Yao, G., & Li, X. (2018). Facile Synthesis of 10 nm Surface Clean TiB2 Nanoparticles. *Materials Letters*.
- Ma, C., Chen, L., **Cao, C.**, & Li, X. (2017). Nanoparticle-induced unusual melting and solidification behaviours of metals. *Nature communications*, *8*, 14178.
- Javadi, A., Zhao, J., **Cao, C.**, Pozuelo, M., Yang, Y., Hwang, I., & Li, X. (2017). Stretching Micro Metal Particles into Uniformly Dispersed and Sized Nanoparticles in Polymer. *Scientific reports*, *7*(1), 7098.
- Javadi, A., **Cao, C.**, & Li, X. (2017). Manufacturing of Al-TiB2 Nanocomposites by Flux-Assisted Liquid State Processing. *Procedia Manufacturing*, *10*, 531-535.
- Liu, W., **Cao, C.**, Xu, J., Wang, X., & Li, X. (2016). Molten salt assisted solidification nanoprocessing of Al-TiC nanocomposites. *Materials Letters*, *185*, 392-395.
- Ma, C., Zhao, J., **Cao, C.**, Lin, T. C., & Li, X. (2016). Fundamental Study on Laser Interactions With Nanoparticles-Reinforced Metals—Part I: Effect of Nanoparticles on Optical Reflectivity,

Specific Heat, and Thermal Conductivity. *Journal of Manufacturing Science and Engineering*, *138*(12), 121001.

- Ma, C., Zhao, J., **Cao, C.**, Lin, T. C., & Li, X. (2016). Fundamental Study on Laser Interactions With Nanoparticles-Reinforced Metals—Part II: Effect of Nanoparticles on Surface Tension, Viscosity, and Laser Melting. *Journal of Manufacturing Science and Engineering*, *138*(12), 121002.
- Lin, T. C., Zhao, J., **Cao, C.**, Javadi, A., Yang, Y., Hwang, I., & Li, X. (2016). Fabrication of Metal–Polymer Nanocomposites by In-Fiber Instability. *Journal of Micro and Nano-Manufacturing*, *4*(4), 041008.
- Xu, J., **Cao, C.**, Das, S., Chen, L., Ma, C., Mishra, R. S., & Li, X. (2015). High performance Mg6Zn nanocomposites fabricated through friction stir processing. In *Magnesium Technology 2015* (pp. 383-386). Springer, Cham.
- Wu, M., **Cao, C.**, He, X., & Qu, X. (2013). Brazing diamond/Cu composite to alumina using reactive Ag-Cu-Ti alloy. *Transactions of Nonferrous Metals Society of China*, *23*(6), 1701-1708.
- Wu, M., **Cao, C.**, Wang, Y., Chen, X. He, X., & Qu, X. (2013). Microstructure and mechanical properties of diamond/Cu composite joint using Ag-Cu-Ti active brazing alloy. *Transactions of Materials and Heat Treatment*, *34*(3), 30-34.
- Wu, M., Chen, X., **Cao, C.**, Zhao, C., He, X., & Qu, X. (2012). Effect of tungsten particle size distribution on sheet resistance of alumina ceramic metallization. *Materials Science and Engineering of Powder Metallurgy*, *5*, 007.

PATENTS

- Li, X., Jiang, Q., **Cao, C.**, & Wu, S., (2018). Ceramics with Self-Dispersed Nanostructures via Casting.
- Li, X., Cao, C., (2018) Nanostructure Assisted Casting of Thermally Stable, Ultrafine Grained, Nanocrystalline Metals.
- Li, X., Cao, C., Yao, G., Pan, S., (2018) Scalable Manufacturing of Cu Nanocomposites with Unusual Properties.

Chapter 1 Introduction

1.1 Background and Motivation

Solidification processing such as casting is one of the most significant manufacturing processes for mass production of complex materials and components throughout human history. Phase control during solidification processing is vital to achieve desired structures and properties for numerous applications [Labrecque 1998, Liu 2013, Jiang 2017, Kim 2015, Wang 2010, and Chen 2016]. However, it is a long-standing challenge to achieve effective phase control during solidification processing mainly due to the high diffusivity in liquid state (ten orders of magnitude higher than solid state) and harsh environment of molten metal (such as high temperature, extreme chemical conditions and high conductivity) [Chen 2015, Chen 2014 and Cao 2018].

Over the past few decades, various approaches such as inoculation, adding alloy elements (e.g. rare earth elements) [Pan 2016, Chang 1998, and Hantzsche 2010], rapid cooling [Greer 1994, Sun 2006], or adding organic surfactants [Yin 2004, Akyol 2007] have been explored through both theoretical and experimental pathways to achieve optimal structures for various applications. However, these approaches have encountered certain technical and/or fundamental limits. One of the most common methods for phase control in metal casting industry is using inoculation, which refers to an addition of grain refiners to promote nucleation of new grains to obtain refined grain sizes [Greer 2000, Arnberg 1982, and Banerji 1986]. The grain refiner generally provides both particles to serve as heterogeneous nucleation sites and extra solute alloy elements to restrict grain growth. However, due to the low efficiency of the nucleant particles and limited growth restriction effect, the best grain refinement achieved by inoculation falls into tens of micrometers during regular casting [Chen 2015, Stjohn 2005]. The addition of some special alloy elements for phase

control has attracted some attentions in the past decades. For example, Mg element or some rare earth elements are added to molten iron to produce ductile iron containing spherical graphite phases instead of flake shapes. It is believed that Mg atoms might form some solid particles in the liquid for more effective nucleation of graphite phase and as surface modifier to control the shape by coating on the surface of the growing graphite [Labrecque 1998]. However, this approach heavily based on trial-and-errors and only work for very specific material systems. Rapid cooling ($> 10^4$ K/s) is also widely used for phase control in solidification processing. However, the rapid cooling rates significantly limit the sample size, complexity and processing window. Organic surfactants or molecules have been developed to control the size and morphology of crystal growth and nanoparticles synthesis. But organic molecules and surfactants have low thermal stability and high sensitivity to chemical conditions. They are not capable of effective phase control under the extremely harsh environments in molten metals due to the high processing temperatures and high electrical conductivity. These long-standing barriers impede the effective phase control for solidification processing to achieve enhanced properties for numerous applications.

Metal matrix nanocomposites with nano-sized elements incorporated in the metal matrix have great potentials for widespread applications because of the unusual mechanical, electrical and thermophysical properties and so on [Chen 2015', Cha 2015, Li 2018 and Ma 2015]. Furthermore, recent studies start to show that nanoparticles potentially have huge impacts on the phase control during solidification processing [Chen 2014, Chen 2015, Guo 2018 and Lin 2003]. Therefore, nanoparticles could provide us a promising new pathway to control the phase evolution during solidification processing. It is thus of significance to initiate studies to understand how nanoparticles control phase evolution during solidification and then utilize nanoparticles to break the technical and/or fundamental limits encountered by conventional phase control approaches.

Moreover, this study is also motivated to tackle the processing challenges for different alloy systems by the addition of nanoparticles. For example, immiscible alloys are of significance for its scientific importance and wide applications. However, it is very challenging to control the size, shape and distribution of secondary minority phase. Nanoparticles potentially provide us a new and powerful tool to mitigate the processing problems of immiscible alloys. In addition, grain refinement during casting of metals is very important for better mechanical properties and processability. It is also important to investigate the capability of nanoparticles for unprecedented grain refinement.

1.2 Research Objectives

The objectives of this study include: (1) Develop effective pathway for incorporation and dispersion of nanoparticles in solidification processing of metals; (2) Understand the mechanisms of liquid-liquid, solid-liquid and solid-solid phase control by nanoparticles; (3) Overcome the existing technical and/or fundamental limits of the phase control during solidification by nanoparticles such as solving the solidification processing issues of immiscible alloys and achieving unprecedented grain refinement in solidification processing of pure metals.

1.3 Work Summary

The remaining part of the dissertation will be organized as follows.

- Chapter 2 reviews the existing research of high relevance to this study.
- Chapter 3 introduces the salt-assisted nanoparticle incorporation method for production of metal matrix nanocomposites.
- Chapter 4 conducts experimental and theoretical studies on the nanoparticles enabled liquid-liquid phase control for immiscible alloy systems.

- Chapter 5 conducts experimental and theoretical studies on solid-liquid and solid-solid phase control by grain refinement and grain structure thermal stability, respectively.
- Chapter 6 summarizes the results of this study.
- Chapter 7 provides recommendations for future work.

Chapter 2 Literature Review

2.1 Nanoparticle Effects in Metals

2.1.1 Strengthening Effects

The strengthening effects of nanoparticles in metals are due to several strengthening mechanisms, namely: load bearing strengthening, Orowan strengthening, Hall-Petch strengthening, dislocation density difference induced by the coefficient of thermal expansion (CTE) mismatch during manufacturing.

(1) Load bearing strengthening

The load-bearing transfer from the soft and compliant matrix to the stiff and hard particles, under an applied external load, contributes to the strengthening of the base material [Zhang 2006, Zhang 2008 and Sanaty 2012]. A modified Shear Lag model proposed by Nardone [Nardone 1986] is often used to predict the contribution in strengthening from the load bearing strengthening in particulate reinforced composites materials:

$$\Delta\sigma_{Load} = 1.5V_p\sigma_i \tag{2-1}$$

where $\Delta\sigma_{Load}$ is the yield strength increment due to load bearing transfer, V_p is the volume fraction of particles and σ_i is the interfacial strength of matrix. A strong interfacial bonding between metal matrix and particles is necessary for significant load bearing transfer. Only with a strong interface, the load can be effectively transferred from soft matrix to hard particles for strengthening.

(2) Orowan strengthening

Orowan strengthening is a significant factor for the strengthening of MMNCs. The closely spaced hard nanoparticles could impede the movement of dislocations. The non-shearable ceramic reinforcement nanoparticles pin the crossing dislocations and promote dislocations bowing around the particles (Orowan loops) under external load [Hull 2001]. Even with only a small volume fraction, these highly-dispersed nanoparticles (smaller than 100 nm) can significantly enhance its strength due to the small interparticle space. Orowan strengthening can be determined by the Orowan-Ashby equation

$$\Delta\sigma_{Orowan} = \frac{0.13 G_m b}{d_p[\left(\frac{1}{2V_p}\right)^{\frac{1}{3}} - 1]} ln\frac{d_p}{2b} \tag{2-2}$$

where G_m, b, V_p and d_p are the shear modulus of the matrix, the Burger vector, the volume fraction and the diameter of the nanoparticles, respectively. This model was validated by experiments. However, to achieve ideal Orowan strengthening, it is crucial to achieve a uniform dispersion of nanoparticles in grains, which is very challenging in processing of MMNCs.

(3) Hall-Petch strengthening

Adjacent grains have different orientation so that the dislocations must change orientations when they move from one grain into another. This process will consume more energy to prevent the dislocations move in a continuous slip plane. Therefore the strength will be improved by refined grains. The famous Hall-Petch equation is used to describe the strengthening effect by grain refinement [Hull 2001]:

$$\Delta\sigma_{H-P} = k_y(d_m^{-\frac{1}{2}} - d_c^{-\frac{1}{2}}) \tag{2-3}$$

where k_y is the strengthening coefficient (characteristic constant of each material), d_m is average grain size in the monolithic sample, d_c is average grain size in the nanocomposite sample.

(4) CTE Mismatch

Geometrically necessary dislocations (GNDs) will form during material processing due to the mismatch in coefficient of thermal expansion (CTE) between the reinforcements and the metal matrix. The enhanced dislocation density could further increase the strength. The strengthening effect could be describe by:

$$\Delta\sigma_{CTE} = \sqrt{3}\beta Gb\sqrt{\frac{12\Delta\alpha\Delta T V_p}{\boldsymbol{b}d_p}} \tag{2-4}$$

where β is a constant, $\Delta\alpha$ is the CTE difference between hard particles and matrix, ΔT is the temperature difference between test and processing. However, the strengthening effect from CTE mismatch is generally less significant for MMNCs because little dislocations could be generated with nanoscale reinforcements.

(5) Mitigate the trade-off between strength and ductility

Most strengthening mechanisms will deteriorate ductility at the same time. Nevertheless, nanostructure has the potential to increase the strength and ductility simultaneously. Jiang et al. established an ultrastrong steel via high density of nanoprecipitates with minimal lattice misfit and achieved a strength up to 2.2 GPa and 8.2% ductility [Jiang 2017]. They found that, with high density coherent nanoprecititates in steel, the strength can be significantly improved without deterioration of ductility. Liu et al. [Liu 2013] also demonstrated that nanostructures could even bring unprecedented tensile ductility to high-strength molybdenum alloys. They reported a strategy that enables the control of grains and precipitated nanoparticles in a nanostructured regime which

allows Mo alloys to deliver a yield strength over 800 MPa and a tensile elongation as large as 40% at room temperature. A major source of the low ductility of Mo alloys (and some other bcc alloys) is their sensitivity to some solutes unavoidable in commercial products, such as O and N, especially when these impurities segregate at grain boundaries. The refined microstructure will result in not only a significant increase in strength, but also abundant grain boundary areas that can dilute the concentration of deleterious solutes into the lattice. Moreover, some second particles such as rare-earth oxide particles are particularly effective because they also gather solutes owing to strong rare-earth oxygen interactions. Jiang el al. [Jiang 2016] reported a toughening mechanism via spatial arrays of nanoparticles in Al matrix nanocomposites. They designed a special microstructure with nanoparticles distributed in nanoparticle free zone and nanoparticle rich zone that improve strength and toughness simultaneously. Therefore, the addition of nanoparticles has significant effect to the microstructure and property of materials, and it is of significance to understand how these nanoparticles affect these properties.

2.1.2 Phase Control Effects

Nanoparticles can also be applied for phase control or microstructure modification in solidification processing of metals. Previous studies about MMNCs mainly focus on the strengthening effects from the addition of nanoparticles. However, the phase control effects from nanoparticles are equivalently important for processing metals and alloys especially those that are difficult to process by conventional microstructure modification approaches.

(1) Nucleation

Nanoparticles could serve as heterogeneous nucleation sites during solidification and thus refine grain microstructures. The nanoparticle benefit in nucleation has been investigated by De

Cicco et.al [De Cicco 2011]. Nanoparticles were shown to refine grain microstructures in Al alloys A356 and A206. Yi et al. [Yi 2012] fabricated A206-Al_2O_3 nanocomposites by ultrasonic processing, and the optical micrographs of the pure A206 alloy and its nanocomposites samples in as-cast form are shown in Figure 2-1. The polarized light images clearly showed that the average grain size of A206-1wt.%Al_2O_3 nanocomposites is much smaller than pure A206 alloy. And the grain structure of α-Al changes from large dendritic crystal to small equiaxed crystal in Al-Al_2O_3 nanocomposites. This suggests that nanoparticles can serve as heterogeneous nucleation sites for primary phase and refine grain structures. Nanoparticles could also be beneficial for nucleation of any other processing routes involved with solidification such as welding and additive manufacturing. Martin et al. [Martin 2017] added nanoparticles to Al7075 powders for laser based additive manufacturing to print high strength Al. The addition of nanoparticles assisted the nucleation of Al grains and enabled them to print Al alloys that were impossible to print before.

For the heterogeneous nucleation theory, the classical spherical cap model for nucleation breaks down at small wetting angles and attempts to verify the spherical cap model experimentally have been unsatisfactory to correlate experimental results to the theory. Greer et al. [Greer 2000, Greer 2006] established a free growth model for prediction of Al-alloys grain size with the addition of Al-Ti-B grain refiner and identified a particle for free grain initiation at a necessary undercooling:

$$\Delta T_{fg} = \frac{4\gamma}{\Delta S_v d} \tag{2-5}$$

where ΔT_{fg} is free growth undercooling, γ is the solid/liquid interfacial energy, ΔS_v is the entropy of fusion per unit volume and d is the particle diameter. This free growth theory agrees well with the experimental data for the commercial Al-Ti-B grain refiner with effective particle size up to

micrometer scale. The examination of nanoparticle enabled nucleation was conducted by De Cicco [De Cicco 2009] and it was found that the experimental results matched well with the theoretical prediction in AC43A and A356 alloys by SiC, TiC and Al_2O_3 nanoparticles.

It is noticed that these previous studies about the nanoparticles enabled grain refinement mainly focus on the nucleation effects activated by low percentage of nanoparticles (e.g., < 3 vol%) partly due to the lack of methods to incorporate and disperse higher percentage of nanoparticles to molten metal during solidification processing which will be resolved in this study.

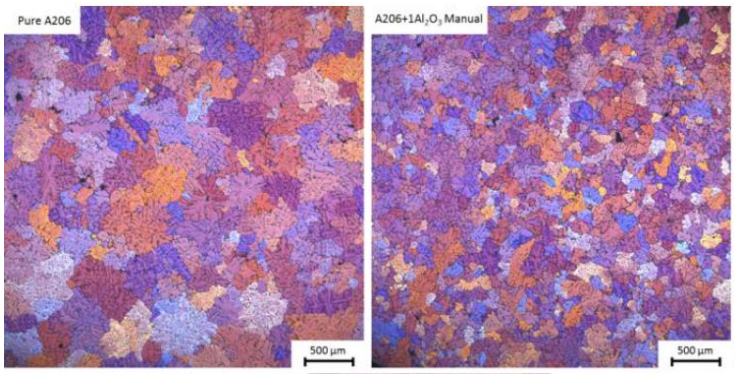

Figure 2-1 Polarized-light micrographs of as-cast pure A206 and A206 – 1 wt%Al_2O_3 nanocomposites.

(2) Modify Secondary Phase

In recent studies, nanoparticles were not only utilized as strengthening reinforcements, but also applied to modify the secondary phase and dendrite growth during solidification of alloys to resolve processing challenges. For example, Choi et al. [Choi 2013] added Al_2O_3 nanoparticles into Al-Cu (A206) alloys and found that Al_2O_3 nanoparticles modified the solidification microstructure of the eutectic θ-Al_2Cu and α–Al, resulting in the enhancement the hot-tearing resistance. Guo et al. [Guo 2018] incorporated SiC nanoparticles into Mg alloys and studied the

dendrite growth evolution by 4D (3D plus time) synchrotron tomography. They revealed that nanoparticles can increase nucleation and slow down dendritic growth by restriction in Zn's effective diffusivity ahead of the dendrite tip.

(3) Zener Pinning

At sufficiently high temperatures the grain boundaries in a recrystallized specimen will migrate so as to reduce total number of grains and thereby increase the mean diameter. However, the nature of normal grain growth with the presence of a second nanoscale phase deserves special consideration. The nanoparticles in metals can interact with grain boundaries as pinning points, retarding or stopping the grain growth during recovery, recrystallization, and heat treatment. Suitable nanoparticles could also stay at specific phase boundary to impede the boundary movement. The moving boundaries will be pinned by a pulling force exerted by the nanoparticles at the boundaries. The increase of V_p (volume fraction) and the decrease of d (particle diameter) lead to a finer structure, as theoretically modeled by the Zener equation:

$$d_m = \frac{4fd_p}{3V_p} \tag{2-6}$$

where d_m is the average grain size, f is a proportional constant. Equation 2-6 described the relationship between refined grain size and particle volume fraction as well as particle diameter. Zener pinning effect limits grain size during cooling, recovery, recrystallization and grain growth to achieve fine grain size [Humphreys 1996, Zhou 2001]. The Zenner Pinning effect provides us a pathway to stabilize UFG/nanocrystalline metals at elevated temperatures through the addition of nanoparticles [Darling 2016].

2.1.3 Other Functional Effects

With nanoparticles in metal matrix, functional properties such as electrical, thermal, magnetic and optical properties could be modified for wide range applications.

Nanoparticles reinforced metals are identified a promising candidate for high strength and high electrical/thermal conductors for wide range applications such as lead frame, electric motors, high voltage transmission lines and electronic packaging materials. With the addition of nanoparticles, the strength, wear resistance, modulus, and coefficient of thermal expansion could be significantly improved without significant deterioration of electrical/thermal conductivities [Meng 2005, Zweben 1992, Zweben 1998 and Kim 2007]. For example, pure copper has ideal electrical conductivity but it is too soft for a lot of applications. Conventional strengthening method such as alloying will deteriorate electrical conductivity significantly due to the severe electron scattering with solute atoms. Nanotwinned Cu with high strength and electrical conductivity can be fabricated by electrodeposition [Lu 2004]. However, it is extremely difficult to produce/manufacture bulk nanotwinned Cu through electrodeposition for real applications. Therefore, we are still facing the dilemma between mechanical properties and electrical/thermal conductivity. MMNCs are promising to mitigate the trade-off between. Unlike solute atoms, electrons will scatter less with nanoparticles and thus the electrical/thermal conductivity will still be remained at a high level. For example, Ag-based nanocomposites filled with SnO_2 nanoparticles, fabricated during a reactive milling process, were hot pressed to electrical contact materials, which exhibit outstanding thermal and electrical conductivity while maintaining superior wear resistance [Wang 2014]. Moreover, if well aligned nanowires (such as carbon nanotubes) with higher electrical conductivity can be arranged in Cu matrix, it is even possible to increase the electrical conductivity and mechanical properties simultaneously. Thermally stable nanoparticles can also

provide superior properties at elevated temperatures without obvious softening. For example, Mg-SiC nanocomposites exhibited a yield strength of 123 MPa at 400 °C, which is about twice as much as that of the most heat-resistant magnesium alloys [Chen 2015']. Some Al and Cu based composites with SiC or diamond powders as the second phase have excellent thermal conductivity and compatible thermal expansion coefficient with silicon chips, making them ideal electrical packaging materials [Fathy 2013, Molina 2008 and Qu 2011].

Nanoparticles could also tune the thermal-physical properties of materials for better processability. Ma et al. [Ma 2015, Ma 2016 and Ma 2016'] measured the change of optical reflectivity, specific heat, thermal conductivity, surface tension, and viscosity brought by the addition of Al_2O_3 nanoparticles into Ni matrix and concluded that the modification of these parameters significantly improved the laser processing by reducing the heat affect zone and tuning the capillary flow.

In addition, nanoparticles could also work as interfacial energy modifier. The basic mechanism is that nanoparticles assemble at the interface boundary and thereby modify the interfacial energy between the two phases. Surfactants are frequently used in nanostructure synthesis for phase control, as the surfactants effectively tune the interfacial energy between different phases. With suitable nanoparticle, they could also self-assemble to the interface to modify the interfacial energy.

2.2 Processing of Metal Matrix Nanocomposites

As mentioned above, MMNCs can deliver outstanding properties for mechanical, electrical, and magnetic applications. However, to realize widespread applications for MMNCs, a relatively low cost, scalable manufacturing process for high quality nanocomposites is necessary. The cost

of nanoscale reinforcements and the complexity of nanocomposites synthesis and processing are the two major limiting factors for manufacturing of MMNCs. Moreover, due to the high surface area of nanoparticles, they naturally tend to agglomerate to reduce their overall surface energy, making it difficult to obtain a uniform dispersion by most conventional processing methods. Also, due to their high surface area and surface dominant characteristics, nanoparticles tend to be more reactive with molten metal matrices. Therefore, after efforts for decades, there are still challenges to fabricate MMNCs with good dispersion/distribution through a low cost processing route.

2.2.1 Solid State Processing

Solid state processing methods were widely used to fabricate MMNCs. The most common method is powder metallurgy consisting the preparation of nanocomposite powders, mixing fine powders, pressing them into a desired shape or form (compacting), and then heating the compressed material in a controlled atmosphere to bond the material (sintering). Mechanical alloying is frequently used to prepare nanocomposite powders [Suryanarayana 2001, Suryanarayana 2011, Suryanarayana 2013 and Alam 2006]. In mechanical alloying, high energy ball milling process is able to break the nanoparticles clusters and achieve an ideal dispersion [Zhou 2016, 2017, 2018, and Zeng 2017]. As shown in Figure 2-2, some metal powders will be trapped between the grinding balls when they collide with each other. With hard ceramic nanoparticles in the powder mixture, these nanoparticles tend to be smashed into the softer metal powders and get uniformly dispersed in the metal matrix by the momentum of the grinding balls. Moreover, nanostructure metal powder can also be prepared by this method attributing to the severe plastic deformation during the process. In situ MMNCs involving the reaction to form nanoscale reinforcements can also be manufactured by mechanical alloying process. Taking advantages of the relative slow solid state diffusivity, the precipitates formed during the processing

could be readily controlled to nanoscale. Molecular level mixing is another common approach to prepare nanocomposites powders [Wang 2015, Mohammad 2016]. By mixing nanoscale reinforcements (e.g. CNTs, graphene) with solutions containing metal ions at molecular level, researchers are able to uniformly disperse nanoscale reinforcements in metal powders. Different compaction and sintering methods such as HIP, hot pressing, hot extrusion, cold pressing and SPS have been applied to compact and sinter nanocomposite powders.

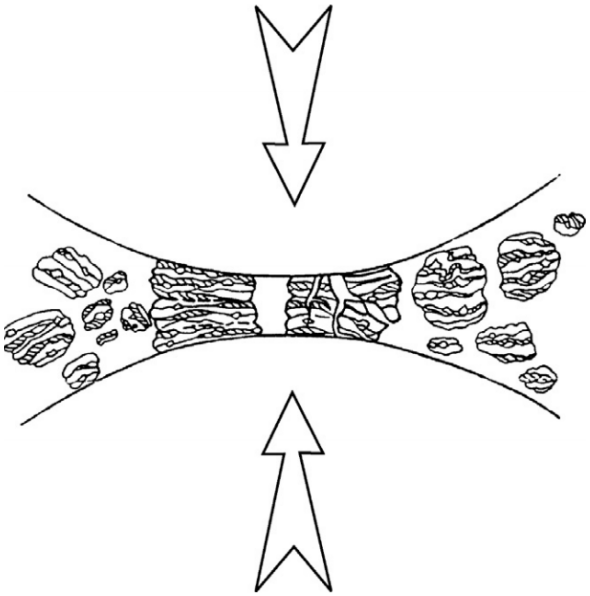

Figure 2-2 Ball-powder-ball collision of powder mixture during mechanical alloying [Suryanarayana 2001].

Severe plastic deformation (SPD) methods such as equal channel angular pressing (ECAP) and accumulative roll bonding (ARB) have also been applied to fabricate MMNCs [Casati 2013, Quang 2007, Jamaati 2014 and Kadkhodaee 2013]. With intense plastic deformation in the metal matrix, nanoparticle clusters could be sheared open and disperse well in the metal matrix. However, the size and geometry complexity of the materials are severely limited.

Friction stir processing (FSP) is another a powerful tool to fabricate MMNCs [Akramifard 2014, Chen 2012 and Xu 2015]. As shown in Figure 2-3, rotational tool with a specially designed pin and shoulder is plunged into the plate and traversed in certain direction. SiC nanoparticles located at the pre-drilled holes will be mixed and dispersed by the rotating pin. Agglomeration of nanoparticles could be readily avoided by this FSP. Moreover, nanoparticles could serve as nucleation sites for dynamic recrystallization of metal matrix during FSP and refine the microstructure.

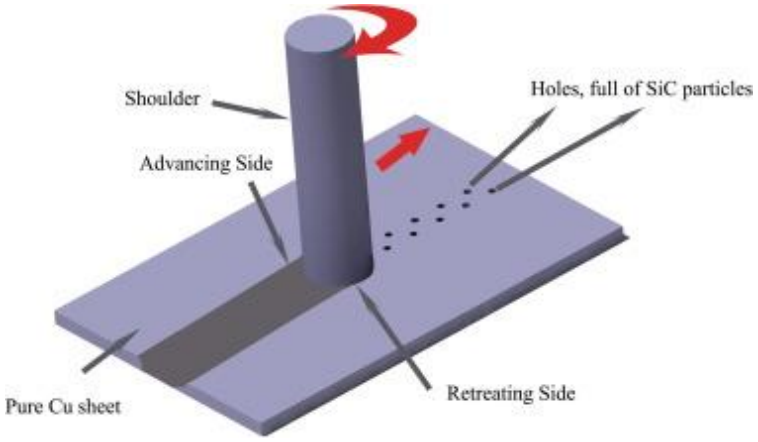

Figure 2-3 Schematic illustration of friction stir processing to fabricate Cu-SiC nanocomposites [Akramifard 2014].

Other methods such as electrodeposition [Shi 2006, Liu 2011], CVD, PVD [Strauss 2011, Musil 2001] were applied to deposit MMNCs thin films with dispersed multiphase microstructures, multilayered microstructures, or homogeneous nanostructured coatings. These thin film deposition techniques have wide range of applications and are powerful methods to study fundamental science of MMNCs. However, these approaches are extremely difficult to produce bulk samples.

The common drawbacks of solid-state processing for fabrication MMNCs are the limited size, geometry complexity and the high cost of processing.

2.2.3 Solidification Processing of MMNCs

Among these processing methods for synthesis and processing of bulk MMNCs, the least expensive method is solidification processing. However, due to the poor wettability and high specific surface area of nanoparticles, it is extremely difficult to incorporate nanoparticles into molten metal. Even after nanoparticles being incorporated into molten metal, severe agglomeration and aggregation frequently occur because of the van der Waals attraction between nanoparticles [Casati 2014, Chen 2013 and He 2008]. The common methods to disperse nanoparticles in aqueous solution such as organic molecular, polymer surfactants and electrical double layer cannot survive in the harsh environment of molten metals due to the high temperatures and high electrical conductivity. Therefore, there are still significant challenges to disperse nanoparticles in molten metal.

High-intensity ultrasonic processing to incorporate and disperse nanoparticles in molten metal has been extensively studied [Li 2008, Cao 2008, Cao 2008' and Yang 2007]. The ultrasonic waves could generate non-linear transient cavitation and acoustic streaming in the molten metal for refining microstructures, degassing to reduce porosity and most importantly dispersing the nanoparticle clusters. As shown in Figure 2-4, the acoustic cavitation involves the formation, growth, pulsating and collapsing of bubbles in liquid under cyclic ultrasonic waves. The implosively collapse of the tiny bubbles could produce transient so called "hot spots" with temperature up to 5000 °C, pressure up to 1000 atm and heating/cooling rates above 10^{10} K/s. The intense implosive impact could be strong enough to break up the nanoparticle clusters and the local transient high temperatures could improve the wettability between nanoparticles and molten metal. In addition, the acoustic streaming from the acoustic pressure gradient is effective for stirring. With the combination of the transient cavitation and streaming effects, nanoparticles could be well

dispersed uniformly in the molten liquid. SiC nanoparticles were incorporated and dispersed by the ultrasonic processing in Al and Mg alloys [Yang 2007, Lan 2004]. The mechanical properties got improved significantly by the addition of nanoparticles.

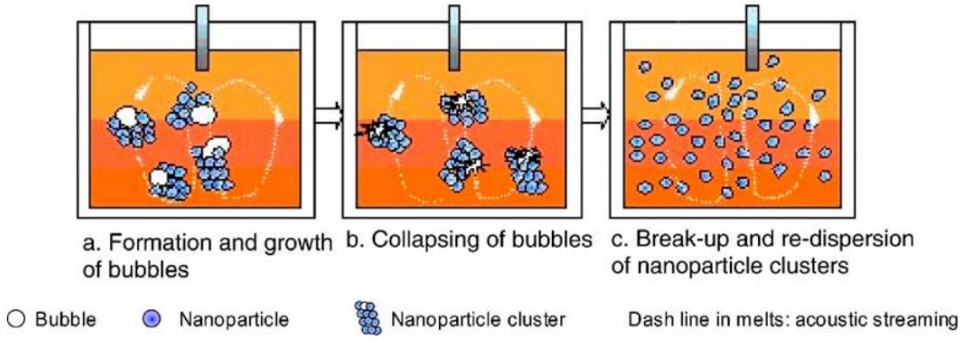

Figure 2-4 Schematic of the cavitation and streaming effects for nanoparticle dispersion and wetting in metal melts [Lan 2004].

Semi-solid processing has been widely applied to process metal matrix composites with micro meter scale reinforcements [Casati 2014]. And semi-solid processing was found to be very effective to incorporate nanoparticles into metal matrix [Xu 2015, De Cicco 2009, and Chen 2013]. The viscosity of semi-solid melt is significantly higher than single liquid melt, which enables the melt to trap nanoparticles inside the metal matrix effectively. Moreover, because the processing temperature of the semi-solid state is lower, severe burning issue of the nanoparticles could be avoided. Another advantage of semi-solid processing is that higher percentage of nanoparticles could be incorporated. Compare with powder metallurgy method which normally can only add less than 3vol% of nanoparticles, semi-solid processing could incorporate more than 6 vol% of nanoparticles. The major drawback of the semi-solid processing is the lack of dispersion mechanisms. Nanoparticles still tend to form clusters in the melt due to the van der Waals attraction and high surface areas. The lack of dispersion mechanisms of semi-solid processing limited the

success of the semi-solid processing to some degree. However, combination of the semi-solid mixing with a solid state process such as friction stirring could provide MMNCs with well dispersed high percentage of nanoparticles [Xu 2015, Chen 2012].

In situ methods to produce MMNCs have been widely investigated in both liquid and solid state processing. Rely on the chemical reaction between different alloying elements, various precipitates at nano-scale could form as the reinforcements. Cu-NbC [Zeng 2017], Cu-TiB_2 [Guo 2009, Chrysanthou 1995 and Božić 2009], Al-TiC [Tyagi 2005, Tong 1998 and Li 2005] and Al-TiB_2 [Li 2017, EStruga 2013, Liu 2018 and Chen 1996] systems have been extensively studied. Among these in situ methods, the flux assisted processing method has attracted significant attentions because of the potential capability for large scale production. As shown in Figure 2-5, mixed salts of potassium hexafluorotitanate (K_2TiF_6) and potassium tetrafluoroboride (KBF_4) are loaded on the surface of Al melt. Exothermal reactions between the flux and Al melt could form TiB_2 particles by the following equation:

$$3K_2TiF_6 + 6KBF_4 + 10Al \rightarrow 3TiB_2 + K_3AlF_6 + 9KAlF_4 \quad (2\text{-}7)$$

With the assistance of mechanical stirring, Al-TiB_2 composites could then be cast to a mold after the salts were removed. Other flux systems such as K_2TiF_6-KBF_4-Na_3AlF_6 [Liang 2008], TiO_2-Na_3AlF_6-KBF_4 [Chen 1996] and TiO_2-H_3BO_3-Na_3AlF_6 [Chen 1999] were also investigated to fabricate Al-TiB_2 composites. This flux assisted in situ method can be readily used for large scale productions. There are several drawbacks limited the application of in situ methods to produce MMNCs: (1) the size of particles cannot be easily controlled especially in liquid state processing. With the fast diffusivity of atoms in liquid state, particles can easily grow to micrometer scale. Fast cooling method is used to achieve refined nanoparticles, but fast cooling techniques are

difficult to produce bulk samples at low cost; (2) nanoparticle percentage is limited. The percentage of nanoparticles produced in the metal matrix is limited by either the thermodynamics of different material system or the processing techniques. Recently, newly developed manufacturing methods have been applied to improve the in situ methods. For example, ultrasonic processing [Estruga 2013] has been used to modify the in situ reaction process. They found that ultrasonic processing could reduce the size of TiB_2 particle significantly and provide clean interface between Al-TiB_2 nanoparticles. Li et al. [Li 2017] also utilized the salt assisted reaction method to produce TiB_2 nanoparticle decorated AlSi10Mg powder by gas atomization for laser based additive manufacturing.

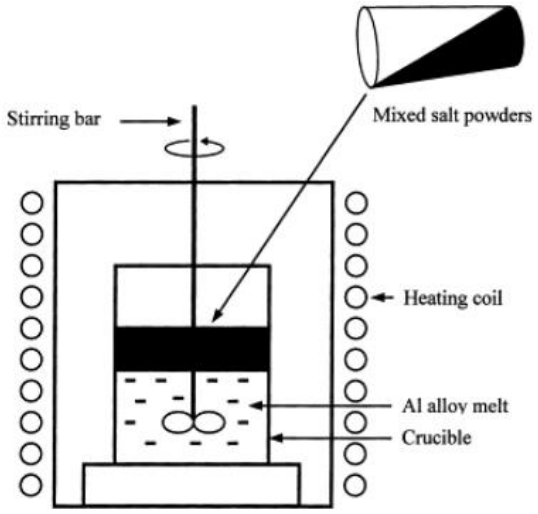

Figure 2-5 Schematic diagram of an apparatus for fabricating in situ MMCs by means of flux-assisted synthesis [Tjong 2000].

Additive manufacturing has been established and extensively studied in recent years. MMNCs have also been fabricated through the additive manufacturing route. Various material systems such as AlSi10Mg-TiB_2 [Li 2017], AlSi10Mg-TiC [Gu 2014], Al-Si10Mg-AlN [Dai

2018], Al7075-Zr [Martin 2017], Al-TiC [Yuan 2015], Inconel-WC [Shi 2018], 316L stainless steel-TiB_2 [AlMangour 2016, AlMangour 2016'], 316L stainless steel-TiC [AlMangour 2016'', AlMangour 2016'''] have been developed by laser based additive manufacturing. The fast heating/cooling rates of lased based processing provide new opportunity for fabrication of MMNCs. In addition, might be more important, nanoparticles are shown to be very effective to solve challenges of additive manufacturing or laser based processing. For example, Ma et al. [Ma 2017] incorporated nanoparticles into the Ni matrix by electrodeposition for laser processing, and suggested that the undesired heat affect zone was significantly reduced by the addition of nanoparticles due to the change of thermal physical properties (such as conductivity, viscosity, reflectivity etc.) brought by nanoparticles. Martin et al. [Martin 2017] found that nanoparticles could also serve as potent nucleation particles during additive manufacturing and print high strength Al 7075 alloy for the first time. They suggested that the addition of nanoparticles modified the solidification behaviors of Al alloys and avoid crack formation during the manufacturing.

Infiltration techniques entail infiltrating a preform or partial matrix containing the reinforcements with a liquid metal. The preform consists of particles formed in a particular shape with some binding agent. Infiltration methods include ultra-high pressure, where the pressure used to infiltrate a high-density preform of nanoparticles is in excess of 1 GPa, and pressure less infiltration, where a block of metal is melted on top of a lower density preform of nanoparticles and allowed to seep into the preform [Rohatgi 2007].

2.2.2 Dispersion of Nanoparticles in Molten Metal

Dispersion of nanoparticles in molten metals is the most crucial factor for the properties, processability, microstructure refinement etc. However, it is very challenging to achieve uniform dispersion and distribution of nanoparticles in molten metal because of the high specific area of

nanoparticles and van der Waals attraction between nanoparticles. Ultrasonic processing for de-agglomeration of nanoparticles in molten metal seems to be the only effective way. Other dispersion mechanisms based on organic molecules, surfactant, and electrical double layers are not suitable for the dispersion of nanoparticles in molten metal due to the high temperature, high electrical conductivity environment of molten metal. For ultrasonic processing, however, the dispersion of nanoparticles in molten metal is not stable once the ultrasonic process stops due to the lack of effective repulsive force between nanoparticles. Recently, a thermal activated self-stabilization mechanism is proposed by Chen et al. [Chen 2015] and Xu [Xu 2015']. They studied the physics that governs the interaction between nanoparticles in molten and discovered the thermal activated effective self-stabilization mechanism to achieve a uniform dispersion of nanoparticles in molten metals. A simplified model, as shown in Figure 2-6, assumes that two same spherical nanoparticles with radius *R* interacting in liquid metal with distance *D*. And the chemical reaction between nanoparticles and molten metal, macroscopic convection, electrostatic interaction between nanoparticles, buoyance and gravity forces are assumed to be negligible. There are three major factors governing the dispersion of nanoparticles in molten metal: interfacial energy, van der Waals attraction and thermal Brownian motion.

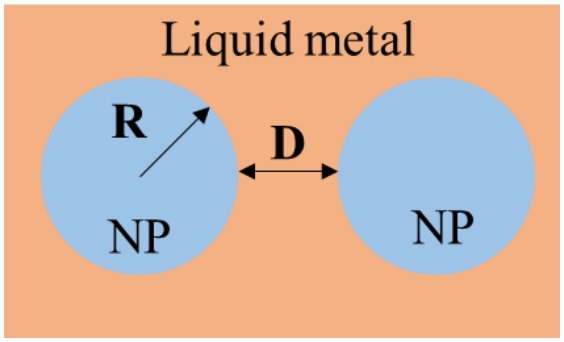

Figure 2-6 Model for two same nanoparticles in molten metal.

(1) Interfacial energy

When two nanoparticles are sintered together (D = 0), there will be no physical interface between them which is set as the global minimum energy to be zero. The interfacial energy of two separated nanoparticles in molten metal can be described as $G_b = 2S_{pl}\sigma_{pl}$where S_{pl} is the surface area of a nanoparticle interface and σ_{pl} is the interfacial energy between nanoparticle and molten metal. When the two nanoparticles approach to each other and squeeze all metal atoms out from the gap between nanoparticles, there are vacuum-nanoparticle interfaces. The interfacial energy can be described as $G_b' = 2(S_{pl} - S)\sigma_{pl} + 2S\sigma_p$, where S is the effective contact area between two nanoparticles, σ_p is the interface energy of the nanoparticle-vacuum surface.

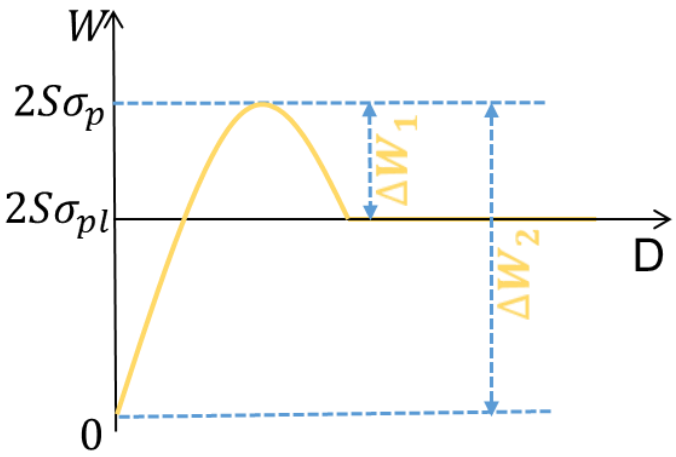

Figure 2-7 Interfacial energy change along the distance between two nanoparticles [Xu 2015'].

As shown in Figure 2-7, when two nanoparticle move to each other and squeeze out the metal atoms to create a void, the change of Gibbs free energy can be calculated as

$$\Delta W_1 = G_b' - G_b = 2S(\sigma_p - \sigma_{pl}) \quad 2\text{-}8$$

When the two nanoparticles further move forward to each other and start to form chemical bonds, the interface of nanoparticle-vacuum disappear and the change of Gibbs free energy can be calculated as

$$\Delta W_2 = -2S\sigma_p \quad 2\text{-}9$$

Therefore, from the interfacial energy point of view, the most stable state is two nanoparticles sintering together. However, there exist an interfacial energy barrier ΔW_1 to fuse two nanoparticles. When ΔW_1 is large enough, it is hard for the two nanoparticles to overcome the energy barrier and sinter together.

(2) van der Waals attraction

The van der Waals potential between two identical nanoparticles in molten metal can be described as [Israelachvili 2011]

$$W_{vdw} = -\frac{R(\sqrt{A_{np}}-\sqrt{A_{liquid}})^2}{12D} \quad 2\text{-}10$$

where R is the radius of nanoparticles, A_{np} and A_{liquid} are the Hamaker constant of nanoparticle and molten metal, respectively. D is the distance between two nanoparticles. The van der Waals potential is always negative that means two identical nanoparticles always attract each other. A small attractive van der Waals potential is preferred to disperse nanoparticles.

(3) Brownian motion

Nanoparticles move randomly in molten metal under the thermal fluctuations. In this model, only the movement along two nanoparticles is considered. The kinetic energy of the Brownian

motion is *kT/2* at one dimension for one particle. Therefore, the Brownian motion energy for two nanoparticles system at one dimension is *kT*.

As shown in Figure 2-8, by integrating the interfacial energy, van der Waals potential and Brownian motion energy in one graph, three possible cases for nanoparticle dispersion could occur: cluster, pseudo-dispersion and self-dispersion. For the cluster case, the energy barrier from the interfacial energy is smaller than *kT*, and the secondary minimum from van der Waals attraction is larger than *–kT*. Under this circumstance, the Brownian motion energy *kT* could drive nanoparticles to overcome the energy barrier and secondary minimum to contact with each other and fuse together. For the pseudo-dispersion case, the energy barrier is much larger than Brownian motion *kT*, the secondary minimum is smaller than *–kT*. The high energy barrier would protect the nanoparticles from sintering but the secondary minimum would kinetically trap nanoparticles into the energy well, forming a nanoparticle rich zone with dispersed nanoparticles inside. For the self-dispersion case, the energy barrier is also larger than Brownian motion *kT* and the secondary minimum is larger than *–kT*. The good wetting between nanoparticle and metal liquid provides a high energy barrier (> 10 *kT*) which make the Brownian motion kinetically insufficient to drive nanoparticles to fuse together. Also, the secondary minimum is too shallow to trap nanoparticles so that nanoparticles could move freely in the molten metal without forming clusters. This theory study provide a guideline to achieve the self-dispersion dispersion: (1) good wetting between molten metal and nanoparticles for the high energy barrier; (2) small van der Waals attraction between nanoparticles in the molten metal. Two approaches could achieve smaller van der Waals attraction: choose nanoparticle with similar Hamaker constant with the molten metal; use smaller nanoparticles; (3) Higher processing temperature is preferred for larger *kT* to enable nanoparticles move freely.

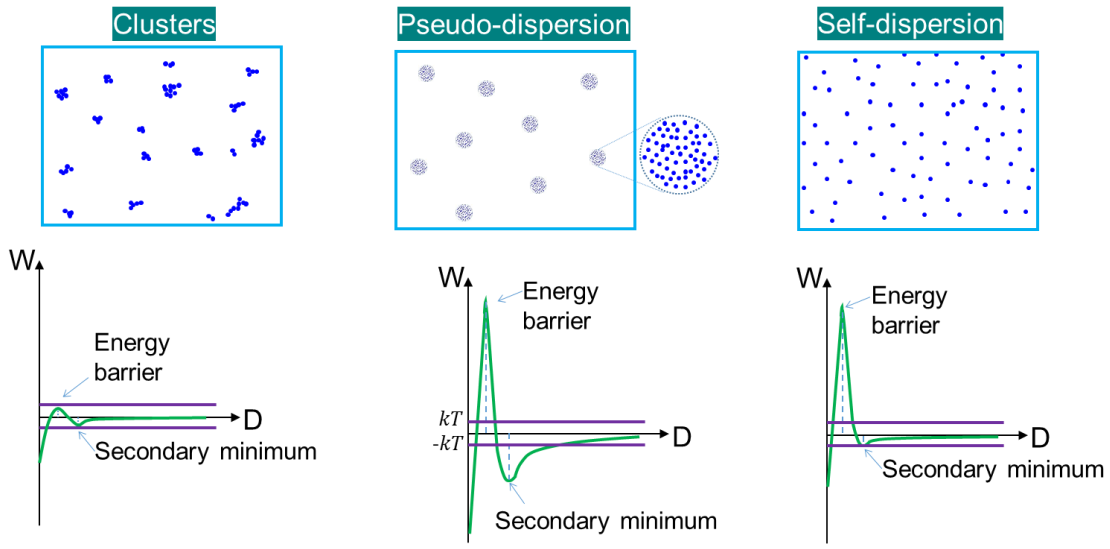

Figure 2-8 Interaction potential for nanoparticles to form cluster, pseudo dispersion and self-dispersion [Xu 2015'].

Based on the theory, Chen et al. [Chen 2015'] achieved uniform dispersion of SiC nanoparticles in Mg alloy matrix. They dispersed 1vol% SiC nanoparticles in Mg-Zn alloy by ultrasonic processing and then evaporate Zn and part of Mg to condense nanoparticles to as high as 14vol%. The SEM images of the Mg-14vol%SiC are shown in Figure 2-9, high volume fraction nanoparticles is uniformly distributed and dispersed in the Mg matrix. The good dispersion provides evidence that SiC nanoparticles were dispersed effectively by ultrasonic processing and self-stabilized in the molten Mg alloy. Moreover, they found that, at molten state, the samples remained the dispersed state even after the ultrasonic processing stopped for 4 h.

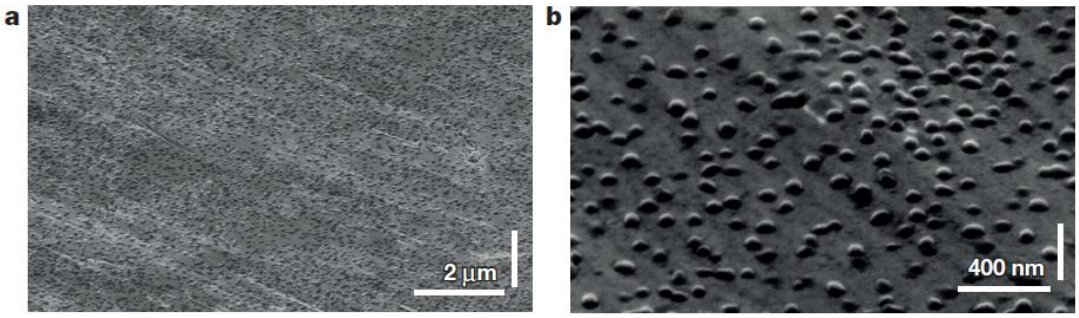

Figure 2-9 Uniform dispersion of SiC nanoparticles in as-solidified Mg alloy matrix [Chen 2015'].

This dispersion mechanism is explained by the previously mentioned self-dispersion theory. The wetting angle between Mg melt and SiC nanoparticle is 83° at the processing temperature, which provides an energy barrier of 3.87×10^4 zJ to protect nanoparticles from sintering and fuse together. The attractive van der Waals potential is calculated to be about -12.17 zJ at the secondary minimum. Meanwhile, the Brownian thermal energy is about 13.8 zJ at the processing energy. The secondary minimum is smaller than the thermal energy which suggest that the thermal energy could drive SiC nanoparticles overcome the energy well and move freely in the Mg melt. The high energy barrier (3.87×10^4 zJ) caused by the interfacial energy is three orders of magnitude higher than the thermal energy which means it could be very effective to prevent the formation of clusters.

2.3 Immiscible Materials Processing

Immiscible materials with a miscibility gap in the liquid state are not only scientifically important, but also they can offer unusual properties that can enable a wide range of applications [Ratke 1995, Kaban 2011, Ma 2005 and Wang 2002]. However, it has been a long-standing challenge to effectively control the diffusional growth and coagulations of immiscible minority droplets during cooling in order to obtain micron or nanoscale minority phase well-dispersed in

bulk alloy liquids and/or in the solids, which is essential for the unique properties and applications envisioned [Ratke 1995, Kaban 2011]. After decades of effort, several methods are developed to process immiscible alloys. Unfortunately, each of these methods can only address one aspect of the challenge. The uniform distribution of the small-sized minority phase in the whole sample was rarely achieved so far. The processing methods can be grouped to two categories, solid state processing and liquid state processing.

2.3.1 Solid State Processing

In solid state processing, powders of immiscible metals are mixed together and sintered by using powder metallurgy technology [Mackay 1977, Koch 1989, Kumar 2015 and Lavernia 1986]. This method avoids phase segregation in the miscibility gap and obtain homogeneous distributed minority phase. However, the powders are easy to be oxidized or contaminated, which leads to poor coherence between powders. Furthermore, this solid state processing is still not cost effective and hard to produce large parts.

2.3.2 Liquid State Processing

Liquid state processing is potentially a low-cost and high quality alternative for immiscible alloy processing. However, the miscibility gap poses huge challenge to get a uniform distribution of the small-sized minority phase in matrix.

Casting under microgravity condition [Carlberg 1980, Gelles 1978 and Ozawa 2004], electromagnetic forces [Da Daoan 1988] have been investigated. While these methods can reduce the sedimentation trend induced by the gravity, they cannot control the diffusional growth of the minority phase. Rapid cooling can reduce the diffusional growth time of the minority phase. Currently, rapid solidification is the most effective way to control the size of the minority phase

during cooling by reducing the time for both diffusional and colliding growths of the minority liquid phases. Inert gas atomization [Wang 2002], melt spinning [Kim 1991], spray deposition [Rudrakshi 2004] and laser cladding [Zhou 2014, Zhou 2018] were usually used to cool immiscible liquid alloy rapidly to solid state. However a high temperature gradient under rapid cooling will induce severe thermocapillary forces [Doi 1993, Ratke 1995] to push these droplets to the hotter region. Also the sample size will be severely limited by the rapid cooling techniques. Therefore, a novel method to effectively control the growth of minority droplets in immiscible materials is highly demanded.

2.4 Conventional Phase Control Methods for Solidification Processing

Phase control during materials processing is vital to achieve desired properties. Numerous materials with excellent properties could be designed if effective phase control can be achieved. However, it is a long-standing challenge to achieve effective phase control in solidification processing of metals due to the harsh environment such as high temperature, extreme chemical conditions, highly electrical conductive liquid and fast atoms diffusion at liquid state. In traditional bulk metal solidification processes, conventional methods such as rapid cooling, inoculation and alloying have generally been used for phase control to achieve better properties. Unfortunately, these conventional methods have reached certain technical or fundamental limits. For example, to achieve rapid cooling rates, the material sample size and processing window will be significantly limited. This barrier impedes the scalable manufacturing of numerous materials for desired properties. Therefore, there are strong demands to break the limits for solidification process and provide new opportunities for metal researches and industries.

2.4.1 Inoculation

Grain refinement in metals during solidification is of great interest due to the enhanced mechanical properties, more homogeneous microstructure and improved processability with refined microstructures. It is now well established that the grain refinement of the as solidified metal is mainly dictated by the nucleation and grain growth [Fan 2018]. In inoculation method, the added particle and extra alloying elements are frequently used to control the nucleation and grain growth, respectively. The potency, size distribution and number density of nucleant particles affect the process of nucleation by inoculation. The extra solute alloy elements, however, control the rate of growth restriction by the alloy chemistry.

(1) Free growth theory

The classical heterogeneous nucleation theory, based on the spherical cap model, identifies that the interface between particles and melt can reduce the free energy barrier to nucleate. The wetting angle between particle and molten metal becomes the major factor determining the effectiveness of the inoculation particles. However, this classical spherical model breaks down at small wetting angles, corresponding to small undercooling required, at which the thickness of the edges of the spherical cap become less than the diameter of an atom and lost the physical meaning. For example, numerous researches have shown that the undercooling of Al-Ti-B grain refiner for pure Al is very small (< 0.5 K and perhaps < 0.01 K) [Greer 2000, Johnsson 1993]. The classical spherical-cap model for heterogeneous nucleation cannot be applied.

Greer et al. [Greer 2000] built the free growth theory that is now commonly used to predict the grain size would be obtained in Al with the addition of Al-Ti-B grain refiner. As shown in Figure 2-10, they assumed that a nucleus is formed on the face of a particle at low undercooling

either by low contact angle spherical cap or by adsorption. The nucleus cannot survive if the radius is below the critical *r** at the instantaneous temperature. *r** is defined by the classical nucleation theory:

$$r^* = (\frac{2\gamma T_m}{L_v})\frac{1}{\Delta T} \qquad 2\text{-}11$$

where γ is the solid/liquid interface energy, T_m is the melting temperature, L_v is the latent of fusion per unit volume, ΔT is the undercooling of the liquid metal. The free growth is not possible if the diameter of the particle *d* is smaller than *2r**. Only when *r** is reduced by the increased undercooling (ΔT), then the free growth becomes possible. Therefore, the critical condition for free growth to occur is when *d=2r** at which the undercooling for free growth $\Delta T_{fg} = \frac{4\gamma}{\Delta S_v d}$ (Equation 2-5). Thus the undercooling needed for free growth is inversely related to the substrate size. Also, the condition of free growth model is not depended on whether the wetting angle between crystal and particle is good or not.

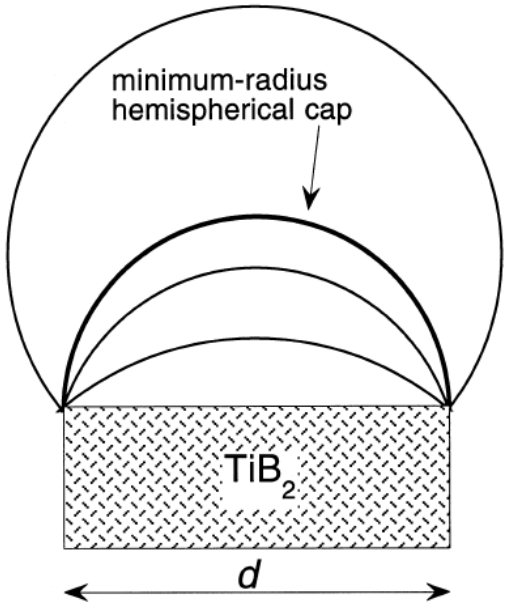

Figure 2-10 Schematic of cluster growth in the adsorption model highlighting the critical radius.

Instead of considering the barrier for grain initiation in the formation of the solid for the classical heterogeneous nucleation theory, free growth model assumes that the barrier is the free growth from the particle. Therefore, from the free growth theory the nucleation is a deterministic behavior depending on the undercooling rather than a stochastic process controlled by nucleation, which benefits us to quantitatively model the grain refinement in casting metals. Greer et al. [Greer 2006] mapped out regions of grain initiation controlled by nucleation or free growth with respect to particle size and undercooling as shown in Figure 2-11. Grain initiation is controlled by nucleation/adsorption at high undercoolings because high undercooling is enough to pass through the free growth limit. Meanwhile, at low undercoolings, the grain initiation is controlled by the free growth from the particles. When particle is really small, the undercooling required for free growth is so large that nucleation could occur elsewhere (e.g., crucible wall, impurities) in the melt.

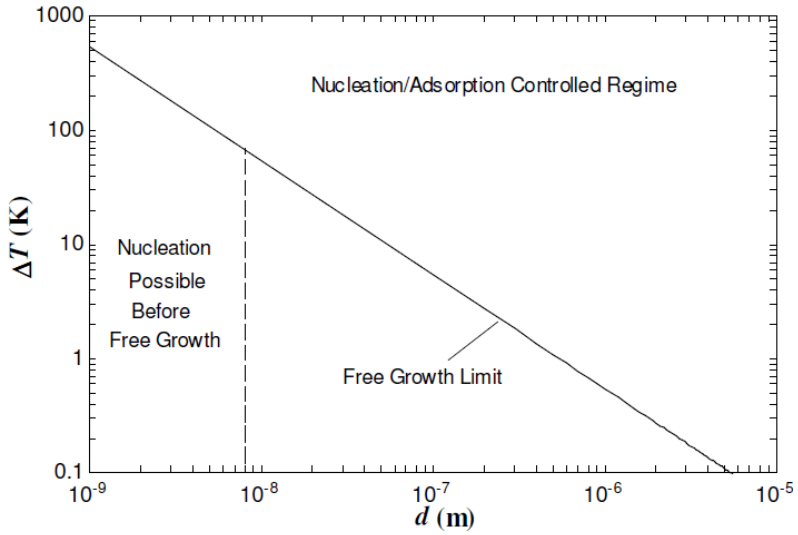

Figure 2-11 Map of grain initiation regions showing that the initiation of a grain may be controlled by the nucleation/absorption or by the onset of free growth [Greer 2006].

(2) Growth restriction by alloying

As previously mentioned, while particles control the grain initiation either by nucleation or free growth, the grain growth is generally controlled by the solute atoms in the alloy system described by the alloy chemistry. During the solidification of metallic alloys, due to the solubility difference between solid and liquid phases, solute atoms tend to either accumulate or deplete at the solid/liquid interface depending on the alloy chemistry. It is well established that the accumulation/depletion of solutes can restrict the grain growth during solidification. On one hand, the grain growth speed is slowed by the accumulation/depletion zone due to the requirement for diffusion of solute atoms to occur prior to continuing grain growth. This delay of grain growth reduces the rate of latent heat release and allows additional nucleation to occur. On the other hand, solutes are able to create constitutional supercooling zone in front of the solidification front. As shown in Figure 2-12a, the solute profile in front of the solid/liquid shows an accumulation zone in the liquid phase. Figure 2-12b is the temperature profile corresponding to the solute concentration profile showing a constitutional supercooling zone (CS zone) between the liquidus temperature (T_E) and actual temperature (T_A) in the melt. It is well recognized [Stjohn 2011, Qian 2006] that CS zone with sufficient undercooling can induce nucleation, especially with existence of potent particles, due to the extra undercooling caused by constitutional supercooling. The formation of new nucleus prevents dendrite formation and produces equiaxed grain structures.

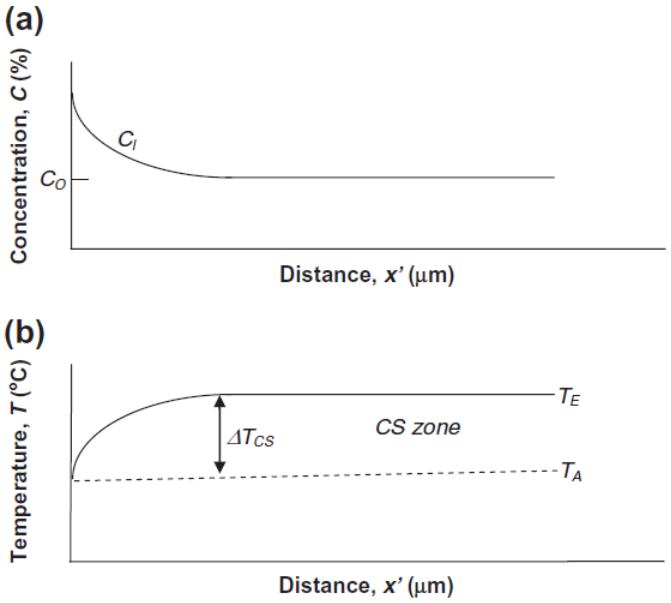

Figure 2-12 Schematic description of the constitutional supercooling. (a) Concentration of solute in front of solid/liquid interface; (b) The temperature profile ahead of solid/liquid interface. x' is the distance to the solid/liquid interface, T_e is the liquidus temperature, T_A is the actual temperature and ΔT_{cs} is the constitutional supercooling [Stjohn 2011].

As shown in Figure 2-13, Easton et al. [Easton 2016] summarized that grain size could be predicted by the sum of x_{cs} (distance between nucleus center and solid/liquid interface), x'_{dl} (diffusional length described by the accumulation zone of the solutes) and average interparticle spacing (x_{sd}). The first two terms determine the size of nucleation-free zone in which the undercooling is insufficient to activate nucleation ($\Delta T_n < \Delta T_{cs}$). It has been reported that nucleation free zone can contribute more than 50% of the final grain size [Stjohn 2015, Stjohn 2011, Prasad 2013]. Therefore, reduction the nucleation-free zone is the key to strategy for grain refinement.

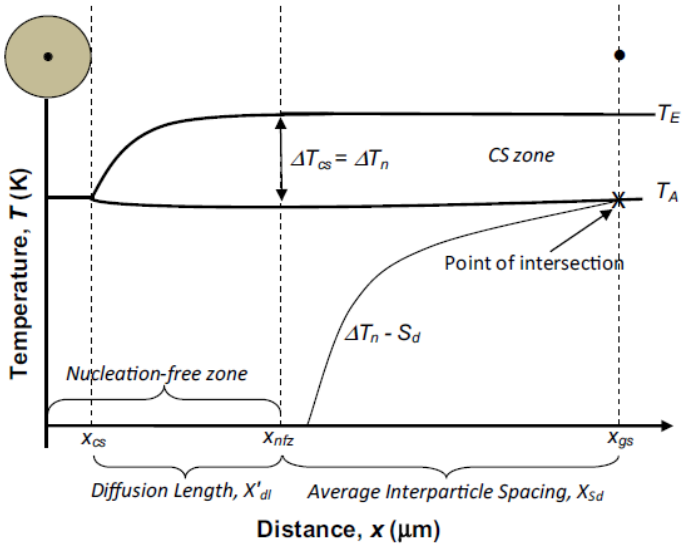

Figure 2-13 Schematic illustration showing the three regions that together establish the grain size: x_{cs} , x'_{dl} and x_{sd} (the distance from the end of the diffusion field to the next most potent particle) [Stjohn 2015].

The growth restriction by alloy solute is described by the restriction factor Q and it is extensively used to predict grain size for different alloy systems. Q is defined as

$$Q = mC_0(k-1) \qquad 2\text{-}12$$

where m is the liquidus slope in a linear phase diagram, C_0 is the solute content in the alloy and k is the equilibrium solute partition coefficient. In addition, it has been suggested that Q could also be defined as the available undercooling for the formation of the initial solid as shown in Figure 2-14 and therefore Q can be expressed as

$$\mathrm{Q} = \left(\frac{\partial(\Delta T_c)}{\partial f_s}\right)_{fs\to 0} \qquad 2\text{-}13$$

where ΔTc is the constitutional undercooling, and f_s is the solid fraction.

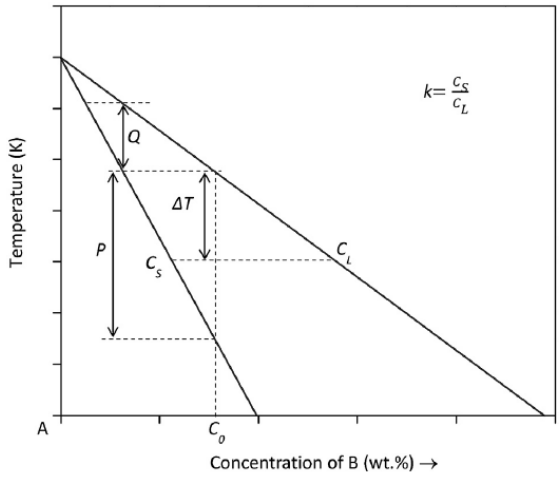

Figure 2-14 Schematic illustration of a linear phase diagram showing the growth restriction factor *Q* [Fan 2018].

In addition, extensive published studies have shown an empirical relationship between average grain size (d) and restriction factor *Q* for alloys [Qian 2010, Easton 2008 and Stjohn 2005]:

$$d = a + \frac{b}{Q} \qquad 2\text{-}13$$

where *a* is a constant related to the number density of nucleant particles and *b* is a constant related to the potency of the particles. As shown in Figure 2-15a, the grain size changes with different potency of particles while keeping the number density of particles constant. A smaller slope (*b''*) corresponds to a larger potency. The intercept (*a*) is related to the number density of particles at infinite *Q*. Figure 2-15b shows the grain size change with the particle number density (increase the density of particles result in a smaller *a*) while the potency of the particle is a constant.

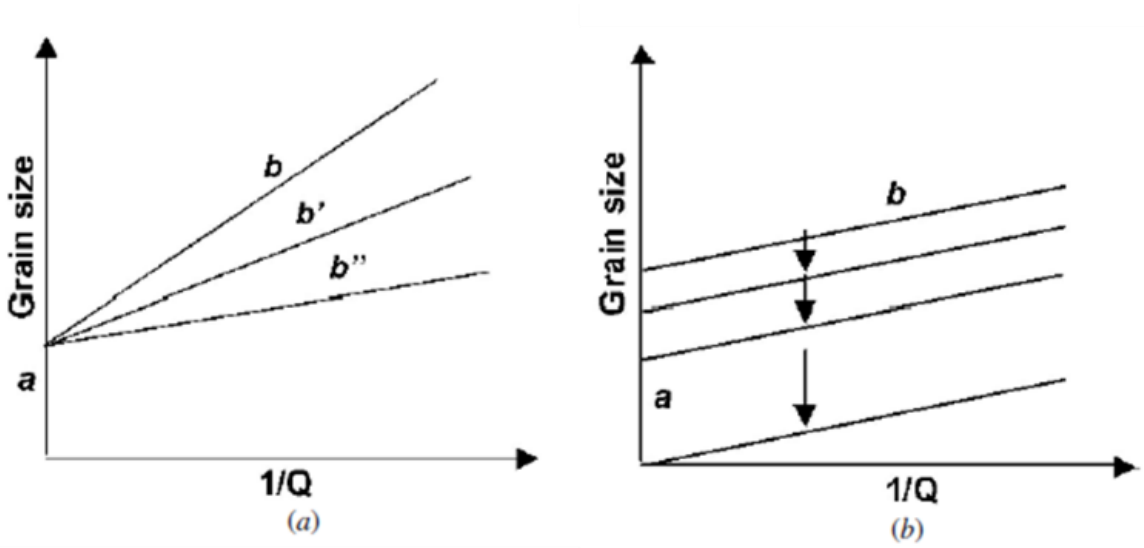

Figure 2-15 (a) Effect of changing potency of the particle on the gradient *b*. The particle is more potent with smaller slope. (b) Effect of changing number of particles [Qian 2005].

Table 2-1 Growth Restriction Factor, *m(k-1)*, of various alloying elements in Al and Mg. [Easton 2005, Stjohn 2005]

For Al		For Mg	
Element	m(k-1)	Element	m(k-1)
Ti	~220	Fe	52.56
Ta	105	Zr	38.29
V	30	Ca	11.94
Hf	11.2	Si	9.25
Mo	7.5	Ni	6.13
Zr	6.8	Zn	5.31
Nb	6.6	Cu	5.28
Si	5.9	Ge	4.41
Cr	3.5	Al	4.32
Ni	3.3	Sr	3.51
Mg	3	Ce	2.74
Fe	2.9	Sc	2.61
Cu	2.8	Yb	2.53
Mn	0.1	Y	1.7
		Sn	1.47
		Pb	1.03
		Sb	0.53
		Mn	0.15

It is worth to notify that the growth restriction factor *Q* is limited by the phase diagram and alloy composition thus it cannot reach infinite. Table 2-1 summarizes the growth restriction factor *m(k-1)* for different alloy elements in Al and Mg. The maximum value of *m(k-1)* for common Al alloys and Mg alloys are around 220 K and 53 K, respectively. Restricted by the limited growth restriction factor and low nucleation efficiency of inoculation particles, the best grain refinement achieved by inoculation falls into tens of micrometers.

(3) Lattice matching

The free growth theory is based on the assumption that the inoculant particle has high potency to allow solidifying phase to absorb on the particle. Lattice matching between the inoculant and the forming solid phase has been used as the gauge to identify the potency of the inoculant particle [Greer 2016]. The strain energy for the solidifying phase to align with the

inoculant particle could be calculated based on the misfit between the particle and solidifying phase. The less strain needed to align at the particle-solid interface, the more potent of a nucleation will be. The misfit between the particle and solid phase has become one of the major considerations to choose the most suitable inoculation particles for grain refinement.

2.4.2 Rapid Cooling

To modify microstructure of materials during solidification, adjusting the cooling rate is commonly used. With fast cooling rates, a refined microstructure can be obtained. However, to achieve a refined grain structure, very large cooling rates (e.g., thousands to millions degree Kelvin per second) are necessary due to the fast grain growth speed at higher cooling rates. Rapid solidification methods such as melt spinning (a liquid metal stream is impinged on a spinning cold copper drum), or spray atomization (a superheated liquid metal is atomized with gas jets and impinged on a cold substrate) can lead to nanosize grains as well as amorphous metals [Zhang 1999, Zhang 2014, Peker 1993 and Johnson 1999].

For the rapid cooling techniques, the size of the samples and processing windows are significantly limited. To achieve high cooling rates, at least one dimension of sample is limited to micrometers (e.g. ribbons produced by melt spinning). Therefore, it is extremely difficult to produce bulk samples with complex geometry by rapid cooling approach.

Chapter 3 Molten Salt-Assisted Incorporation of Nanoparticles into Metal Matrix

Effective nanoparticle incorporation and dispersion have been long-standing challenges for solidification processing of metal matrix nanocomposites. To investigate the nanoparticles enabled phase control in solidification processing, the incorporation and dispersion issues should be solved first. This chapter reports a novel molten salt assisted self-incorporation method that provides us an effective incorporation of nanoparticles into molten metal with dense and well-dispersed nanoparticles. TiC nanoparticles were successfully incorporated into Al matrix with the assistance of $KAlF_4$ salt. In addition, to maximize the Orowan strengthening effect and study the phase control effect from smaller nanoparticles, TiC nanoparticles with approximately a diameter of 10 nm, which is not available commercially, were synthesized by a simple molten salt based reaction approach. To further improve and simplify the processing of Al-TiC (10 nm) nanocomposites, a novel in-situ reaction and incorporation method was explored, which enable us to finish the synthesis and incorporation by just one-step mixing. High strength and high conductivity Cu-WC nanocomposites were also successfully fabricated by this molten salt method after different salts were tested for optimized processing.

3.1 Salt-assisted Incorporation of TiC Nanoparticles into Al

This chapter reports a molten salt assisted method that enables an effective incorporation of TiC nanoparticles into molten aluminum to produce master nanocomposites with dense and well-dispersed nanoparticles. By dilution of this master nanocomposites into pure aluminum, Al-TiC nanocomposites with various concentrations of nanoparticles can be readily fabricated. Microhardness of the nanocomposites was dramatically enhanced. This simple and scalable

manufacturing process paves a practical way for mass solidification processing of metal matrix nanocomposites.

3.1.1 Introduction

Metal matrix nanocomposites (MMNCs) have great potential in a wide range applications such as aerospace, automotive and 3C industries since they can offer low density, high specific strength, high specific stiffness and high temperature thermal stability. Numerous studies have been carried out to synthesize/ process MMNCs, of which the most widely used are mechanical alloying [Poirier 2010, Suryanarayana 2013], friction stir processing [Berbon 2001, Salehi 2012 and Azizieh 2011] and solidification processing [Hassan 2007, Chen 2013]. Solidification processing is cost effective and promising for mass production of MMNC components. High intensity ultrasonic waves have been applied to disperse nanoparticles (NPs) up to about 3 vol% by the intense transient cavitation and acoustic streaming during solidification processing. However, effective incorporation and dispersion of high percentage of nanoparticles into molten metals are still very difficult due to the high specific surface energy and van der Waals attraction force between NPs. Another major challenge is the oxide layer formed on the surface of the molten metal acting as an obstacle for an effective incorporation of NPs.

Molten fluoride salts can dissolve oxide films and thus have been experimented for the incorporation of ceramic particles into aluminum melts [Kennedy 1999, Kennedy 1999' and Nabawy 2015]. Here we report a simple solidification nanoprocessing method, which utilizes fluoride salt for self-incorporation of high loading TiC nanoparticles to Al to produce master nanocomposites which can be diluted to get bulk MMNCs. A uniform dispersion of TiC nanoparticles in the aluminum matrix nanocomposites offers a dramatic mechanical property enhancement.

3.1.2 Materials and Methods

$KAlF_4$ powders (AMG Aluminum, melting temperature: 600 °C) were mixed with 10 vol% TiC nanoparticles (with an average diameter of 50 nm, US Research Nanomaterials, Inc) in acetone and ultrasonic processed for 2 h to obtain powder mixture. Then acetone was evaporated and the powder mixture was dehydrated in a vacuum furnace at 150 ℃ for 12 h. Under argon gas protection, a pure Al ingot (Rotometals, 99.8%) was then melted at 820 ℃ in a graphite crucible with an inner diameter of 100 mm and a height of 150 mm. Then the mixed $KAlF_4$-10vol% TiC powders were manually loaded on the surface of the molten Al. The volume fraction of TiC nanoparticles in Al was designed to be 15 vol%. Then a titanium propeller (with boron nitride coating) was located below the Al-$KAlF_4$ interface and stirred the melt at a speed of 200 rpm for 50 min until the molten salt become clear. Finally, the molten melt was allowed to solidify in air (~ 1 K/s), which produced a "master nanocomposites" with approximately 9 vol% TiC nanoparticles. The microstructures were characterized by Field Emission Scanning Electron Microscopy (SEM) (Zeiss Supra 40) equipped with Energy Dispersive Spectrometry (EDS). Samples of the Al matrix nanocomposites were cut from the as-solidified ingots and prepared by grinding and low-angle ion milling. Vickers hardness tests were conducted using a 200 gf load for 10 s by LM 800AT microhardness tester.

3.1.3 Results and Discussion

Figure 3-1a shows the SEM and TEM images of the as received TiC nanoparticles with an average diameter of 50 nm. The mixture of $KAlF_4$ and TiC nanoparticles after ultrasonic processing and dehydration is shown in Figure 3-1b. Nanosize TiC particles stay on the surface of micro size $KAlF_4$ salt crystals. Figure 3-2a shows the schematic illustration of the process and mechanism of salt assisted self-incorporation for production of Al-TiC master nanocomposites.

When $KAlF_4$-TiC powder mixture was added on the surface of molten Al, molten $KAlF_4$ can dissolve the aluminum oxide film on the surface of the Al melt to provide a clean Al-$KAlF_4$ interface [Liu 2016, Kennedy 1999]. Furthermore, because of the partial metallic bond in TiC, TiC wets better with Al melt than the $KAlF_4$ melt. Thus during mechanical mixing, TiC nanoparticles can be self-incorporated or transferred from molten $KAlF_4$ to Al to reach a more favorable energy state. The efficiency of the self-incorporation of nanoparticles was around 60%, which means that some TiC nanoparticles will still remain in the $KAlF_4$ salt. The remained $KAlF_4$-TiC mixture could be recycled in practical industrial production. This self-incorporation method enabled us to realize the scalable manufacturing of high volume fraction Al-TiC master nanocomposites, which can be readily diluted to Al-Bi immiscible alloy.

Figure 3-2b shows the SEM image of the Al-9vol% TiC master nanocomposites. As marked by the white dash line in Figure 3-2b, TiC nanoparticles are mainly distributed in the TiC nanoparticles rich domains. It is observed that these nanoparticles rich zones are mainly distributed around the Al grain boundaries. This phenomenon is originated from the pushing effect during the solidification [Xu 2012]. Nanoparticles were repulsed by the van de Waals force from the solidification front and accumulated in the last solidified zone which is grain boundary region, as shown in Figure 3-2c, TiC nanoparticles are well dispersed inside the nanoparticles rich domain. It is interesting to note that even though TiC nanoparticles existed as micrometer scale clusters on the surface of $KAlF_4$ before incorporation, they were well dispersed in nanoparticles rich domain. This dispersion might originate from the good dispersion of TiC nanoparticles in $KAlF_4$ melt. It is highly possible that TiC nanoparticles were able to disperse well in salt melt due to the free floating ions. TiC nanoparticle could attract a layer of cations or anions on the surface so that nanoparticles could be dispersed [Chen 2015', Zhang 2017]. During the process of self-incorporation, each TiC

nanoparticle could be incorporated in to the molten Al individually and keep the dispersed state. Thus salt assisted self-incorporation method can also offer a good dispersion in metal matrix nanocomposites production. The salt assisted self-incorporation method enable us to fabricate master Al-TiC nanocomposites by just mechanical mixing which can be easily applied to industrial scale production.

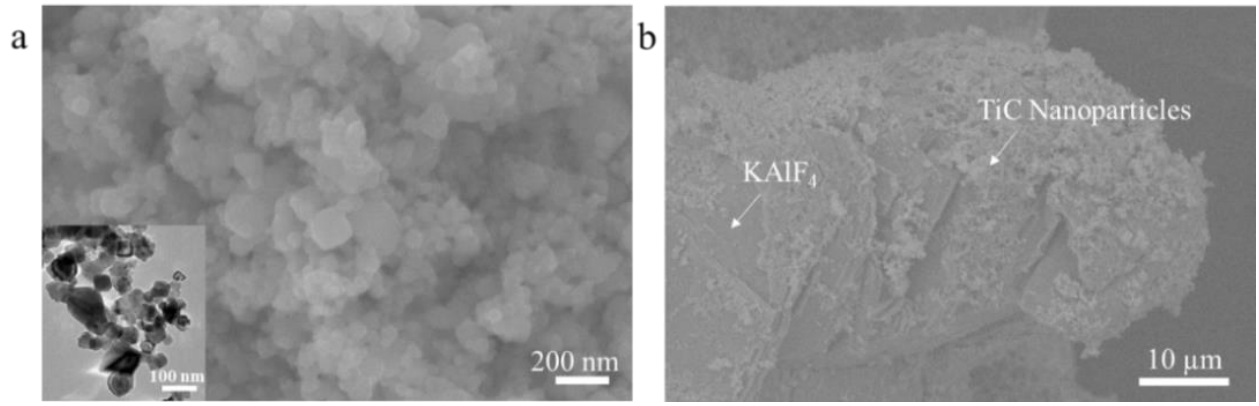

Figure 3-1 (a) SEM image of the as received TiC nanoparticles, inset is the TEM image of as received TiC nanoparticles; (b) SEM image of the mixed $KAlF_4$ powder and TiC nanoparticles.

Moreover, it is very common to observe the reaction between TiC and Al melt described by the following equation:

$$13Al_{(l)} + 3TiC_{(s)} \rightarrow 3Al_3Ti_{(s)} + Al_4C_{3(s)} \qquad 3\text{-}1$$

However, it is observed in Figure 3-2 that there are little Al_3Ti phase in the Al-9vol%TiC master nanocomposites. It could be explained by the thermodynamic calculations and the designed processing temperature. Karantzalis et al. [Karantzalis 2011] calculated that the free energy of equation ΔG is negative at 750 °C while it is positive at 800 °C. This calculation suggests that the reaction of equation is favorable below 750 °C. When the temperature is above 750 °C, TiC could thermodynamically stay stable in Al melt. The reaction between Al and TiC should only occur

during cooling of the melt. In this study, we kept the processing temperature at 820 °C which is capable to prevent the reaction between TiC and Al melt. Therefore, there are little Al_3Ti intermetallic phase found in the Al-TiC master nanocomposites.

Microhardness enhancement of the Al-TiC nanocomposites is shown in Figure 3-3. With the addition of TiC nanoparticles, mechanical property of Al matrix was dramatically enhanced. The microhardness of Al-9vol% TiC nanocomposite reaches as high as 114 HV, which is nearly four times more of pure Al (23 HV). A higher volume fraction of TiC nanoparticles, offers higher microhardness for the nanocomposites. Al-9vol% TiC nanocomposite exhibits significant microhardness increment among the nanocomposites fabricated by solidification process, and only slightly lower than that fabricated by time-consuming powder metallurgy. However, much further enhancement of the Al-TiC nanocomposite synthesized here can be achieved by plastic deformation in the future. Moreover, this method can also be applied to process alloys to further strengthen and tune the microstructure of the alloys.

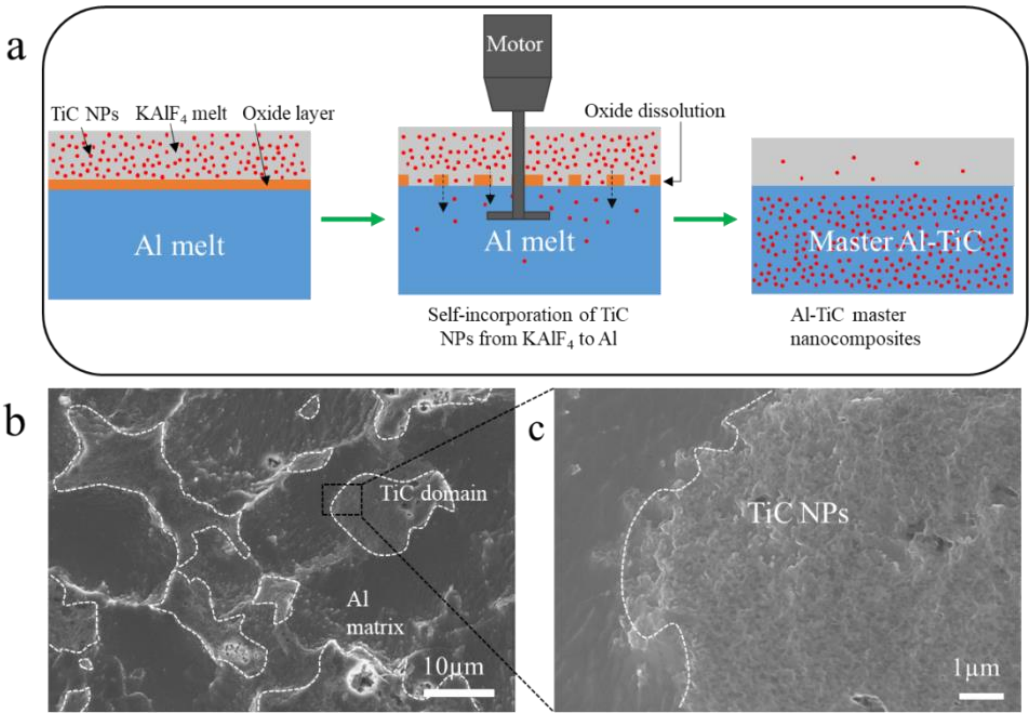

Figure 3-2 Production of master Al-TiC nanocomposites. (a) Schematic illustration of the salt assisted self-incorporation to fabricate master Al-TiC nanocomposites; (b, c) SEM image of Al-9vol%TiC master nanocomposite.

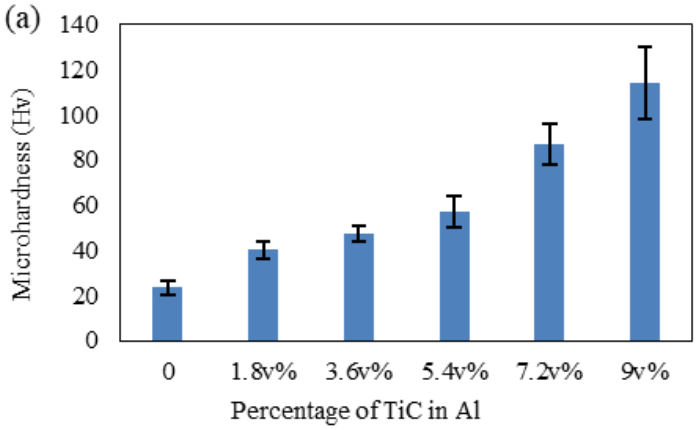

Figure 3-3 Microhardness of Al-TiC nanocomposites with different volume fraction of nanoparticles.

3.1.4 Summary

A self-incorporation of high loading TiC nanoparticles into Al assisted by molten salt was successfully demonstrated to produce master nanocomposites, which provides a cost-effective and scalable manufacturing process to fabricate bulk MMNCs through solidification processing. The simple method with a pre-processing at room temperature and a mechanical stir during melting process, can largely overcome the long-standing problems of nanoparticles incorporation and dispersion in solidification nanoprocessing. The novel method paves a way for mass production of high performance metal matrix nanocomposites for industrial applications.

3.2 Synthesis TiC Nanoparticles (10 nm) by Molten Salt Reaction

Titanium carbide (TiC) nanoparticles have great potential for strengthening metals as TiC has high hardness, high Young's modulus, good conductivity and excellent wear resistance. To enable effective Orowan strengthening effect, smaller TiC nanoparticles (e.g. < 10 nm) are highly preferred. However, small TiC nanoparticles (< 10 nm) are not commercially available. Current production methods either cannot produce such small TiC nanoparticles or cannot manufacture nanoparticles in large scale. Here we developed a facile molten salt based reaction method that can manufacture TiC nanoparticles with diameter about 10 nm. Diamond nanoparticles were used as the carbon source and reaction template. Titanium powders dissolve in molten salt and deposit on the diamond nanoparticles and then react with diamond to form TiC nanoparticles. This method provides a simple and inexpensive pathway to manufacture TiC nanoparticles and opens up the opportunity for making high performance metal matrix nanocomposites (MMNCs) reinforced by TiC nanoparticles.

3.2.1 Introduction

TiC offers high hardness, high strength, high Young's modulus, and good electrical conductivity due to its partial metallic bonds, and thus it is considered as a good reinforcement for metal matrix nanocomposites (MMNCs) [Miracle 1983, Nemati 2011 and Meenashisundaram 2015]. There are numerous research activities on using TiC micro/nano particles as reinforcements for strengthening metals such as aluminum and magnesium. Recently, we have incorporated as high as 9 volume percent (vol%) 60 nm TiC into Al by using a self-incorporation method with the assistance of $KAlF_4$ flux [Liu 2016]. However, the strengthening effect of resultant MMNC samples was mainly from the load bearing effect instead of Orowan strengthening which involves bowing dislocation between particles during plastic deformation.

To active effective Orowan strengthening in metal matrix nanocomposites, shorter distance between particles is preferred. Thus to achieve a better strengthening effect, smaller nanoparticles (below 10 nm) is desired. As shown in Figure 3-4, the calculated Orowan strengthening effect from TiC nanoparticles in Al matrix indicate that, at the same volume fraction of nanoparticles, strength enhancement from 10 nm nanoparticles is significantly higher than 50 nm nanoparticles. Therefore, there is a strong motivation to incorporate small TiC nanoparticles (e.g. less than 10 nm) into metal matrix for ultra-strong MMNCs.

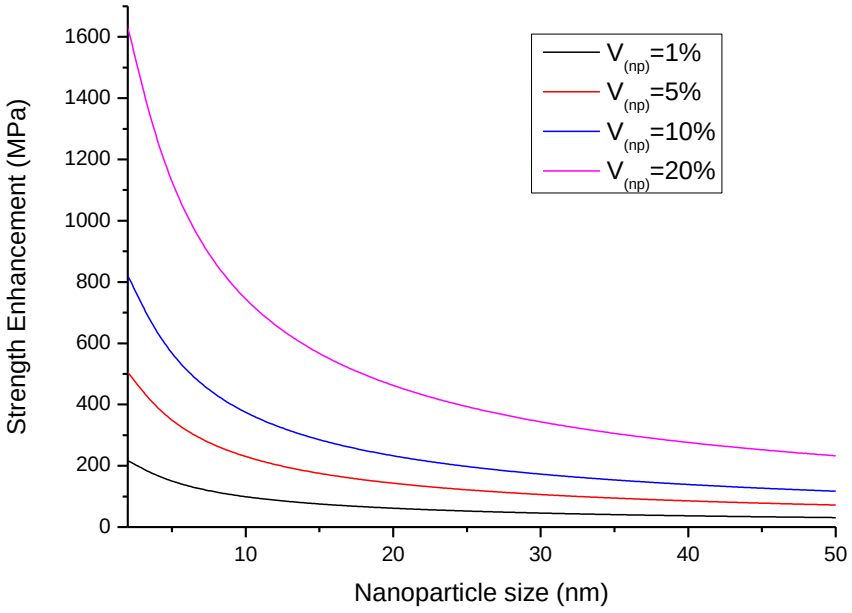

Figure 3-4 Orowan strengthening effect for Al-TiC system.

Nevertheless, TiC nanoparticles below 10 nm are not readily available in the market. Several methods including carbonthermal reduction process, Sol-Gel process, plasma method and combustion synthesis have been developed [Wei 2011, Zhang 2008', Kiesler 2015 and Aruna 2008]. The most popular and commercialized method is the carbonthermal reduction method [Shin 2015, Lee 2007 and Lee 2003]. However, these methods at least will bring one of the following problems: (1) formation of coarse particles due to a high temperature reaction, (2) the formation of a non-stoichiometric powder ($TiC_{0.7\sim0.9}$), (3) time consuming and expensive milling process. Therefore, a new scalable and inexpensive method which can produce small size (below 10 nm) TiC nanoparticles is needed.

Molten salt reaction to produce nanoparticles is a relatively new, simple and low cost method. There are several research activities using molten salt systems for metal deposition

especially titanium on different types of ceramic material such as diamond, TiN, Al_2O_3, SiC, CNTs and carbon fibers [Li 2003', Baumli 2005, Li 2008 and Li 2008']. While other deposition techniques such as Physical vapor deposition (PVD), chemical vapor deposition (CVD) are mainly applied to flat surface, molten salt based reaction enables us to coat different surfaces include particles.

Inspired by molten salt assisted coating method, we deposited a titanium layer on the 10 nm diamond nanoparticles, and then allowed titanium to react with diamond to synthesize TiC nanoparticles. As titanium dissolves in the molten salt, the final size of the TiC nanoparticles is determined by the size of the diamond nanoparticles. Moreover, it is shown that other carbon source such as carbon black, which is significantly cheaper than diamond, can also be used for molten salt based reaction [Li 2011]. Thus this molten salt reaction method opens up a new pathway to manufacture TiC nanoparticles (< 10 nm) for fabrication high performance MMNCs in industrial scale.

3.2.2 Materials and Methods

Diamond nanoparticles (3-10 nm, US Research Nanomaterials, Inc.) were mixed with 40 weight percent (wt.%) Potassium chloride (KCl) (99.1%, Fisher Scientific), 40 wt.% Sodium chloride (NaCl) (99.5%, Fisher Scientific), and 20 wt.% Potassium hexafluorotitanate (K_2TiF_6) (Sigma Aldrich) in ethanol with an ultrasonic processing for 2 hours. For the ultrasonic processing, a titanium probe was inserted about 6 mm deep into the liquid mixture. The probe was attached to a booster (Misonix Sonicator 3000). A peak-to-peak vibration amplitude of 60 μm and a frequency of 20 kHz were used. The volume fraction of diamond nanoparticles in the salt mixture is 5 vol%. Then ethanol was evaporated and the powder mixture was dehydrated in a vacuum furnace at 150 °C for 12 hours. Titanium powders (44 μm, 99%, Alfa Aesar) were added and mixed with the

dehydrated powder mixture by a mechanical shaker (molar ratio between carbon and titanium was designed to be 1:2.5 and 2:1). The schematic of the experiment setup is shown in Figure 3-5. The powder mixture were put inside a graphite crucible with an inner diameter of 100 mm and a height of 120 mm and covered by an aluminium oxide lid. Then the graphite crucible with lid was sealed in a stainless steel autoclave for high temperature reaction. Under argon gas protection, the autoclave was heated up by an electrical resistance furnace to 900 °C and held for 1 hour. Then the autoclave was cooled down in air and synthesized product was removed.

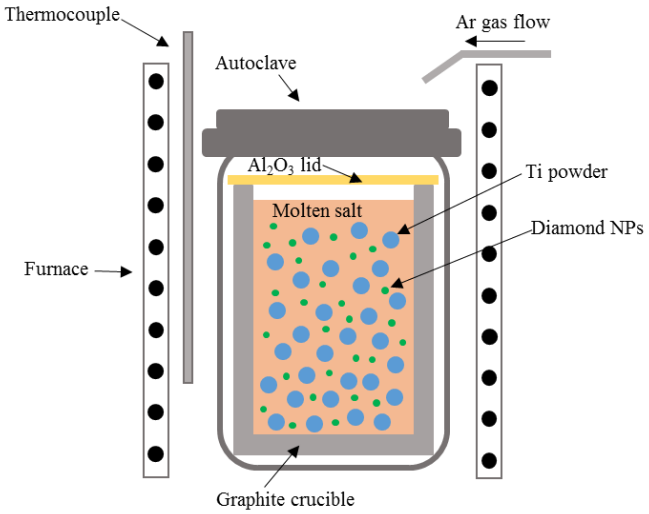

Figure 3-5 Schematic of the experimental setup used for TiC production.

To incorporate synthesized TiC nanoparticles into aluminum (Al), the reaction products were mixed with $KAlF_4$ and grinded to fine powders. Under argon protection, pure Al ingot was then melted at 820 °C in a graphite crucible with an inner diameter of 40 mm and a height of 80 mm. The grinded powders were manually loaded on the surface of the molten Al. The volume fraction of TiC nanoparticles in Al was designed to be 2.5 vol%. Then a mechanical mixer was used to mix the melt at 200 rpm for 30 min. Finally, the molten melt was allowed to solidify in air (~ 1 K/s).

To characterize the synthesized TiC powders, the reaction products were washed by deionized (DI) water and then centrifuged at 4000 rpm for 5 min. The top clear liquid was poured out by a glass pipette (removing the dissolved KCl and NaCl). The process was repeated for diluted 10 vol% HCl solution to remove remaining K_2TiF_6. Then the powders were dried at 90 °C. X-ray diffraction (XRD) was used to identify phases in the washed powders. A BEDE D1 high resolution diffractometer using Cu Kα (λ=0.1542 nm) radiation was used. The size and morphology of the synthesized nanopowders and the microstructures of the Al-TiC nanocomposites were characterized by Field Emission Scanning Electron Microscopy (SEM) (Zeiss Supra 40) equipped with Energy Dispersive Spectrometry (EDS), T12 Quick CryoEM, CryoET (FEI, 120 kV) Transmission Electron Microscope (TEM), and Titan S/TEM (FEI, 300 kV) high resolution TEM (HRTEM). Samples of the Al-TiC matrix nanocomposites were cut from the as-cast ingots and prepared by grinding and low-angle ion milling. Mechanical properties of the nanocomposites were evaluated by a LM 800AT microhardness tester under 200 gf with a load time of 10 s. Five random points were tested before a mean value was determined.

3.2.3 Results and Discussion

Figure 3-6 shows the TEM images of the as-received diamond nanoparticles with a size of 3-10 nm. This gives us the opportunity to use the small diamond nanoparticles as reaction template to manufacture 10 nm TiC nanoparticles.

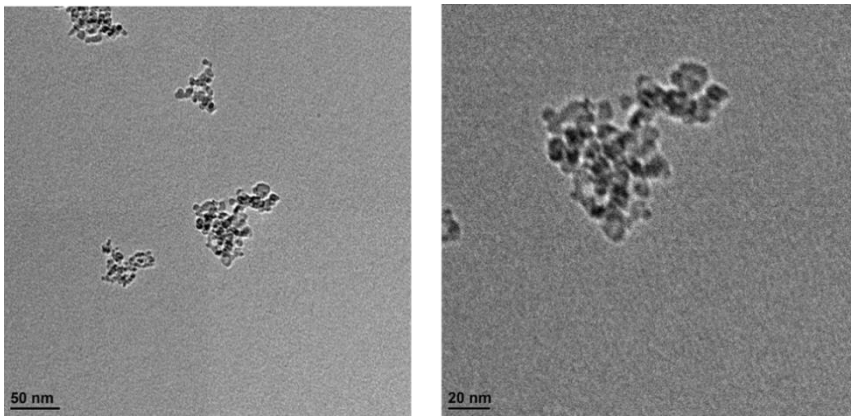

Figure 3-6 TEM images of the as-received diamond nanoparticles.

The XRD results of the synthesized powders of carbon to titanium ratio 2:1 and 1:2.5 are shown in Figure 3-7a and Figure 3-7b, respectively. Although the carbon to titanium ratio is different, the major phase identified is TiC, indicating that the reaction between diamond and titanium occurred. When carbon to titanium ratio is 2:1 (i.e. extra diamond nanoparticles added), there was no titanium remained after the reaction as shown in Figure 3a. However, when we have excessive titanium (C: Ti=1:2.5), there are both diamond and titanium remained in the reaction product.

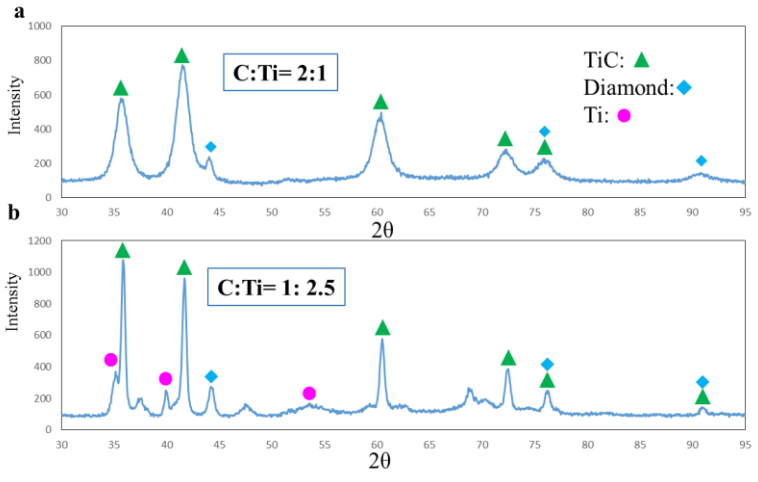

Figure 3-7 XRD patterns of the washed powders (a) C: Ti= 2:1; (b) C: Ti= 1: 2.5.

Figure 3-8 shows a typical SEM image of the washed TiC nanoparticles. Figure 4a and Figure 4b show the size and morphology of the TiC nanoparticles when carbon to titanium ratio is 2:1. Figure 3-8c and Figure 3-8d are the SEM images when the ratio is 1:2.5. There is no obvious difference in terms of the size and shape. These synthesized nanoparticles are spherical shape as shown in the SEM images. As spherical diamond nanoparticles work as the reaction template, the produced TiC nanoparticles are also spherical. It is also observed that small TiC nanoparticles are agglomerated together due to the attractive van der Waals force between nanoparticles.

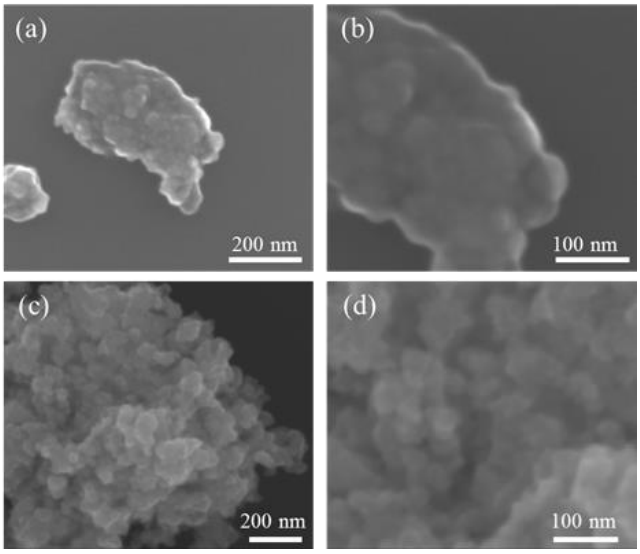

Figure 3-8 SEM images of synthesized TiC nanoparticles. (a) (b) C: Ti= 2:1; (c) (d) C: Ti= 1:2.5.

HRTEM is used to further validate the size and crystal structure of the TiC nanoparticles. Figure 3-9a shows the TEM image of the TiC nanoparticles. Under TEM, we can determine the size of the TiC nanoparticles to be around 10 nm. Figure 3-9b is the HRTEM image to show the atomic scale structure of the TiC nanoparticles. The inset is the Fast Fourier Transform (FFT) image. These dots and rings in the FFT image are corresponded with the TiC crystal structure. By applying mask on these dots in the FFT image and processing the inverse FFT, we can observe the

lattice structure more clearly as shown in Figure 3-9c and 3-9d. The distance between these lattice planes, it is about 0.21 nm and 0.25 nm in Figure 3-9c and 3-9d, respectively. These planes are well matched with (200) plane and (111) plane of TiC crystal.

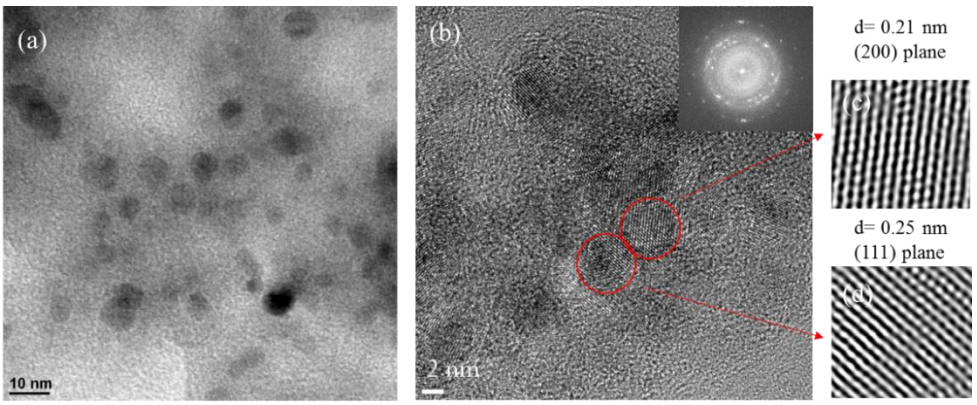

Figure 3-9 TEM images of the synthesized nanoparticles. (a) 120 kV TEM image; (b) HRTEM image of the TiC nanoparticles; The inset is the FFT image; (c) (d) Inverse FFT images of the TiC nanoparticles.

The reaction mechanism can be described as below [Daoush 2014]: in molten salt reactions, K_2TiF_6 dissolved into KCl- NaCl bath and we have free Ti^{4+} cations generated. These Ti^{4+} cations can react with Ti atoms to produce Ti^{2+} in the molten salt base according to the following chemical equation:

$$Ti + Ti^{4+} \rightarrow 2Ti^{2+}(in\ molten\ salt) \qquad 3\text{-}2$$

Then Ti can coat the diamond nanoparticles by the attachment of the Ti^{2+} from the molten salt onto the surface of the diamond nanoparticles. Ti^{2+} decomposed to produce Ti^{4+} and Ti as the following chemical reaction:

$$2Ti^{2+} \rightarrow Ti + Ti^{4+}(on\ diamond\ surface) \qquad 3\text{-}3$$

Then this deposited Ti layer reacted with diamond and form TiC. The reaction between Ti and carbon is a kind of diffusion control reaction. It is necessary to allow deposited Ti fully reacted with diamond nanoparticles, this requires Ti atoms has enough energy and time to diffuse through TiC nanoparticles. Thus shorten time or lower temperature may lead to a core-shell TiC-diamond structure while longer time and higher temperature might lead to larger TiC particles. It is of interests to investigate the relationship between such parameters and the produced TiC nanoparticles in the future work.

The molten salt based reaction method can produce 10 nm TiC nanoparticles efficiently and in a scalable manufacturing way. With a large reaction unit, we can produce large amount of TiC nanoparticles for widespread applications. Moreover, this method is reliable and reproducible, we repeated this reaction experiment over ten times and all of them show consistent results.

Figure 3-10 shows the SEM images, XRD pattern and microhardness data of Al-2.5 vol% TiC nanocomposites. As shown in Figure 3-10a, 3-10b, TiC nanoparticles are well dispersed inside Al matrix. The size of TiC nanoparticles is consistent with synthesized TiC nanoparticles. However, there are also some porosities in the nanoparticle-rich area. These porosities weaken the effect of TiC nanoparticles reinforcing on Al matrix. Figure 3-10c is the XRD spectrum of the as cast Al-2.5 vol% TiC nanocomposites. Figure 3-10d demonstrates the strengthening effect of the incorporated TiC nanoparticles. With only 2.5 vol% addition of 10 nm TiC nanoparticles, the microhardness is improved to 58 HV, which is 2.5 times higher than pure Al. Orowan strengthening, load bearing effect, grain refinement and dislocation density increment by the mismatch of thermal expansion coefficient between nanoparticles and metal matrix all contribute to the strengthening effect. With such small TiC (< 10 nm) nanoparticles incorporated into Al matrix, during plastic deformation, dislocations will be bowed by the TiC nanoparticles effectively

and thus strengthen the composite material significantly. Moreover, based on Orowan theory, smaller gap between particles can bring better strengthening effect. This is the reason why small TiC (<10 nm) is preferred.

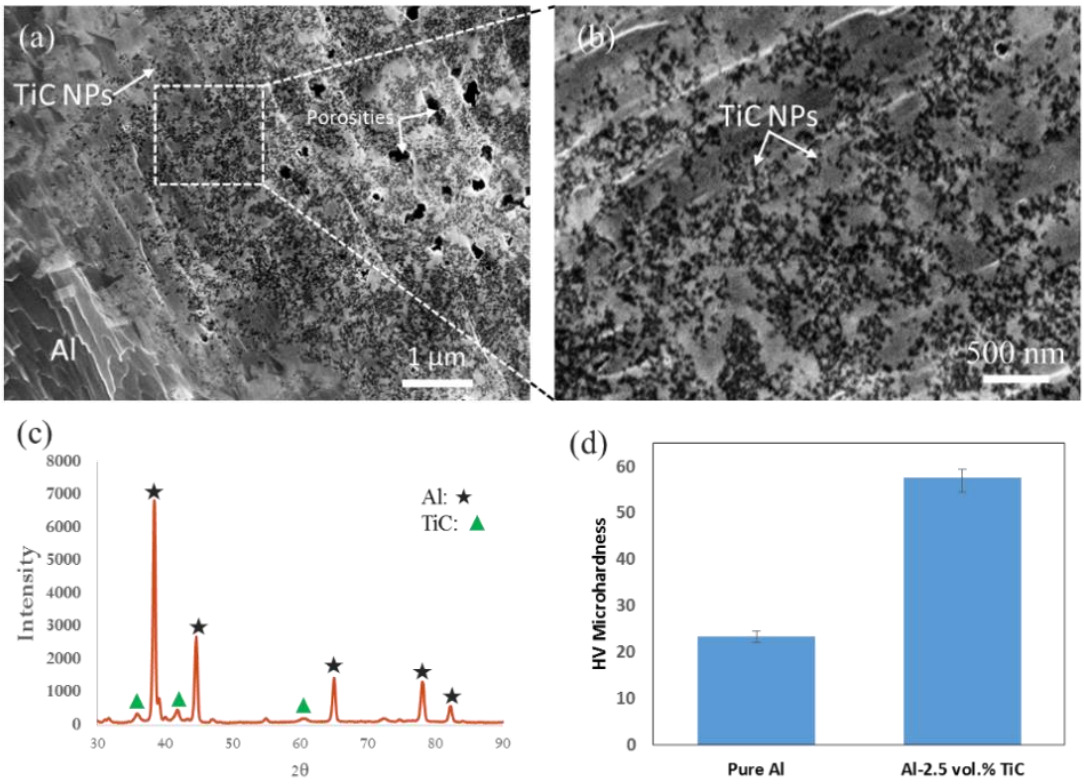

Figure 3-10 (a,b) SEM images of Al-2.5 vol% TiC nanocomposites; (c) XRD pattern of Al-2.5 vol% TiC nanocomposites. (d) Microhardness of as cast pure Al and Al-2.5 vol% TiC nanocomposites.

3.2.4 Summary

TiC nanoparticles with a size of about 10 nm were successfully produced by a new molten salt reaction method. In this process, titanium was deposited on the diamond nanoparticles surface with the assistance of molten salt. Then titanium can diffuse and react with the diamond nanoparticles to produce TiC nanoparticles. This method enable us to produce small (<10 nm) TiC

nanoparticles in a scalable manufacturing route. These synthesized TiC nanoparticles were then incorporated into Al matrix to make Al-TiC nanocomposites. With such small nanoparticles in the matrix, the mechanical property is significantly enhanced. This approach opens up the opportunity to produce MMNCs with high strength and Young's modulus.

3.3 In-situ Molten Salt Reaction and Incorporation of Small TiC Nanoparticles (10 nm) into Al

As mentioned in Chapter 3.2, the size of the nanoparticle is vital for the properties of the MMNCs. Smaller nanoparticles are preferred for a better strengthening effect and better ductility. However, it is extremely difficult to control the size of nanoparticles (e.g., 10 nm) in MMNCs through a scalable solidification process. In this chapter, a novel in-situ molten salt reaction and incorporation method that combines the chemical reaction to synthesis TiC nanoparticles and incorporation of TiC nanoparticles into Al matrix is presented for fabrication Al-TiC nanocomposites. The size of TiC nanoparticles is readily controlled to approximately 11 nm by the diamond nanoparticle reaction templates. The mechanical properties are dramatically enhanced by the incorporation of tiny TiC nanoparticles. This novel in-situ molten salt reaction and incorporation method could potentially be applied to different material systems for high performance MMNCs.

3.3.1 Introduction

The incorporation of nanoscale reinforcements in metal matrix paved a pathway to engineer materials with excellent properties (such as strength, stiffness and ductility) that were challenging to achieve before. The size of the nanoscale reinforcement is the crucial factor determining the properties of the MMNCs. Smaller nanoparticles are highly preferred for a better

strengthening effect and better ductility. The well-known Orowan strengthening theory predicted that smaller nanoparticles, at the same volume fraction, can provide shorter inter-particle spacing and thus a greater resistance to the dislocation movement during plastic deformation leading to a higher strength [Zhang 2008, Zhang 2006 and Nie 2003]. Moreover, it is believed that smaller reinforcement will mitigate the trade-off between strength and ductility for traditional metal matrix composites [De Cicco 2009, Goh 2008 and Jiang 2016]. However, it has been a long-standing challenge to incorporate and disperse small nanoparticles (<10 nm) into metal matrix mainly due to the following reasons: (1) Availability of nanoparticles smaller than 10 nm. Limited by the manufacturing method of nanoparticles, common nanoparticles (such as TiC, WC, TiB_2) used for MMNCs with size below 10 nm are not available on market [Cao 2017]. (2) The active physical/chemical properties of nanoparticles. Nanoparticles have very active physical/chemical properties due to high specific surface area which makes the nanoparticles easily get oxidized or reacted with metal matrix during high temperature processing. (3) Nanoparticles could easily form clusters in metal matrix due to the van der Waals attraction. (4) Nanoparticles coarsening during the processing. Due to the large specific surface area of nanoparticles, they tend to sinter with each other to reduce the system energy. Facing these challenges, it is extremely difficult to fabricate MMNCs with nanoparticles size close to 10 nm for better mechanical properties.

Light metals such as Al based MMNCs are of great interests because of the high specific strength, high specific modulus. TiC nanoparticles have been widely used to strengthen Al because TiC provides high Young's modulus, high hardness and good electrical conductivity [Dikici 2011, Karantzalis 2011]. However, the size of TiC particles used in the previous research is generally larger than 50 nm. For in-situ reaction to fabricate Al-TiC composites, TiC particle size falls into hundreds nanometers to micrometers depend on the cooling rate and reaction time [Amosov 2014,

Bauri 2011 and Tyagi 2005]. It is very difficult to control the size of TiC particles to 10 nm. For ex-situ method, there simply is no TiC nanoparticle smaller than 10 nm available on market. Therefore, previous research failed to produce Al-TiC nanocomposites with particle size less than 10 nm. Moreover, there also exist grand challenges for incorporation of nanoparticles into molten metal. Due to the high surface energy of molten metal, nanoparticles are tend to be repelled by molten metal instead of be incorporated. Ultrasonic processing has been successfully applied to incorporate and disperse nanoparticles into molten metal. But ultrasonic processing can only incorporate and disperse low percentage (e.g., < 3vol%) of nanoparticles and it is difficult for scalable manufacturing.

In this chapter, we proposed a novel salt-assisted in-situ reaction and incorporation method to fabricate Al-TiC nanocomposites with nanoparticle size around 10 nm. The size of TiC nanoparticles are readily controlled by the in-situ reaction template which is diamond nanoparticle in this study. Furthermore, the molten salt based incorporation method allow us to incorporate high percentage of TiC nanoparticles into Al.

3.3.2 Materials and Methods

Diamond nanoparticles (3-10 nm, US Research Nanomaterials, Inc) were mixed with K_2TiF_6 (Sigma Aldrich) and $KAlF_4$ (AMG aluminum) in ethanol and ultrasonic processed for 2 h to obtain mixed solution. For the ultrasonic processing, a titanium probe was inserted about 6 mm deep into the ethanol solution. The probe was attached to a booster (Misonix Sonicator 3000). The volume fraction of diamond nanoparticles in K_2TiF_6-$KAlF_4$ was designed as 5 vol%. Then the mixed solution was dehydrated in a vacuum furnace at 120 °C for 12 h to evaporate ethanol out and get a uniform powder mixture. Pure Al (99.8%, Rotometals, Inc) was melted at 820 °C in a graphite crucible with a diameter of 34 mm and height of 80 mm. Inert argon gas was purged on

the surface of the molten Al to avoid severe oxidation. The mixed K_2TiF_6-$KAlF_4$-Diamond powders were manually loaded on the surface of the molten Al. The volume fraction of newly formed TiC nanoparticles in Al was designed to be 0, 5, 10, and 15 vol%. Then a titanium propeller (with boron nitride coating) was located below the molten Al-salt interface and stirred the melt at a speed of 200 rpm for 20 min. Finally, the molten melt was allowed to solidify in air (~ 1 K/s). Thin plates were cut from the as solidified ingots and cold rolled with a thickness reduction of 20% to further enhance the mechanical properties.

The as cast samples were ground, polished and then ion milled by Precision Ion Polishing System (PIPS, Gatan) for 2 h at an accelerating voltage of 4 kV, with 5° milling angle to expose the microstructure and embedded nanoparticles. X-ray diffraction (XRD) was used to identify phases in the nanocomposite. A BEDE D1 high resolution diffractometer using Cu Kα (λ=0.1542 nm) radiation was used. The microstructural characterization was performed using a ZEISS Supra 40VP Scanning Electron Microscope (SEM) equipped with Electron Dispersive Spectroscopy (EDS) for the elemental composition determination. The TiC nanoparticle size and distribution were analyzed by a T12 Quick CryoEM, CryoET (FEI, 120 kV) Transmission Electron Microscope (TEM). The interfaces between matrix and nanoparticles were studied by a high resolution FEI Titan TEM at 300 kV. The thin film TEM samples were machined by Focus Ion Beam (FIB). Vickers hardness tests were conducted using a 200 gf load for 10 s by LM 800AT microhardness tester.

3.3.3 Results and Discussion

Figure 3-11 shows the schematic illustration of the process and mechanism of the in-situ molten salt reaction and incorporation of 10 nm TiC nanoparticles into aluminum melt. When the K_2TiF_6-$KAlF_4$-Diamond powders were loaded on the molten Al at 820 °C, K_2TiF_6 and $KAlF_4$ will

melt and form a molten salt layer at the top of Al melt. The following exchange reaction is expected [Li 2008', Juhász 2012]:

$$4Al + 3(K_2TiF_6) = 3Ti + 3(KAlF_4) + (K_3AlF_6) \quad 3\text{-}4$$

Ti^{4+} ions from K_2TiF_6 could be reduced by liquid Al and release free Ti atoms and form $KAlF_4$ with K_3AlF_6. With the existence of diamond nanoparticles in the molten salt, Ti atoms will react with carbon atoms in diamond nanoparticles and produce TiC nanoparticles as shown in the following reaction [Wu 2013, Daoush 2014 and Li 2011]:

$$Ti + C\ (Diamond) = TiC \quad 3\text{-}5$$

Since the reduced free Ti atoms could move freely in the molten salt, the sizes of the produced TiC nanoparticles are determined by the size of diamond nanoparticles as they served as the reaction templates. The average diameter of raw diamond nanoparticles is 5-10 nm, thus the formed TiC nanoparticles could also be controlled to approximately 10 nm. Therefore, we could produce 10 nm TiC nanoparticles uniformly distributed in molten salt by the in-situ reaction between Ti atoms and diamond nanoparticles.

To incorporate TiC nanoparticles into Al melt, a salt-assisted incorporation process was implemented by simply mechanical mixing at the interface of the molten salt and liquid Al. As shown in Figure 3-11, molten $KAlF_4$ and K_2TiF_6 can dissolve the aluminum oxide film on the surface of the Al melt to provide a clean liquid Al-molten salt interface. Furthermore, because of the partial metallic bond in TiC, TiC wets better with Al melt than the molten salt. Thus during mechanical mixing, TiC nanoparticles can be self-incorporated from molten salt to Al to reach a more favorable energy state. The incorporation efficiency is typically in the range of 60%-80% from our experiments. Some of the TiC nanoparticles will still remain in the molten salt. Therefore,

by simply adding salt-diamond mixture on the molten Al and applying mechanical mixing, we were able to fabricate Al-TiC nanocomposites through this novel in-situ reaction and incorporation method.

Figure 3-12a shows the image of the dehydrated salt-diamond nanoparticles mixture, due to the greyish color of diamond nanoparticles, the whole mixture present a greyish color. Figure 3-12b is the as cast Al-TiC MMNCs ingot with a solidified salt layer at the top. Due to the remaining TiC nanoparticles in the salt, it presented a black color. The color change of the salt validates the reaction between the molten salt, liquid Al and diamond nanoparticles to form TiC nanoparticles.

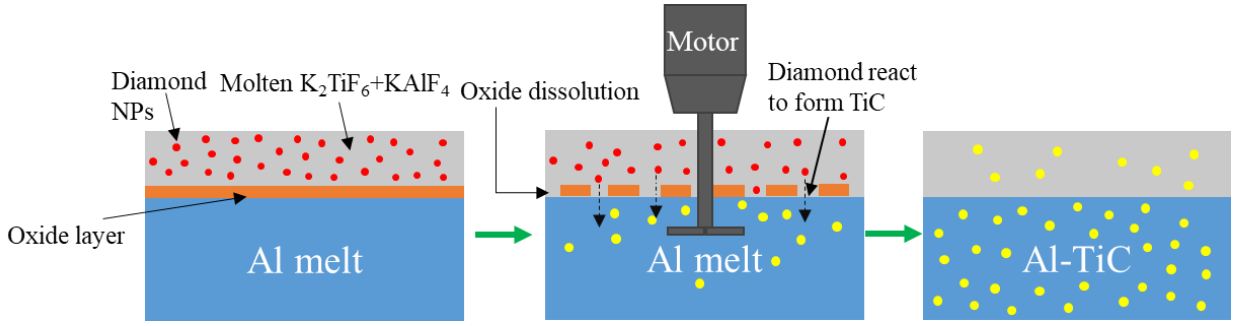

Figure 3-11 Schematic illustration of the reaction and incorporation of TiC nanoparticles into Al melt.

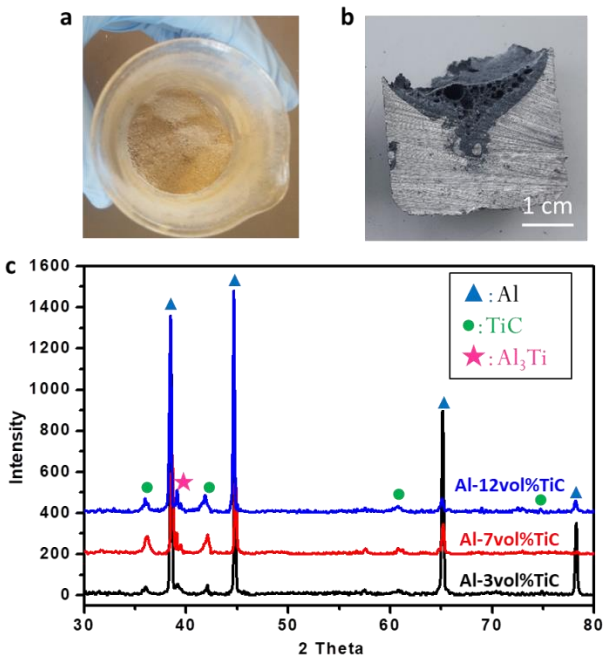

Figure 3-12 In-situ reaction and incorporation of TiC nanoparticles. (a) Mixed K_2TiF_6-$KAlF_4$-Diamond powder; (b) As cast Al-TiC nanocomposites ingot with a layer of residual salt at the top; (c) XRD pattern of Al-TiC nanocomposites with 3vol%, 7vol% and 12vol% TiC nanoparticles.

Figure 3-12c shows the XRD spectrum of Al-TiC nanocomposites with 3vol%, 7vol% and 12vol% TiC nanoparticles. Al and TiC are identified as the major phases as marked in the pattern. There is also a small peak corresponding to $TiAl_3$ intermetallic phase. $TiAl_3$ might form by the reaction between the Ti atoms and molten Al as following equation [Javadi 2017, Arpon 2003]:

$$3Al + Ti = TiAl_3 \qquad 3\text{-}6$$

When Ti^{4+} ions were reduced to Ti atoms by liquid Al, most of the Ti atoms were reacted with diamond nanoparticles to form TiC. However, part of the Ti atoms could dissolve into Al melt and form $TiAl_3$ intermetallic phase.

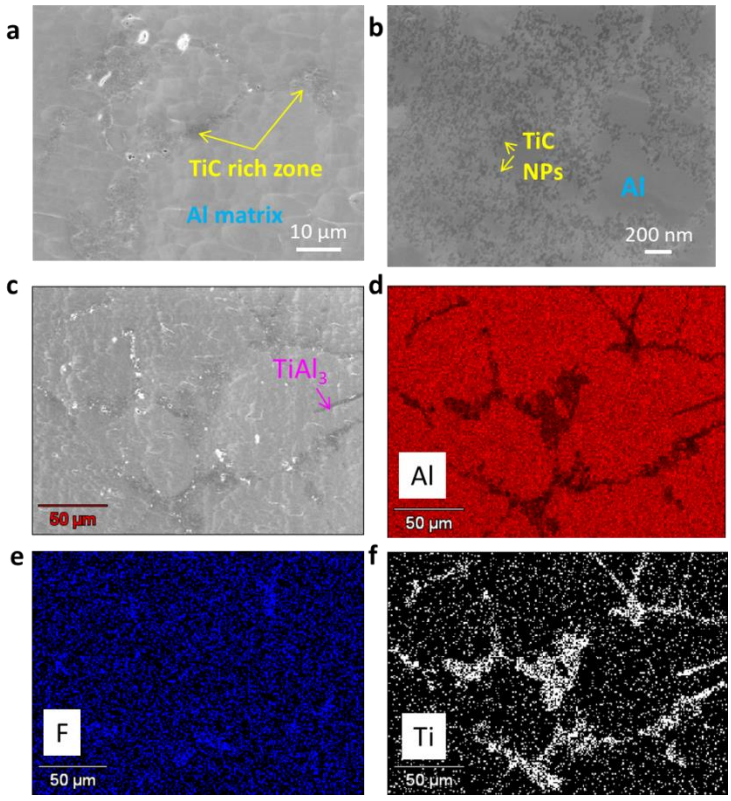

Figure 3-13 SEM-EDS micrographs of Al-3vol%TiC nanocomposites: (a-c) SEM image of Al-3vol%TiC; (d-f) Corresponding element Al, F, and Ti element distribution in (c).

Figure 3-13a shows the microstructure of the Al-3vol%TiC nanocomposites. As marked in the image, TiC nanoparticles are mainly distributed in the TiC nanoparticles rich zone. It is believed that the TiC rich zone is formed due to the van der Waals attraction force between TiC nanoparticles in molten Al. The van der Waals interaction between TiC nanoparticles can be approximately estimated by the following equation:

$$W_{vdw} = -\frac{(\sqrt{A_{Al}}-\sqrt{A_{TiC}})^2}{6D}\frac{R}{2} \qquad 3\text{-}7$$

where A_{Al} and A_{TiC} are the Hamaker constant, D is the distance between two nanoparticles that can be as small as two atomic layers thick (0.4 nm), R is the radius of the nanoparticle. When the

attractive van der Waals interaction is more significant than the Brownian energy (kT), TiC nanoparticles tend to agglomerate and form pseudo clusters. The magnified image of the TiC nanoparticles rich zone is shown in Figure 3-13b. TiC nanoparticles are well dispersed inside the nanoparticles rich zone. The TiC nanoparticles distribution is also studied by means of EDS mapping. Figure 3-13c is the microstructure of Al-3vol%TiC nanocomposites. Figure 3-13d, 13e and 13f reveal the spatial distribution of Al, F and Ti elements, respectively. The distribution of Ti element is corresponding to the TiC nanoparticles and $TiAl_3$ intermetallic phase. The sharp rod shape phases marked in Figure 3-13c are the $TiAl_3$ phase produced by the chemical reaction of Ti atoms and Al matrix. There is also F element detected in the sample due to the contamination from the fluoride salt. Some $KAlF_4$ and K_3AlF_6 salt might be incorporated into the molten Al during the mechanical mixing. Meanwhile, the viscosity of the Al melt will be raised due to the incorporation of solid TiC nanoparticles which makes salt hard to float back to the top of Al melt. These remained salts could deteriorate the properties of the Al-TiC nanocomposites. It is worth to mention that, based on the Gibbs free energy calculation, TiC nanoparticles are chemically and thermally stable when the processing temperature is above 800 °C [Karantzalis 2011] which explains why our TiC nanoparticles can survive the high temperature (~820 °C) process with little chemical reaction with Al matrix.

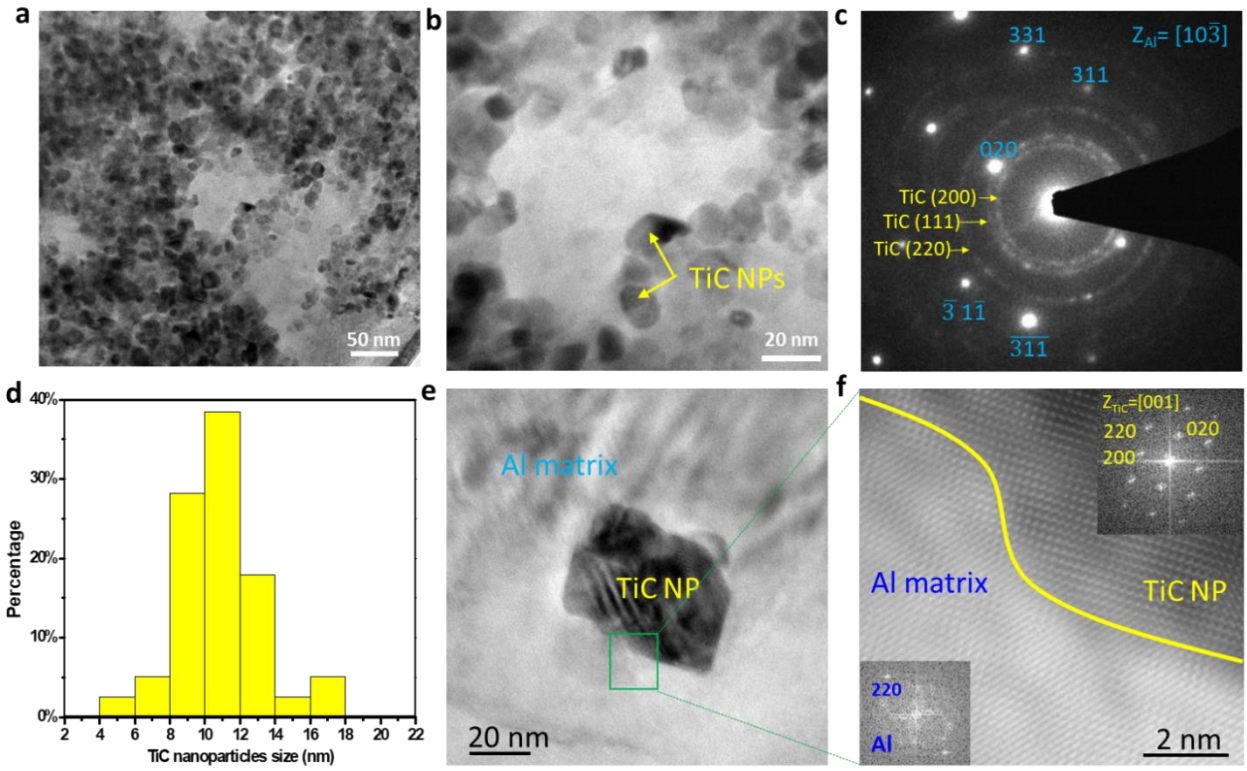

Figure 3-14 (a, b) TEM image of the TiC rich zone; (c) Diffraction pattern of the nanoparticles rich zone; (d) TiC nanoparticles size distribution; (e) High resolution TEM of one single TiC nanoparticles in Al matrix; (f) Fast Flourier Transform (FFT) filtered HRTEM image at the interface between TiC and Al. The insets are the fast Fourier transformation of the Al matrix (bottom left) and TiC nanoparticle (top right).

TEM was applied to study microstructure in the nanoparticles rich zone. Figure 3-14a and 14b show the TEM images of the nanoparticles rich zone in the Al-3vol%TiC sample. Dense TiC nanoparticles are well distributed in Al matrix without sintering. TEM diffraction pattern in Figure 3-14c further validates the crystal structure of TiC nanoparticles and Al matrix. The diffraction rings are corresponding to the multiple TiC nanoparticles with different orientations. The diffraction lattice as marked with indexes are corresponding to Al matrix at the zone axis of $[10\bar{3}]$.

The sizes of TiC nanoparticles are measured from Figure 3-14b. The average diameter of the TiC nanoparticles is approximately 11 nm as shown in Figure 3-14c. The changeless size of TiC nanoparticles proves that diamond nanoparticles did serve as reaction template during the synthesis of TiC nanoparticles and TiC nanoparticles have little sintering or growth during the processing of Al-TiC nanocomposites. The interface between matrix and nanoparticle is a crucial factor for the strengthening effect of nanocomposites materials. We characterized the interfaces between TiC nanoparticle and Al matrix at the atomic scale by high-resolution TEM (HRTEM). Figure 3-14e shows the TEM image of one individual TiC nanoparticles in Al matrix. Figure 3-14f is the Fourier-filtered atomic resolution TEM image at the marked area of Figure 3-14e. Figure 3-14f shows a clean and well bonded Al-TiC interface. The bottom-left and top-right insets in Figure 3-14f are the fast Fourier transformation of the Al and TiC nanoparticles, respectively. This TiC nanoparticles is orientated at a zone axis of [001] and the Al planes shown in the image are (220) planes.

Vickers microhardness tests were performed to evaluate the strengthening effect of the TiC nanoparticles and cold rolling. Figure 3-15 shows the microhardness data for both as cast and cold rolled Al and Al-TiC nanocomposites. The HV microhardness of as cast pure Al, Al-3vol%TiC, Al-7vol%TiC and Al-12vol%TiC are 24.9, 41.8, 76.7 and 83.4, respectively. After cold rolling, the microhardness of pure Al, Al-3vol%TiC, Al-7vol%TiC and Al-12vol%TiC increase to 31.6, 55.7, 94.9 and 110.3, respectively. The hardness data clearly shows that microhardness of as cast and cold rolled samples both increase with the addition of TiC nanoparticles.

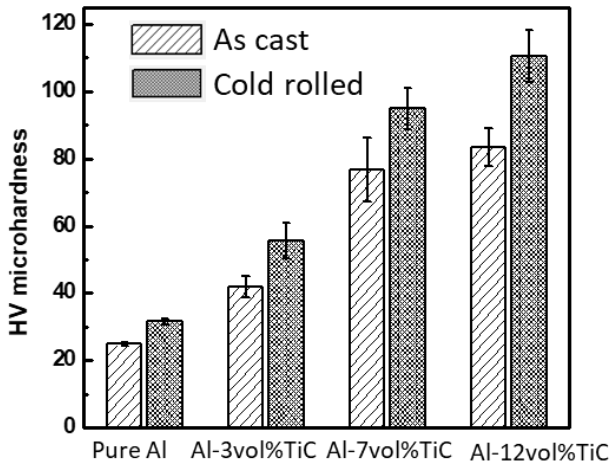

Figure 3-15 Vickers microhardness of the pure Al and Al-TiC nanocomposites with 3vol%, 7vol% and 12vol% TiC nanoparticles.

3.3.4 Summary

In summary, a novel in-situ molten salt reaction and incorporation method that combines chemical synthesis and incorporation of TiC nanoparticles is established to control the size of TiC nanoparticles and effectively incorporate TiC nanoparticles into Al matrix. The size of TiC nanoparticles are readily controlled to approximately 11 nm by the diamond reaction templates. The mechanical properties are enhanced significantly by the incorporated tiny TiC nanoparticles. This novel processing route paves a new pathway to fabricate MMNCs with readily refined nanoparticles through a scalable solidification process, and potentially could be applied to other material systems.

3.4 Molten Salt-assisted Incorporation of WC Nanoparticles into Cu

3.4.1 Introduction

There are significant demands to have high strength and high electrical conductivity Cu for long time. However, there exists a long-standing dilemma between mechanical properties and

electrical conductivity. Pure copper has ideal electrical conductivity but it is too soft for a lot of applications. Conventional strengthening method such as solid solution will deteriorate electrical conductivity significantly due to the severe electron scattering with solute atoms. Precipitation strengthening cannot provide eligible mechanical properties at elevated temperatures due to the softening from the dealloying or coarsening of the precipitates. Nanotwinned Cu with high strength and electrical conductivity can be fabricated by electrodeposition. However, it is extremely difficult to produce/manufacture bulk nanotwinned Cu through electrodeposition for real applications [Lu 2004]. Therefore, we are still facing the difficult situation that there is no bulk high strength and high electrical conductivity Cu available in the market.

Here we report a facile solidification processing method, which utilizes fluoride salt for self-incorporation of high loading WC nanoparticles to Cu to produce nanocomposites. A uniform dispersion of WC nanoparticles in the Cu matrix nanocomposites is achieved by this method. Moreover, the Cu-WC nanocomposites demonstrate significantly improved mechanical properties without severely deteriorate the electrical conductivity.

3.4.2 Materials and Methods

WC nanoparticles (US Research Nanomaterials Inc.) with diameter from 150-200 nm (as shown in Figure 3-16) were mixed with $KAlF_4$ salt (AMG Aluminum) powders by a mechanical shaker (SK-O330-Pro) for 1.0 h. The volume fraction of nanoparticles in the salt is fixed as 10vol%. Then pure oxygen free Cu (99.99%, Rotometals, Inc) ingots were melted at 1150 °C in a graphite crucible by the induction heater (as shown in Figure 3-17). The induction heater allows us to melt high melting temperature metals such as Cu, Fe and Ti. Inert Ar gas was purged on the molten Cu to avoid severe oxidation. The mixed salt-WC nanoparticles were manually loaded on the surface of the molten Cu. A graphite propeller was located below the Cu-salt interface and stirred at a

speed of 200 rpm for 20-90 min to incorporate WC nanoparticles into Cu melt. The volume fraction of WC nanoparticles in Cu was designed to be 0, 10, 15, and 20 vol.%. The 0% pure Cu sample is designed for comparison. Then the melt was taken out from the induction heater and cool down in air (approximately 5-10 K/s cooling rate) with continuous Ar gas protection. The as cast ingots were sliced to sheets for further cold rolling. Other salt systems including NaCl (Fisher Chemical), borax ($Na_2B_4O_7$, anhydrous, 99.5%, Alfa Aesar) and $Na_2B_4O_7$-5wt%CaF_2 (99.99%, Sigma Aldrich) were also tested for the incorporation of WC nanoparticles into Cu. The as cast ingots were sliced to sheets for further cold rolling.

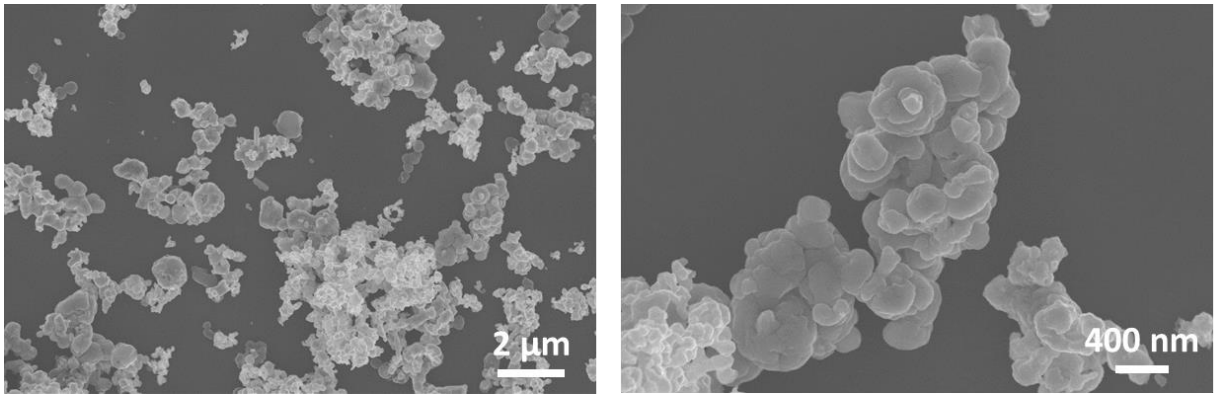

Figure 3-16 SEM image of as received WC nanoparticles.

Figure 3-17 Induction heater (EQ-SP-25TC) with a vacuum chamber and a temperature control system (up to 1700 °C).

To clean the surface and reveal the nanoparticles in metal matrix, the mechanically grinded and polished as-cast samples were further polished by low-angle ion milling (Model PIPS 691, Gatan). The microstructure, distribution and dispersion of nanoparticles in metals were studied by means of scanning electron microscope (SEM). The composition of the material was characterized by energy-dispersive X-ray spectroscopy (EDS). The volume fraction of nanoparticles was estimated based on the atomic fraction of the major element in the base metal and nanoparticles.

To evaluate the mechanical properties, Vickers hardness tests were conducted under a 200 gf load with a dwell time of 10 s in a LM 800AT microhardness tester. Micropillars of approximately 4 μm in diameter and 9 μm in length were machined by FIB. An MTS Nanoindenter with a flat punch tip was used for microcompression tests at a strain rate of 5×10^{-2} s^{-1} under room

temperature. To evaluate the elastic modulus, microindentation tests with an indent depth of 2 μm were performed by the same MTS nanoindenter with a Berkovich tip. The cold rolled Cu-WC sheets were cut to dog-bone tensile bars by wire electric discharge machining (EDM) for tensile testing. Figure 3-18 shows the dimension of the Cu-WC tensile bar with a gauge length of 10 mm and width of 4 mm. Tensile testing was measured by Instron 5966 with a laser based video extensometer followed a strain rate of 8×10^{-3} 1/s. The electrical conductivity of the Cu-WC samples were measured based on four point probe method by CDE ResMap.

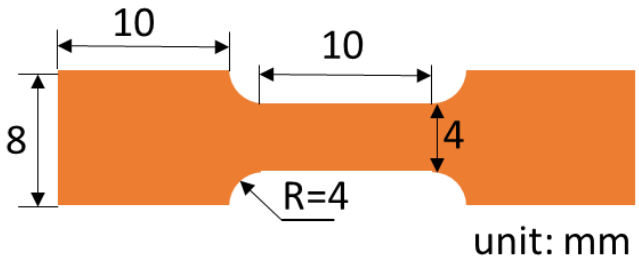

Figure 3-18 Schematic of the dimension of Cu-WC tensile bar.

3.4.3 Results and Discussion

The processing route of the molten salt-assisted incorporation for high strength and high electrical conductivity Cu-WC nanocomposites is shown in Figure 3-19. When Cu melt and stay at 1150 °C, even with the protection of inert Ar gas, there still exists an oxide film on the Cu melt surface due to the oxidation. It is extremely difficult to incorporate nanoparticles into molten metal with the oxide film at the top. Here the molten salt added together with nanoparticles can dissolve oxide film on the surface of Cu melt and provide a clean Cu-molten salt interface. Then, because the good wettability between Cu and WC (wetting angle below 20° at temperatures above 1150 °C as shown in Figure 3-20), WC prefer to wet Cu instead of molten salt. Thus during the mechanical

mixing, WC nanoparticles can be incorporated from the molten salt to Cu to reach a more favorable energy state. Moreover, the molten salt can also protect active nanoparticles from oxidation or burning at this high processing temperature. This molten salt assisted incorporation method enables us to scalable manufacture Cu-WC nanocomposites for high strength and high electrical conductivity applications.

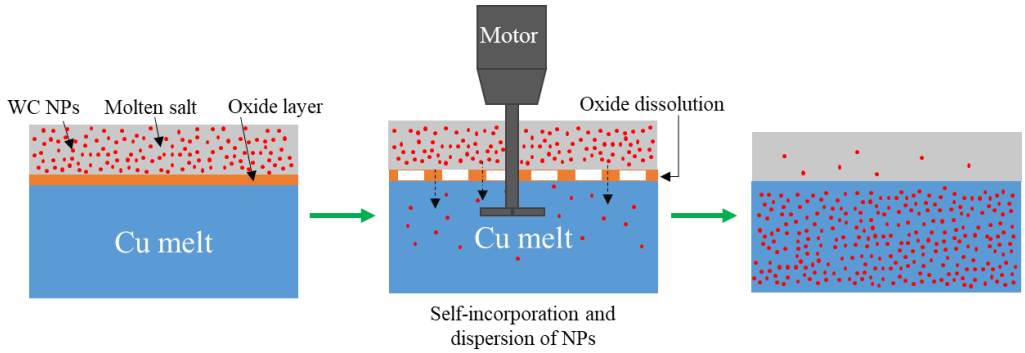

Figure 3-19 Schematic illustration of the molten salt-assisted incorporation for Cu-WC materials system.

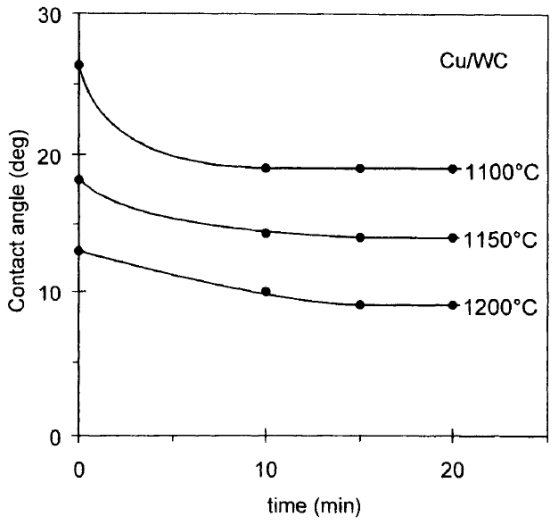

Figure 3-20 Contact angles of Cu on WC plotted as a function of time [Eustathopoulos 1999].

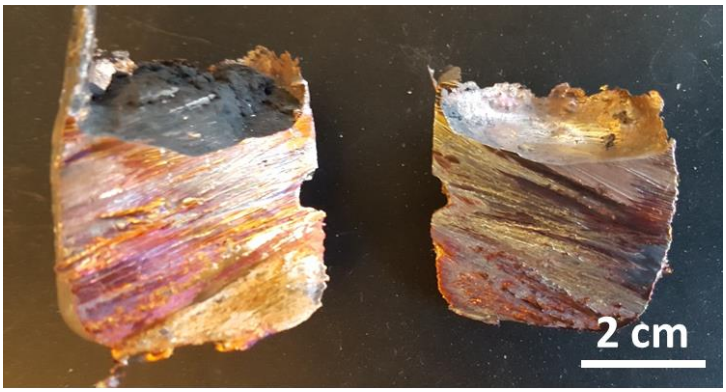

Figure 3-21 Image of a typical as cast Cu-WC nanocomposite ingot by molten salt-assisted incorporation method.

Then the as cast Cu-WC ingots were cut and prepared for following cold rolling and characterization. Figure 3-21 shows the typical image of a Cu-WC ingot fabricated by the molten salt-assisted incorporation. The black layer at the top of the ingot is the remained salt and nanoparticles. Due to the incorporation efficiency of nanoparticles is not one hundred percent, some nanoparticles might still stay in the salt. We then characterized the distribution and dispersion of the WC nanoparticles in Cu matrix via SEM and EDS. SEM samples were cut from the cross-section of the as cast Cu-WC ingots. Low angle ion milling was used to polish the sample to clean the surface and expose the nanoparticles.

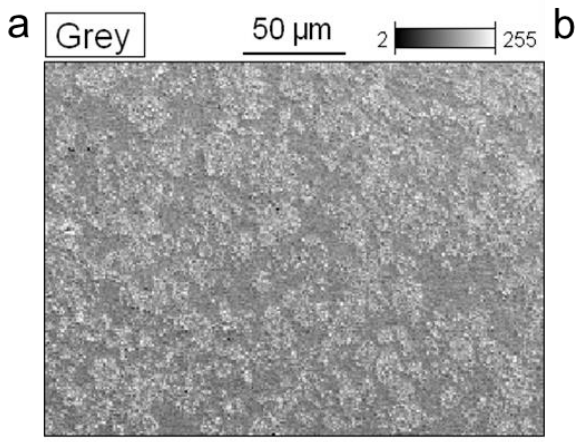

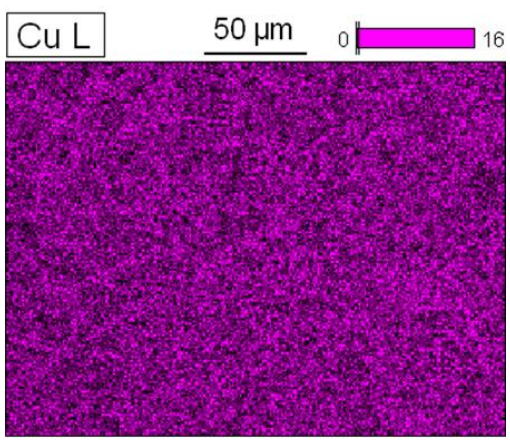

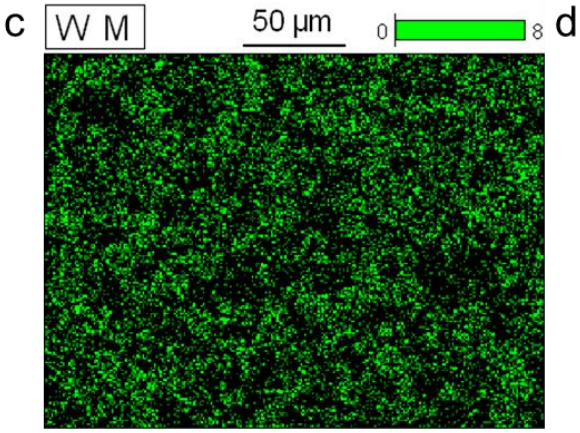

d

Element	Weight %	Atomic %
Cu	87.16	90.39
W	11.5	4.12
O	1.33	5.49

Figure 3-22 EDS mapping result of Cu-7.6vol%WC. (a) The corresponding SEM image of Cu-7.6vol%WC; (b) Cu element distribution; (c) W element distribution; (d) Element content measured by EDS mapping.

The volume fraction of WC nanoparticles is identified by EDS mapping. As an example, Figure 3-22 shows the typical EDS mapping results of Cu-7.6vol%WC showing that WC nanoparticles uniformly distributed in Cu matrix. The volume fraction of WC nanoparticles is calculated from the atomic ratio between Cu and W elements due to the inaccurate measurement of C atoms by EDS. The same method is used to determine the volume fraction of Cu-WC nanocomposites to be 5.1vol%, 7.6vol%, 14.4vol% and 20.5vol%.

The SEM images of Cu-WC containing various percentage of WC are shown in Figure 3-23. WC nanoparticles form pseudo clusters in Cu-5.1vol%WC and Cu-7.6vol%WC samples while distribute uniformly in Cu-14.4vol%WC and Cu-20.5vol%WC samples. These pseudo clusters could be explained by the nanoparticle dispersion and self-stabilization mechanisms. It has been reported that there are three major factors dictating the dispersion of the nanoparticles: (1) the energy barrier from the interfacial energy due to the good wettability between nanoparticles and molten metal. This energy barrier can be calculated by the following equation [Chen 2015']:

$$W_{barrier} = S\sigma_{Cu}cos\theta \quad 3\text{-}8$$

where S is the effective area and can be calculated by $S=\pi RD_0$ (D_0=0.2 nm), σ_{Cu} is the surface energy of Cu at the processing temperature (about 1.27 J m^{-2}), and θ is the wetting angle, e.g. at 1150 °C (15°). In the Cu-WC system, an energy barrier of 6.9×10^4 zJ is obtained; (2) the van der Waals potential between nanoparticles to lessen the attraction of nanoparticles from each other to form nanoparticles clusters in molten metals. A small attractive van der Waals potential is preferred. It can be calculated by the following equation:

$$W_{vdw} = -\frac{(\sqrt{A_{Cu}}-\sqrt{A_{WC}})^2}{6D}\frac{R}{2} \quad 3\text{-}9$$

where A_{Cu} = 410 zJ and A_{WC} are the Hamaker constants, D is the distance between two nanoparticles that can be as small as two atomic layer thick (0.4 nm), R is the radius of the nanoparticle (100 nm). Although the Hamaker constant of WC is not available, it could be estimated to be 200-500 zJ because WC has similar properties with metals. Thus W_{vdw} is estimated to be in the range of 0 to 776 zJ. (3) thermal energy that enable nanoparticles to move randomly in the molten melt by overcoming the attractive van der Waals potential between nanoparticles. A higher thermal energy is preferred. The processing temperature is 1150 °C, which provide a

thermal energy of $E=k_bT$=19.6 zJ. Therefore, a 7×10^4 zJ energy barrier is several orders of magnitude higher than thermal energy and van der Waals attraction potential which suggests that the interfacial energy barrier is large enough to avoid severe sintering issues in Cu-WC nanocomposites. However, because of the uncertainty the Hamaker constant of WC, the relationship between van der Waals attraction potential and thermal energy varies. When W_{vdw} is smaller than the thermal energy (19.6 zJ), the thermal energy is large enough to prevent nanoparticles being trapped in the energy well caused by the van der Waals attraction and thus nanoparticles could be self-dispersed in the melt. However, when W_{vdw} is larger than the thermal energy (19.6 zJ), the van der Waals potential energy well could trap nanoparticles to stay at the energy well and form pseudo-dispersion. The microstructure observed in Cu-5.1vol%WC and Cu-7.6vol%WC samples validate that WC nanoparticles form pseudo clusters in Cu melt. Fortunately, WC nanoparticles are well dispersed in the pseudo clusters because the interfacial energy barrier prevent nanoparticles to form true clusters. As shown in Figure 3-24 acquired at 52° to exposed WC nanoparticles after FIB polishing, WC nanoparticles are uniformly dispersed with each other. When the percentage of WC nanoparticles increases to more than 14vol%, nanoparticles could fill the gap between pseudo clusters and thus a uniform distribution and dispersion of WC nanoparticles is achieved.

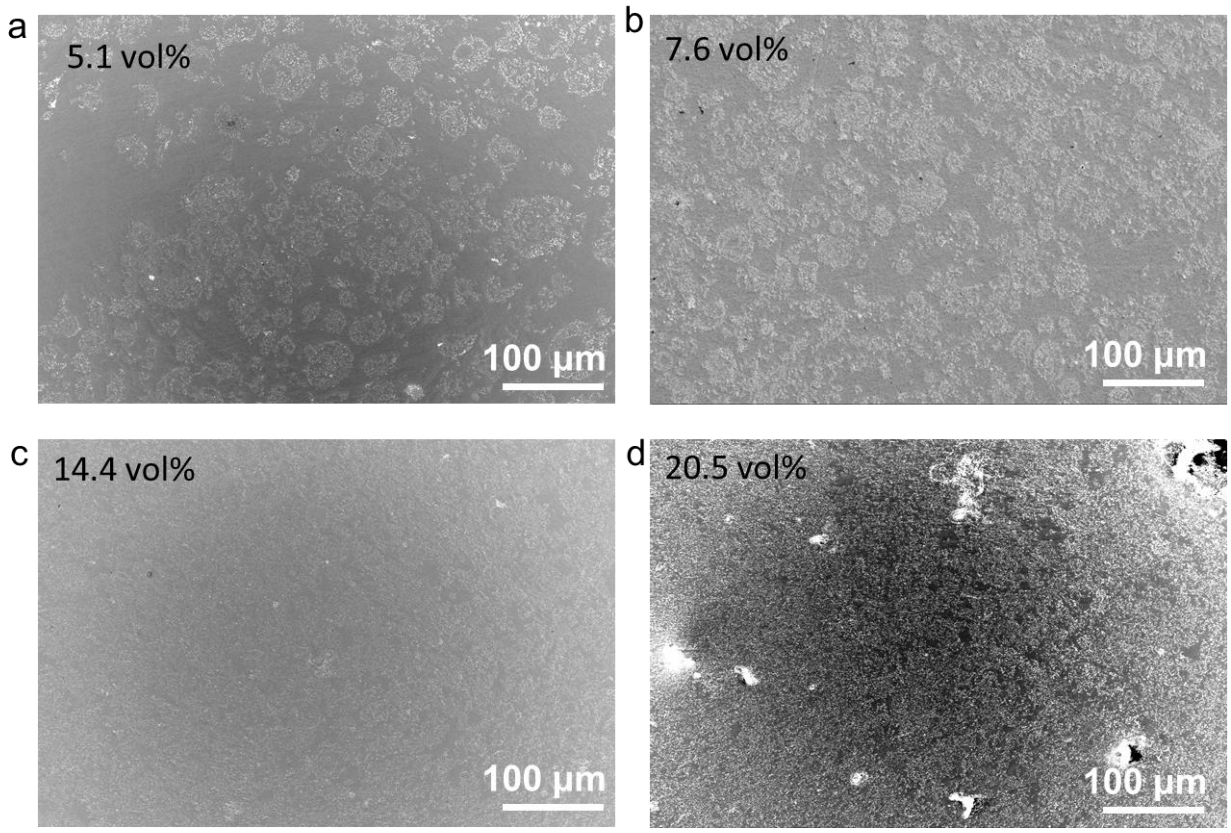

Figure 3-23 SEM image of Cu-WC with different volume fraction of nanoparticles. (a) Cu-5.1vol%WC; (b) Cu-7.6vol%WC; (c) Cu-14.4vol%WC; (d)Cu-20.5vol%WC.

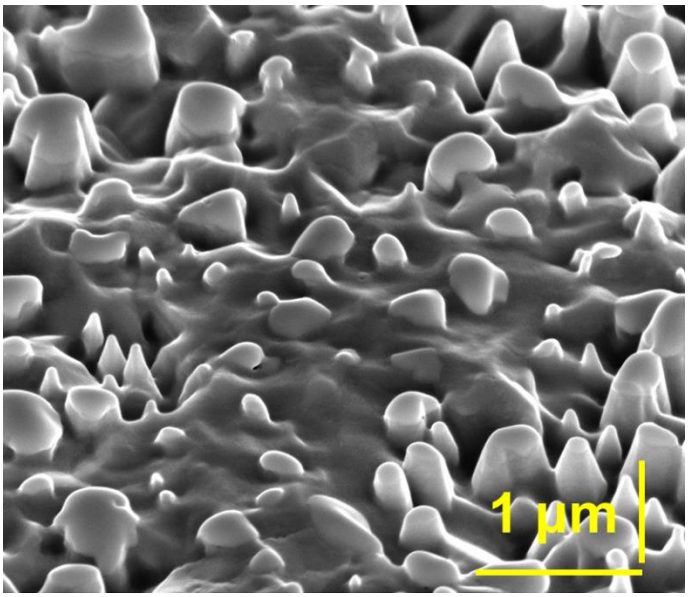

Figure 3-24 SEM image acquired at 52° showing the dispersion of WC nanoparticles in Cu matrix.

Cold rolling was then applied to as cast samples to further increase the strength and to improve the nanoparticle dispersion and distribution. Figure 3-25a shows a post rolled Cu-7.6vol%WC nanocomposites sheet with a thickness reduction of 70%. The nanocomposite sheet can be readily cold rolled to 70% thickness reduction without forming severe edge cracks, indicating that this nanocomposite material has good deform capability. The optical microscope image (Figure 3-25b) and SEM image (Figure 3-25c) are showing that the WC nanoparticles pseudo clusters are elongated along the rolling direction, making nanoparticles distribute more uniformly in the Cu matrix. It is also believed that the mass flow during deformation could shear the nanoparticles clusters and improve the dispersion of nanoparticles. The magnified SEM image of Figure 3-25d in the elongated pseudo cluster zone shows the uniform dispersion of nanoparticles after deformation.

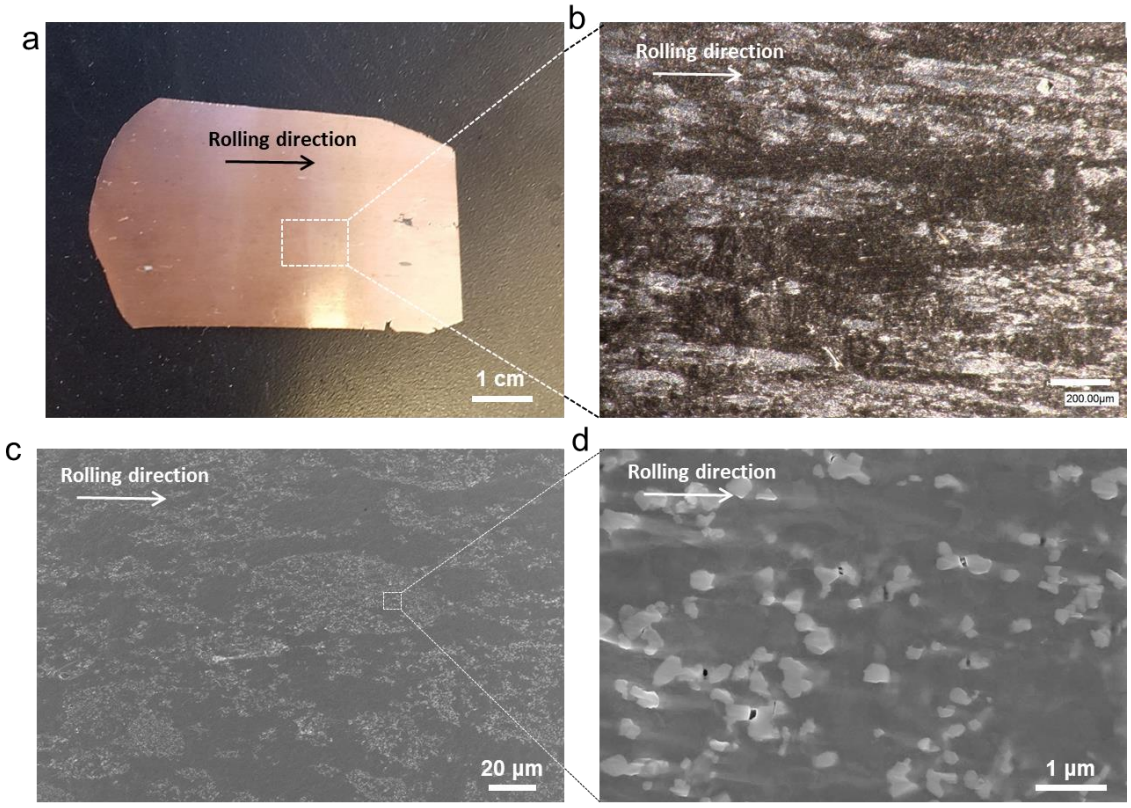

Figure 3-25 Cold rolling of Cu-7.6vol%WC sample. (a) Image of the cold rolled Cu-7.6vol%WC sheet; (b) Optical microscope image; (c-d) Corresponding SEM images of the cold rolled Cu-7.6%WC sample.

HV microhardness, micropillar compression, tensile test and nanoindentation were applied to analyses the mechanical properties of Cu-WC nanocomposites. Figure 3-25 shows the HV microhardness of as cast pure Cu, Cu-5.1vol%WC, Cu-7.6vol%WC, Cu-14.4vol%WC and Cu-20.5vol%WC are 74.3 ± 4.1, 124.1± 9.1, 133 ± 17.8, 150.3 ± 3.9 and 188.6 ± 8.2, respectively. From the experimental results, the relationship between HV microhardness and volume fraction of WC nanoparticles is close to a linear relationship. With each one percent of WC nanoparticles, the HV microhardness increase approximately by 5. After cold rolling the HV microhardness of Cu-5.1vol%WC, Cu-7.6vol%WC, Cu-14.4vol%WC and Cu-20.5vol%WC increase to 166 ± 4.5,

195 ± 8.4, 209.4 ± 9 and 223 ± 15.8, respectively. Therefore, WC nanoparticles are very effective to strength the nanocomposites. And the microhardness can be further by cold rolling with better nanoparticles distribution and dispersion.

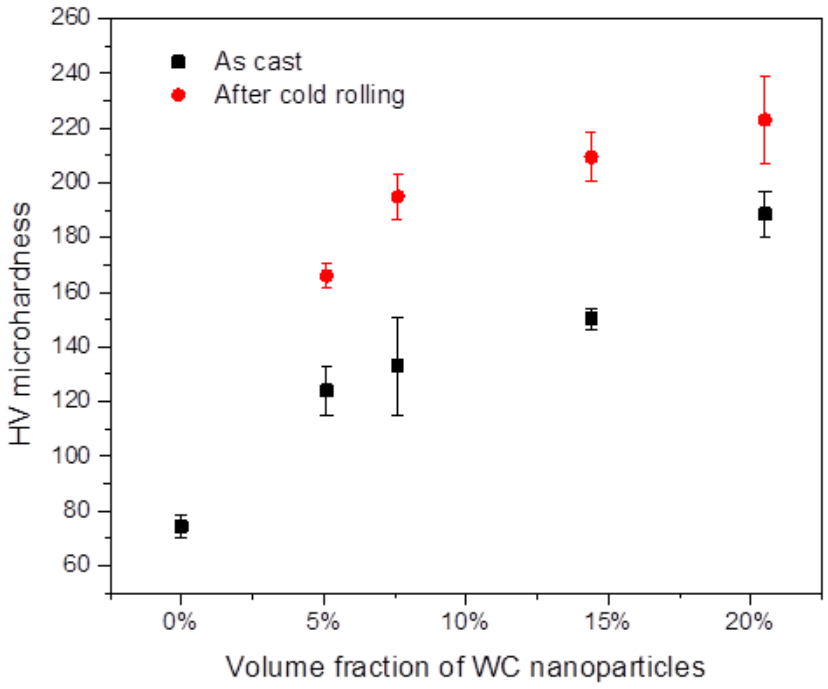

Figure 3-26 HV microhardness of as cast and cold rolled Cu-WC nanocomposites with different volume fraction of WC nanoparticles.

Figure 3-27 shows the micropillars of pure Cu, Cu-5.1vol%WC and Cu-20.5vol%WC machined by FIB. The dimension of the micropillar is designed to be approximately 4 μm in diameter and 9 μm in length to avoid obvious size effect. Populous WC nanoparticles can be observed in the SEM images of Cu-WC micropillars. The typical results from the micropillar compression are shown in Figure 3-28. The yield strength of pure Cu, Cu-5.1vol%WC and Cu-20.5vol%WC are 180 ± 8 MPa, 232 ± 11 MPa and 429 ± 3 MPa, respectively. Moreover, micropillars from Cu-5.1vol%WC and Cu-20.5vol%WC can gradually bear load up to 400 MPa

and 1000 MPa, strain up to 15% and 25%, respectively. In comparison, the pure Cu sample experienced extensive slip as the strain increases discontinuously. As shown in Figure 3-29, after deformation, multiple slip traces were observed in the pure Cu samples, while only one slip trace appeared in the Cu-WC samples.

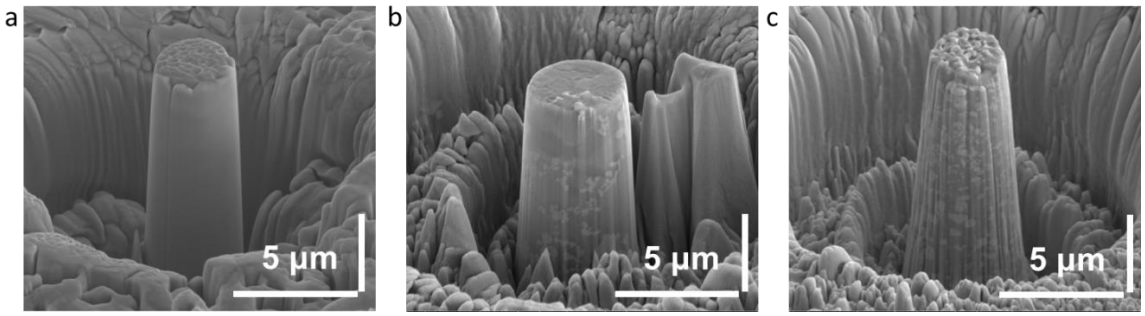

Figure 3-27 Micropillars machined by FIB: (a) Pure Cu; (b) Cu-5.1vol%WC; (c) Cu-20.5vol%WC.

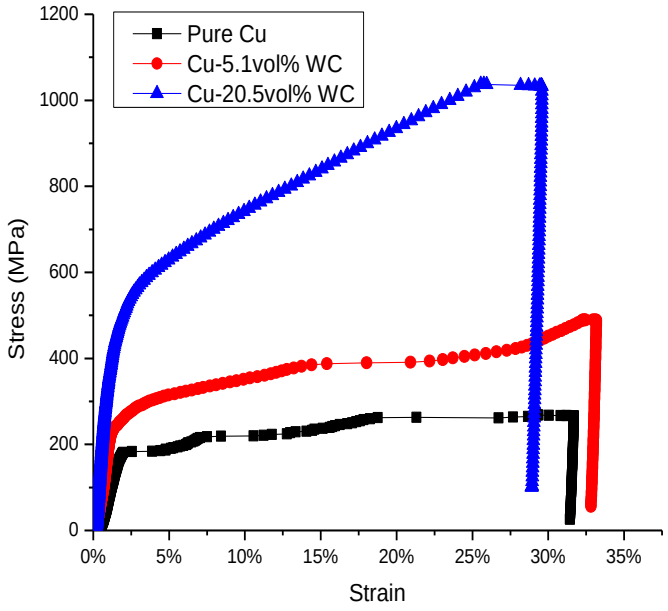

Figure 3-28 Engineering stress-strain curve of pure Cu, Cu-5.1vol%WC and Cu-20.5vol%WC from micropillar compression tests.

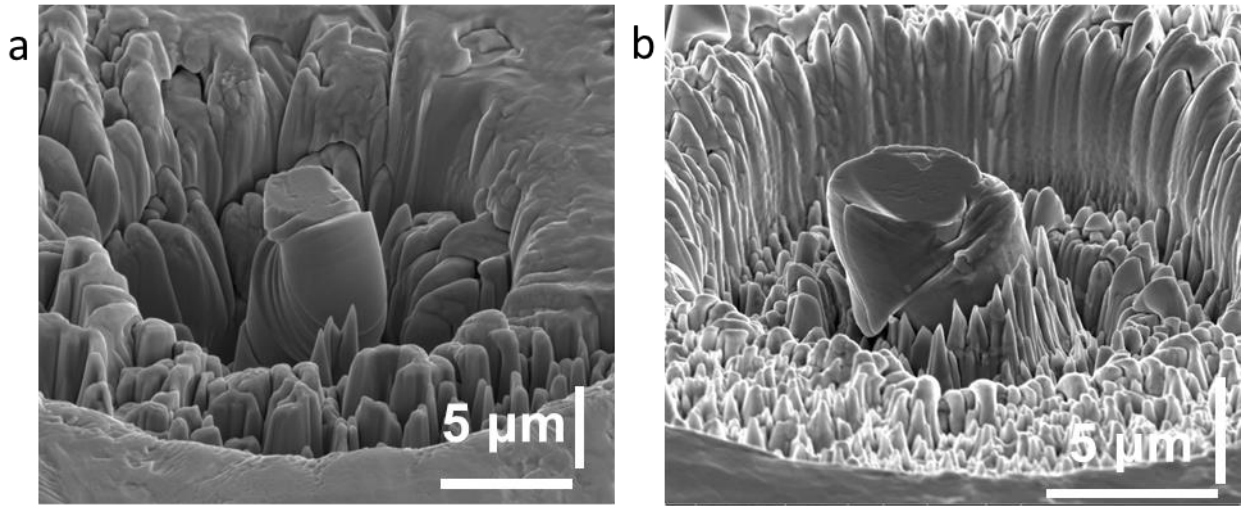

Figure 3-29 SEM images of micropillars after compression. (a) Pure Cu; (b) Cu-5.1vol%WC.

The engineering stress-strain curves from tensile tests are shown in Figure 3-30, the yield strength, ultimate tensile strength and elongation of different samples are listed in Table 3-1. It shows that the hot forging process can increase strength and elongation simultaneously, it is highly possible that porosities formed during solidification were removed by the hot wrought process. After cold rolling, the yield strength and tensile strength increase while the elongation decrease significantly. Compare with the thickness reduction percentage, 70% thickness reduction sample has higher strength while lower elongation than 30% thickness reduction sample. Cold rolled Cu-7.6vol%WC shows an ultimate tensile strength up to 614 MPa which is very promising for widespread applications.

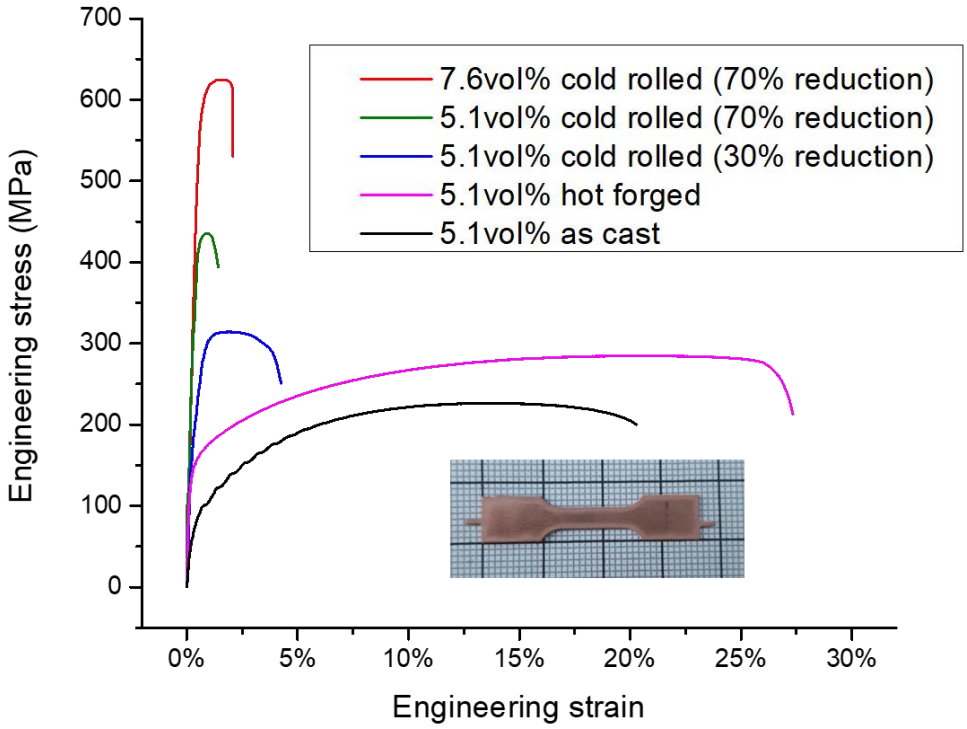

Figure 3-30 Engineering tensile stress-strain curve of Cu-5.1vol%WC and Cu-7.6vol%WC at different processing route.

Table 3-1 Yield strength, ultimate tensile strength and elongation of Cu-WC samples with different percentage nanoparticles and process route.

	Yield Strength (MPa)	Ultimate Tensile Strength (MPa)	Elongation (%)
5.1 vol%WC as cast	78 ± 6	228 ± 2	18.5
5.1vol%WC hot forged	90 ± 11	245 ± 9	24
5.1vol%WC cold rolled (30%)	219 ± 4	311 ± 5	3.6
5.1vol%WC cold rolled (70%)	326 ± 38	396 ± 33	1.2
7.6vol%WC cold rolled (70%)	533 ± 66	614 ± 15	2.1

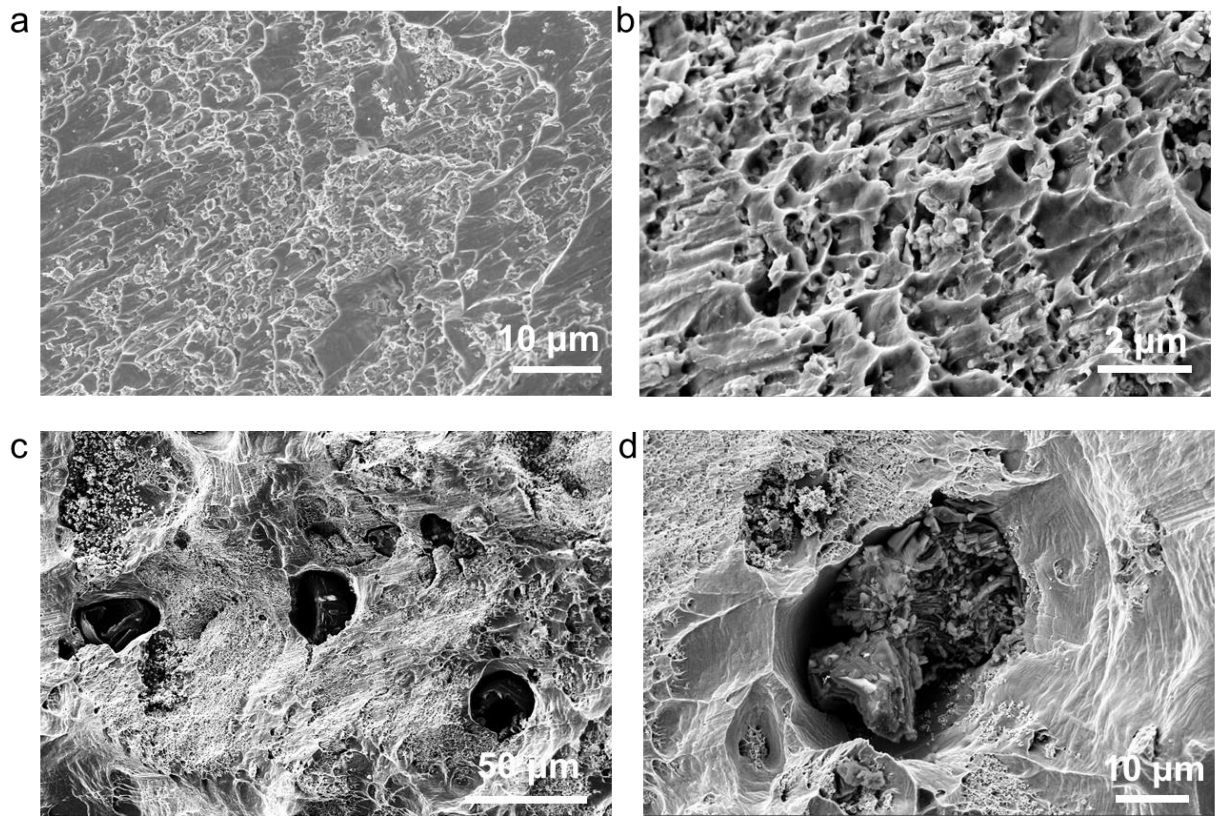

Figure 3-31 Fracture surface of Cu-5.1vol%WC after tensile test. (a-b) SEM images showing the ductile fracture surface with dimples; (c-d) Remaining salt exposed on the fracture surface.

It is worth to mention that the low ductility of the Cu-WC nanocomposites may be caused by the remaining salt. The fracture surface of Cu-5.1vol%WC sample after tensile testing is shown in Figure 3-31. A typical ductile fracture surface with homogeneous dimples up and down is observed in the area without salt (Figure 3-31a and 31b). WC nanoparticles can also be observed on the facture surface indicating some cracks propagate along Cu-WC interface. However, some remaining $KAlF_4$ salt chunks are also observed on the fracture surface as shown in Figure 3-31c and 31d. The salt chunks are the stress concentration spots during tensile test and deteriorate the strength and ductility. This may explain the relatively low ductility of our tensile testing results.

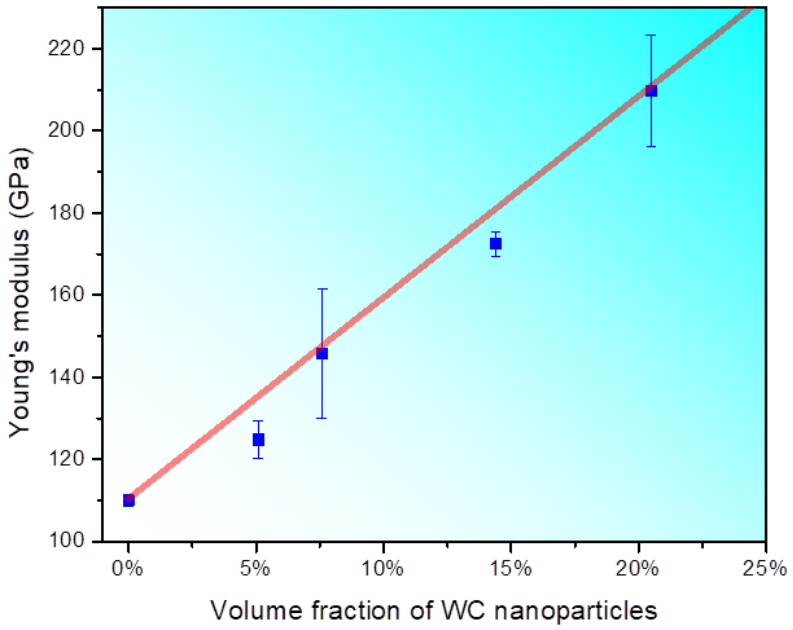

Figure 3-32 Young's modulus of Cu-WC samples measured by nanoindentation.

The Young's modulus of Cu-WC nanocomposites was measured by the nanoindentation method with a Berkovich tip. Figure 3-32 shows the Young's modulus enhancement of the Cu-WC nanocomposites with different percentage of WC nanoparticles. The Young's modulus of pure Cu, Cu-5.1vol%WC, Cu-7.6vol%WC, Cu-14.1vol%WC and Cu-20.5vol%WC are 110 GPa, 124.8 ± 4.5 GPa, 145.7 ± 15.7 GPa, 172.5 ± 3 GPa and 209.8 ± 13.5 GPa, respectively. The enhancement of Young's modulus is due to the high Young's modulus of WC nanoparticles (~600 GPa) and the effective load transfer by the nanoparticles. The Young's modulus calculated by the rule of mixture is shown as the red line in Figure 3-32, which is in good agreement with the value determined by the microindentation tests.

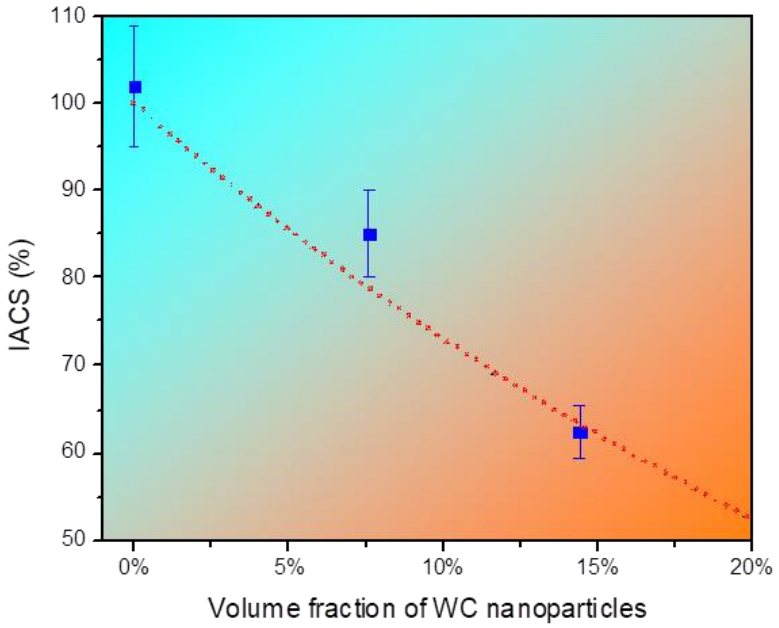

Figure 3-32 Electrical conductivity of Cu-WC samples at different volume fractions of WC nanoparticles.

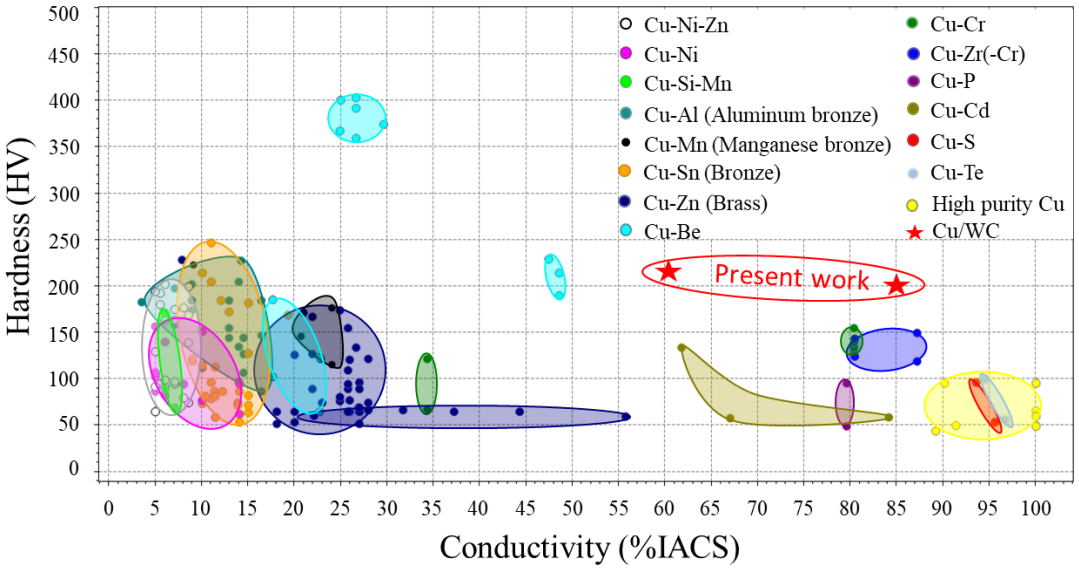

Figure 3-33 HV hardness vs. electrical conductivity Ashby chart of Cu based metals.

The results of electrical conductivity measurement of Cu-WC nanocomposites are shown in Figure 3-32. With the incorporation of WC nanoparticles, the electrical conductivity generally decrease due to the lower electrical conductivity of WC (8.6% IACS) and more interface scattering due to the introduction of Cu-WC interfaces and refined grain structures. The average electrical conductivity of Cu-7.6vol%WC and 14.4vol%WC sample are decreased to 85% IACS and 62% IACS. The calculated theoretical electrical conductivity by the Maxwell model is shown as the red dotted line in Figure 3-32, indicating a good match with the experimental value. Although the electrical conductivity deceases with the incorporation of nanoparticles, nanoparticles are very promising to mitigate the trade-off between mechanical properties and electrical conductivity. The mean free path of electrons in Cu at room temperature is around 38 nm. If the interparticle spacing is larger than 38 nm, the interface scattering of electrons at Cu-WC interface will be less effective. Therefore the electrical conductivity of Cu-WC nanocomposites could still remain relatively higher than Cu alloys. The Ashby chart of electrical conductivity- HV hardness is shown in Figure 3-33, it is shown that our present work with 85% IACS and 200 HV microhardness have better comprehensive properties compare with all other Cu based materials.

In addition, different salt systems such as NaCl, $Na_2B_4O_7$ and $Na_2B_4O_7$-CaF_2 have been tested. The results suggested that these salts are also effective to incorporate WC nanoparticles into Cu. Figure 3-34 shows the SEM images of Cu-WC samples fabricated by NaCl, $Na_2B_4O_7$ and $Na_2B_4O_7$-CaF_2 salts. The microstructure of Cu-10vol%WC and Cu-20vol%WC fabricated by NaCl are shown in Figure 3-34a and 3-34b, respectively. Similar with samples processed by $KAlF_4$, WC nanoparticles formed pseudo dispersion in Cu matrix. It is observed that, compare with Cu-10vol%WC, nanoparticles free zone is less in Cu-20vol%WC samples, indicating that more WC nanoparticles were successfully incorporated into the Cu-20vol%WC sample. NaCl is more

environmental friendly compare with $KAlF_4$, making it a promising candidate for industrial production. Fig. 3-34c shows the microstructure of Cu-10vol%WC fabricated by $Na_2B_4O_7$-5wt%CaF_2 salt, it shows similar nanoparticle dispersion and distribution with other Cu-10vol%WC samples made by $KAlF_4$ and NaCl. However, Cu-10vol%WC fabricated by pure $Na_2B_4O_7$ shows much denser WC concentration in the nanoparticles rich zone as shown in Figure 3-34d. It suggested that the dispersion of WC nanoparticles is related to the salt system for the incorporation. It is deduced that the dispersion state of nanoparticles in molten salt will affect the dispersion in the final metal matrix nanocomposites. With 5wt% CaF_2 addition into $Na_2B_4O_7$, it is possible that Ca^{2+} and F^- ions could coat on WC nanoparticles and improve the dispersion of WC nanoparticles.

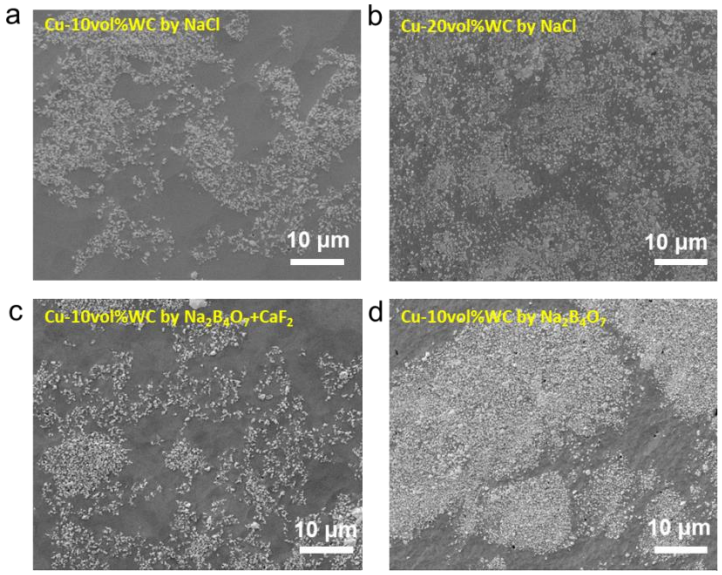

Figure 3-34. Microstructure of Cu-WC samples fabricated by different salts. (a) Cu-10vol%WC by NaCl; (b) Cu-20vol%WC by NaCl; (c) Cu-10vol%WC by $Na_2B_4O_7$-5wt%CaF_2; (d) Cu-10vol%WC by $Na_2B_4O_7$ salt.

3.4.4 Summary

In this study, a novel salt assisted incorporation method is utilized to fabricate Cu-WC nanocomposites. WC nanoparticles form pseudo clusters in Cu melt due to the overall potential of interfacial energy barrier, van der Waals attractive potential and thermal energy. WC nanoparticles are well dispersed in the pseudo clusters. Mechanical properties such as hardness, strength and Young's modulus of Cu-WC nanocomposites are significantly improved by the addition of WC nanoparticles. Cu-WC nanocomposites provide a promising approach to mitigate the trade-off between electrical conductivity and mechanical properties. This molten salt assisted incorporation method paves a pathway to scalable manufacturing metal matrix nanocomposites with excellent mechanical properties and electrical conductivity for widespread applications.

Chapter 4 Liquid-Liquid Phase Control by Nanoparticles: Immiscible Alloys

In this chapter, the nanoparticles enabled liquid-liquid phase control was studied both experimentally and theoretically in immiscible alloys which have a miscibility gap in liquid state. The miscibility gap of immiscible alloys lead to the unusual properties. Immiscible alloys are used for wide range applications such as self-lubricating bearings and electric contacts. However, as mentioned in Chapter 2.3, it has been a long-standing challenge to process immiscible alloys for practical applications due to the difficulties to effectively control the secondary phase growth, coagulations and sedimentation during cooling in order to obtain micron or nanoscale minority phase well-dispersed in bulk alloy liquids and/or in the solids, which is essential for the unique properties and applications envisioned [Wang 2002, Kundan 2015]. In this chapter, a novel nanoparticle enabled phase control approach is proposed to process immiscible alloys. TiC nanoparticles were utilized for the scalable manufacturing of Al-Bi immiscible alloys for bearing applications. To strengthen the Al-Bi immiscible alloy for self-lubricating application, it is shown that the addition of Cu element can effectively enhance the strength without deteriorating the distribution and size of secondary Bi phase. Zn-Bi immiscible alloy is a promising material system for plain bearing. It is shown that W nanoparticles can be incorporated into Zn-Bi melt by a semi-solid mixing method and control the size and distribution of secondary Bi phase to achieve a homogeneous microstructure. Organic immiscible SCN-CTB systems were tested to validate that nanoparticle is also effective for organic materials systems. In addition, the transparent organic system provides us a promising way to study the fundamental physics of nanoparticles enabled phase control in solidification processing.

4.1 Scalable Manufacturing of Immiscible Al-Bi alloy by Self-assemble Nanoparticles

Immiscible Al-Bi alloys are promising for bearing materials for the self-lubricating properties. However, it is still difficult to control the distribution and size of minority Bi phase during cooling and solidification. In this chapter, we show that by applying a scalable molten salt assisted incorporation process, TiC nanoparticles can be incorporated into Al matrix to produce Al-TiC master nanocomposites, which can be readily used to process Al-Bi immiscible alloy and restrict the size of minority Bi phase. TiC nanoparticles can be self-assembled on the Al-Bi interface and restrict Bi phase size substantially. In addition, submicron minority Bi phase can be achieved by combining the addition of nanoparticles with high cooling rates. Mechanical properties of Al-Bi immiscible alloys can be further enhanced by the addition of Cu element and cold rolling.

4.1.1 Introduction

Al-Bi immiscible alloys are long believed to be ideal bearing materials that offer outstanding friction properties [Feyzullahoğlu 2010, Lepper 1997]. However, it is difficult to realize the scalable manufacturing of immiscible alloys because it is hard to effectively control the fast growth and coagulations of minority phase droplets during cooling, which is essential for the unique properties and applications. For example, during cooling of Al-Bi melt, Bi droplets will grow and tend to sink down to the bottom of melt due to the higher density of Bi (three times higher than Al).

As mentioned in Chapter 2.3, different approaches have been experimented to tackle this problem. Conventional solid state processing, rapid cooling and casting under microgravity

environment have been studied in the previous researches. Unfortunately, these methods have encountered certain technical/fundamental limits. Recently, a novel method for phase control in Al-Bi immiscible alloy was successfully demonstrated [Chen 2014, Cao 2016 and Sun 2017] by using nanoparticles. But this method requires applying ultrasonic processing to incorporate and disperse nanoparticles in molten metal, which is hard for large scale production. Therefore, a novel method addressing the challenge posed by the miscibility gap is highly demanded to obtain well-dispersed minority phase in bulk immiscible alloys.

In this chapter, we explored a novel scalable manufacturing method that can substantially restrict the size of minority Bi phase to submicron during processing of Al-Bi immiscible alloy through a nanoparticles self-assemble mechanism. Moreover, addition of Cu element and cold rolling of Al-Bi immiscible alloy will be applied to further enhance the mechanical properties for its proper use as bearing material.

4.1.2 Materials and Methods

To cast plates and tensile bars of Al-20Bi-1Cu-2vol%TiC nanocomposites, the Al-9vol% TiC master nanocomposites were diluted in pure Al melt at 820 °C and then Bi and Cu elements were added to the melt. To form a single liquid phase in the Al-Bi material system, the temperature was heated to 900 °C. Mechanical mixing was applied at this temperature for 15 min with a rotation speed of 200 rpm. The melt was then cast to a steel plate mold to get the designed shape. The cooling rate was around 10 K/s measured by a thermocouple during solidification. To further investigate the effect of the cooling rate on the growth phase control of Al-Bi immiscible alloy by TiC nanoparticles, the molten metal was also cast to a copper wedge mold. The cooling rate R at the thickness d in the copper wedge mold have a relationship of $R = \frac{1000Kmm^2}{s} / (\frac{d}{2})^2$. Four

samples from different thickness of copper wedge mold were prepared and the cooling rate were 28 K/s, 50 K/s, 200 K/s and 400 K/s respectively. To further improve the mechanical properties of the Al-20Bi-1Cu-2vol%TiC nanocomposites, the as cast plate was cold rolled to a thickness reduction of 40%.

The as cast and rolled samples were ground, polished and then ion milled by Precision Ion Polishing System (PIPS) for 3 h at an accelerating voltage of 4 kV, with 6° milling angle to expose the microstructure and embedded nanoparticles. The microstructural characterization was performed using a ZEISS Supra 40VP SEM equipped with Electron Dispersive Spectroscopy (EDS) at an operation voltage of 15 kV and a spot size of 15 nm. Bi phase size distribution was evaluated from SEM images using the image analysis software Image J. Vickers hardness tests were conducted using a 200 gf load for 10 s by LM 800AT microhardness tester. Tensile testing was measured by Instron 5966 with a video extensometer followed ASTM E8/E8M standard with a strain rate of 3.3×10^{-3} 1/s.

4.1.3 Results and Discussion

The as-solidified Al-TiC master nanocomposites were then diluted to immiscible Al-20Bi alloy melt to control the phase nucleation and growth during cooling. Figure 4-1 shows the mechanism of the nanoparticles enabled phase control in the Al-Bi immiscible system. The challenge of processing the Al-Bi immiscible alloy is shown in Figure 4-1a. Above the miscibility gap where a single liquid phase of Al-Bi melt exists, the alloy components are completely miscible with each other. Mechanical mixing was applied in the single liquid phase to homogenize the melt. When this homogeneous liquid is cooled down into the miscibility gap, Bi droplets nucleate and start to grow. Due to the high diffusion coefficient (up to 10^{-8} m^2s^{-1}) in liquid metals [Roy 1988,

Oberg 1973 and Tiller 1953], the Bi droplets can grow rapidly to become large droplets and tend to coalesce and sink down to the bottom of the melt due to its higher density than the Al melt. The nanoparticles enabled phase control is demonstrated in Figure 4-1b. With dispersed TiC nanoparticles homogeneously distributed in the melt, when the melt is cooled down to the miscibility gap, some TiC nanoparticles can serve as heterogeneous nucleation sites to promote the formation of more Bi droplets. Moreover, during the cooling through the miscibility gap, TiC nanoparticles can self-assemble to Al-Bi interface driving by decreasing the system surface energy and form a nanoparticles coating. TiC nanoparticles move to Al-Bi interface and cover the Bi droplets rapidly. This nanoparticle coating layer can slow down the diffusion of atoms into the Bi droplets. Thus, the growth of Bi phase can be substantially impeded and the size of Bi is significantly smaller than in pure Al-Bi.

The favorable energy state at the Bi-Al interface can be explained by a simple model as shown in Figure 4-2. R is the radius of the nanoparticle, γ_0, γ_1, and γ_2 are the interfacial energy of Bi/Al interface, TiC/Al interface and TiC/Bi interface respectively, while θ is the wetting angle of the TiC nanoparticle at Bi-Al interface. There are three parts contributed to the net interfacial energy when TiC nanoparticles assemble to the Bi/Al interface:

(1) The negative energy of missing Bi-Al interface: $E_0 = -\gamma_0 \cdot \pi R^2(1 - cos^2\theta)$; (2) The energy increase of TiC/Al interface: $E_1 = \gamma_1 \cdot 2\pi R^2(1 - cos\theta)$; (3) The energy increase of TiC/Bi interface: $E_2 = \gamma_2 \cdot 2\pi R^2(1 + cos\theta)$. Therefore, the net interfacial energy would be

$$E = E_0 + E_1 + E_2 = \pi R^2[2(\gamma_1 + \gamma_2) + 2cos\theta(\gamma_2 - \gamma_1) + \gamma_0 - \gamma_0 cos^2\theta] \quad 4\text{-}1$$

When $\cos\theta = \frac{\gamma_2 - \gamma_1}{\gamma_0}$, the total interfacial energy has a minimum $E_{min} = \pi R^2[2(\gamma_1 + \gamma_2) + \frac{(\gamma_2 - \gamma_1)^2}{\gamma_0} + \gamma_0]$. For a particle not adsorbed at the interface, the total interfacial energy will be $E' = 4\pi R^2\gamma_1 or\ 4\pi R^2\gamma_2$ when particle stay in Al or Bi respectively. When a nanoparticle binds to the interface from Al, the binding energy

$$\Delta E = E' - E_{min} = min[\pi R^2\gamma_0(1 \pm cos\theta)^2] \quad 4\text{-}2$$

Therefore, unless the wetting angle θ is 0° at which $\gamma_2=\gamma_1$, binding energy ΔE will be larger than zero. In Al-Bi-TiC case, it is less likely that γ_2 will be equal to γ_1 due to the different physical properties of Al and Bi. Thus the binding energy for TiC nanoparticles in Al-Bi melt will be larger than zero and the energy difference leads to these nanoparticles prefer staying at the Bi-Al interface.

In Al-Bi-TiC system, R is approximately equal to 25 nm, the interfacial energy between Al and Bi γ_0 at 1173 K is ~1.6×10^{-2} Nm^{-1}. Although the wetting angle of TiC nanoparticle at Al-Bi interface is unknown, it is estimated to be close to 128° since the similar physical properties between TiC and $TiC_{0.7}N_{0.3}$ [Chen 2015]. Then the binding energy is estimated to be 4.6×10^{-18} J. It should be noticed that the thermal Brownian motion energy will tend to move nanoparticles freely instead of staying at the interface. The Brownian motion energy is $E_B = kT/2$ where k is the Boltzmann constant and T is the temperature of the melt. At the processing temperature 1173 K, Brownian motion energy of the TiC nanoparticles is calculated to be 8×10^{-21} J. Therefore, the binding energy (4.6×10^{-18} J) is more than three orders of magnitude higher than Brownian motion energy (~8×10^{-21} J). Therefore, the binding energy can effectively trap TiC nanoparticles at the Al-Bi interface. Therefore, once Bi droplets nucleate in Al melt, TiC nanoparticles tend to cover the Bi-Al interface to achieve a more favorable energy state.

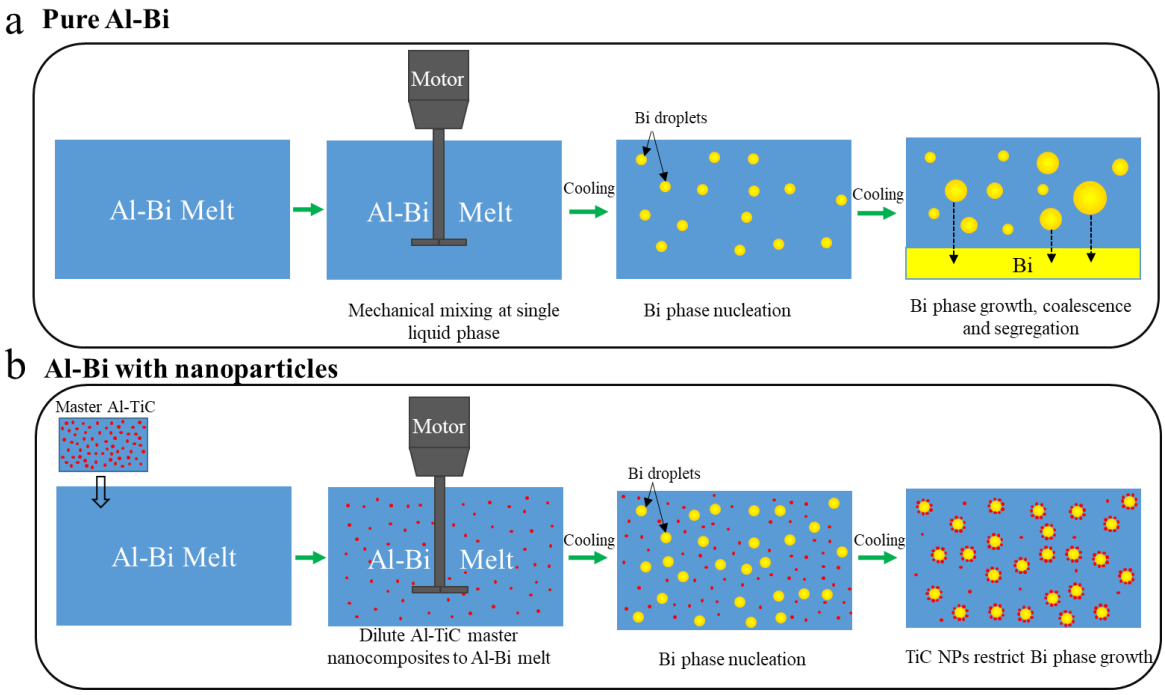

Figure 4-1 Schematic of the phase evolution during cooling. (a) Pure Al-Bi immiscible alloy; (b) Al-Bi with TiC nanoparticles during cooling.

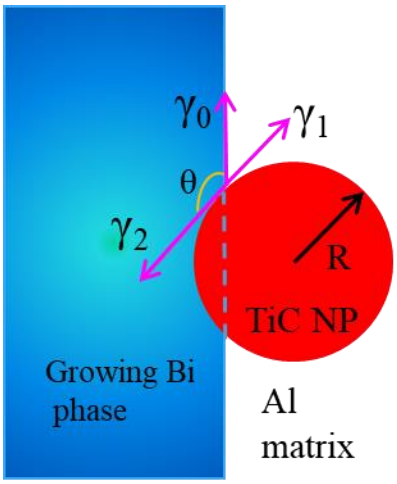

Figure 4-2 Schematic illustration shows an adsorbed spherical nanoparticle with radius *R* at Bi/Al interface. γ_0, γ_1, and γ_2 are the interfacial tensions of Bi/Al, particle/Al and particle/Bi interfaces. θ is the wetting angle of the particle at Bi-Al interface.

To verify the nanoparticles enabled phase control, the microstructure of as cast Al-20Bi-1Cu-2vol% TiC nanocomposites and pure Al-20Bi with the same processing route are shown in Figure 4-3a and Figure 4-3b. The relatively bright phases are Bi phase while the dark phases are Al matrix. It clearly shows that the size of Bi phase in nanocomposites sample is much smaller than pure Al-20Bi. Based on the image processing, the average area of Bi in pure Al-20Bi and Al-20Bi-1Cu-2vol% TiC nanocomposites are 199.8 μm^2 and 8.54 μm^2, respectively. Moreover, the distribution of Bi phase size in pure Al-20Bi is not as homogeneous as in the nanocomposites sample. Without nanoparticles phase control mechanism, Bi droplets could grow much larger and coalesce during cooling thus form large Bi droplets which lead to the inhomogeneous size distribution. To further validate the nanoparticles enabled phase control, we looked at the interface between Bi phase and Al matrix. As shown in Figure 4-3c, the relative bright phase at the center is Bi and the rest dark phase is Al matrix. It is observed this Bi phase with diameter around 2 μm is wrapped up by a layer of TiC nanoparticles. The magnified image at the Al-Bi interface is shown in Figure 4-3d, we could identify the condense TiC coating clearly. Figure 4-3e and Figure 4-3f are the EDS line-scan results followed the track of pink arrow in Figure 4-3c. The signals of Al and Bi element are shown in Figure 4-3e, it is reasonable that Bi signal decrease and Al signal increase when the scan go across the interface. Figure 4-3f shows a Ti element signal peak at the Al-Bi interface which means TiC nanoparticles do self-assemble to Al-Bi interface and form a coating. The Al-Bi interface with TiC nanoparticles coating were further studied by EDS elemental mapping as shown in Figure 4-4. Figure 4-4a is the SEM image of one typical Bi phase coated by TiC nanoparticles. Figure 4-4b, 4-4c and 4-4d reveal the spatial distributions of Ti, Al and Bi, respectively. Ti element corresponds to TiC nanoparticles are mainly distributed along the interface of Al and Bi elements which further validate the self-assembly of TiC nanoparticles. This

phase control mechanism by nanoparticles is different with the typical nucleation theory. Heterogeneous nucleation in Al-Bi has certain limit for control the size of Bi phase. The incorporation of nanoparticles can increase nucleation sites of Bi, but it is not the major mechanism to refine the microstructure of Al-Bi-TiC nanocomposites.

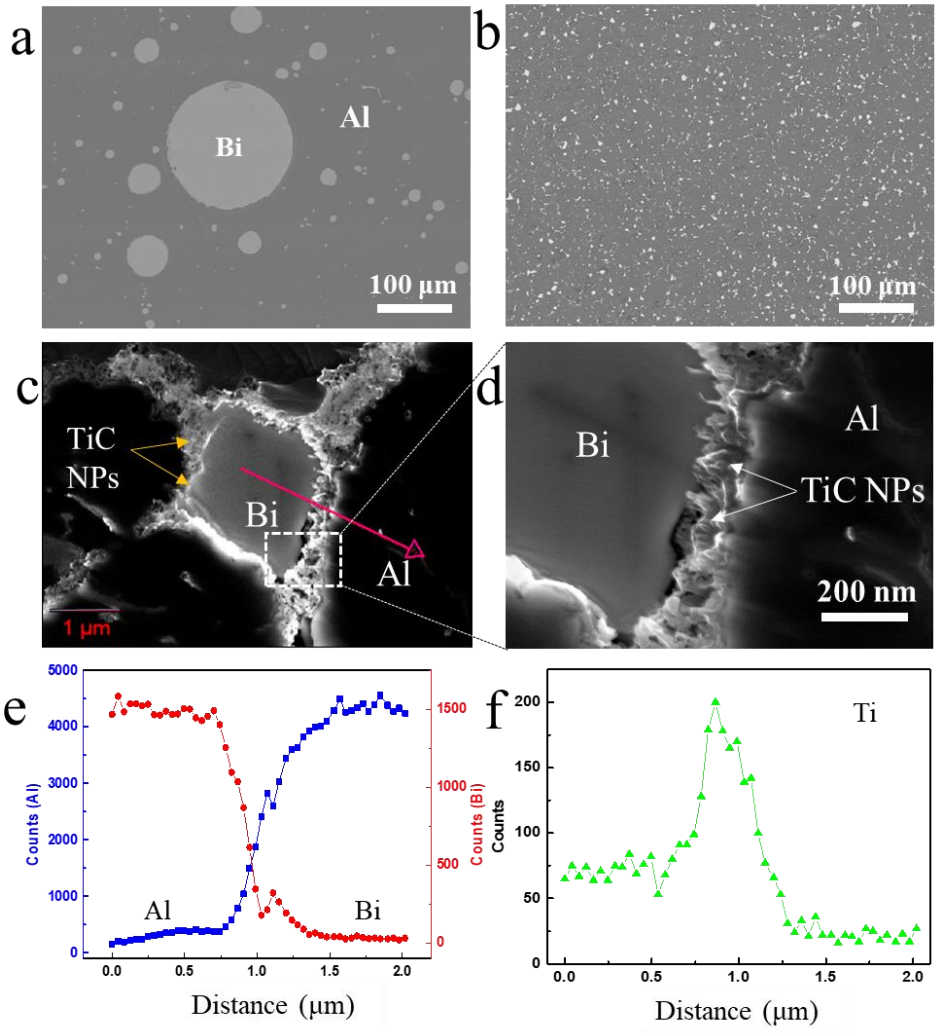

Figure 4-3 Nanoparticle enabled phase control in Al-Bi alloy system. (a) SEM image of pure Al-20Bi alloy under a cooling rate of 10 K/s; (b) SEM image of Al-20Bi-1Cu-2vol%TiC under a cooling rate of 10 K/s; (c) and (d) SEM image of Bi phase with TiC nanoparticles coating. (e) and (f) EDS line scan data of Bi, Al and Ti element along the pink arrow in (c).

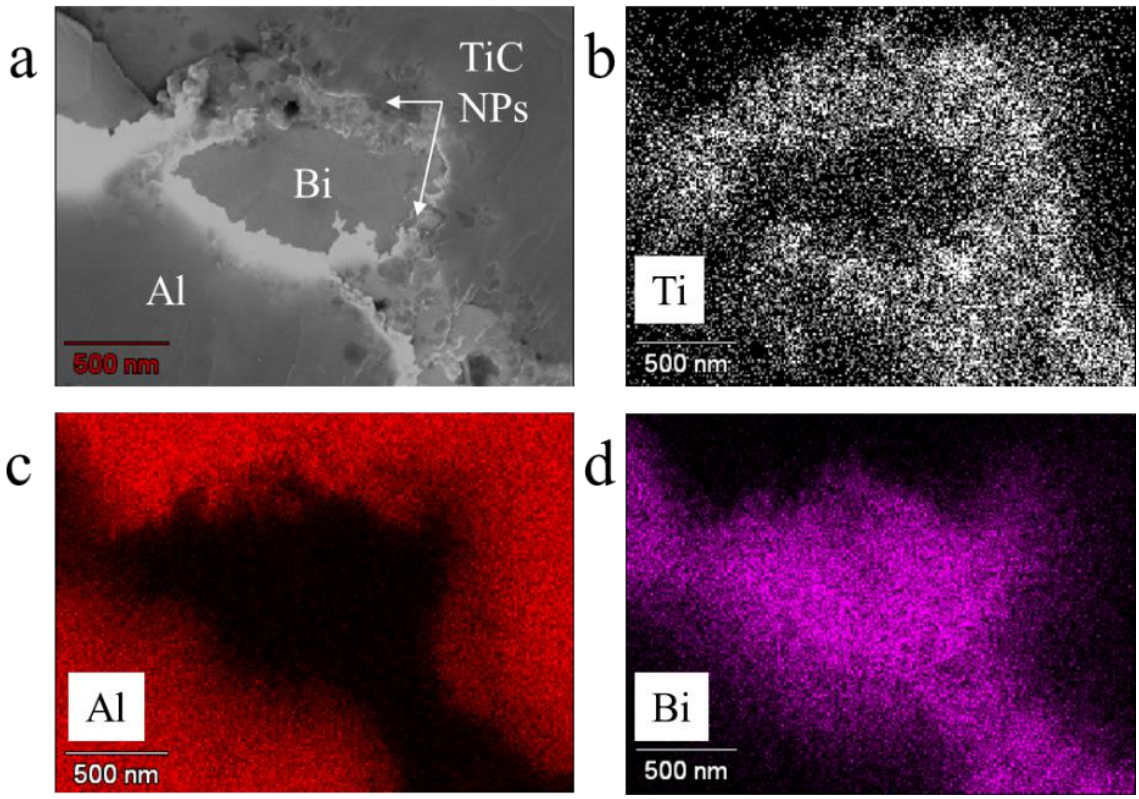

Figure 4-4 SEM-EDS micrographs of Al-20Bi-1Cu-2vol%TiC nanocomposites: (a) SEM image of Al-20Bi-1Cu-2vol%TiC under a cooling rate of 10 K/s; (b) Ti element distribution; (c) Al element distribution; (d) Bi element distribution.

One more step forward, if submicron or nanoscale secondary phase can be obtained in bulk immiscible alloys, exciting properties can be realized for revolutionary technical applications, such as superconductors (e.g. Cu-V), giant magnetoresistive (GMR) materials (e.g. Cu-Co) [Wang 1998], and Li-ion battery electrode materials (Sn-Si) [Kasavajjula 2007]. Cooling rate is another important parameter governing the size of Bi phase. Assuming Bi droplets nucleate and grow by the diffusion of Bi atoms, the diameter of Bi droplet then can be determined by $d_{Bi} = 2\sqrt{2DSt}$, where *D* is diffusion coefficient of Bi atoms, *t* is cooling time in the immiscible region, and *S* is supersaturation of Bi. From this equation, the cooling time in the immiscible region is depended

on the cooling rate. With faster cooling rate, the cooling time *t* in the immiscible region is reduced and thus less Bi atoms could transport into the Bi droplets leading to the refinement of Bi size.

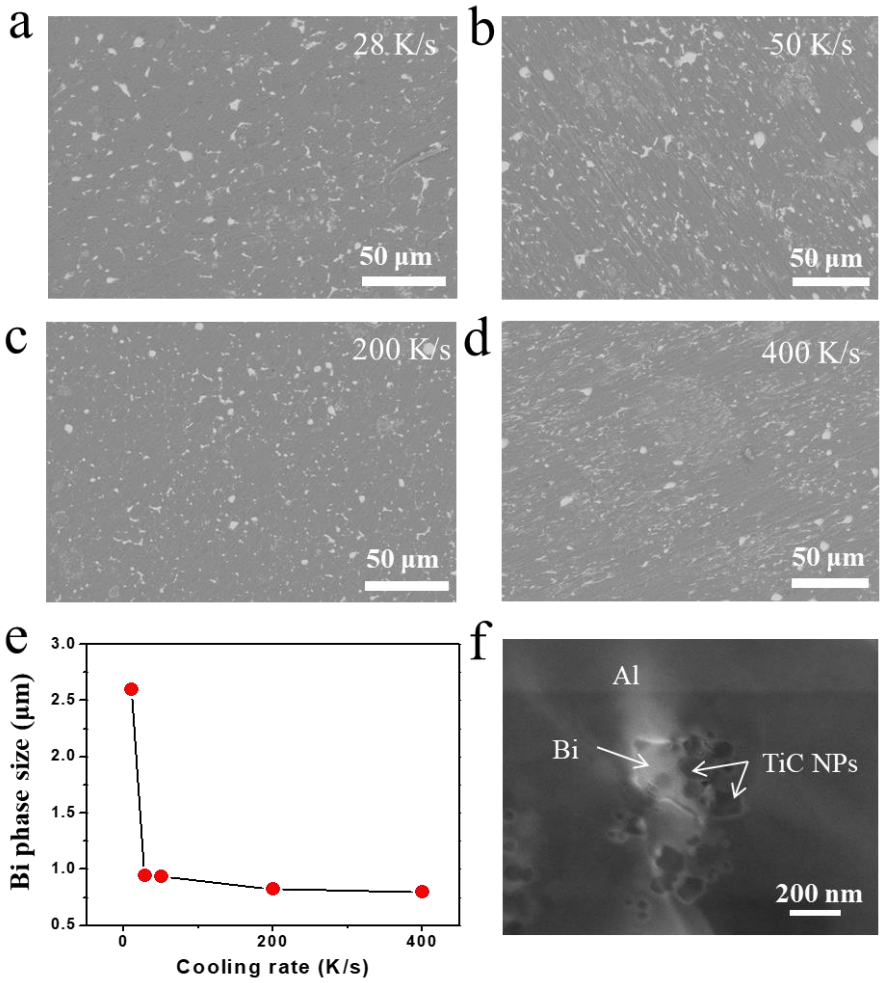

Figure 4-5 Control minority Bi phase down to submicron. (a-d) SEM image of Al-20Bi-1Cu-2vol% TiC at cooling rate of 28 K/s, 50 K/s, 200 K/s and 400 K/s, respectively; (e) Bi size as a function of the cooling rate for Al-20Bi-1Cu-2vol% TiC; (f) SEM image of a submicron size Bi phase with TiC nanoparticles coating in Al-20Bi-1Cu-2vol% TiC under a cooling rate of 400 K/s.

To study the influence of cooling rates on the nanoparticles enabled phase control, Al-20Bi-1Cu-2vol%TiC melt was cast to a copper wedge mold, different cooling rates were obtained at different height of the cast ingot. In the microstructure of Al-20Bi-1Cu-2vol%TiC as shown in Figure 4-5 (a-d), Bi phase sizes are substantially decreased with faster cooling. The relationship of Bi phase size with cooling rate is shown in Figure 4-5e. The Bi phase sizes of 10 K/s, 28 K/s, 50 K/s, 200 K/s and 400 K/s cooling rates are 2.6 μm, 0.946 μm, 0.878 μm, 0.823 μm and 0.797 μm, respectively. It is observed that with the increase of cooling rate, the average size of Bi phase decreases gradually. When the cooling rate is higher than 28 K/s, the size of Bi phase can be reduced to submicron meter scale. The smallest average size of Bi phase we can obtain here is approximately 800 nm under the cooling rate of 400 K/s. Figure 4-5f shows the zoom-in SEM image of Al-20Bi-1Cu-2vol%TiC nanocomposites which the cooling rate is 400 K/s. The Al matrix, Bi phase and TiC nanoparticles are indicated in the figure. It is observed that the size of Bi phase in this image is in the range of hundreds nanometers. Moreover, it is interesting that TiC nanoparticles did not form a dense coating at the Al-Bi interface (as shown in Figure 4-5b), instead only several nanoparticles decorated on Bi phase. It is highly possible that with higher cooling rates, TiC nanoparticles do not have enough time to coat whole Bi droplets before the alloy solidify. However, TiC nanoparticles are still capable control the size of Bi phase down to submicron. At this scale, without nanoparticles fully coated the Al-Bi interface, only several nanoparticles at the interface are good enough to hinder the diffusional growth significantly. Combining the fast cooling with the nanoparticles enabled phase control mechanism, submicron minority phase in liquid processed immiscible alloys system can be achieved to break the fundamentals and technical limits of the processibility of immiscible alloys.

The mechanical properties of Al-Bi alloys can be further enhanced by addition of one percent of Cu element and cold rolling. Figure 4-6a shows the SEM image of the cold rolled Al-20Bi-1-Cu-2vol%TiC. Bi phases are well distributed in Al matrix. Figure 4-6b is the magnified SEM image of the area marked in Figure 4-6a. It is observed that this Bi phase is elongated along the rolling direction. HV microhardness and tensile testing were carried out to analyses the mechanical properties of this nanocomposites material. Figure 4-7a shows that the HV microhardness of pure Al-20Bi, Al-20Bi-2vol%TiC, Al-20Bi-1Cu-2vol%TiC nanocomposites and cold rolled Al-20Bi-1Cu-2vol%TiC nanocomposites are 0.32, 0.35, 0.50 and 0.80 GPa, respectively. Compared with pure Al-20Bi immiscible alloy, the microhardness improvement of Al-20Bi-2vol%TiC is not very significant due to the nanoparticles are distributed at the Al-Bi interface instead of uniformly disperse in the Al matrix. The microhardness increment of Al-20Bi-1Cu-2vol%TiC nanocomposites is mainly due to the addition of Cu element. Cu could form precipitates to enhance the mechanical performances. To validate the scalability of this processing, ASTM standard tensile testing of the nanocomposites samples was done. The engineering stress-strain curve is shown in Figure 4-7b, the yield strength and ultimate tensile strength of Al-20Bi-1Cu-2vol%TiC nanocomposites were 124 MPa and 157 MPa, respectively. Also, the yield strength and ultimate tensile strength of cold rolled Al-20Bi-1Cu-2vol%TiC nanocomposites were 248 MPa and 258 MPa, respectively. The ductility is observed approximately 2.5-3.0 vol% for the Al-20Bi-1Cu-2vol%TiC nanocomposites. The low ductility may originate from the brittleness of Bi phase and defects formed during casting process. It is also observed that the slope at the elastic deformation region is different for the as cast and cold rolled samples. This could be explained by the elimination of casting defects during cold rolling. The tensile tests were not performed for pure Al-Bi due to the segregation of Bi phase. Without the addition of nanoparticles, the Bi phase

separates from the Al matrix and sinks down to the bottom of the ingot. The fracture surface after tensile test is shown in Figure 4-8a and 4-8b. Al matrix shows a typical ductile fracture surface with homogeneous dimples up and down [Aoki 1990, Lee 2003 and Ishikawa 1990]. However, we can clearly observe cracks in Bi phases which might be the reason of the relatively low ductility. Cracks preferred to form and propagate at Bi phase due to the brittle nature of Bi. Figure 4-8b shows the high magnification SEM image of one cracked Bi phase coated with TiC nanoparticles. We can observe that the crack only propagate along the area without nanoparticles. This might due to the crack deflection caused by the nanoparticles [Yang 2014].

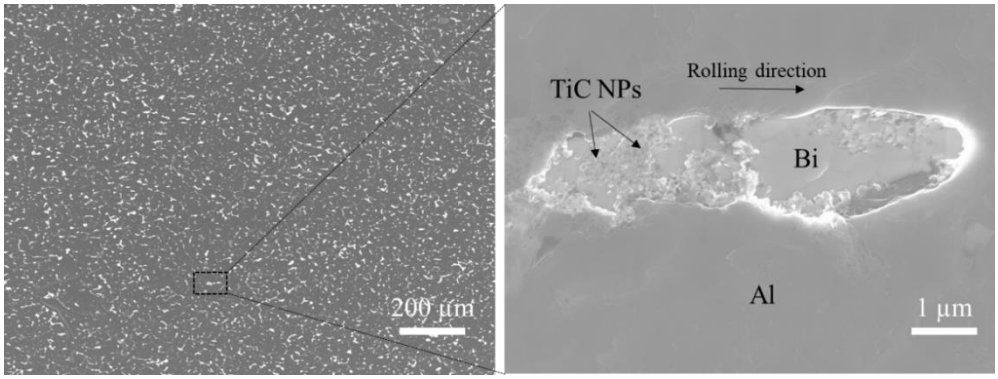

Figure 4-6 Microstructure of cold rolled Al-20Bi-1Cu-2vol% TiC. (a) SEM image of cold rolled Al-20Bi-1Cu-2vol% TiC; (b) SEM image of one deformed Bi phase in the marked area in (a).

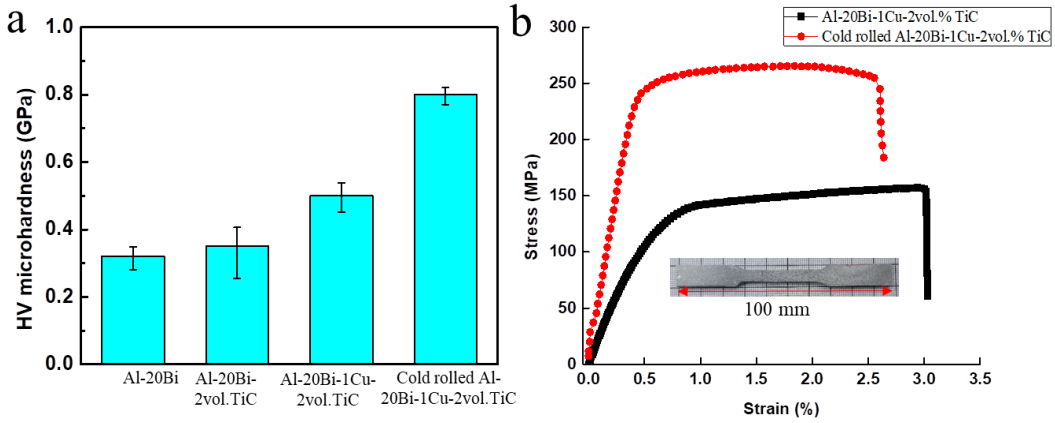

Figure 4-7 Mechanical properties of Al-Bi alloy with nanoparticles. (a) Vickers microhardness and (b) tensile test of as cast Al-20Bi, as-cast Al-20Bi-2vol%TiC, as cast Al-20Bi-1Cu-2vol%TiC and cold rolled Al-20Bi-1Cu-2vol%TiC.

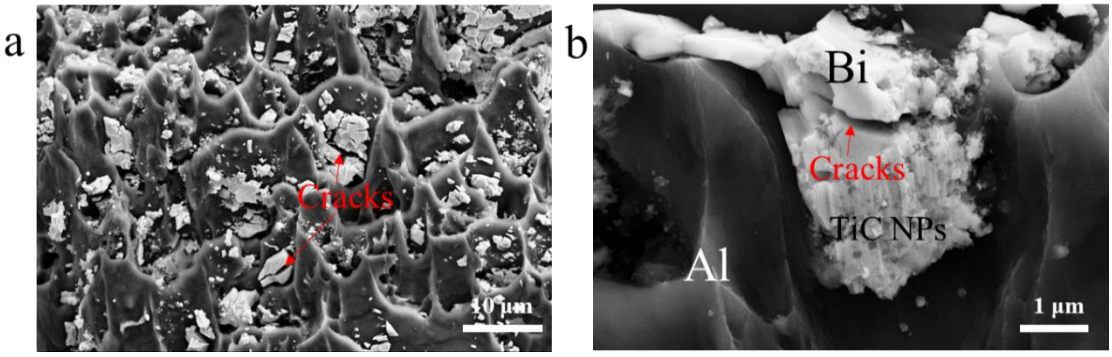

Figure 4-8 Fracture surface of cold rolled Al-20Bi-1Cu-2vol%TiC. (a), (b) SEM image of the fracture surface of the tensile bar after test.

4.1.4 Summary

In summary, master Al-TiC nanocomposites with a high volume fraction of TiC nanoparticles were produced by a scalable manufacturing method, i.e. molten salt assisted solidification. The master Al-TiC nanocomposites can be readily diluted for processing Al-Bi immiscible alloys. TiC nanoparticles can self-assemble at the Al-Bi interface and restrict the growth of Bi phase substantially. This nanoparticle-enabled phase control mechanism allows us to process Al-Bi immiscible alloy in large scale. With the increase of cooling rate, the average diameter of Bi phase decreases and the size of the minority Bi phase can be reduced to submicron, breaking the fundamental and technical limits of processing immiscible alloys and opening up more exciting applications. The mechanical properties of Al-Bi immiscible alloy with TiC nanoparticles can be further enhanced by Cu element addition and cold rolling for practical applications.

4.2 Strengthening Al-20Bi-$TiC_{0.7}N_{0.3}$ Nanocomposites by Cu Addition and Grain Refiner

$TiC_{0.7}N_{0.3}$ nanoparticles are used to control Bi phase growth in immiscible Al-Bi alloy during solidification, producing Al-20Bi-$TiC_{0.7}N_{0.3}$ nanocomposites with homogeneously distributed Bi phases. Cu element and Al-5Ti-1B grain refiner were added to further strengthen the nanocomposite. Significant microhardness enhancement was achieved without deteriorating the distribution of Bi phase.

4.2.1 Introduction

A typical bearing consists of three main types of materials: a relatively hard matrix material (such as Al or Cu), a soft component to provide self-lubricating properties, and small quantities of various additives that modify the microstructures and properties of the matrix metals [Kopeliovich 2001]. Al alloys with a homogeneous distribution of Bi are long believed to be ideal bearing materials that offer outstanding overall properties [Feyzullahoğlu 2010, Lepper 1997]. Comparing with the most commonly used Al-Sn bearing alloy, the soft component Bi could bring superior lubricating properties than tin. Al-Pb alloys are also of interests but they are not widely used since lead is not environment friendly. There was significant effort to cast Al-Bi system in order to harness the self-lubricating properties for energy savings. However, it is very difficult to obtain homogeneous distributed Bi phase by conventional casting methods due to the rapid growth of Bi phase and the large density difference (Bi is 3.6 times heavier than Al). Bi tends to sink down to the bottom leading to phase separation [Ratke 2007].

Recently, a novel way for rapid phase control was successfully demonstrated [Chen 2014] by using nanoparticles to self-assemble at the interface between the major and minority phases.

Friction tests showed that the coefficient of friction of Al-20Bi-2vol% $TiC_{0.7}N_{0.3}$ (all compositions are in wt.% unless otherwise specified) is one order of magnitude lower than that of pure Al-20Bi. However, the strength of the Al-20Bi-2vol% $TiC_{0.7}N_{0.3}$ nanocomposites is still relatively low due to the lack of strengthening mechanisms.

The strength and microstructure of the Al-Bi alloys are key factors for the friction and wear properties [Rosales 2014]. Alloy strengthening is widely used for Al alloy. However, it should be noted that some regular alloy elements may not be suitable for Al-Bi immiscible system due to the reactive property of Bi. For example, Mg will react with Bi and may deteriorate the microstructure and performance [Nayeb 1985]. Therefore, strengthening Al-Bi-$TiC_{0.7}N_{0.3}$ nanocomposites with alloying elements is more complicate than regular aluminum alloys. Cu element can be very effective to strengthen Al-Bi alloys and it will not react with Bi as suggested by the Cu-Bi phase diagram. Al-5Ti-1B grain refiner is also widely used to improve Al alloys properties by grain refinement. However, it is still unknown the grain refinement effect for Al-Bi-$TiC_{0.7}N_{0.3}$ system. This chapter is to explore the Cu alloying and grain refiner effects for strengthening Al-20Bi-2vol% $TiC_{0.7}N_{0.3}$ nanocomposites.

4.2.2 Materials and Methods

Al-20Bi was prepared by melting pure Al (99.5%, AA1350) and Bi (99.9%, from Alfa Aesar) in an alumina crucible (with diameter of 36 mm and height of 90 mm) using electrical resistance furnace. $TiC_{0.7}N_{0.3}$ nanoparticles (diameter of ~80 nm, from Sigma Aldrich) were fed and dispersed by an ultrasonic cavitation-based method [Lan 2004, Choi 2012]. Figure 4-9 illustrates the schematic of the experiment setup. The heating system consists of an electrical furnace and alumina covered thermocouple to control the heating temperature. A refractory niobium alloy with a diameter of 12.7 mm and a length of 175 mm was attached to a booster

(Sonicator 3000, Misonix Inc), which was mounted in a transducer working under a maximum 600 W power output. Vibration amplitude is 60 μm peak-to-peak with a frequency of 20 kHz. When the Al-Bi alloy was melted in the alumina crucible at 973 K, the tip of the probe was inserted around 6mm into the melt during the nanoparticle feeding process. Inert argon gas was used to protect the melt and nanoparticles to avoid severe oxidation. A double-capsulate feeding method was applied to feed nanoparticles. $TiC_{0.7}N_{0.3}$ nanoparticles were wrapped with a thin Al foil (alloy 1000, thickness: 0.0127 mm) before it was rolled into a rod shape. The rod with nanoparticles was wrapped again by another Al thin foil. The second Al foil will help release the nanoparticles into melt gradually. When the melt temperature reached 973 K (two liquid phase zone), two volume percent preheated nanoparticles (423 K for 1 hour) were fed into the melt by this double capsulate method. Then the temperature was further heated to 1173 K (single liquid phase zone) and ultrasonic processing was applied for 15 minutes to ensure nanoparticles dispersion. The crucible was then taken out from the furnace and cool down in air (cooling rate about 1 K/s) to solidify.

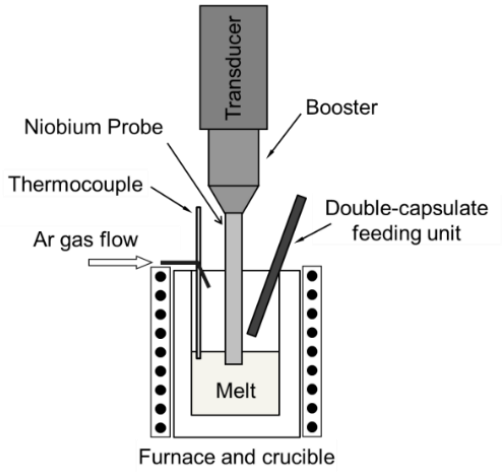

Figure 4-9 Experiment setup for melting and nanoparticles feeding process.

The Al-20Bi-2vol%$TiC_{0.7}N_{0.3}$ nanocomposites was melt again at 973 K (two liquid state), and pure Cu was fed under ultrasonic processing for 15 minutes. Then the temperature was heated up to 1173 K (single liquid state) and ultrasonic processing for one more minutes to ensure nanoparticle dispersion. Finally, the crucible was taken out from the furnace and cool down in air (~1 K/s) to solidify. One or two percent Cu were added for different samples. After this, 0.3% Al-5Ti-1B grain refiner was added by the same procedure.

The solidified samples were ground, polished and then ion milled by Precision Ion Polishing System (PIPS) to expose the microstructure and embedded nanoparticles. Scanning electron microscope (ZEISS Supra 40VP SEM) were used to analyze microstructure. Electron backscattering diffraction (EBSD) detector was used for grain size analysis. The grain size is measured by following ASTM E112-96. Vickers hardness tests were conducted using a 200 gf load for 10 s by LM 800AT microhardness tester.

4.2.3 Results and Discussion

SEM images of the samples after processing are showed in Figure 4-10. Figure 4-10a shows that a good distribution of refined minority Bi phase is obtained under a slow cooling rate of 1 K/s by dispersing the $TiC_{0.7}N_{0.3}$ nanoparticles in the single liquid zone. Some Bi phase with nanoparticles existed in or near grain boundaries, most likely due to nanoparticles being pushed by the solidification fronts during solidification [Xu 2002]. Figure 4-10b shows that $TiC_{0.7}N_{0.3}$ nanoparticles are trapped at the interface between Al and Bi and refine the Bi size to about 10 μm. Comparing with pure Al-20Bi sample that Bi will settle down to the bottom due to sedimentation, the distribution of Bi is homogeneous in Al-20Bi-2vol% $TiC_{0.7}N_{0.3}$ nanocomposites.

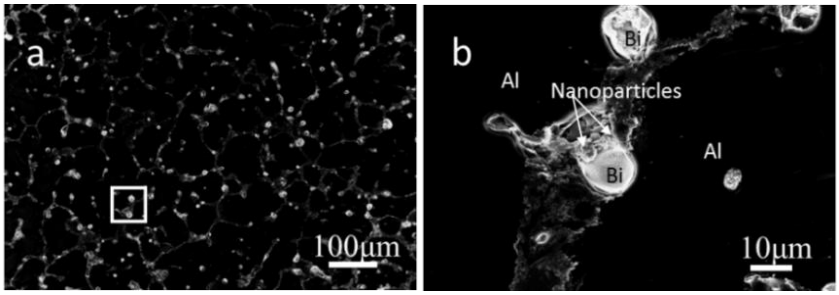

Figure 4-10 SEM images of Al-20Bi alloy with 2vol% $TiC_{0.7}N_{0.3}$ nanoparticles under a cooling rate of 1 K/s.

It is also important to compare the microstructure after the incorporation of the strengthening Cu element. The microstructure of Al-20Bi-2vol%$TiC_{0.7}N_{0.3}$ nanocomposites with 1% Cu is showed in Figure 4-11. In Figure 4-11a, the white phase distributed around the grain boundary consists of Bi phase and $TiC_{0.7}N_{0.3}$ nanoparticles. The black region is the Al-Cu solid solution matrix with a small amount of Al-Cu precipitation phase. With the addition of 1% Cu, the minority Bi phase still keeps the good distribution. Figure 4-11b and Figure 4-11c show that $TiC_{0.7}N_{0.3}$ nanoparticles can still self-assemble at the Al-Bi interface forming a dense coating layer. Al-20Bi-2vol% $TiC_{0.7}N_{0.3}$ nanocomposites with 2% Cu and 0.3% Al-5Ti-1B grain refiner show similar microstructure without sedimentation. With the strengthening Cu element and Al-5Ti-1B grain refiner, the incorporation of nanoparticles could still successfully refine the size of Bi phase.

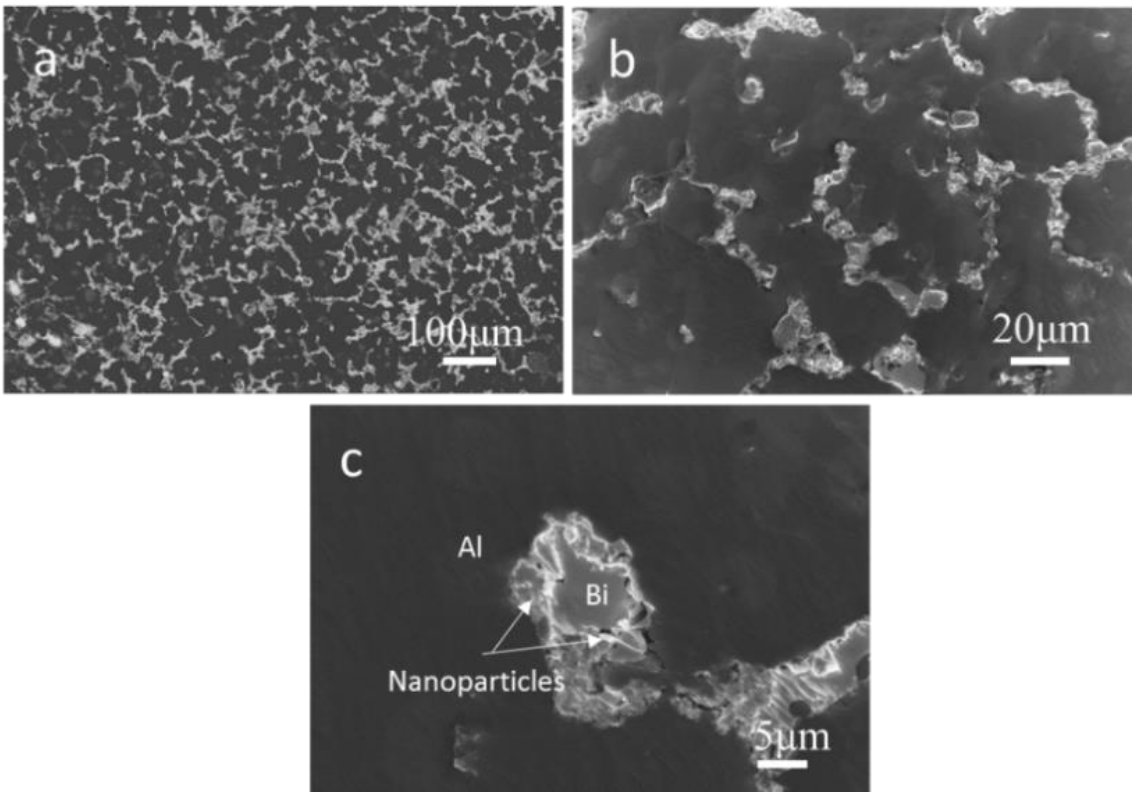

Figure 4-11 SEM images of Al-20Bi-1Cu alloy with 2vol% $TiC_{0.7}N_{0.3}$ nanoparticles.

Figure 4-12 shows that Al-Cu precipitation phase is distributed in Al matrix region. Since the solubility of Cu in Al will reduce to approximately 0.1% at room temperature, Al-Cu precipitation phase will precipitate out during solidification process when 1-2% Cu was added. Compare Figure 4-12a (1% Cu addition) with Figure 4-12b (2% Cu addition), more precipitates are generated with higher Cu content.

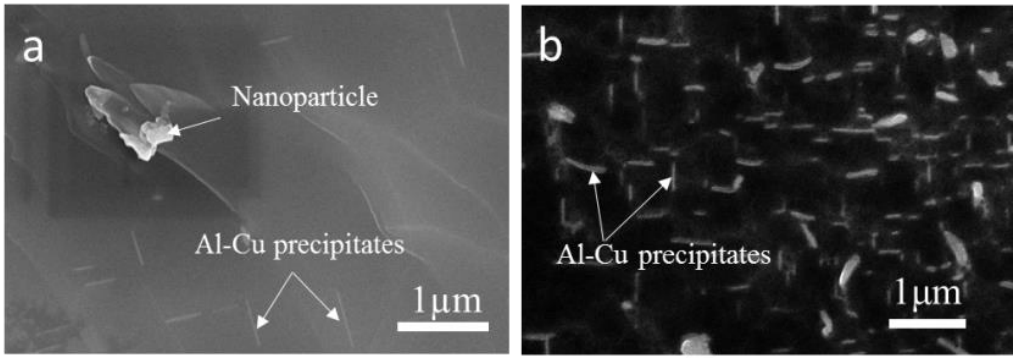

Figure 4-12 Al-Cu precipitates in (a) Al-20Bi-1Cu-2vol% $TiC_{0.7}N_{0.3}$; (b) Al-20Bi-2Cu-2vol% $TiC_{0.7}N_{0.3}$.

The grain size is analyzed by EBSD images. As showed in Figure 4-13, the grain size decrease after the addition of 0.3% Al-5Ti-1B grain refiner. It is measured that the average grain size reduce from approximately 143 μm to 97 μm after the addition of Al-5Ti-1B grain refiner. However, the grain refinement in Al matrix nanocomposites by the grain refiner is not as effective as in pure Al or Al alloy because the incorporated nanoparticles can already reduce the grain size before Al-5Ti-1B grain refiner was used.

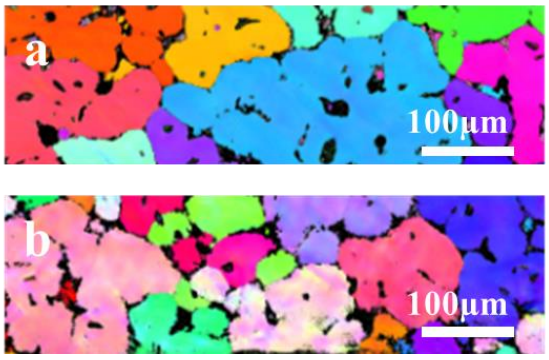

Figure 4-13 EBSD images of (a) Al-20Bi-2Cu-2vol% $TiC_{0.7}N_{0.3}$ nanoparticles; (b) Al-20Bi-2Cu-2vol% $TiC_{0.7}N_{0.3}$ with 0.3% Al-5Ti-1B grain refiner.

Figure 4-14 shows the microhardness data as a function of the contents of Cu and Al-5Ti-1B grain refiner. Microhardness improvement of 56% and 63% was obtained by adding 1% and 2% Cu respectively. Vickers microhardness of original nanocomposites material without Cu is 35.44 while 55.44 for the sample with 1% Cu and 57.88 for the sample with 2% Cu. This enhancement is mostly attributed to the formation of Al-Cu solid solution and Al-Cu precipitation phase. The solute Cu atoms and Al-Cu precipitates in Al matrix will impede the motion of dislocations and enhance the strength. Moreover, after the addition of 0.3% Al-5Ti-1B grain

refiner, the Vickers microhardness was further increased to 65.18 attribute to grain refinement effect.

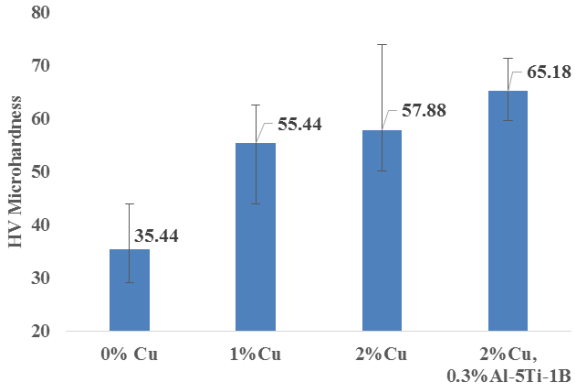

Figure 4-14 Plot of the microhardness for the Al-20Bi-2vol%$TiC_{0.7}N_{0.3}$ nanocomposites with different Cu and Al-5Ti-1B grain refiner content.

For Al-Bi-$TiC_{0.7}N_{0.3}$ nanocomposites, minority Bi phase will nucleate during cooling, and nanoparticles will rapidly assemble on the growing phase driven by a reduction of the system surface energy. This energy difference leads these particles to preferably stay at the Al-Bi interface. When compared with the Brownian motion energy kT/2, the Gibbs free energy needed to move nanoparticles from interface is three orders of magnitude higher [Reardon 2011, Chen 2014]. Therefore, such an energy well will effectively trap nanoparticles at the interface. After nanoparticles coat at the Al-Bi interface, this coating could effectively impede the diffusion growth by blocking Bi atoms diffuse into Bi droplets and thus reduce the growth significantly. With this nanoparticles enabled phase control method, we could obtain refined Bi phase distribute homogeneously in Al matrix instead of sedimentation. Moreover, because of the nanoparticle coating on the surface of Bi, colliding Bi droplets cannot merge because of a high capillary pressure in the liquid film between nanoparticle-coated droplets.

The strengthening of Al-Bi-$TiC_{0.7}N_{0.3}$ nanocomposites is accomplished by the incorporation of Cu. From the microstructure analysis, it shows that, by addition of strengthening Cu element, the nanoparticles could still self-assemble to Al-Bi interface and form a dense thin layer to achieve rapid phase control. Therefore, Cu will not deteriorate the rapid phase control effect in the nanocomposites.

In order to further increase the mechanical properties, 0.3% Al-5Ti-1B grain refiner is added to reduce the grain size. It is widely accepted that the morphology and size of $TiAl_3$ particles, as heterogeneous nucleation sites, are important factors determining the grain refinement efficiency [Xu 2013]. Here the grain size reduce from 143 μm to 97 μm by 0.3% Al-5Ti-1B grain refiner addition and further strengthening was achieved, which is attributed to the Hall-Petch effect.

4.2.4 Summary

Al-Bi-$TiC_{0.7}N_{0.3}$ nanocomposites were cast with an ultrasonic-assisted processing method. Microstructure analysis shows that $TiC_{0.7}N_{0.3}$ nanoparticles are self-assembled on the Al-Bi interface driven by the reduction of system surface energy so that the Bi droplets are refined and homogeneously distributed in Al matrix. The Al-Bi-$TiC_{0.7}N_{0.3}$ nanocomposites were further strengthened by additions of Cu element and Al-5Ti-1B grain refiner. The microhardness test shows that the addition of Cu and Al-5Ti-1B grain refiner could improve the mechanical properties significantly without deteriorating the rapid phase control effect of the nanoparticles. High performance Al-Bi nanocomposites have great potential for self-lubricating bearing applications.

4.3 Phase Control in Immiscible Zn-Bi Alloy by Tungsten Nanoparticles

Immiscible Zn-Bi alloy has a good potential to replace lead-based alloys to serve as a running layer in plain bearings. However, it is still a major challenge to uniformly disperse Bi

phase in Zn matrix during solidification processing since Bi droplets grow fast in liquid state and readily coagulate to induce phase sedimentation. In this chapter, tungsten (W) nanoparticles were, for the first time, used and effectively incorporated into the Zn-Bi melt for phase control. Tungsten nanoparticles were able to self-assemble to the Zn-Bi phase interfaces to slow down the growth of the Bi phase and prevent their coagulations, resulting in a significant size reduction of the Bi phase and microstructure refinement. Moreover, the incorporation of W nanoparticles into the Zn-Bi alloy enhanced its microhardness significantly. This new approach of using chemically-stable metal nanoparticles has a great potential for scale-up manufacturing of immiscible alloys for widespread applications.

4.3.1 Introduction

Immiscible Zn-Bi alloys have been suggested as potential environmentally benign alloys for running layers in plain bearings to replace lead-based alloys [Gollas 2013]. Zn-Bi alloys with better lubrication property, are considered to be superior to Zn-Sn alloys for plain bearings. Gollas et al. [Gollas 2013] electrodeposited a thin layer Zn-Bi biphasic layer on Cu sheets. However, it is difficult to cast bulk Zn-Bi alloys with a homogeneous distributed Bi phase due to the rapid growth and coagulations of the Bi phase and its sedimentation induced by the gravity force. The earlier study [Chen 2014, Cao 2016'] presented a novel method for rapid phase control in the immiscible Al-Bi alloy using ceramic nanoparticles. However, the poor wettability between the ceramic nanoparticles and the molten melt made the nanoparticle incorporation troublesome. In this chapter, chemically stable tungsten (W) nanoparticles were incorporated to Zn-Bi immiscible alloy. With a good wettability, W nanoparticles were easily incorporated into the Zn-Bi melt, making this process highly promising for large scale production.

4.3.2 Materials and Methods

Zn-8wt.%Bi alloy (all compositions are in wt.% unless otherwise specified) was prepared by melting pure Zn and Bi (99.9%, from Alfa Aesar) in an alumina crucible (with a diameter and height of 50 and 80 mm, respectively) using an electric resistance furnace under argon gas protection. Tungsten nanoparticles with an average diameter of 50 nm (US Research Nanomaterials) were incorporated by a semi-solid mixing method [De Cicco 2009, Xu 2015]. Based on the phase diagram of Zn-Bi immiscible alloy [Malakhov 2000], after melting Zn and Bi at 723 K, the temperature was cooled down to a semi-solid state temperature of 683 K. A mixing blade of grade 5 titanium was placed at one third height of the molten metal with a rotation speed of 700 rpm. W nanoparticles were then fed and incorporated into the semi-solid melt. After feeding, the temperature was raised up to 873 K for 15 minutes ultrasonic processing. For the ultrasonic processing, a C103 alloy probe was inserted about 6 mm deep into the melt. The probe was attached to a booster (Misonix Sonicator 3000). A peak-to-peak vibration amplitude of 60 μm and a frequency of 20 kHz were used [Yang 2004]. Finally, the crucible was taken out from the furnace and cool down in air.

X-ray diffraction (XRD) was used to identify phases in the nanocomposite. A BEDE D1 high resolution diffractometer using Cu Kα (λ=0.1542 nm) radiation was used. For microstructure analysis, after grinding and polishing, these samples were ion milled by a Precision Ion Polishing System (PIPS) for 1.5 h at an accelerating voltage of 4 kV, with a 2° milling angle. The microstructural characterization was performed using a ZEISS Supra 40VP SEM and the elemental composition was determined by electron dispersive spectroscopy (EDS). Bi phase size distribution was evaluated from SEM images using the image analyses software ImageJ. Vickers hardness tests were conducted under a 200 gf load with a dwell time of 10 s in a LM 800AT microhardness tester.

4.3.3 Results and Discussion

One of the prerequisites for the nanoparticle enabled phase control in Zn-Bi immiscible alloys is that W nanoparticles must be chemically stable during processing. Figure 4-15 shows the XRD spectrum of the as-cast Zn-8Bi-2vol%W nanocomposite. Only pure Zn, Bi and W phases are identified without the presence of other phases. The result suggests that W nanoparticles are chemically stable in the Zn-Bi melt.

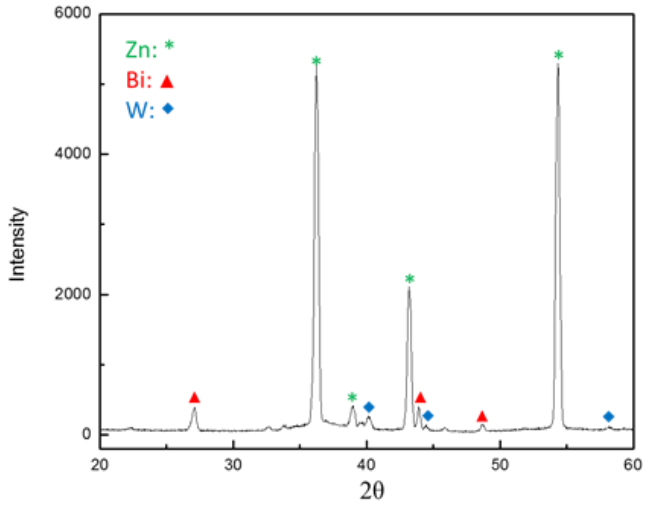

Figure 4-15 X-ray diffraction (XRD) spectrum of the Zn-8Bi-2vol%W nanocomposite.

We used SEM and EDS analyses to study the microstructure. Pure Zn-8Bi alloy samples processed under the same conditions were also studied for comparison. For the pure sample, Figure 4-16a shows two different regions: the Zn rich region at the top and the Bi rich region at the bottom as a result of sedimentation. In contrast, for the nanocomposites sample, Figure 4-16b shows a good distribution of the Bi phase. We can also observe that Bi phase is inconsecutively located around Zn grain boundaries (GBs) and only part of Zn GBs are wetted by Bi phase. A higher magnification SEM image (Figure 4-16c) shows that W particles are located at the interface between Bi and Zn. However, Bi phase is not fully covered by W nanoparticles, only a part of the

Zn-Bi interface have a W nanoparticle coating. We can observe that the size of the Bi phase is significantly constrained. Figure 4-16d displays a histogram of the Bi phase size distribution with the majority of the particle sizes around 2.5 μm.

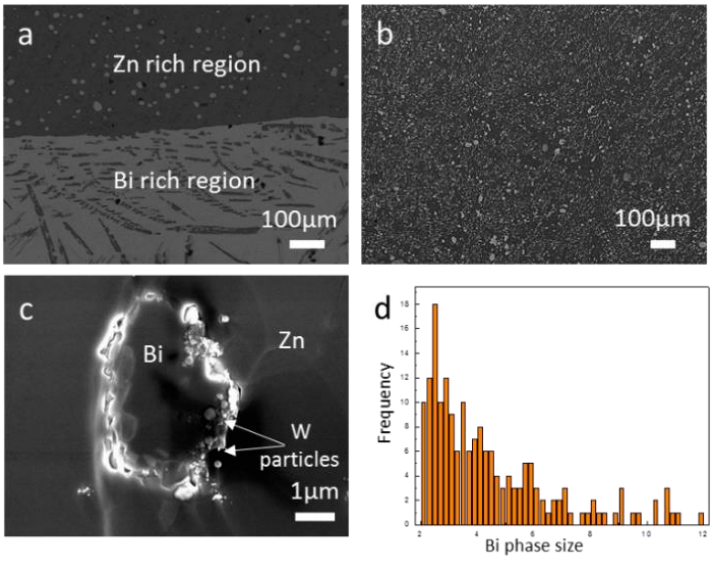

Figure 4-16 SEM images and size distribution of the Bi phase in Zn-Bi alloys: (a) Pure Zn-8Bi; (b-c) Zn-8Bi-2vol%W nanocomposites; (d) Histogram of Bi phase size distribution in Zn-8Bi-2vol%W nanocomposites.

Figure 4-17 shows the EDS analyses of the aforementioned phases present in Figure 4-16c. An EDS line-scan was performed along the arrow highlighted in Figure 4-17a. We can observe an obvious W signal peak at the Zn-Bi phase interface (Figure 4-17b). A more detailed analysis of the Zn-Bi phase interface highlighted by a white rectangle in Figure 4-17a is shown in Figure 4-17c-f. Figure 4-17c shows a higher magnification SEM image of the interface confirming the presence of W nanoparticles. Their corresponding elemental EDS mappings, color coded for clarity, show spatial distributions of Zn, Bi and W.

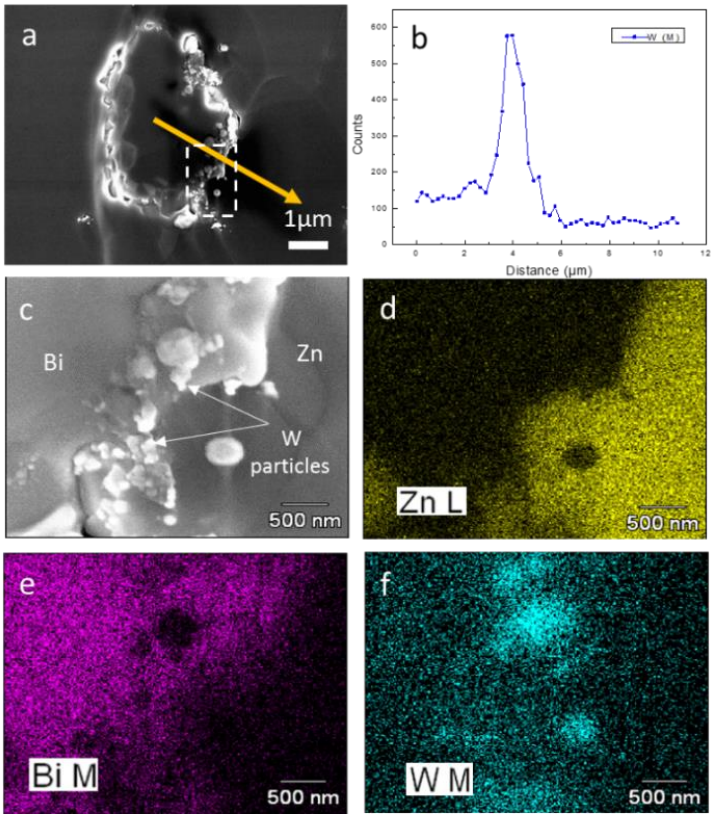

Figure 4-17 SEM-EDS micrographs of Zn-8Bi-2vol%W nanocomposites: (a) SEM image of Zn-8Bi-2vol%W nanocomposites; (b) EDS line-scan of W element at the Zn-Bi interface; (c) Higher magnification SEM image of the Zn-Bi interface highlighted in (a); (d) Zn element rich distribution; (e) Bi element rich distribution; (f) W element rich distribution.

Vickers microhardness tests were performed in order to evaluate the effect of W nanoparticles on the mechanical properties of the Zn-8Bi-2vol%W nanocomposite. These results are compared with those from the pure Zn-8Bi alloy. Figure 4-18 shows the microhardness data for both the Zn-8Bi alloy and Zn-8Bi-2vol%W nanocomposite samples. For the Zn-8Bi sample, the microhardness values from the top and bottom parts are 46.3 and 20.7 Kg mm^{-2}, respectively. These results are expected due to the non-uniform Bi phase segregation as shown earlier in Figure 4-18a. Since Bi is softer than Zn, the microhardness value of the bottom part is much lower than

the top part. However, the microhardness from the top and bottom parts in the Zn-8Bi-2vol%W nanocomposite sample is 48.98 and 46.9 Kg mm^{-2} respectively, indicating a well distributed Bi phase in the whole sample. Since the top part of the Zn-8Bi-2vol%W nanocomposite contains much more soft Bi phase that that of the pure Zn-8Bi alloy, it is clear that the strong W nanoparticles strengthen the nanocomposite samples effectively.

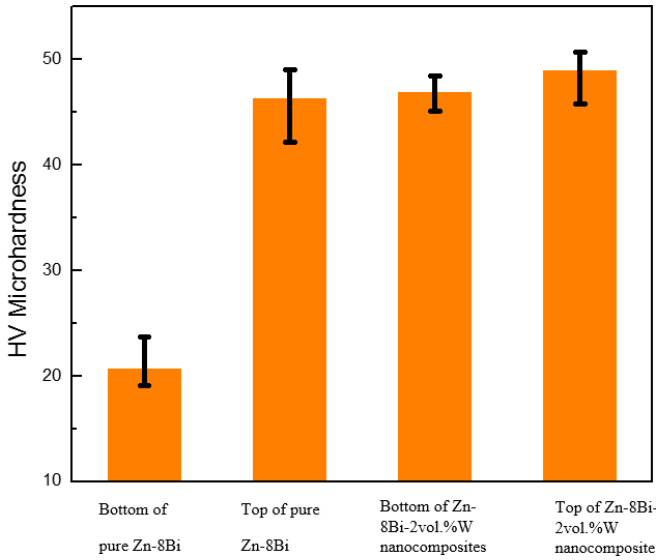

Figure 4-18 Vickers microhardness of the Zn-8Bi alloy and Zn-8Bi-2vol%W nanocomposite.

In this chapter, we have developed a strategy, to uniformly distribute Bi phase and eliminate the Bi sedimentation by adding metallic W nanoparticles in a Zn-Bi immiscible alloy casting. For pure Zn-Bi immiscible alloy, once the primary Bi phase nucleates at liquid state, the growth rate of Bi phase is very fast due to the high diffusion coefficient. Moreover, if multiple primary Bi droplets collide with each other, they will coalesce into one larger droplets driven by the reduction of the interfacial energy. The large Bi droplets start to sediment due to the gravity force.

Our approach utilizes W nanoparticles to suppress the growth and prevent the collisions of the Bi droplets in Zn-Bi melt. After the initial nucleation of a Bi phase in the Zn solution, the dispersed W nanoparticles rapidly self-assemble at the Zn-Bi interface to restrict the phase growth and coalescence. Thus, a refined Bi phase with little sedimentation is achieved. Our experimental study using W nanoparticles for phase control in the Zn-Bi immiscible alloy validated the effectiveness of the method. With only 2 vol% W nanoparticles, the size of the minority Bi phase has significantly been reduced to around 2.5 μm. It is also likely that W nanoparticles worked as heterogeneous nucleation sites for Bi phases to refine microstructure [Chen 2015]. In addition, it would be important to study the wetting behavior at GBs and interfaces. Based on the criteria [Straumal 2008, Straumal 2001 and Straumal 2010] that every GB was considered to be completely wetted only when a layer had covered the whole GB, here Bi phase is incomplete wetting to Zn GBs because Bi phase is inconsecutively distributed around the GBs. It is also of interest to investigate the W nanoparticles' wetting behavior at the Zn-Bi interface because W nanoparticle coating can directly affect the effectiveness of this nanoparticle enabled phase control mechanism. As shown in Figure 4-16c, Bi phase is not fully covered by W nanoparticles, thus it is also incomplete wetting. It is noteworthy that the processing cooling rate is about 1 K/s, there is no annealing or heat treatment during processing. It would be interesting in the future to research the GB wetting behavior transition by annealing at different temperature and time.

4.3.4 Summary

For the first time, W nanoparticles were easily incorporated and dispersed in Zn-8Bi alloy melt by semi-solid mixing and ultrasonic-assisted processing for Zn-8Bi-2vol%W nanocomposites. XRD analysis indicated that W nanoparticles were chemically stable in the Zn-8Bi melt. SEM and EDS analyses demonstrated that W nanoparticles self-assembled at the Zn-Bi interface driven by

the reduction of system surface energy. W nanoparticles significantly refined the size of the Bi phase and prevented the Bi sedimentation during Zn-Bi immiscible alloy casting. Microhardness test showed that W nanoparticles significantly enhanced the mechanical properties of Zn-Bi. The unprecedented use of chemically-stable metal nanoparticles for phase control in immiscible alloys simplifies the processing since metal nanoparticles offer excellent wettability with immiscible alloys to allow effective nanoparticle feeding/incorporation and dispersion. This new approach has a great potential for scale-up manufacturing of immiscible alloys with a uniform distribution of secondary phases for widespread applications.

4.4 Phase Control in Organic Immiscible CTB-SCN by B_4C Nanoparticles

4.4.1 Introduction

SCN (Succinonitrile) is a transparent organic material having similar solidification behaviors to metallic alloys and thus is widely used for in-situ optical observation of nucleation and microstructure development to provide insights for the solidification behavior of metallic alloys [Rai 1998]. CTB (carbontetrabromide) is also transparent to visible light for optical observations. CTB–SCN system, whose phase diagram is shown in Figure 4-19, has been used as a very good organic analog of immiscible alloy systems. The low temperature, transparent SCN-CTB system will allow us to readily set up high-speed optical systems (such as laser scattering and high speed camera) to study the fundamental issues related to diffusional control and phase stabilization by nanoparticles. We would like to in-situ observe the whole phase evolution during immiscible CTB-SCN solidification. Based on the in-situ experiment, the nanoparticles enabled minority phase stabilization and minority droplet capture during solidification will be examined.

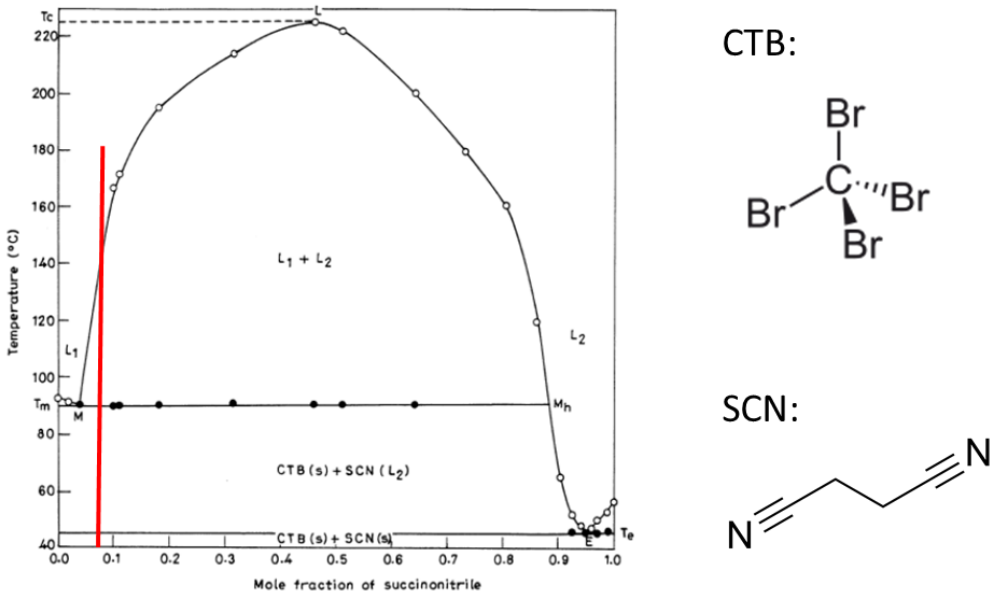

Figure 4-19 Phase diagram and molecule structure of CTB-SCN.

4.4.2 Materials and Methods

Processing CTB-SCN sample. The experimental set-up for CTB-SCN processing is shown in Figure 4-20a. CTB-7.5mol% SCN were melt at 145 °C (two liquid phase) inside a glass beaker in a silicon oil bath on a hot plate under argon protection. During heating and processing, a glass slide or aluminum foil are applied to cover the opening of the beaker to reduce oxidation and sample evaporation. A K-type Thermocouple is inserted into the silicon oil for temperature control. After CTB-7.5mol% SCN is fully melt, 2 vol% B_4C nanoparticles are poured into the melt and manually mixed. Then the temperature is raised to 195 °C and ultrasonic processing is used for 5mins to disperse nanoparticles in single liquid phase region. The parameter of ultrasonic processing is 20 kHz with a 20μm peak-to-peak amplitude. Temperature keeps increasing to 215°C because the ultrasonic processing will deliver energy to the liquid sample. Once the processing stops, a rectangle shaped capillary glass tube (with different thicknesses of 300μm, 400μm and 500μm) is inserted into the melt and suck sample into the tube by capillary force for further in-situ

experiment. After solidification in the glass tube, the tube is sealed by a fiberglass stove gasket cement withstands 2000 °F. A pipette is also used to suck some liquid samples and drop them on one glass slide for characterization. Other bulk CTB-7.5mol% SCN -2vol% B_4C nanocomposites is taken out from the silicon oil bath and cool down in air to room temperature. Optical microscope and variable pressure SEM are used to observe the microstructure and in-situ process. Pure CTB-7.5mol% SCN and pure SCN without nanoparticles are also prepared with the same processing parameter for comparison. To observe the phase evolution during heating and solidification in real time, the rectangle glass tube with solidified sample inside is put on a strip heater with a temperature control system. An optical microscope is used to record the microstructure evolution during experiment.

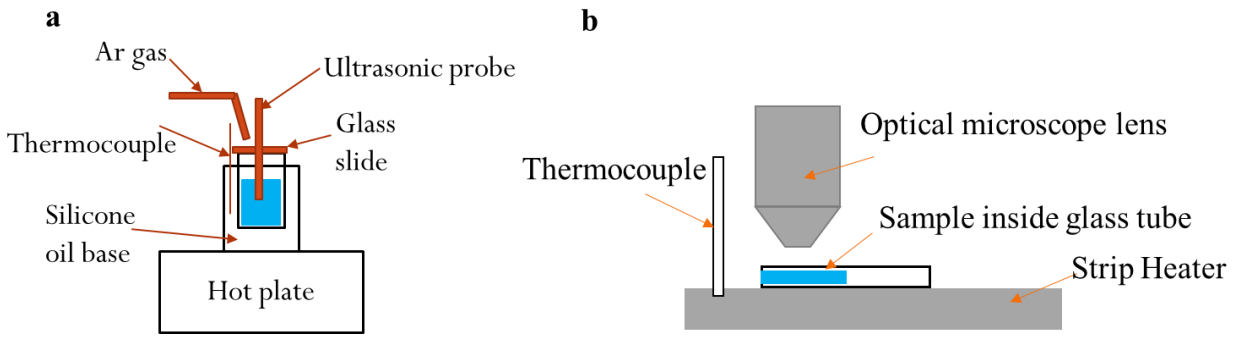

Figure 4-20 Experimental set-up for (a) CTB-SCN processing, (b) in-situ observation during heating and solidification.

4.4.3 Results and Discussion

Distribution of SCN minority phase. Figure 4-21 shows optical microscopy images of the pure CTB-7.5mol% SCN and CTB-7.5mol% SCN-2vol% B_4C nanocomposites after processing. It clearly shows that SCN droplets in pure CTB-SCN grow much larger than those in CTB-SCN-B_4C nanocomposites. Software Image-J is used for analyzing the sizes of SCN droplets.

The average diameter of the SCN in pure sample is around 104 μm, while it is only around 7.7 μm for nanocomposites sample. The diameter decrease more than one order of magnitude, which demonstrates that the nanoparticles enabled phase control is very effective in CTB-SCN system. In addition, the distribution of droplet size for pure CTB-SCN is much more scattered than nanocomposites sample. It is believed that these large droplets in pure sample are formed due to coalescence while nanoparticle coating could against coalescence to obtain more homogeneous size distribution.

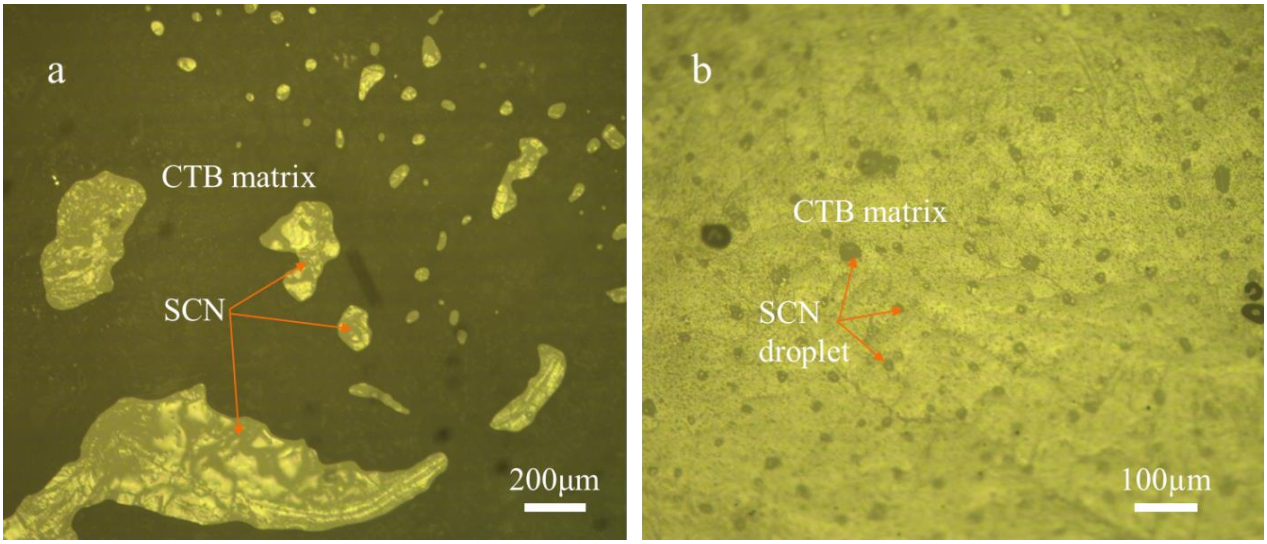

Figure 4-21 Microstructure of (a) pure CTB-7.5mol.% SCN, (b) CTB-7.5mol.% SCN -2vol% B_4C nanocomposites in the rectangle tube.

To further understand the self-assembly of nanoparticles, we also cut a small piece from CTB-7.5mol% SCN-2vol% B_4C nanocomposites and observe by Variable Pressure SEM (VPSEM) with a pressure of 20 Pa. Nevertheless, CTB evaporates very fast under this pressure (vapor pressure of CTB at 96.3 °C is 5.33 kPa, SCN at 100°C is 0.3 kPa). Once the sample is placed into SEM vacuum chamber and start pumping, almost all the CTB will evaporate away immediately

and leave nanoparticle scaffold with SCN droplets on the top. Figure 4-22 is the VPSEM image of a SCN droplet on the nanoparticle scaffold. It is observed that B_4C nanoparticles self-assemble on the surface of SCN droplets to form a thin layer. This thin layer coating could block diffusional growth during solidification and refine the size of SCN minority phase. In addition, this thin nanoparticle coating also severely reduce the evaporation rate of SCN during VPSEM observation in the vacuum chamber. In contrast, the pure CTB-SCN sample cannot survive in the VPSEM chamber, all the sample evaporate away after pumping starts,.

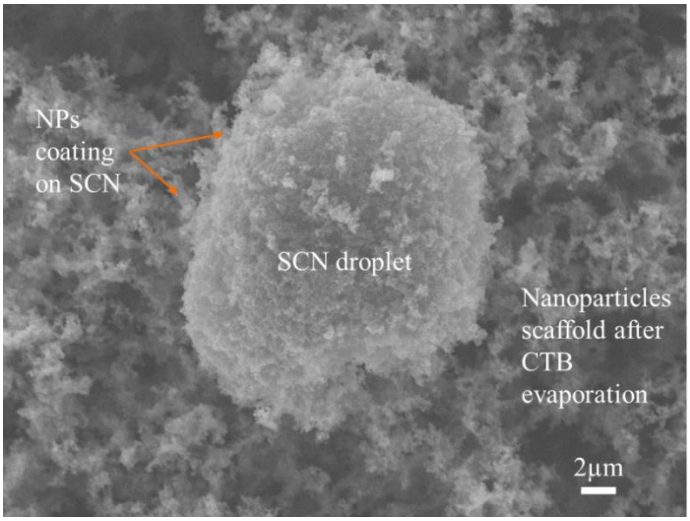

Figure 4-22 Variable pressure SEM image of one SCN droplet coated with nanoparticles on nanoparticles scaffold after CTB evaporated away. The sample is from CTB-7.5mol% SCN - 2vol% B_4C nanocomposites.

(2) Theoretical calculation

To understand the insights of nanoparticles enabled phase control in CTB-7.5mol% SCN - 2vol% B_4C nanocomposites, theoretical calculation was implemented. The size of the minority phase $d_{(SCN)}$ is calculated $\mathrm{d(SCN)} \approx \sqrt{2DSt_{np} + 2(1-f)DSt}$. Figure 4-23 shows the size

dependence of SCN droplet on cooling rate. The black line and red line shows the theoretical trend of pure CTB-7.5mol%SCN and CTB-7.5mol%SCN-2vol%B_4C nanocomposites (with blocking efficiency f=0.99789) respectively. The red marks in the figure are the real experimental data. When the blocking efficiency f is zero which means there is no nanoparticle coating at the interface (black line in the figure), the size of SCN droplets is much larger. It is found that under 1 K/s cooling rate, the experiment data fit the theoretical value quite well. The SCN droplet size is severely refined by the nanoparticle coating. And by experimental data, the blocking efficiency is identified around 0.99789 which verify that the nanoparticle coating is very effective in terms of the diffusional phase control.

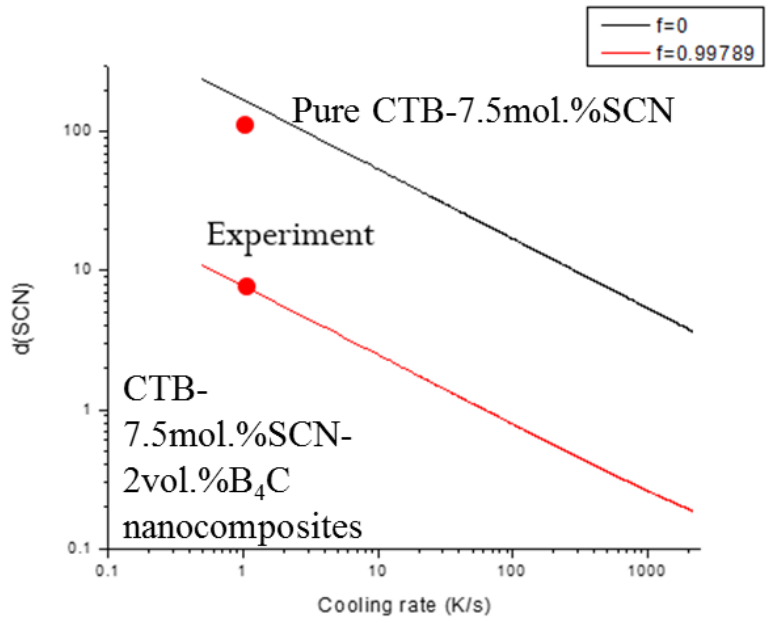

Figure 4-23 Diameter of SCN droplets as a function of cooling rate for pure CTB-7.5mol.%SCN and CTB-7.5mol.%SCN-2vol% B_4C nanocomposites.

For the in situ observation, we used pure SCN to test the in-situ experiment set-up. As shown in Fig. 4-20b, the rectangle capillary glass tube with pure SCN inside is put on the strip

heater. An optical microscope system records the phase evolution during melting and solidification. Under room temperature, SCN is solid and it melts at 57 °C. First, we raise the temperature to 60 °C and all SCN is in liquid state. Then the glass tube cools down with a cooling rate around 3 °C/min. Figure 4-24 (a-d) shows the dendrite growth during cooling. The time interval between each image is 0.4 s. It suggests that this experiment set-up works well for the in-situ observation with the highest temperature of 60 °C.

To get the phase evolution of immiscible CTB-SCN materials, a single liquid zone where the temperature is about 160 °C is required. However, under this temperature, CTB and SCN evaporate very fast and the sealed glass tube easily get leakage. For the next step, we will improve the experiment set-up and run the in-situ observation of pure CTB-7.5mol%SCN and CTB-7.5mol%SCN-2vol%B_4C nanocomposites samples to gain insights of nanoparticles enabled minority phase stabilization and minority droplet capture during solidification.

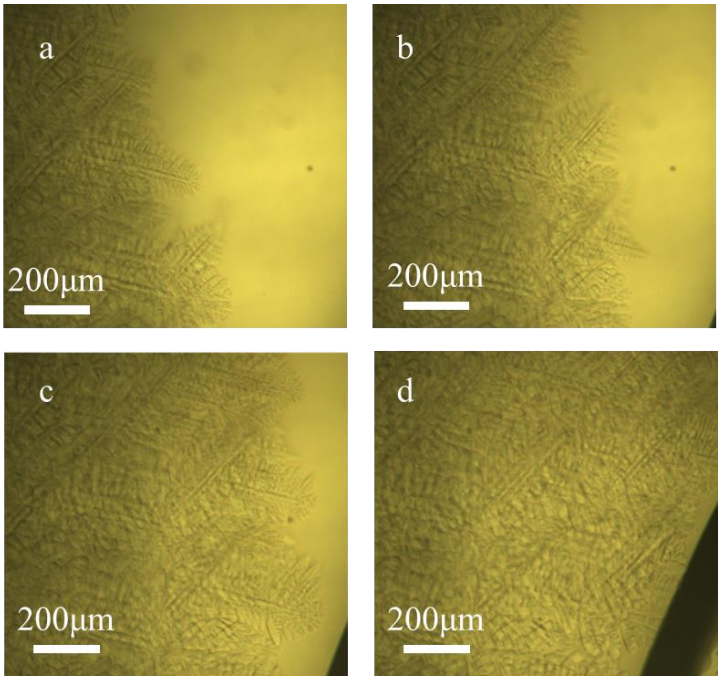

Figure 4-24 Dendrite growth of pure SCN under cooling rate of 3 °C/min.

4.4.4 Summary

For organic material systems, the polarity of the molecules is crucial for nanoparticle selection. SCN has high polarity while CTB is non-polar. So nanoparticle with intermediate polarity would be good. Carbide nanoparticles normally offer intermediate polarity, and therefore B_4C is selected for the CTB-SCN material system. The density of B_4C is also lower than other carbides so that B_4C nanoparticles could move faster to coat the minority SCN droplets. The experimental results validate the effectiveness of the nanoparticle selection.

There remaining difficulties for in-situ experiment of CTB-SCN immiscible material due to the high temperature needed to reach single liquid zone for the material. They evaporate fast and make sample unstable. Moreover, the experiment set-up need to be improved.

Chapter 5 Solid-Liquid Phase Control by Nanoparticles: Grain Refinement

In this chapter, the nanoparticles enabled solid-liquid phase control was studied by conducting experimental and theoretical studies of grain refinement of metals during solidification. Cooling, nucleation, and phase growth are ubiquitous processes of paramount significance in almost every aspect of life and landscape in nature, such as cloud formation [Kirkby 2011], ice nucleation [Kiselev 2017], and volcanic rock evolution [Coombs 2003]. It is universally established that effective control of nucleation and phase growth will yield refined microstructures with enhanced performance for materials, and hence vital to numerous broad fields, including materials science, climate and atmospheric sciences, biomedicine [Nielsen 2014] and chemistry [Frens 1973]. Widely used technologies that involve cooling, such as casting, are of significance for the mass production of complex materials and components. Recent studies reveal that ultrafine grained (UFG)/nanocrystalline metals exhibit extraordinary properties [Valiew 2004, Zhao 2006 and Lu 2004]. However, it has been considered impossible to fabricate bulk ultrafine grained/nanocrystalline metals by casting, a technology that has been used for over 6000 years, partly due to its slow cooling (e.g., less than 100 K/s). Conventional microstructure refinement methods, such as fast cooling (thousands to millions K/s) and inoculation, have reached certain fundamental or technical limits [Greer 2016, Stjohn 2005, Easton 2005 and Chen 2015]. Fast cooling substantially restricts the size and complexity of the as-solidified materials. The minimum grain size achievable by inoculation in casting falls in the range of tens of micrometers. Here we report a new discovery that nanoparticles can refine metal grains down to ultrafine or even nanoscale by instilling a continuous nucleation and growth control mechanism during slow solidification. When casting pure Cu with tungsten carbide (WC) nanoparticles, the grain sizes of Cu are refined substantially down to ultrafine and even nano scale. The as-solidified bulk

ultrafine/nanocrystalline Cu reveals an unprecedented thermal stability up to 1023 K (0.75 melting point of Cu) and high mechanical properties. Furthermore, this newly revealed grain control mechanism is successfully applied in other materials systems such as Al-TiB_2 and Zn-WC for ultrafine grains via slow cooling. This revolutionary method paves a pathway for the mass production of bulk stable UFG/nanocrystalline materials that may be readily extended to any other processes that involve cooling, nucleation and phase growth for widespread applications.

5.1 Introduction

Grain refinement in metals during solidification is of great interest due to the enhanced mechanical properties, more homogeneous microstructure and improved processability of refined microstructures. Over the past few decades, different approaches such as inoculation [Greer 2000, Murty 2002 and Birol 2006], growth restriction by adding alloy elements [Stjohn 2015, Tamirisakandala 2005] and fast cooling (up to 10^7 K/s) [Yu 2010, Wu 2008] have been widely investigated through both theoretical and experimental pathways in an effort to attain optimal grain refinement effects. However, these approaches have failed to demonstrate whether it is possible to cast UFG/nanocrystalline metals via conventional casting process, which would represent a revolutionary approach given the pervasiveness of casting in manufacturing. A consequence of our inability to implement solidification processes to fabricate UFG/nanocrystalline metals, various methods have emerged for the fabrication of UFG/nanocrystalline metals, including: mechanical alloying [Suryanarayana 2001, Morris 1991], severe plastic deformation [Valiev 2004, Zhao 2006 and Valiev 2006] and thin film deposition [Gianola 2006, Wu 2017], and although some degree of success has been achieved using these processes they remain limited to the solid state and present challenging issues for economical mass production of bulk samples with complex geometries. Recent work has shown that the

solidification behavior of metals can be controlled by the addition of nanoparticles [Chen 2015, Chen 2014, Cao 2016, Cao 2018 and Guo 2018]. These studies about nanoparticle controlled solidification have paved a new pathway for casting metals with refined microstructures. In the present study we demonstrate, for the first time, bulk UFG/nanocrystalline metals can be cast directly via slow cooling by dispersed nanoparticles in a molten metal.

5.2 Materials and Method

5.2.1 Bulk Cu-WC Nanocomposite Ingots Fabrication

To fabricate bulk Cu-WC nanocomposite ingots, WC nanoparticles were mixed with Borax ($Na_2B_4O_7$)-5wt%CaF_2 salt powders by a mechanical shaker (SK-O330-Pro) for 1.0 h. The volume fraction of nanoparticles in the salt mixture is designed as 10%. As shown in Figure 5-1, the pure oxygen free Cu (99.99%, Rotometals, Inc) ingots were melted at 1250 °C in a graphite crucible by induction heater. Inert Ar gas was purged on the molten Cu to avoid severe oxidation. The mixed $Na_2B_4O_7$-5wt%CaF_2-WC nanoparticles were manually loaded on the surface of the molten Cu. A graphite propeller was located below the Cu-salt interface and stirred at a speed of 400 rpm for 20 min to incorporate WC nanoparticles into Cu melt. Then the melt was allowed to cool down to 900 °C to allow Cu solidify first while salt mixture was still in liquid state. Liquid salt was poured out from the crucible and leave a Cu-WC ingot. The volume fraction of WC nanoparticles in Cu was designed to be 0, 5, 10, and 20 vol%.

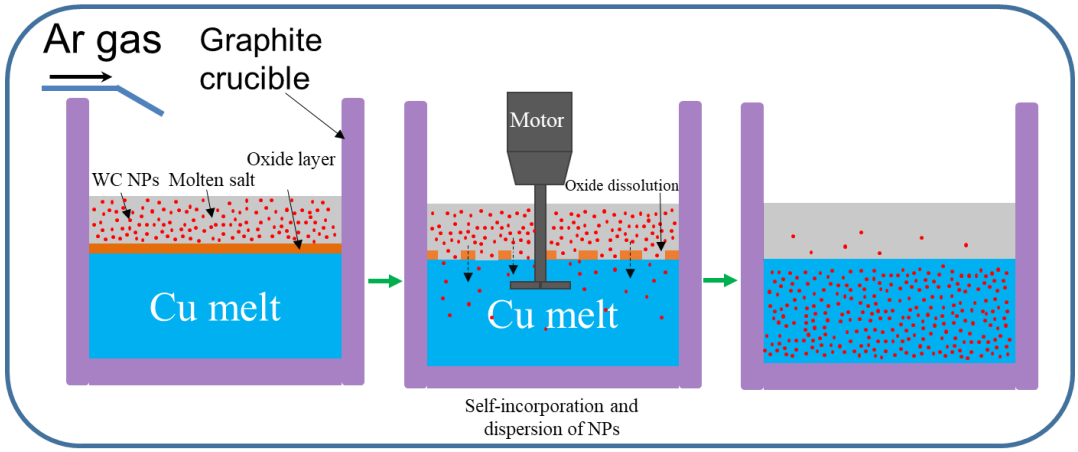

Figure 5-1 Schematic illustration of the salt-assisted self-incorporation for Cu-WC before casting bulk ingots.

5.2.2 Bulk Al-TiB_2 Nanocomposites Ingots Fabrication

Surface clean TiB_2 nanoparticles were synthesized by the magnesiothermic reduction of TiO_2 nanoparticles and B_2O_3 powders in molten salt [Javadi 2018]. The synthesized TiB_2 nanoparticles and $KAlF_4$ flux were then mechanically mixed at solid state for 3.0 h. Mixed powders were dehydrated at 120 ºC for 1.0 h in a vacuum oven. An electrical resistance furnace was used to melt the Al ingots at 820 ºC under argon (Ar) gas protection. Then, the mixed powders were added to the melt surface and melt was mechanically stirred at 200 rpm for 10 min with titanium (Ti) mixing blade. The designed volume fraction of TiB_2 in Al is 10vol%. The melt was taken out from the furnace and naturally cooled down to room temperature under Ar gas protection.

5.2.3 Fabrication of Cu-WC/Zn-WC Ingots by Powder Melting

Cu powders (Sigma Aldrich, < 10 μm) and Zn powders (Alea Aesa, 150 μm) were first mixed with a designed volume fraction of WC nanoparticles (US Research Nanomaterials, 150-200 nm) for 1.0 hour by a mechanical shaker (SK-O330-Pro). The mixed powders were then compressed into disks with 2.0 cm in diameter under 250 MPa by a hydraulic machine. Cu-WC

cold compacted disks were compression-melted at 1250 ℃ by an induction heater while under a pressure of 7-10 MPa under a graphite disk and alumina piston. After solidification in air, Cu ingots with WC nanoparticles were obtained. Zn-WC cold compacted billets were then melted at 500 °C and ultrasonic processed by a Niobium (Nb) probe for 10 min to disperse WC nanoparticles in Zn melt. Then the melt was taken out from the furnace and cool down under Ar gas protection.

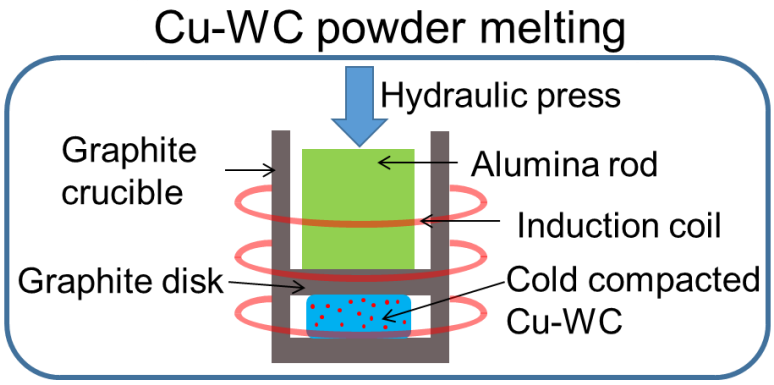

Figure 5-2 Schematic illustration of the powder melting method to cast Cu/Zn containing WC nanoparticles.

5.2.4 Casting with Different Cooling Rates

For our casting study, these ingots were re-melted again at 1250 ℃ under a protection of Argon gas in the induction furnace and then cooled down in furnace, air and water for different cooling rates. The cooling rate was measured by a K-type thermocouple connected to an Arduino UNO board for recording the cooling curve.

5.2.5 Structure Characterization

The microstructure, distribution and dispersion of nanoparticles in metals were studied by means of scanning electron microscope (SEM), focus ion beam (FIB) imaging, electron backscatter diffraction (EBSD) and transmission electron microscope (TEM). To clean the surface

and reveal the nanoparticles in metal matrix, the mechanically grinded and polished as-cast samples were further polished by low-angle ion milling (Model PIPS 691, Gatan). SEM images were acquired at 0° and a tilted 52° by ZEISS Supra 40VP and FEI Nova 600, respectively. The composition of the material was characterized by energy-dispersive X-ray spectroscopy (EDS). The volume fraction of nanoparticles was estimated based on the atomic fraction of the major element in the base metal and nanoparticles. Taking advantages of the channeling contrast of different grains induced from the ion beam, FIB imaging was used to reveal the grain structure. Grain size and orientation were studied by EBSD (FEI Quanta 3D) at 30 kV with a current of 12 nA and FIB with a CDEM detector. The interfaces between matrix and nanoparticles were studied by a FEI Titan TEM at 300 kV. The thin film TEM samples were machined by FIB.

5.2.6 Solidification Behavior Study

To study the solidification behaviors during cooling, Cu-WC and pure Cu samples with the same mass (50 mg) were analyzed by Differential Scanning Calorimetry (DSC) (TA Instruments, Q600). Samples were heated up to 1250 °C with a heating rate of 40 °C/min and then cool down with a cooling rate of 5 °C/min.

5.2.7 Solid-solid Phase Control by Nanoparticles: High Temperature Stability

The thermal stability of UFG metals with nanoparticles was studied as the showcase of nanoparticles enabled solid-solid phase control. To study the UFG/nanocrystalline structures stability at high temperatures, in situ heating Scanning Transmission Electron Microscope (STEM) was conducted at 300 kV with a convergence angle of 4.3 mrad and geometric aberrations in the probe corrected to third order. The small convergence angle was chosen to enhance diffraction contrast for grain identification. An FIB milled TEM sample was quickly heated to 200 °C, 400 °C, 600 °C, 700 °C and 850 °C by a Gatan in-situ heating holder and held for 10 min at each step for

imaging. The diffraction camera length was increased at higher temperatures in order to enhance diffraction contrast, emphasizing the difference between individual Cu grains for robust identification. The collection semiangle was 48-240 mrad at room temperature, 15-75 mrad at 400 °C, and 12-60 mrad at 600 °C and above. Moreover, the bulk solidified Cu-34vol%WC (air cooling, 7K/s) samples were heated up to 750 °C (1023K, 0.75 of T_m) and stayed at that temperature for 2.0 hours under the protection of Argon gas. The grain structure was then studied by FIB imaging and EBSD. Mechanical properties were studied by microcompression test.

5.2.8 Mechanical Properties Characterization

An MTS Nanoindenter with a flat punch tip was used for microcompression tests at a strain rate of 5×10^{-2} s^{-1} under room temperature. Micropillars of approximately 4 μm in diameter and 9 μm in length were machined by FIB. To evaluate the elastic modulus, microindentation tests with an indent depth of 2 μm were performed by the same MTS nanoindenter with a Berkovich tip. For each sample, at least ten points were measured. Accordingly micropillars with a diameter and a length of 4 μm and 9 μm, respectively, were machined by FIB from the as solidified (air cooling, cooling rate of 7 K/s) and heat treated samples (750 °C for 2.0 h). Note that the average grain size for the as solidified and heat treated Cu-34vol%WC samples are 168 nm and 207 nm, respectively.

5.3 Results and Discussion

We prepared bulk Cu ingots with WC nanoparticles by two different methods. The first method is a salt-assisted self-incorporation of nanoparticles into molten metal. As shown in Figure 5-1, molten salt (Borax + 5% CaF_2) could dissolve the oxide layer at the top of molten metal and provide a clean interface between Cu melt and nanoparticles. In addition, the wetting angle between Cu and WC at 1250 °C is below 10°, which indicates a good wettability between Cu and

WC so that WC nanoparticles prefer to transport from the molten salt to the Cu melt to reduce the system energy [Liu 2016]. Combined with mechanical mixing, WC nanoparticles can be readily incorporated into molten Cu. This salt-assisted incorporation method opens up a scalable manufacturing method to fabricate metals containing different percentage of nanoparticles. In this study, bulk Cu ingots with 5%, 10% and 20% volume fraction of WC nanoparticles were cast. Figure 5-3 shows one typical bulk Cu-WC ingot cast after the salt-assisted incorporation method. Another method is a powder melting process especially suitable for high volume percent of nanoparticles as shown in Figure 5-2. The cold compacted Cu-WC powder preforms were melted by an induction heater under a pressure of 7-10 MPa. Cu ingots with 19% and 34% volume fraction of WC nanoparticles were fabricated by this powder melting method.

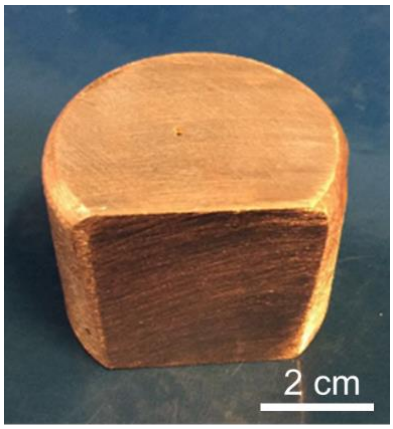

Figure 5-3 As cast Cu-5vol%WC ingot with a diameter of 5 cm.

To study the effects of the cooling rate under a same initial condition, all these Cu-WC samples were then melted again and cast under different cooling rates, i.e., furnace cooling (2-4 K/s), air cooling under the protection of argon gas (7-12 K/s) and water quenching (70-100 K/s). The typical cooling curves are shown in Figure 5-4, the thermal arrest caused by the solidification

of Cu is clearly identified in the furnace and air cooling curve, while not so obvious in the water quenching curve due to the rapid heat dissipation.

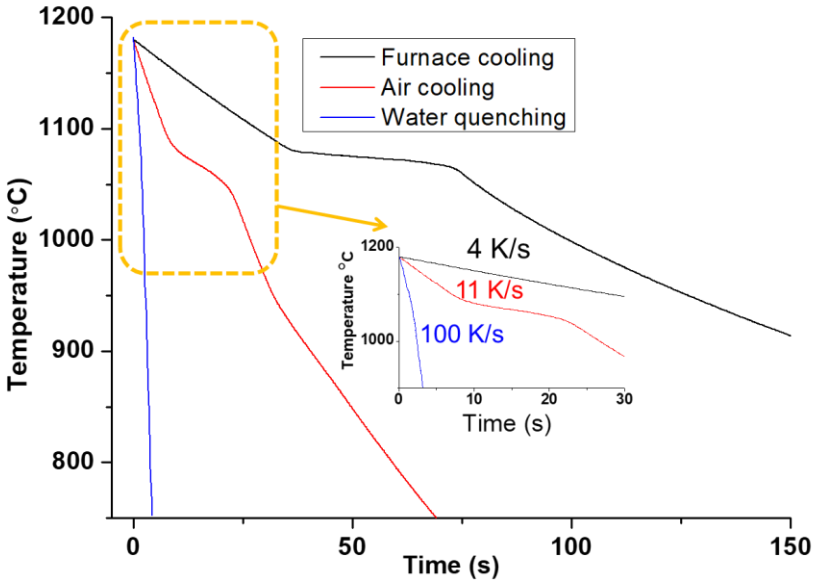

Figure 5-4 Cooling curves for furnace cooling, air cooling and water quenching of Cu-WC samples.

5.3.1 Nanoparticles Distribution and Dispersion

We then characterized the distribution and dispersion of WC nanoparticles and grain structures in cast bulk Cu samples via scanning electron microscope (SEM), transmission electron microscope (TEM), focused ion beam (FIB) imaging, scanning transmission electron microscope (STEM) and electron backscatter diffraction (EBSD). SEM samples were sectioned along the cross-section of the sample. To clearly reveal the nanoparticles, the mechanically ground and polished samples were further polished by low-angle ion milling at 4° for 1.5 hours. Figure 5-5a shows the typical SEM microstructure of Cu-5vol%WC by furnace cooling. The relatively bright

phases are the WC nanoparticles while the dark phase is the Cu matrix. WC nanoparticles are reasonably well distributed and dispersed in the sample. Figure 5-6 shows a histogram indicating the WC nanoparticle size distribution with an average diameter of 200 nm.

We analyzed the nanoparticle dispersion and self-stabilization mechanisms. Prior studies reported silicon carbide nanoparticles could be dispersed in magnesium matrix by a self-dispersion and self-stabilization mechanism [Chen 2015', Xu 2015']. There are three major factors contributing in this theory: (1) Good wetting between molten metal and nanoparticles creates an energy barrier to prevent atomic contact and sintering of nanoparticles in the melt. In our Cu-WC system, the energy barrier can be calculated by the following equation:

$$W_{barrier} = S\sigma_{Cu}cos\theta \qquad 5\text{-}1$$

where S is the effective area and can be calculated by $S=\pi RD_0$ (D_0=0.2 nm), σ_{Cu} is the surface energy of Cu at the processing temperature (about 1.27 J m^{-2}) [Keene 1993], and θ is the wetting angle, e.g. at 1250 °C (10°) [Eustathopoulos 1999]. In the Cu-WC system, an energy barrier of 7×10^4 zJ is obtained; (2) Thermal energy that enable nanoparticles to move randomly in the molten melt by overcoming the attractive van der Waals potential between nanoparticles. A higher thermal energy is preferred. The processing temperature for Cu-WC is 1250 °C, which provide a thermal energy of $E=k_bT$=21.0 zJ. (3) A van der Waals potential between nanoparticles to lessen the attraction of nanoparticles from each other to form nanoparticles clusters in molten metals. A small attractive van der Waals potential is preferred. It can be calculated by the following equation [Israelachvili 2011]:

$$W_{vdw} = -\frac{(\sqrt{A_{Cu}}-\sqrt{A_{WC}})^2}{6D}\frac{R}{2} \qquad 5\text{-}2$$

where A_{Cu} = 410 zJ and A_{WC} are the Hamaker constants, D is the distance between two nanoparticles that can be as small as two atomic layer thick (0.4 nm), R is the radius of the nanoparticle (100 nm). Although the data of A_{wc} is not available, a 7×10^4 zJ energy barrier is several orders of magnitude higher than thermal energy. Since WC is conductive ceramic materials, A_{wc} could range from 200 to 500 zJ [Israelachvili 2011], suggesting that $W_{barrier}$ would always be much higher than W_{vdw} for stabilization of dispersed WC nanoparticles in Cu melt.

5.3.2 Grain Structures

The SEM image of Figure 5-5b clearly reveals the UFG microstructures (some Cu grains marked by white dash lines) in the Cu-5vol%WC (4 K/s) sample. Grains in this SEM image are smaller than 1 μm. It should be noted that some areas without nanoparticles from a top view under SEM may have nanoparticles beneath the surface as shown in the SEM image of the cross-section cut by FIB (Figure 5-5c). Cu grains are pinned by nanoparticles beneath the surface. Pt coating is used to protect the Cu surface during the FIB cutting.

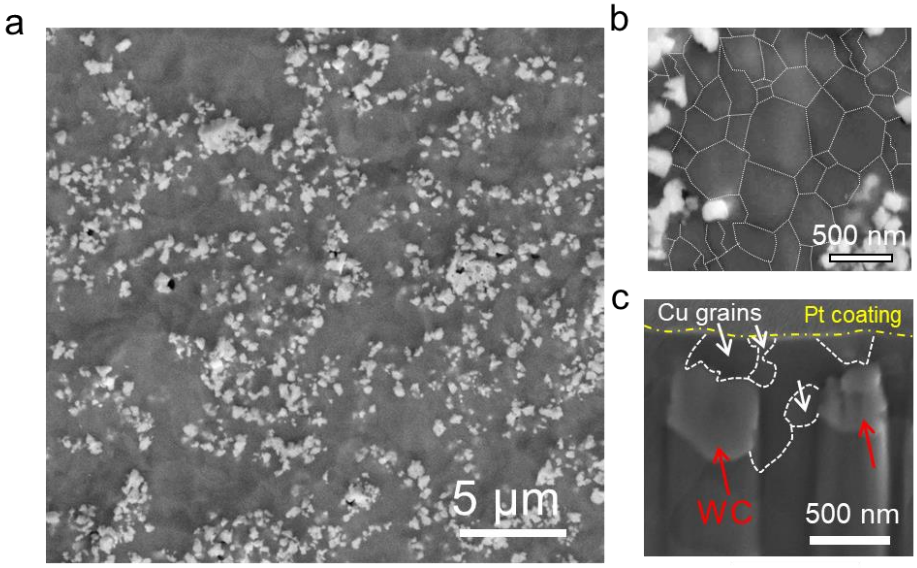

Figure 5-5 (a) SEM image of Cu-5vol%WC (by a cooling rate of 4 K/s) showing well distributed and dispersed WC nanoparticles in the Cu matrix. (b) Magnified SEM image of Cu-5vol%WC (4 K/s) showing the ultrafine and nano scale Cu grains. (c) SEM image of the cross section showing ultrafine-grained Cu matrix and WC nanoparticles present beneath surface of the sample.

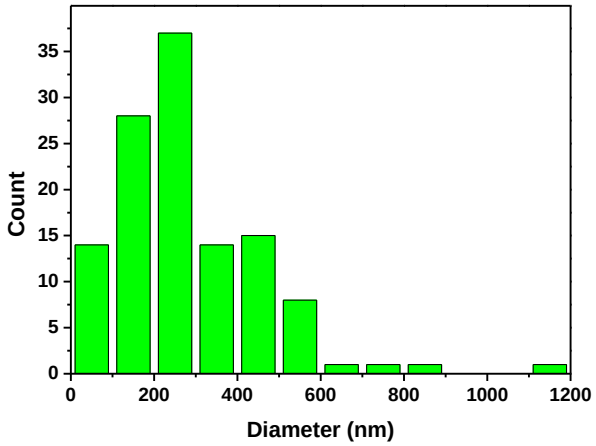

Figure 5-6 Size distribution of WC nanoparticles in as-solidified Cu-WC sample.

The channeling contrast of different grains induced by ion beam makes FIB a powerful tool to characterize grain structures. Figure 5-7 shows the typical ion beam micrographs of pure Cu, Cu-5vol%WC, Cu-10vol%WC and Cu-20vol%WC cast under the same casting condition (2-4 K/s), respectively. The dark phase corresponds to WC nanoparticles whereas the white or grayish phases indicate the Cu grains. With the addition of WC nanoparticles into Cu, the grain sizes are readily refined to ultrafine and even nano scale. From the FIB micrographs, we can observe that a higher percentage of nanoparticles yield more dense nanoparticles distribution and thus more refined grain microstructures. For comparison, the as-solidified pure Cu sample, however, has an average grain size of 270 ± 132 μm under the same cooling rate.

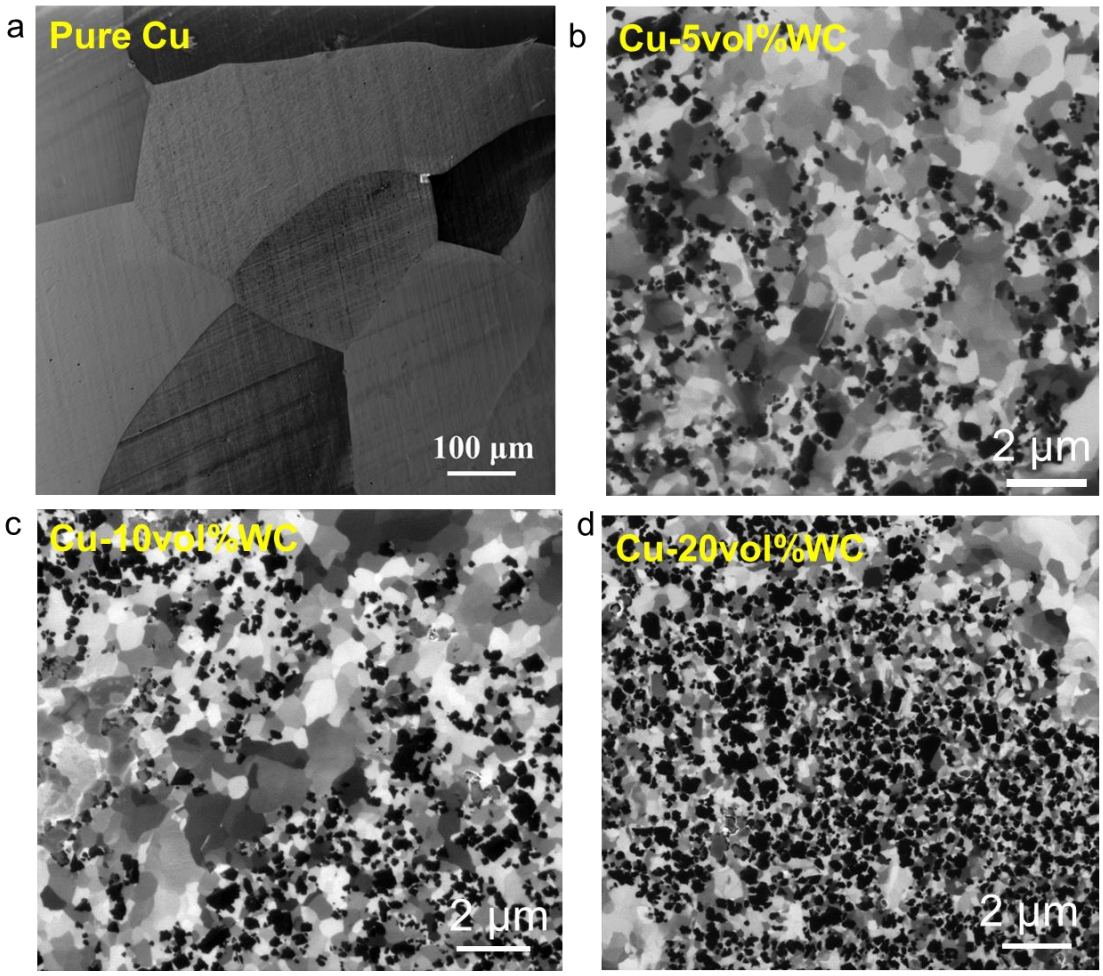

Figure 5-7 Microstructure of Cu containing different volume fraction of WC nanoparticles. a-d, FIB image of pure Cu, Cu-5vol%WC, Cu-10vol%WC and Cu-20vol%WC, respectively.

EBSD analysis was used to further investigate the grain sizes. Figure 5-8 shows the typical EBSD micrograph of Cu-5vol%WC cast by a cooling rate of 4 K/s. The black phases are corresponding to the WC nanoparticles. Due to the fact that the surfaces of nanocomposites samples were not perfectly flat (nanoparticles stick out from the matrix) after ion milling, some regions (marked as greyish region) were not able to be identified during the EBSD scanning. The colors of different grains correspond to different sizes, as shown in the legend. Red grains are

smaller than 100 nm, yellow and orange grains are smaller than 1.0 μm, while green and deep blue grains are smaller than 2.0 μm. The majority of the Cu grains are smaller than 1.0 μm and significant number of nanosized Cu grains (marked with red color in the EBSD micrograph) can be observed in the nanoparticle-rich areas.

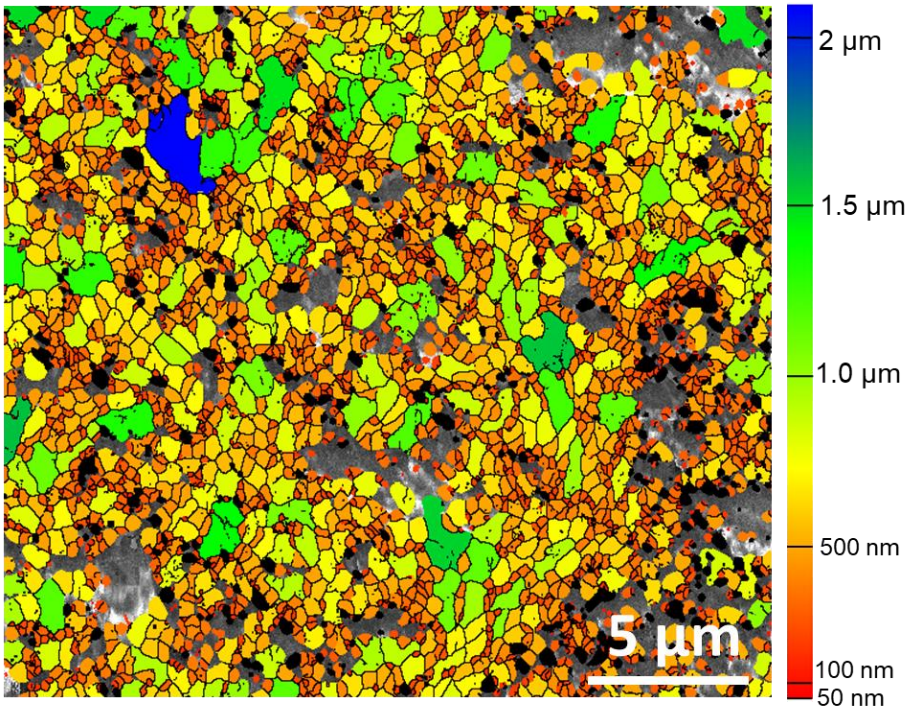

Figure 5-8 EBSD image of Cu-5vol%WC (4 K/s) with grain size color code. Black phases are WC nanoparticles, red grains are smaller than 100 nm, yellow and orange grains are smaller than 1.0 μm.

The average grain sizes of different microscopic areas under different cooling rates are summarized in Figure 5-9. The average grain size of Cu-WC samples with different fraction of WC nanoparticles ranges from 236-434 nm, 227-384 nm and 193-347 nm for furnace cooling, air cooling and water quenching, respectively. The error bars indicate the standard deviation of the grain size measurements. It is shown that a higher percentage of nanoparticles yields more refined

grains. Figure 5-9 also indicates that the grain size slightly decreases with an increased cooling rate although the differences from the cooling rates are not significant. The EBSD scanning suggests that the addition of WC nanoparticles can refine Cu grains to ultrafine/nano scale by regular casting.

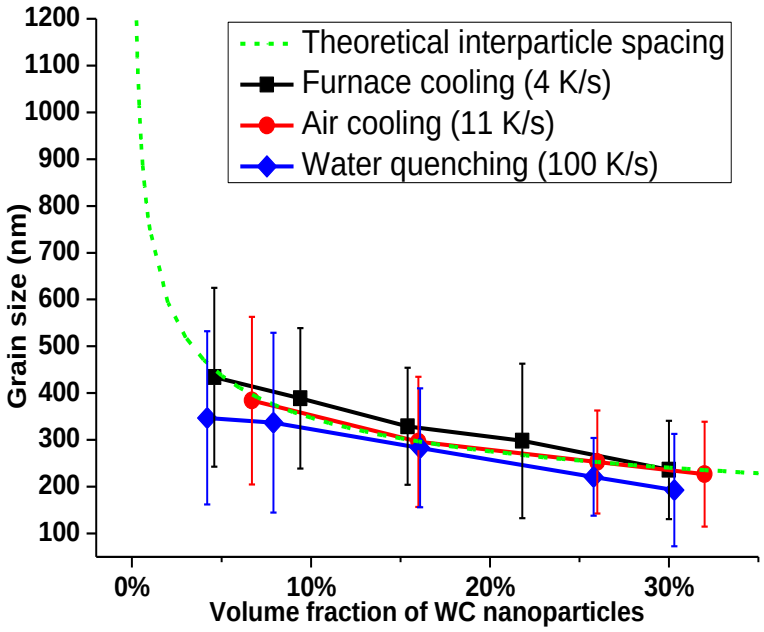

Figure 5-9 Summary of the average Cu grain sizes for different volume fractions of nanoparticles under different cooling rates. Error bars show the standard deviation.

5.3.3 Nanoparticles Enabled Grain Refinement Mechanisms

To establish the nanoparticle-enabled grain control mechanism, we conducted theoretical analysis. If we assume nanoparticles are spherical and homogeneous distributed in the matrix, the theoretical inter-particle spacing between WC nanoparticles could be calculated by:

$$d = r\left(\frac{4\pi}{3f_v}\right)^{\frac{1}{3}} \qquad 5\text{-}3$$

where d is the theoretical inter-particle spacing, r is the radius of the particles (e.g., about 100 nm in this study), and f_v is the volume fraction of particles. The green dotted line in Figure 5-9 corresponds to the theoretical inter-particle spacing of the WC particles at different volume fractions. It is noted that the experimental results for Cu grain sizes are close to the theoretical interparticle spacing between nanoparticles. Figure 5-10 shows the STEM image of the nanoparticle rich area, which suggests that Cu grain size is related to the WC interparticle spacing.

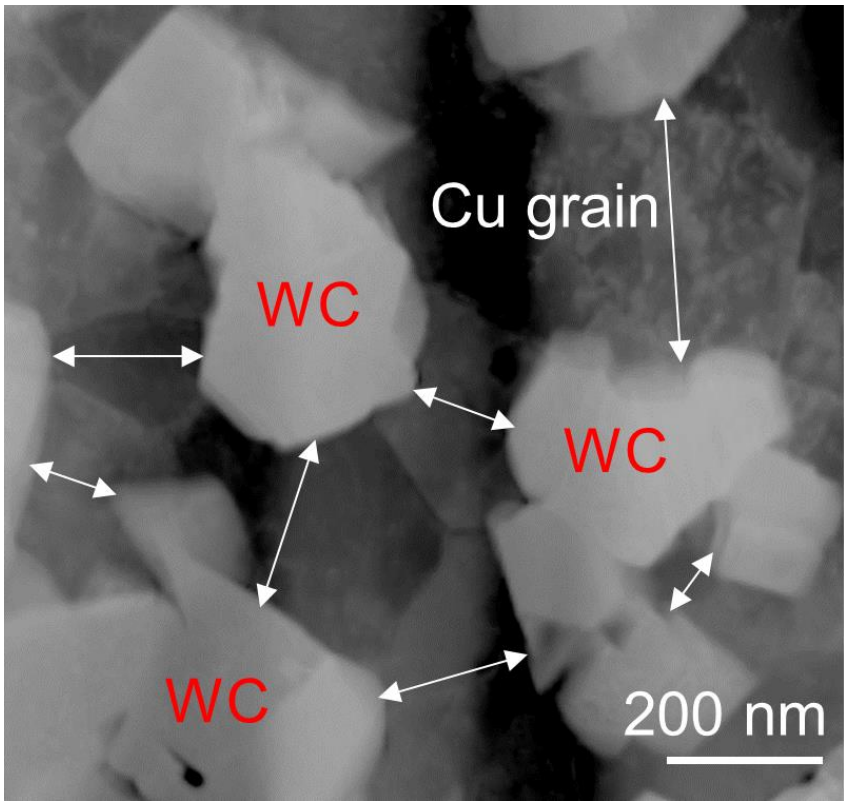

Figure 5-10 STEM image of the WC nanoparticle rich area showing that Cu grain size is correlated with WC inter-particle spacing.

To further provide fundamental insight into the underlying phase change and growth phenomena, differential scanning calorimetry (DSC) studies were conducted and the typical cooling curves for solidification of pure copper and Cu with WC nanoparticles (samples have the

same mass, ~50 mg) are shown in Figure 5-11. In Figure 5-11a, the bump on the cooling curve of pure Cu sample corresponds to the exothermal peak from the solidification of Cu started at 1033 °C, which indicates a 51 °C undercooling needed to activate major nucleation of Cu grains. However, the starting point of the exothermal peak of Cu-10 vol% WC is 1078 °C, which means only 6 °C undercooling was needed by the addition of WC nanoparticles. The undercooling difference indicates that WC is a highly potent nucleation particle for Cu. Moreover, the width (time) of the peak in pure Cu is 1.38 min, while it is 2.52 min in the Cu-10vol%WC sample, indicating a 83% longer nucleation period than in pure Cu. The heat flow curves during DSC tests were shown in Figure 5-12. The exothermal peaks correspond to the latent heat release from the solidification. The width of the peak in pure Cu is 6.9 °C, while it is 12.6 °C in the Cu-10vol%WC sample which means exothermal peak in pure Cu is sharp and intensive and it is gradual and wide in Cu-WC samples. These results suggest that the nanoparticles are able to slow down solidification and enable a continuous nucleation and an effective grain growth control during solidification.

Following the initial nucleation of grains from the melt, the nucleated grains grow rapidly and release latent heat, which usually prevents the nucleation of new grains nearby. In contrast, with nanoparticles in the molten metal, nanoparticles can rapidly assemble/adhere to the solid-liquid interface to effectively restrict the grain growth, preventing other potential nucleation sites from being suppressed by the latent heat release. Therefore, later nucleation events could occur continuously during the solidification, which is crucial for this new grain refinement and growth control mechanism. This growth restriction and continuous nucleation can be validated by comparing the width of the exothermal peaks of pure Cu and Cu with nanoparticles in DSC study.

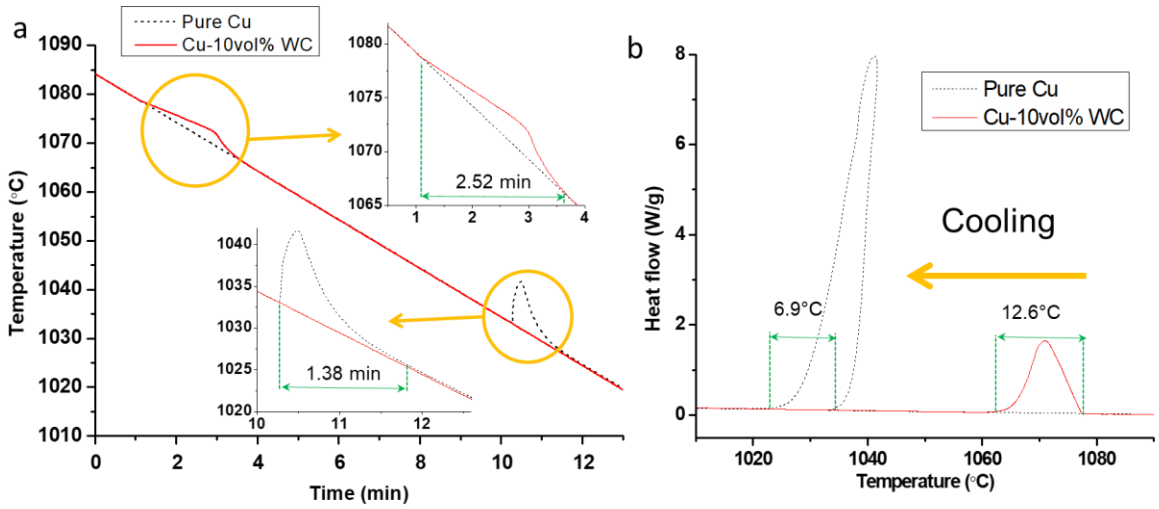

Figure 5-11 Typical DSC scanning result during the cooling (cooling rate: 5 °C/min) of pure Cu and Cu-10vol%WC: (a) temperature-time curve; (b) Heat flow-temperature curve.

For effective nucleation, the crystallographic lattice discrepancy between particles and matrix is crucial for the nucleation, thus the interface between matrix and nanoparticles were studied at atomic scale by HRTEM. Figure 5-12 shows the typical interface between WC nanoparticles and Cu matrix. Figure 5-12b is the Fourier-filtered atomic resolution TEM image at the marked area of Figure 5-12a. The atomic structure indicates a clean and well-matched Cu-WC interface with no intermediate phases present. The top-right and bottom-left insets are the fast Fourier transformation of the Cu matrix and WC nanoparticles, respectively. It is identified that the $(10\bar{1}1)$ planes of WC nanoparticles are parallel with (200) planes of Cu matrix. The plane distance of (200) Cu and $(10\bar{1}1)$ WC are 0.1806 nm and 0.1881 nm, respectively. Thus the misfit is calculated to be 4.1%, which implies a coherent lattice matching at this specific interface. The presence of a clean and coherent interface suggests a strong interfacial bond. The coherent

interface also indicates that WC nanoparticles could serve as potent nucleation sites for Cu grains when the required undercooling is reached. As shown in Figure 5-12c, 12d and 12e, there exist other orientation relationships at the Cu-WC interface such as WC (0001) and Cu (220). The angle between WC (0001) planes Cu (220) planes is approximately 50°.

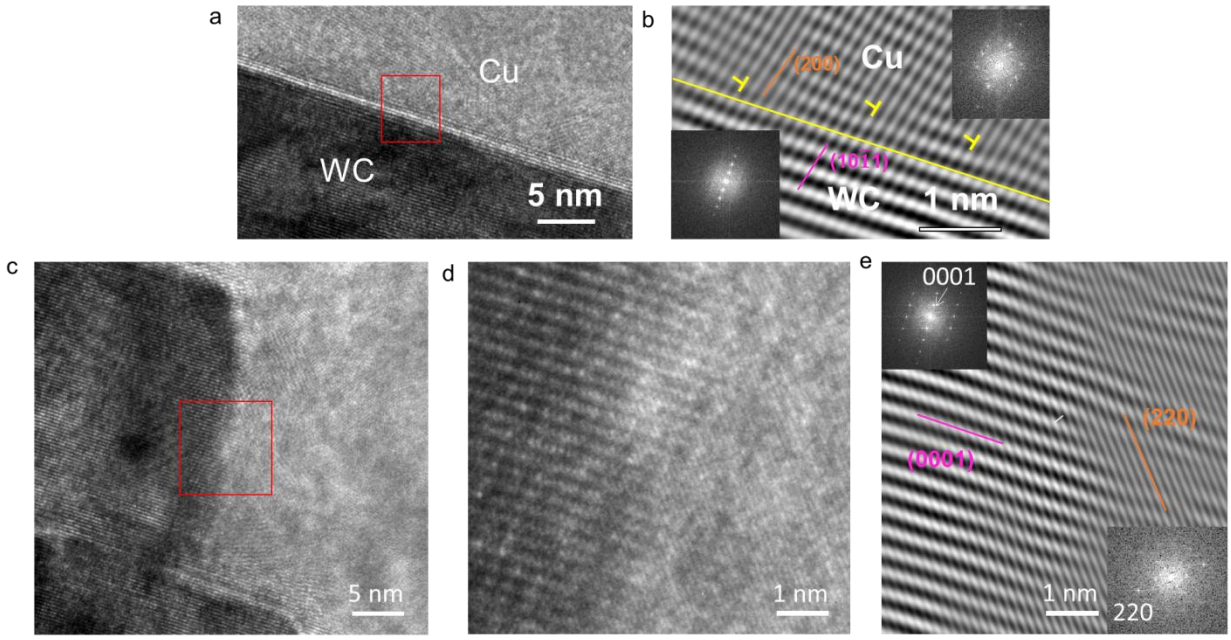

Figure 5-12 (**a)** A typical TEM image of Cu-WC interface showing the interface between Cu and WC nanoparticle. **(b)** Fourier-filtered high resolution TEM image of the marked red rectangle area in (a) showing a characteristic interface between WC nanoparticle and Cu matrix. Insets are the fast Fourier transformation of the Cu matrix (top right) and WC nanoparticle (bottom left). **(c)** TEM image of another Cu-WC interface aligned at different orientation. **(d)** High-resolution TEM image of the region marked by a red rectangle in (d). **(e)** Fourier-filtered high resolution TEM image of the region marked by a red rectangle in (c).

It is well known that, after nucleation, grain growth control during solidification is vital to achieve refined grain structures. It is proposed here that nanoparticles will impede grain growth during solidification by forcing the solidification front to grow with a non-linear geometry (e.g., curved solidification front). When Cu grains form curvatures with a small radius during solidification, the free energy (Gibbs-Thomson effect) increases. The molar free energy increase can be calculated by:

$$\Delta G_\gamma = \frac{2\gamma V_m}{r} \qquad 5\text{-}4$$

where ΔG_γ is the molar free energy increase, γ is the interfacial energy of the interface, V_m is the molar volume of the phase, and r is the radius of curvature of the interface. If this increment of free energy is large enough (thus larger undercooling is needed), the growth of Cu grains may be inhibited [Chen 2015]. The undercooling needed to overcome a curved interface generated by nanoparticles pinning can be described by the Gibbs-Thompson effects and can be calculated by:

$$\Delta T = \frac{2\gamma T_m}{r H_f} \qquad 5\text{-}5$$

where γ is the interface energy of solid-liquid interfaces (Cu: 0.185 J/m^2, Al: 0.116J/m^2 and Zn: 0.09 J/m^2), T_m is melting of the metal, r is the radius of curvature of the solidification front and H_f is the enthalpy of fusion. The undercooling needed to overcome the grain front curvatures when pinned by nanoparticles for Cu, Al, and Zn are shown in Figure 5-13a.

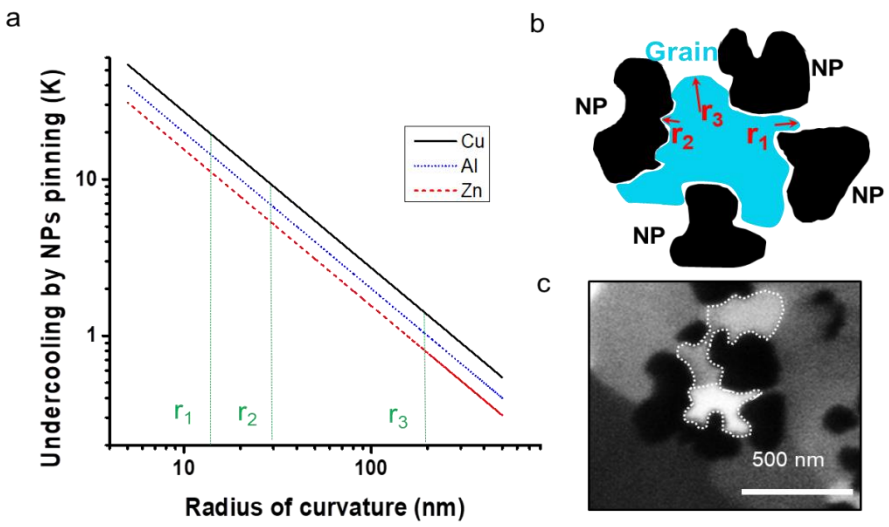

Figure 5-13 (a) Undercooling required to overcome Gibbs-Thompson pinning effect for Cu, Al and Zn. (b) Schematic illustration of the nanoparticles pinning effects. **(c)** SEM image of a Cu grain refined by WC nanoparticles.

As shown in the schematic illustration (Figure 5-13b) of the nanoparticles pinning effects, there are mainly two types of curvature generated by nanoparticles: (1) Marked as r_1 and r_3 in Figure 5-13b, when a solidification front meets with dispersed nanoparticles, the Cu phase can grow through the micro/nano-channels between nanoparticles and form a curvature with a small radius that results in an increase of free energy (Gibbs-Thomson effect). (2) Marked as r_2 in Figure 5-13b, nanoparticles have curved surfaces and when Cu solidification front meet nanoparticles, the curvature at the interface between Cu and WC nanoparticles will need extra undercooling to remain solid. The range of the undercooling needed by the curvatures generated by nanoparticles pinning effects are approximately in the range of tens degrees of Kelvin as marked by r_1, r_2 and r_3 in Figure 5-13a. The curvatures generated by nanoparticles are observed in SEM image as shown in Figure 5-13c. The Cu grain is surrounded by several WC nanoparticles and shows both two types of curvatures as mentioned above.

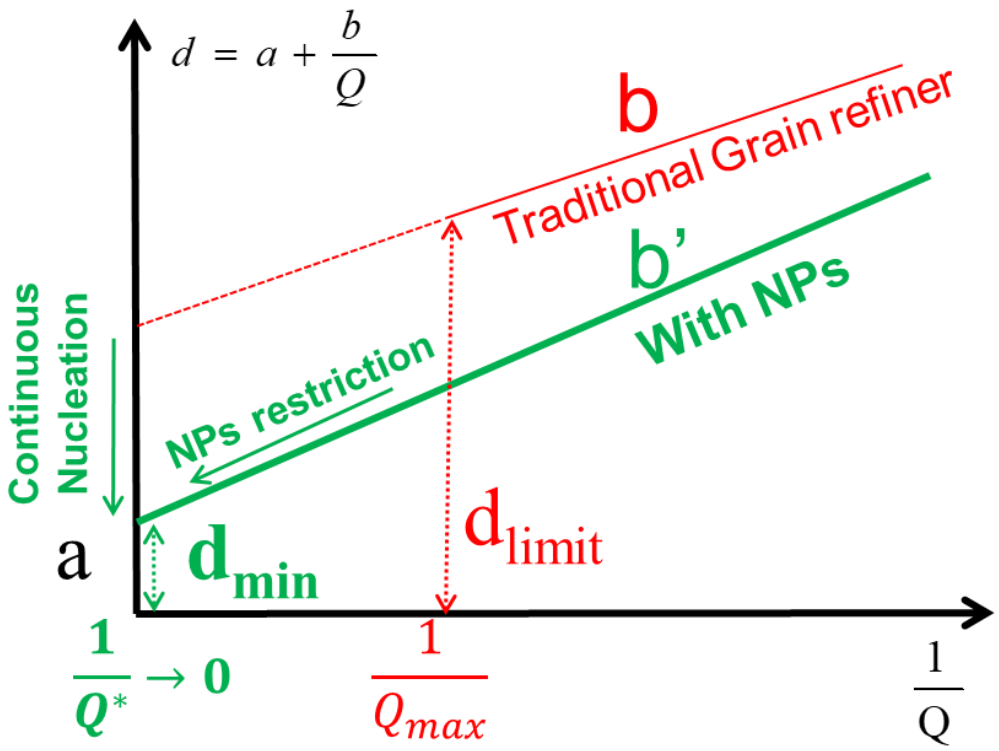

Figure 5-14 Nanoparticles break the fundamental limit existed in conventional grain refinement methods.

On the basis of classic theories for nucleation and grain growth in alloys, it is well recognized that grain growth velocity can be reduced by the solute atoms at the solid/liquid interface during alloy solidification. Published studies have revealed that an empirical relationship (as shown in Figure 5-14) between average grain size (d) and the restriction factor Q [StJohn 2005, Easton 2005] for alloys:

$$d = a + \frac{b}{Q} \qquad 5\text{-}6$$

where a is a constant related to population density of nucleation particles and b is a constant related to the potency of the nucleation particles. Q is the restriction factor, which is inversely

proportional to the constitutional undercooling. For growth restriction by extra solute atoms, the constitutional undercooling could be described by [StJohn 2005]:

$$\Delta T_c = mC_0(1 - \frac{1}{(1-f_s)^{(1-k)}}) \quad 5\text{-}7$$

where ΔT_c is the constitutional undercooling, m is the liquidus slope in a linear phase diagram, C_0 is the solute content in the alloy and k is the equilibrium solute partition coefficient, f_s is the solid fraction solidified. By taking the derivative of this equation respect to f_s, it has been suggested that Q can be expressed as [StJohn 2005, Easton 2005]:

$$Q = mC_0(k-1) = (\frac{\partial(\Delta T_c)}{\partial f_s})_{fs\to 0} \quad 5\text{-}8$$

This equation indicates that the physical meaning of growth restriction factor is the initial rate of development of constitutional undercooling. From the definition of Q, we can see that the restriction factor is determined by the phase diagram and the specific chemical composition of the specific alloy. Thus the chemical restriction from solute atoms is very limited. It has been reported that the maximum value of Q (Q_{max}) in some practical alloys can be around 50 K [Easton 2005]. Taking Al-Ti as one example, the constitutional undercooling of Al-Ti alloy system is shown in Figure 5-15. Ti is the one of the most effective atoms to restrict grain growth in Al. The growth restriction factor is described as Q_1, Q_2 and Q_3 for different Ti concentration of 0.05, 0.10 and 0.15, respectively. With higher concentration of Ti atoms in Al melt, the growth restriction factor increases. As marked by the black arrow in the Figure 5-15, a steeper slope provides larger growth restriction factor. However, the maximum solubility of Ti atoms in Al is 0.15 which limits Q to reach a maximum value as Q_{max}. As shown in Figure 5-14, with the limited Q_{max}, the smallest grain

size achievable by traditional inoculation and solute atoms is d_{limit}, which is approximately tens of micrometers.

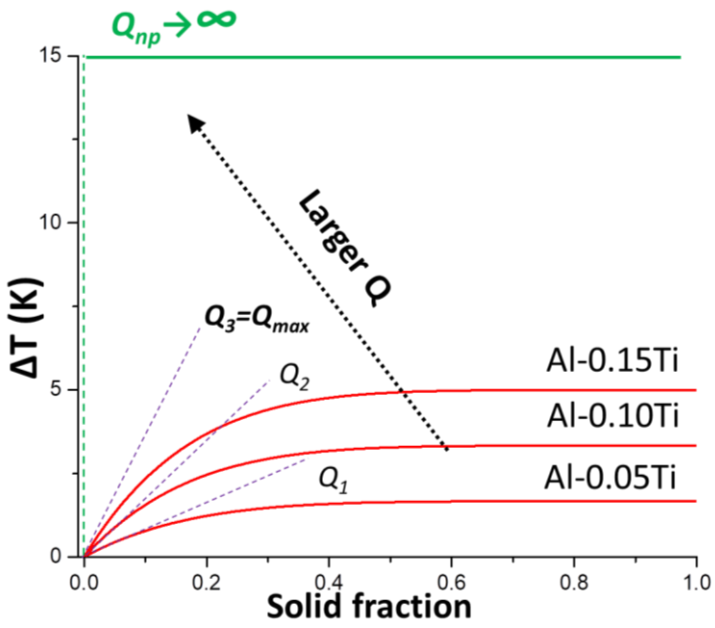

Figure 5-15 Undercooling profile respect to solid fraction. The red curves correspond with the constitutional undercooling for Al-Ti alloys. Limited by the phase diagram and the maximum solubility of Ti in Al, the growth restriction factor reaches to a maximum value of Q_{max} in the Al-0.15Ti alloy. The green line corresponds with the undercooling profile of the nanoparticle enabled phase growth restriction, indicating an almost infinity large Q_{np}.

In contrast, here we proposed that nanoparticles pinning can induce a new restriction factor, Q_{np}, which can break the fundamental limit sets by Q that depends on constitutional undercooling. As far as the solidification front touches with a nanoparticle with curved shape or a nano-scale channel between nanoparticles, unlike the constitutional undercooling built gradually ahead of the solidification front, an undercooling is immediately established by the Gibbs-Thompson effect. As shown in Figure 5-15, the undercooling profile established by Gibbs-Thompson effect is a step

function with an infinite large slope at the initial point. Thus Q_{np} which is the initial rate of the undercooling development by nanoparticles can be readily increased to a significant large number, if not infinity.

Moreover, populous nanoparticles (five orders of magnitude more) could serve as potent nucleation sites in the continuous nucleation, thus a (related to the number of effective nucleation sites) is significantly reduced. The average grain size can be reduced to d_{min} when $1/Q_{np}$ approaches to zero. We propose that d_{min} achievable is determined by the theoretical inter-particle spacing. The trend line of theoretical inter-particle spacing in Figure 5-9 is consistent with our experimental data of average grain sizes in Cu-WC samples. This indicates that nanoparticle enabled nucleation and grain growth control could enable us to refine grains down to the inter-particle spacing limit *for the first time* under slow cooling. Therefore, nanoparticles effectively break the fundamental limits set by conventional solidification process and readily refine grains down to ultrafine or even nano scale by regular casting process.

Based on the experimental results and theoretical analysis, the mechanisms of nanoparticles enabled grain refinement and control, in comparison to the classic grain refinement, during regular casting are schematically illustrated in Figure 5-16.

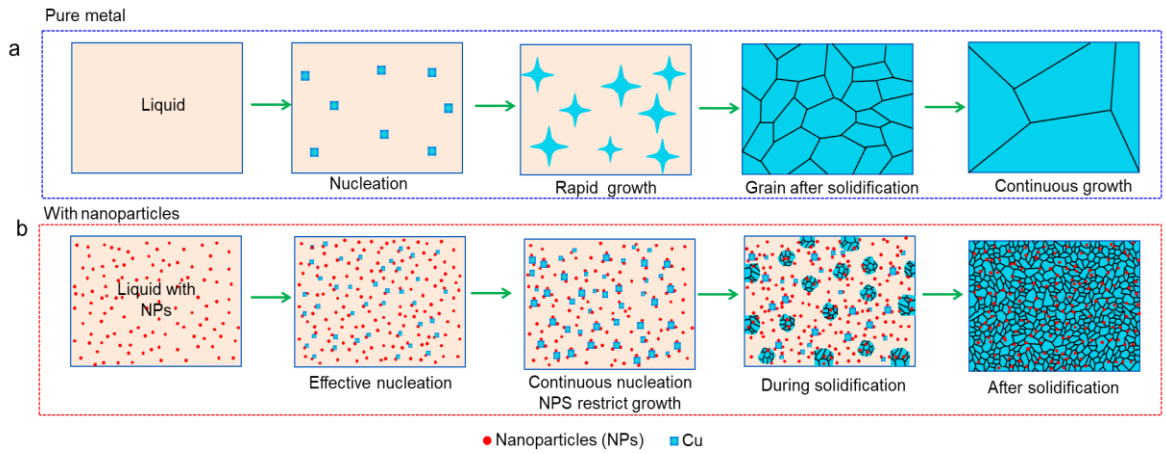

Figure 5-16 Schematic illustrations of phase evolution during solidification of pure metal (a) and metal with nanoparticles (b).

Other less dominant mechanisms may also play minor roles in phase growth control, such as blocking of the diffusion of atoms to the surface of the growing phase and modification of the local temperature field by nanoparticles. Nanoparticles can remain at the solidification front and block the transportation of the atoms, thus slowing down the grain growth [Chen 2015, Chen 2014, Cao 2016 and Cao 2018]. When the density of nanoparticles is low, this effect will not play a major role. Moreover, when WC nanoparticles are close to the solidification front, the nanoparticles could affect the local thermal fields. The lower thermal conductivity of ceramic nanoparticles could slow down the transportation of latent heat from the solidification front and protect potential nucleation sites.

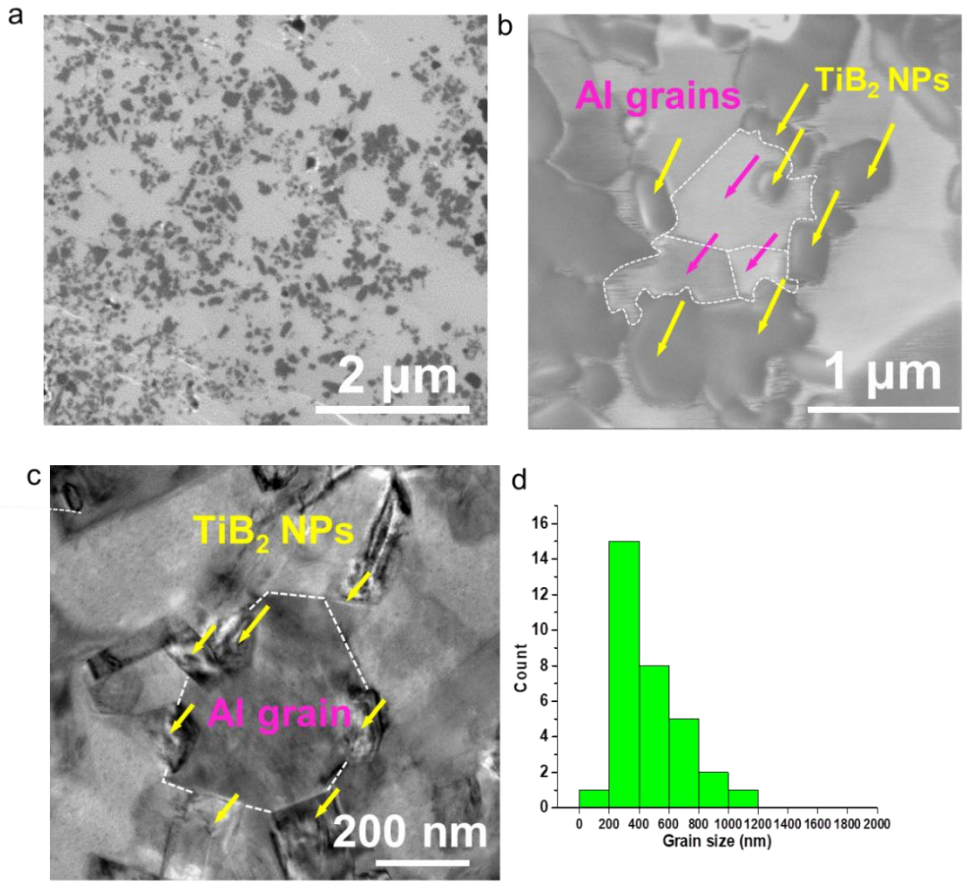

Figure 5-17 (a),(b) FIB images of Al-10vol%TiB_2 cast by furnace cooling (0.7 K/s) showing the distribution of TiB2 nanoparticles and ultrafine AL grains. **c,** TEM image of Al-10vol%TiB_2 (0.7 K/s) showing one ultrafine Al grain surrounded by TiB_2 nanoparticles. **d,** Al Grain size distribution of Al-10vol%TiB_2 (0.7 K/s).

5.3.4 Nanoparticles Enabled Grain Refinement in Other Material Systems

The nanoparticle enabled grain refinement has also been validated for other materials systems. Al-TiB_2, Zn-WC were also studied in order to determine whether it is possible to achieve UFG/nanocrystalline microstructures via slow cooling for different metals. The salt-assisted self-incorporation method was used to fabricate Al containing 10 vol% TiB_2 nanoparticles (with an average size of about 100 nm) by furnace cooling (0.7 K/s as measured). Figure 5-17a shows the

FIB image of Al-10vol%TiB_2, the dark phases are TiB_2 nanoparticles while the grey matrix is Al. TiB_2 nanoparticles are reasonably well dispersed in the Al matrix. The higher magnified image is shown in Figure 5-17b, we can clearly identify Al grains (marked by white dash lines and pink arrows) smaller than 1.0 μm surrounded by TiB_2 nanoparticles (marked by yellow arrows). TEM image of Figure 5-17c demonstrate one ultrafine Al grain (marked by white dash lines) been controlled by several TiB_2 nanoparticles. The grain size distribution of Al is shown in Figure 5-16 with an average grain size of 460 ± 220 nm.

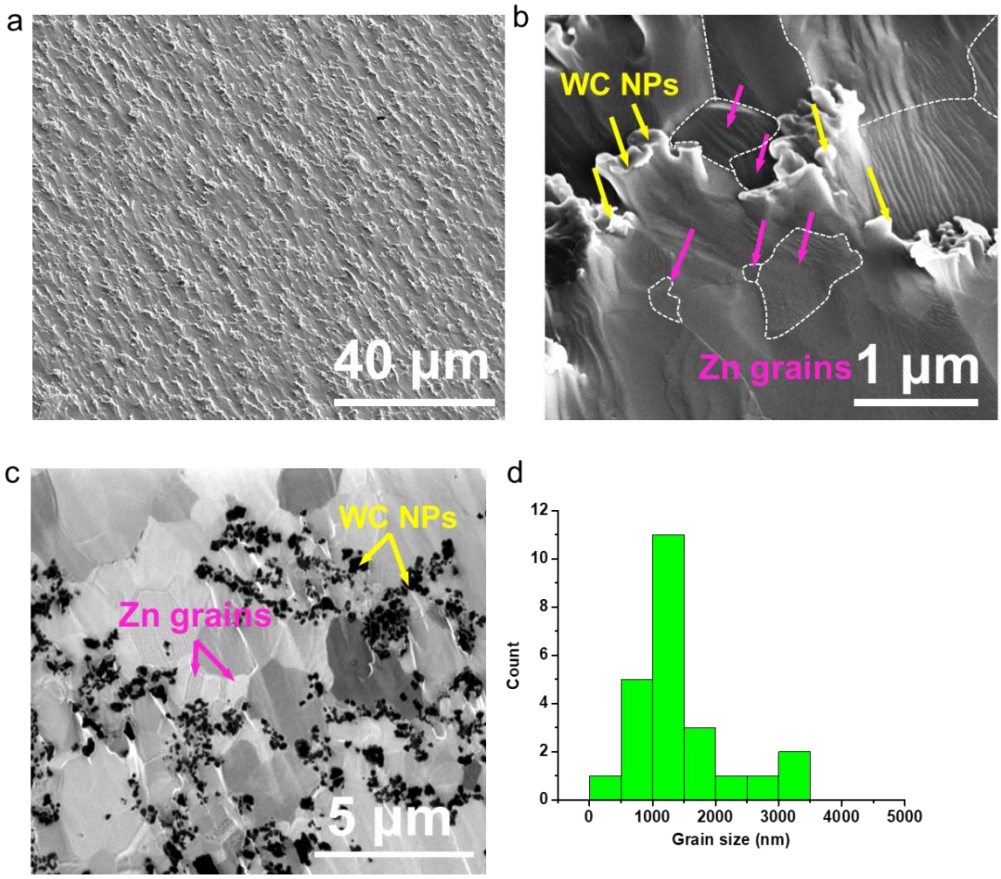

Figure 5-18 (a), (b) SEM image of Zn-5vol%WC by air cooling (3.7 K/s). **c,** FIB image of Zn-5vol%WC (3.7 K/s). **d,** Zn Grain size distribution of Zn-5vol%WC (3.7 K/s).

Zn-5vol%WC samples were also fabricated by melting with a cooling rate of 3.7 K/s (see Methods). As shown in Figure 5-18a and 18b (SEM images of Zn-5vol%WC), WC nanoparticles are distributed and dispersed, though not as good as in Cu and Al cases. Zn grains (marked by white dash lines and pink arrows) close to 1.0 μm are clearly identified. The FIB image of Figure 5-18c shows a better contrast from the Zn grains. The size distribution of Zn grains is shown in Figure 5-18d with an average grain size of 991 ± 746 nm. It is validated that Zn grains were refined to approximately 1.0 μm by the addition of 5 vol% WC nanoparticles, although not as effective as in the Cu and Al cases. The reason is mainly due to the smaller undercooling required to overcome the Gibbs-Thompson pinning effects for Zn than for Al and Cu, as shown in Figure 5-13a. This nanoparticle enabled grain refinement approach provides an additional general pathway to produce UFG/nanocrystalline metals by regular casting.

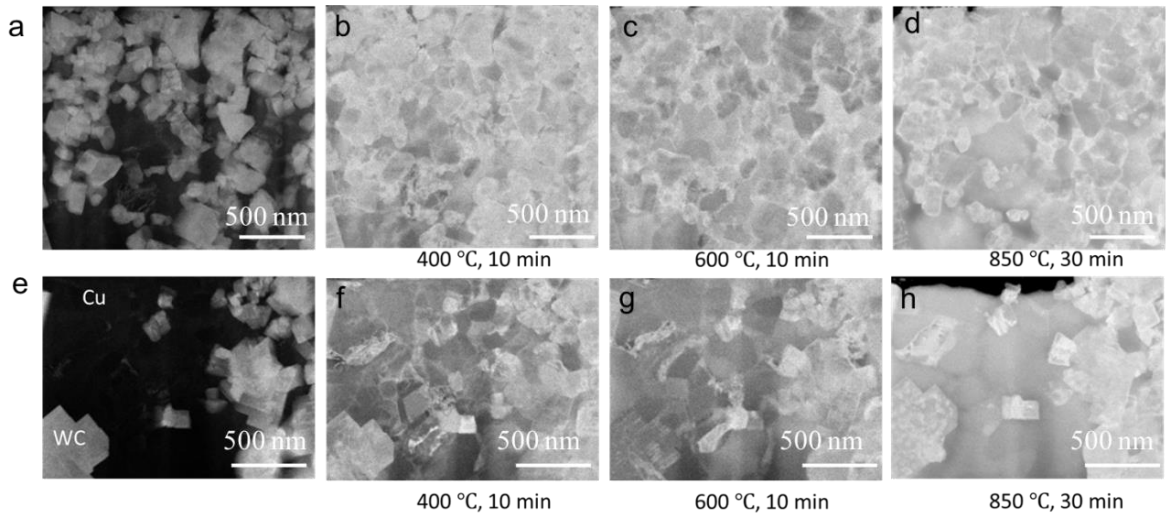

Figure 5-19 (**a-d)** STEM images of an area with a high percentage of WC nanoparticles at room temperature, 400 °C, 600 °C and 850 °C, respectively. (**e-h)** STEM image of an area with a relative low percentage of WC nanoparticles at room temperature, 400 °C, 600 °C and 850 °C, respectively.

5.3.5 Solid-Solid Phase Control: Thermal Stability

The thermal stability of UFG/nanocrystalline metals is another grand challenge that limits their widespread use in many applications. It has been reported that pure nanocrystalline metals (Al, Cu, Sn, Pb, Zn, and Mg) exhibit extensive grain growth even at room temperature (~300 K). Nanocrystalline metals with higher melting points (~1700 K), such as Co, Ni, and Fe, see a rapid grain growth over a moderate temperature range of 220-450 °C (493-723 K), resulting in micrometer-sized grains at a temperatures less than a half of their melting temperatures [Tschopp 2014, Wang 2014]. Approaches that involve adding solute atoms to stabilize nanocrystalline metals by pinning the grain boundaries or lowering the grain boundary energy have yielded some successful results [Darling 2016, Chookajorn 2012]. However, these approaches remain inherently limited by the thermodynamic properties of the particular alloy systems. It is proposed that dispersed nanoparticles could stabilize the UFG/nanocrystalline metals at elevated temperatures. To study the nanoparticle-enabled stabilization in the as-cast Cu-WC nanocomposites at elevated temperatures, the grain growth was further investigated by STEM equipped with in-situ heating capability. The in-situ heating path is staying at 200, 400, 600 °C for 10 min and 850 °C for 30 min. Figure 5-19a and Figure 5-19e show the local microstructures of as solidified Cu-WC samples with different local volume percentages of nanoparticles. The local nanoparticle concentration in Figure 5-19a is higher than that in Figure 5-19e. The relatively bright phases are WC nanoparticles and the black phase is the Cu matrix. The grain structures at 400, 600 and 850 °C shown in Figure 5-19b to 19d and Figure 5-19f to 19h are acquired at longer camera lengths than Figure 5-19a and Figure 5-19e to enhance the diffraction contrast of the image in order to distinguish individual Cu grains. In the nanoparticle rich local area, Figure 5-19a to 19d show that nano-scale grains were thermally stable at temperatures up to 850 °C (Figure 5-19d). In the area with fewer nanoparticles

(Figure 5-19e to 19h), ultrafine/nano-scale grains were thermally stable up to about 600 °C. However, when the temperature was raised to 850 °C, ultrafine/nano-scale grains started to grow and became larger grains (Figure 5-19h). Although we observed that the grains starting to grow at 850 °C, this growth was restricted by nanoparticles close to this area and therefore the grain sizes did not exceed the ultrafine grain size. This restriction indicates that nanoparticles effectively inhibit grain growth in solid state up to a temperature of 850 °C (1123 K), which significantly corresponds to approximately 0.83 of the melting temperature of Cu (1353 K).

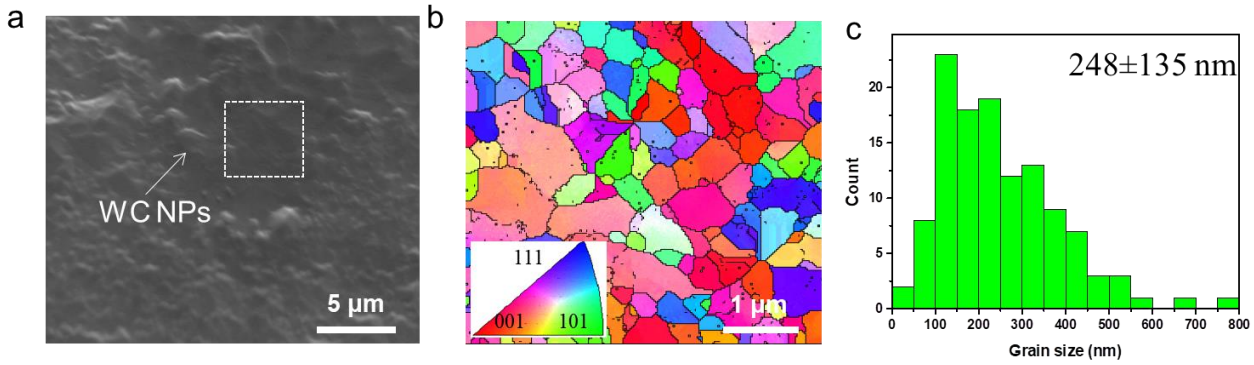

Figure 5-20 **(a)** SEM image of Cu-34vol%WC after heat treatment (750 °C for 2.0 hours). **(b)** EBSD image corresponds to the marked white rectangle in (a). **(c)** Cu grain size distribution of the heat treated Cu-34vol%WC sample.

To further validate the thermal stability of the refined Cu grains and study the effects on mechanical properties by heat treatment, we heated the Cu-34vol%WC sample obtained by casting under air cooling (cooling rate of 7 K/s), which had an average grain size of 208 ± 94 nm, to 750 °C (1023 K, 0.75 of the melting point of Cu) and held the sample at this temperature for 2.0 hours under the protection of argon. Figure 5-20a shows a typical SEM image of the Cu-34vol%WC sample after the high temperature exposure. EBSD was utilized to study the potential grain growth

in the nanoparticle-poor zone such as the marked white rectangle area in Figure 5-20a. Figure 5-20b clearly shows that most Cu grains are still smaller than 1.0 μm while a significant number of nano-scale grains remained after the heat treatment. The grain size distribution in Figure 5-20c confirms that the average Cu grain size is 248 ± 135 nm after the heat treatment, which is close to the average grain size, 208 ± 94 nm, before the heat treatment.

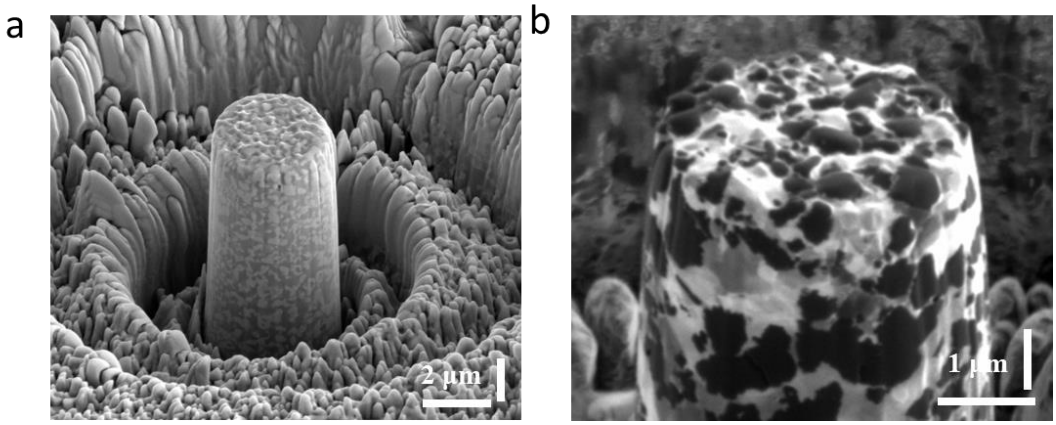

Figure 5-21 (**a)** SEM image of a Cu-34vol%WC micropillar machined by FIB. (**b)** FIB image of the micropillar showing polycrystalline Cu matrix with WC nanoparticles.

The thermal stability may be attributable to a Zenner pinning effect derived from the presence of dispersed nanoparticles. A maximum mean grain size can be theoretically estimated by:

$$D_{max} = \frac{4r}{3f_v} \qquad 5\text{-}9$$

where r is the nanoparticle radius and f_v is the volume fraction of the nanoparticles. The D_{max} for Cu-34%WC is estimated to be 392 nm, which is comparable with our experimental data. When compared with other precipitate particles from alloy systems, the ex-situ WC nanoparticles will

not dissolve in the Cu matrix at high temperatures offering a superior thermal stability than conventional alloys.

5.3.6 Mechanical Properties

The presence of fine, well-dispersed nanoparticles in a metal matrix is anticipated to significantly enhance mechanical responses [Chen 2015', Chen 2012 and Yang 2004]. To gain fundamental insights into the property enhancement induced by the refined grains and nanoparticles, we conducted micropillar compression tests on the Cu samples. Figure 5-21a shows the micropillar of the as solidified Cu-WC with populous dispersed nanoparticles in the pillar. The poly-crystalline nature of the micropillar is shown in Figure 5-21b where the FIB image reveals the contrast of different grains. This pillar of 4 μm in diameter contains multiple grains. The typical results from the micropillars compression studies are shown in Figure 5-22. The yield point increased from 180 ± 8 MPa to 827 ± 74 for pure Cu and as-solidified Cu-34vol%WC, respectively. Moreover, micropillars from Cu-34vol%WC sustained a gradually increasing load up to 1490 MPa and strain over 25% without catastrophic failure. In comparison, the pure Cu sample experienced extensive slip as the strain increases discontinuously. As shown in Figure 5-23, after deformation, multiple slip traces were observed in the pure Cu samples, while no obvious slip traces appeared in the Cu-WC samples.

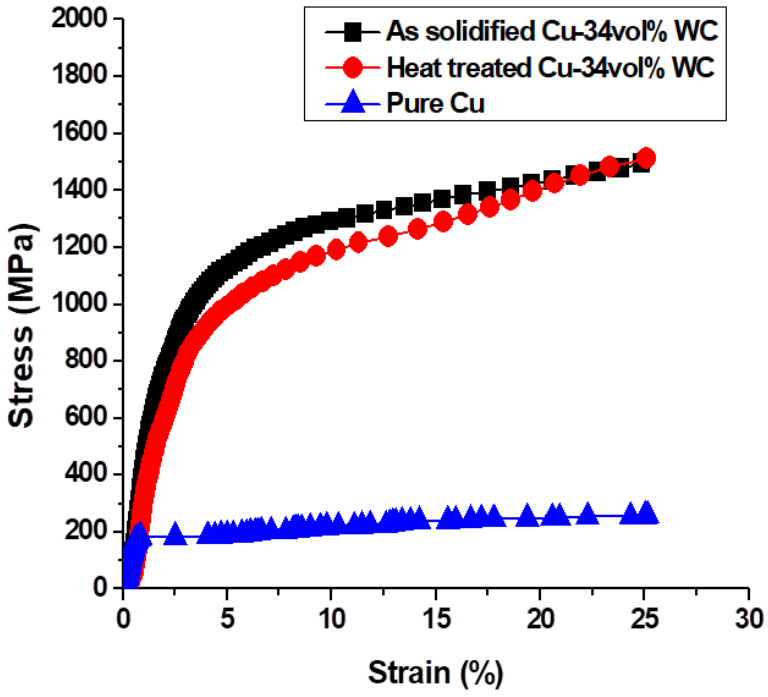

Figure 5-22 Engineering stress-strain curves of as-solidified pure Cu samples (blue), with nanoparticles (black) and heat treated sample (red).

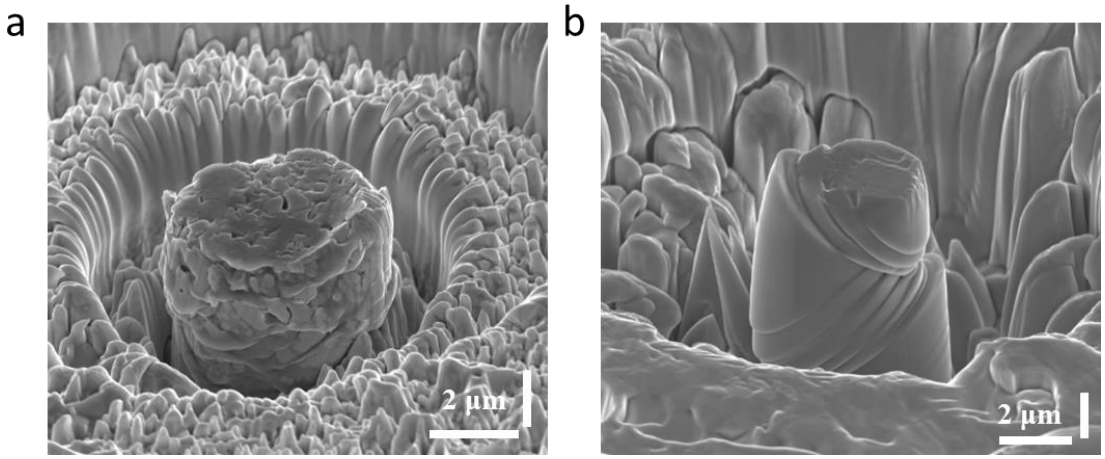

Figure 5-23 SEM images showing the morphology of post-deformed samples with (a) and without (b) nanoparticles.

The strengthening from nanoparticles and refined grain structures in the as solidified samples of Cu-34vol%WC is about 647 MPa. The major strengthening mechanisms include Orowan strengthening induced from the populous and dispersed nanoparticles, Hall-Petch effect, and load bearing transfer.

The contribution from Orowan strengthening ($\Delta\sigma_{Orowan}$) from well-dispersed nanoparticles can be calculated by the following equation [Zhang 2006, Liu 2013]:

$$\Delta\sigma_{Orowan} = \frac{0.13G_m b}{d_p\left[\left(\frac{1}{2V_p}\right)^{\frac{1}{3}}-1\right]} ln\frac{d_p}{2b} \quad 5\text{-}10$$

where G_m, b, V_p and d_p are the shear modulus of the matrix, the Burger vector, the volume fraction and the size of the nanoparticles, respectively. In this study, G_m= 46 GPa, b = 0.256 nm, V_p = 0.34 and d_p = 200 nm, the calculated $\Delta\sigma_{Orowan}$ is 333 MPa. It should be noted that this value is estimated based on ideal dispersion.

The contribution from Hall-Petch effect can be calculated by the following equation [Chen 2015']:

$$\Delta\sigma_y = kd^{-1/2} \quad 5\text{-}11$$

where d is the grain size and k is a material constant. For Cu, k = 0.11 MPa·m, and d = 208 nm, the calculated $\Delta\sigma_y$ = 246 MPa.

The load bearing strengthening can be calculated by the following equation [Nardone 1986]:

$$\Delta\sigma_{load} = 1.5V_p\sigma_i \quad 5\text{-}12$$

where σ_i is the interfacial bonding strength between nanoparticles and metal matrix. The strong interfacial bonding between Cu and WC nanoparticles contributes in the load bearing mechanism. It is difficult to estimate the interfacial bonding strength though.

The mechanical properties of the heat treated samples were also tested by the micropillar test. The red curve in Figure 5-22 shows a typical stress-strain curve of a heat treated Cu-WC sample, with a corresponding yield point of 780 ± 9 MPa and a maximum sustained load of 1500 MPa, which is very close to those of the as-solidified sample. These results suggest that mechanical properties did not change much after a thermal exposure at 750 °C for 2.0 hours, which further confirms that the Cu samples with WC nanoparticles exhibit excellent thermal stability.

Furthermore, a clean and strong interfacial bond between Cu matrix and WC nanoparticles also leads to a substantial increment in Young's modulus. Figure 5-24 shows the Young's modulus enhancement of the as solidified bulk samples (by a cooling rate of 7 K/s) measured by the nanoindentation method with a Berkovich tip. The Young's modulus of pure Cu, Cu-19vol%WC, and Cu-34vol%WC are 139 ± 8 GPa, 192 ± 13 GPa, and 223 ± 16 GPa, respectively. We hypothesize that the enhancement of Young's modulus is due to the high Young's modulus of WC (~530-700 GPa) and the effective load transfer by the nanoparticles. The Young's modulus calculated by the rule of mixture is about 253 GPa for the Cu-34vol%WC sample and 190 GPa for the Cu-19vol%WC sample, which are in good agreement with the value determined by the microindentation tests.

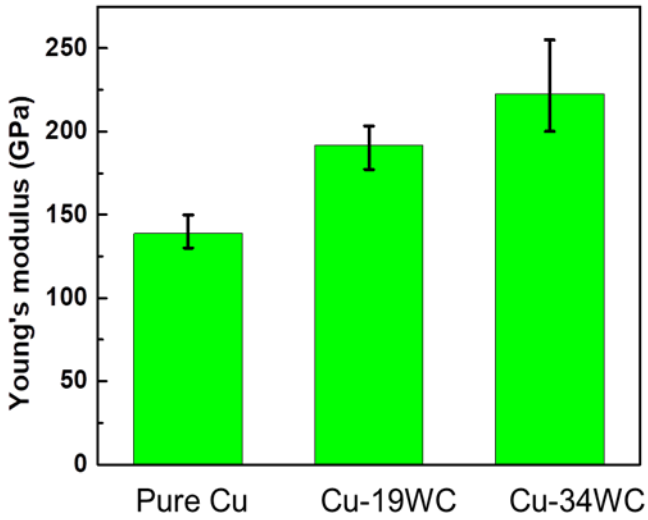

Figure 5-24 Young's modulus of pure Cu, Cu-19vol%WC and Cu-34vol%WC.

5.4 Summary

In summary, a revolutionary approach to effectively control nucleation and grain growth down to ultrafine/nano scale during slow solidification was discovered by use of dispersed nanoparticles in molten metals. The nanoparticles enabled new grain refinement mechanisms, which combines continuous nucleation and grain growth control, breaks the fundamental limit of conventional grain refinement methods. This new discovery enables a pathway to directly cast bulk UFG/nanocrystalline metals under slow cooling rates (e.g., less than 100 K/s) for large scale production. An unprecedented thermal stability up to 1023 K, 0.75 T_m of Cu, for the as-cast bulk UFG/nanocrystalline Cu is demonstrated. As-cast bulk UFG/nanocrystalline metals with nanoparticles also show exceptional strengths and Young's modulus enhancement. Furthermore, this general approach is valid for different materials systems such as Al-TiB_2 and Zn-WC. This

approach, will not only have a significant impact on the solidification processes for metals, but also on numerous applications such as biomedical, chemical, and atmospheric sciences.

Chapter 6 Conclusions

The study is motivated by the growing requirements of effective phase control during solidification processing for desired materials. Conventional phase control approaches have gradually encountered certain technical and/or fundamental limits. The emerging nanotechnology could provide a new pathway to control the phase evolution during solidification to break these limits. The objective of this study is to significantly advance the fundamental understanding of nanoparticles enabled phase control during solidification processing and to overcome the limits of the current phase control methods. More specifically, both fundamental and experimental studies were conducted to understand how nanoparticles interact with liquid-liquid phase in immiscible alloys to solve the scalable processing issues, solid-liquid phase during solidification for unprecedented grain refinement and solid-solid phase at high temperatures for unusual thermal stabilities.

To investigate the nanoparticle enabled phase control in solidification processing, key issues of nanoparticles incorporation and dispersion should be tackled first. In this study, a novel salt-assisted incorporation method was developed to fabricate metals containing uniformly distributed and dispersed nanoparticles. Metal matrix nanocomposites of Al-TiC, Al-TiB_2 and Cu-WC can be successfully fabricated by this method. It is discovered that $KAlF_4$ salt is very effective to incorporate TiC nanoparticles into molten Al matrix. This molten salt assisted incorporation method enables us to incorporate high percentage (up to 9 vol.%) TiC nanoparticles into Al matrix. The molten salt has following functions to assist the incorporation of nanoparticles: (1) Remove the oxide layer at the top of the metal melt. Molten salt especially fluoride salt can dissolve oxide effectively. With the molten salt at the top of the molten metal, the oxide film barrier can be removed and a clean interface for better incorporation is provided. (2) Protect nanoparticles from

oxidation. Nanoparticles can be easily oxidized at high processing temperatures. Molten salt can protect nanoparticles from oxygen in the air and avoid severe burning issues. (3) Provide a transportation medium for nanoparticle incorporation. The atomic bonds of carbides nanoparticles such as TiC have partially metallic characteristics, thus carbide usually wet better with metal melt than molten salt. Then nanoparticles can self-transport into molten metal to reach a more favorable energy state. Moreover, TiC nanoparticles are uniformly dispersed in the pseudo clusters (nanoparticle rich zones). This is originated from the interaction potential between nanoparticles. With the addition of TiC nanoparticles, the microhardness of Al-TiC nanocomposites is significantly enhanced. This novel salt-assisted incorporation method paves a new pathway for mass production of metal matrix nanocomposites.

In addition, to maximize the Orowan strengthening and study the phase control effect from smaller nanoparticles, a novel and facile molten salt reaction method was developed to synthesis small TiC nanoparticles with a diameter about 10 nm, which is not commercially available. Molten eutectic NaCl-KCl salt provides a reaction medium, allowing chemical reaction to occur at lower temperatures. K_2TiF_6 react with Ti powders to provide free floating Ti^{2+} ions to decompose to Ti at the diamond surface. Then this deposited Ti layer reacts with diamond nanoparticle to form TiC nanoparticle. The size of the TiC nanoparticles can be well controlled by the reaction template of diamond nanoparticles in this study. Moreover, the as synthesized 10 nm TiC nanoparticles are then incorporated into Al matrix by the molten salt assisted incorporation method and the size of TiC nanoparticles can remain as about 10 nm. In addition, the microhardness of Al-TiC nanocomposites with 10 nm TiC nanoparticles is significantly improved.

To further improve and simplify the processing of Al nanocomposites reinforced by TiC nanoparticles with diameter of 10 nm, a novel one-step in-situ reaction and incorporation method

was explored, by which the synthesis and incorporation of TiC nanoparticles are finished by one-step mechanical mixing process. Ti^{4+} ions from K_2TiF_6 salts were reduced by molten Al to provide Ti atoms in the molten salt. The Ti atoms then react with diamond nanoparticles to produce TiC nanoparticles. Since the reduced free Ti atoms could move freely in the molten salt, the sizes of the produced TiC nanoparticles are determined by the size of diamond nanoparticles as they served as the reaction templates. The average diameter of raw diamond nanoparticles is 5-10 nm, and the size of formed TiC nanoparticles is approximately 11 nm. The as-cast and cold rolled Al-TiC nanocomposites with 11 nm TiC nanoparticles show significantly improved mechanical properties.

Cu-WC nanocomposites with various volume fractions of nanoparticles were also successfully fabricated by the molten salt method after different salts were tested for optimized processing. $KAlF_4$, borax and NaCl were all effective for the incorporation of WC nanoparticles into the molten Cu. WC nanoparticles can be readily incorporated into Cu melt because of the the good wettability between WC and Cu melt. WC nanoparticles can be uniformly distributed and dispersed in Cu matrix and provide much enhanced mechanical properties (strength, hardness and Young's modulus) without significant deterioration of the electrical conductivity, which suggests that the new Cu-WC nanocomposites could serve as high strength and high electrical conductivity materials for a widespread range of applications. .

The nanoparticles enabled phase control in liquid-liquid phase was studied in immiscible alloys both experimentally and theoretically to advance the fundamental understanding and to solve the long-standing challenges in solidification processing of immiscible alloys. It is shown that nanoparticles can move to the interface between the primary phase and secondary phase forming a coating and slowing down the diffusional growth of the secondary phase, which results in a significantly refined microstructure. TiC nanoparticles were successfully utilized in the Al-Bi

immiscible alloy for scalable manufacturing of high performance self-lubrication bearing materials. The nanoparticle-enabled phase control mechanism allows us to process Al-Bi immiscible alloys in large scale. With the increase of cooling rate, the average diameter of Bi phase decreases and the size of the minority Bi phase can be reduced to submicron, breaking the fundamental and technical limits of processing immiscible alloys and opening up more exciting applications. The mechanical properties of Al-Bi immiscible alloy with TiC nanoparticles can be further enhanced by Cu element addition and cold rolling for practical applications. With the addition of Cu element, Al-Cu precipitates were formed during processing and thus the mechanical properties are enhanced. The addition of Al-5Ti-1B grain refiner is also effective to refine the grain size and thus further enhance the mechanical properties.

Tungsten (W) nanoparticle was demonstrated to be effective for the processing Zn-Bi immiscible alloys. For the first time, W nanoparticles were easily incorporated and dispersed in Zn-8Bi alloy melt by semi-solid mixing and ultrasonic-assisted processing for Zn-8Bi-2vol%W nanocomposites. XRD analysis indicated that W nanoparticles were chemically stable in the Zn-8Bi melt. SEM and EDS analyses demonstrated that W nanoparticles self-assembled at the Zn-Bi interface driven by the reduction of system surface energy. W nanoparticles significantly refined the size of the Bi phase and prevented the Bi sedimentation during Zn-Bi immiscible alloy casting. Microhardness test showed that W nanoparticles significantly enhanced the mechanical properties of Zn-Bi. The unprecedented use of chemically-stable metal nanoparticles for phase control in immiscible alloys simplifies the processing because metal nanoparticles offer excellent wettability with molten metal to allow effective nanoparticle incorporation and dispersion.

Nanoparticles are not only effective for processing of metallic immiscible alloys, but also function well in organic immiscible systems. It is shown that B_4C nanoparticles are suitable to

control the immiscible organic SCN-CTB system. The intermediate polarity of B_4C makes it suitable for the phase control of CTB-SCN material system. Therefore, the nanoparticles provide a general approach to control phase evolution of immiscible alloys during solidification processing.

The grain refinement by nanoparticles for pure metals is studied in different model material systems such as Cu-WC, Al-TiB_2 and Zn-WC. In this study, a new discovery that nanoparticles can refine metal grains down to ultrafine or even nanoscale by instilling a continuous nucleation and grain growth restriction mechanism during slow cooling (< 100 K/s) is reported for the first time. When casting pure Cu with WC nanoparticles, the grain sizes of Cu are refined substantially ultrafine and even nanoscale, which is approximate to the inter-particle spacing. Differential scanning calorimetry (DSC) studies showed that Cu-WC samples need significantly longer time (by 83%) to complete the solidification than pure Cu, indicating nanoparticles can substantially slow down the solidification process. It is proposed that nanoparticles can restrict the grain growth by the Gibbs-Thompson effect, thus allowing a continuous nucleation throughout the solidification process. In addition, the as-solidified bulk ultrafine/nanocrystalline Cu reveals an unprecedented thermal stability up to 1023 K (0.75 melting point of Cu) and high mechanical properties. Furthermore, this newly revealed grain control mechanism is successfully applied in other materials systems such as Al-TiB_2 and Zn-WC for ultrafine grains via slow cooling. This revolutionary method paves a pathway for the mass production of bulk stable ultrafine-grained (UFG)/nanocrystalline materials. This method may be readily extended to any other processes that involve cooling, nucleation and phase growth for widespread applications.

In summary, this dissertation presents experimental methods and a theoretical framework to understand and utilize the newly discovered nanoparticles enabled phase control mechanisms during solidification processing. The understanding of the nanoparticles enabled phase control

for immiscible alloys and grain refinement of pure metals is significantly advanced. This approach breaks the fundamental and technical limits for solidification processing of metals for broad applications.

Chapter 7 Recommendations for Future Work

With the scientific and technical advances on nanoparticles enabled control phase in solidification processing in this study, it suggests that nanoparticles would be a very promising approach to tackle more challenges faced by conventional metallurgy. To further understand the nanoparticles enabled phase control and extend its applications, following research directions are recommended:

7.1 In-situ Study on Nanoparticles Enabled Phase Control

In-situ study for the fundamental understanding of nanoparticle enabled phase control is very important. Here two approaches for the in-situ study are proposed: (1) In-situ dynamic transmission electron microscope (DTEM) serves as a unique in-situ electron microscope to observe fast materials process at the micro to nano scale [McKeown 2015, Campbell 2014 and McKeown 2014]. DTEM could be utilized to in-situ study the nucleation and growth for metals containing nanoparticles. With a laser heating system in TEM, it is feasible to melt the material and then directly observe the nucleation and grain growth during cooling which can provide us first hand insights how the nanoparticles affect the solidification behaviors. (2) Taking advantages of the transparency of some organic alloys, it is possible to directly observe the growth of the phases by optical microscope during cooling. The previous study on the SCN-CTB immiscible alloys have validated the feasibility of this approach. The implementation of the in-situ experiment study will unleash the unabridged dynamic procedure how nanoparticles control the phase evolution during solidification.

7.2 Investigate Different Types of Nano-Elements for Phase Control

From the theory proposed in this study, the size and shape of nanoparticles have significant effects on phase control. Thus it will be of scientific significance to investigate the different types and sizes of nano-elements on phase control. For example, the earlier work has shown that TiC nanoparticles of 50 nm in diameter can refine the size of the secondary Bi phase in Al-Bi alloys to several micrometers under regular casting. It is highly possible that smaller nanoparticles could form the coating faster than larger nanoparticles and thus the size of the secondary minor phase could be refine even down to nanoscale. Moreover, nano-elements with different shapes will also be interesting for optimized phase control.

7.3 Nanoparticle Modified Metallurgy

We have shown that nanoparticles can be very effective for immiscible alloys and grain refinement of pure metals. It will be significant to study the capability of nanoparticles to tune other secondary phase such as the eutectic phase, precipitate and even meta-stable phase such as martensite for desired microstructures and thus better performance. Nanoparticles enable phase control opens up a lot of exciting research directions to explore for conventional metallurgy.

7.4 Nanotechnology-enabled Materials Processing

The nanoparticles enabled phase control is successfully demonstrated as an effective method to tune the solidification behaviors of metals. It is highly promising that this methodology would be applied to any other materials manufacturing processes involve melting and solidification, such as welding, casting, thermal spraying, laser processing and additive manufacturing, to effectively control the phase evolution for desired microstructure. In addition,

the incorporation of nanoparticles also has great potential to mitigate the current manufacturing issues in these processes by control the solidification behaviors.

References

- [Akramifard 2014] Akramifard, H. R., Shamanian, M., Sabbaghian, M., & Esmailzadeh, M. (2014). Microstructure and mechanical properties of Cu/SiC metal matrix composite fabricated via friction stir processing. *Materials & Design (1980-2015)*, *54*, 838-844.
- [Akyol 2007] Akyol, E., & Öner, M. (2007). Inhibition of calcium oxalate monohydrate crystal growth using polyelectrolytes. *Journal of Crystal Growth*, *307*(1), 137-144.
- [Alam 2006] Alam, S. N. (2006). Synthesis and characterization of W–Cu nanocomposites developed by mechanical alloying. *Materials Science and Engineering: A*, *433*(1-2), 161-168.
- [AlMangour 2016] Rapid fabrication of bulk-form TiB2/316L stainless steel nanocomposites with novel reinforcement architecture and improved performance by selective laser melting
- [AlMangour 2016'] Selective laser melting of TiB2/316L stainless steel composites: The roles of powder preparation and hot isostatic pressing post-treatment
- [AlMangour 2016'’] Selective laser melting of TiC reinforced 316L stainless steel matrix nanocomposites: Influence of starting TiC particle size and volume content
- [AlMangour 2016'’’] In-situ formation of novel TiC-particle-reinforced 316L stainless steel bulk-form composites by selective laser melting
- [Amosov 2014] Amosov, A. P., Luts, A. R., Ermoshkin, A., & Ermoshkin, A. A. (2014). Role of Halide Salts Na3AlF6 and Na2TiF6 in Self-propagating High-temperature Synthesis of Al-10% TiC Nanocomposite Alloy in Aluminum Melt. *Life Science Journal*, *11*(12s), 570.

- [Aoki 1990] Aoki, S., Kishimoto, K., Yoshida, T., Sakata, M., & Richard, H. A. (1990). Elastic-plastic fracture behavior of an aluminum alloy under mixed mode loading. *Journal of the Mechanics and Physics of Solids*, *38*(2), 195-213.
- [Arnberg 1982] Arnberg, L., Bäckerud, L., & Klang, H. (1982). Intermetallic particles in Al–Ti–B–type master alloys for grain refinement of aluminium. *Metals Technology*, *9*(1), 7-13.
- [Arpon 2003] Arpon, R., Narciso, J., Louis, E., & Garcia-Cordovilla, C. (2003). Interfacial reactions in Al/TiC particulate composites produced by pressure infiltration. *Materials science and technology*, *19*(9), 1225-1230.
- [Aruna 2008] Aruna, S. T., & Mukasyan, A. S. (2008). Combustion synthesis and nanomaterials. *Current opinion in solid state and materials science*, *12*(3-4), 44-50.
- [Azizieh 2011] Azizieh, M., Kokabi, A. H., & Abachi, P. (2011). Effect of rotational speed and probe profile on microstructure and hardness of AZ31/Al2O3 nanocomposites fabricated by friction stir processing. *Materials & Design*, *32*(4), 2034-2041.
- [Banerji 1986] Banerji, A., & Reif, W. (1986). Development of Al-Ti-C grain refiners containing TiC. *Metallurgical Transactions A*, *17*(12), 2127-2137.
- [Baumli 2005] Baumli, P., Sytchev, J., Göndör, Z. H., & Kaptay, G. (2005). Interaction between a titanium-containing molten salt and an alumina plate. In *Materials Science Forum* (Vol. 473, pp. 39-44). Trans Tech Publications.
- [Bauri 2011]Bauri, R., Yadav, D., & Suhas, G. (2011). Effect of friction stir processing (FSP) on microstructure and properties of Al–TiC in situ composite. *Materials Science and Engineering: A*, *528*(13-14), 4732-4739.

- [Berbon 2001] Berbon, P. B., Bingel, W. H., Mishra, R. S., Bampton, C. C., & Mahoney, M. W. (2001). Friction stir processing: a tool to homogenize nanocomposite aluminum alloys.
- [Birol 2006] Birol, Y. (2006). Grain refining efficiency of Al–Ti–C alloys. *Journal of alloys and compounds*, *422*(1-2), 128-131.
- [Božić 2009] Božić, D., Cvijović-Alagić, I., Dimčić, B., Stašić, J., & Rajković, V. (2009). In-situ processing of TiB2 nanoparticle-reinforced copper matrix composites. *Science of Sintering*, *41*(2), 143-150.
- [Campbell 2014] Campbell, G. H., McKeown, J. T., & Santala, M. K. (2014). Time resolved electron microscopy for in situ experiments. *Applied Physics Reviews*, *1*(4), 041101.
- [Cao 2008] Cao, G., Konishi, H., & Li, X. (2008). Mechanical properties and microstructure of SiC-reinforced Mg-(2, 4) Al-1Si nanocomposites fabricated by ultrasonic cavitation based solidification processing. *Materials Science and Engineering: A*, *486*(1-2), 357-362.
- [Cao 2008'] Cao, G., Kobliska, J., Konishi, H., & Li, X. (2008). Tensile properties and microstructure of SiC nanoparticle–reinforced Mg-4Zn alloy fabricated by ultrasonic cavitation–based solidification processing. *Metallurgical and Materials Transactions A*, *39*(4), 880-886.
- [Cao 2016] Cao, C., Chen, L., Xu, J., Zhao, J., Pozuelo, M., & Li, X. (2016). Phase control in immiscible Zn-Bi alloy by tungsten nanoparticles. *Materials Letters*, *174*, 213-216.

- [Cao 2016’] Cao, C., Chen, L., Xu, J., Choi, H., & Li, X. (2016). Strengthening Al–Bi–TiC0. 7N0. 3 nanocomposites by Cu addition and grain refinement. *Materials Science and Engineering: A*, *651*, 332-335.
- [Cao 2017] Cao, C., Liu, W., Javadi, A., Ling, H., & Li, X. (2017). Scalable manufacturing of 10 nm TiC nanoparticles through molten salt reaction. *Procedia Manufacturing*, *10*, 634-640.
- [Cao 2018] Cao, C., Liu, W., Liu, Z., Xu, J., Hwang, I., De Rosa, I., & Li, X. (2018). Scalable manufacturing of immiscible AlBi alloy by self-assembled nanoparticles. *Materials & Design*, *146*, 163-171.
- [Carlberg 1980] Carlberg, T., & Fredriksson, H. (1980). The influence of microgravity on the solidification of Zn-Bi immiscible alloys. *Metallurgical Transactions A*, *11*(10), 1665-1676.
- [Casati 2013] Casati, R., Amadio, M., Biffi, C. A., Dellasega, D., Tuissi, A., & Vedani, M. (2013). Al/Al2O3 Nanocomposite Produced by ECAP. In *Materials Science Forum* (Vol. 762, pp. 457-464). Trans Tech Publications.
- [Casati 2014] Casati, R., & Vedani, M. (2014). Metal matrix composites reinforced by nano-particles—a review. *Metals*, *4*(1), 65-83.
- [Cha 2005] Cha, S. I., Kim, K. T., Arshad, S. N., Mo, C. B., & Hong, S. H. (2005). Extraordinary strengthening effect of carbon nanotubes in metal-matrix nanocomposites processed by molecular-level mixing. *Advanced Materials*, *17*(11), 1377-1381.
- [Chang 1998] Chang, J., Moon, I., & Choi, C. (1998). Refinement of cast microstructure of hypereutectic Al-Si alloys through the addition of rare earth metals. *Journal of materials science*, *33*(20), 5015-5023.

- [Chen 1996] Chen, Y., & Chung, D. D. L. (1996). In situ Al-TiB composite obtained by stir casting. *Journal of materials science*, *31*(2), 311-315.
- [Chen 1999] Z.Y. Chen, Y.Y. Chen, Q. Shu, G.Y. An, (1999) Acta Metall. Sinica, 35, 874.
- [Chen 2012] Chen, L. Y., Konishi, H., Fehrenbacher, A., Ma, C., Xu, J. Q., Choi, H., & Li, X. C. (2012). Novel nanoprocessing route for bulk graphene nanoplatelets reinforced metal matrix nanocomposites. *Scripta Materialia*, *67*(1), 29-32.
- [Chen 2013] Chen, L. Y., Peng, J. Y., Xu, J. Q., Choi, H., & Li, X. C. (2013). Achieving uniform distribution and dispersion of a high percentage of nanoparticles in metal matrix nanocomposites by solidification processing. *Scripta materialia*, *69*(8), 634-637.
- [Chen 2014] Chen, L. Y., Xu, J. Q., Choi, H., Konishi, H., Jin, S., & Li, X. C. (2014). Rapid control of phase growth by nanoparticles. *Nature communications*, *5*, 3879.
- [Chen 2015] Chen, L. Y., Xu, J. Q., & Li, X. C. (2015). Controlling phase growth during solidification by nanoparticles. *Materials Research Letters*, *3*(1), 43-49.
- [Chen 2015'] Chen, L. Y., Xu, J. Q., Choi, H., Pozuelo, M., Ma, X., Bhowmick, S., & Li, X. C. (2015). Processing and properties of magnesium containing a dense uniform dispersion of nanoparticles. *Nature*, *528*(7583), 539.
- [Chen 2016] Chen, G., Peng, Y., Zheng, G., Qi, Z., Wang, M., Yu, H., & Liu, C. T. (2016). Polysynthetic twinned TiAl single crystals for high-temperature applications. *Nature materials*, *15*(8), 876.
- [Choi 2012] Choi, H., Jones, M., Konishi, H., & Li, X. (2012). Effect of combined addition of Cu and aluminum oxide nanoparticles on mechanical properties and microstructure of Al-7Si-0.3 Mg alloy. *Metallurgical and materials Transactions A*, *43*(2), 738-746.

- [Choi 2013] Choi, H., Cho, W. H., Konishi, H., Kou, S., & Li, X. (2013). Nanoparticle-induced superior hot tearing resistance of A206 alloy. *Metallurgical and Materials Transactions A*, *44*(4), 1897-1907.
- [Chookajorn 2012] Chookajorn, T., Murdoch, H. A., & Schuh, C. A. (2012). Design of stable nanocrystalline alloys. *Science*, *337*(6097), 951-954.
- [Chrysanthou 1995] Chrysanthou, A., & Erbaccio, G. (1995). Production of copper-matrix composites by in situ processing. *Journal of Materials Science*, *30*(24), 6339-6344.
- [Coombs 2003] Coombs, M. L., Eichelberger, J. C., & Rutherford, M. J. (2003). Experimental and textural constraints on mafic enclave formation in volcanic rocks. *Journal of Volcanology and Geothermal Research*, *119*(1-4), 125-144.
- [Da Daoan 1988] Da Daoan, J. W., & Yumin, W. (1988). Process of binary monotectic alloy under simulated microgravity effect by electromagnetic force. *Chinese Space Science and Technology*, *6*, 20-24.
- [Dai 2018] Dai, D., Gu, D., Xia, M., Ma, C., Chen, H., Zhao, T., & Poprawe, R. (2018). Melt spreading behavior, microstructure evolution and wear resistance of selective laser melting additive manufactured AlN/AlSi10Mg nanocomposite. *Surface and Coatings Technology*.
- [Daoush 2014] Daoush, W.M., 2014. Fabrication of TiN/cBN and TiC/diamond coated particles by titanium deposition process. Transactions of Nonferrous Metals Society of China, 24(11), pp.3562-3570.
- [Darling 2016] Darling, K. A., Rajagopalan, M., Komarasamy, M., Bhatia, M. A., Hornbuckle, B. C., Mishra, R. S., & Solanki, K. N. (2016). Extreme creep resistance in a microstructurally stable nanocrystalline alloy. *Nature*, *537*(7620), 378.

- [De Cicco 2009] De Cicco, M. P. (2009). *Solidification phenomena in metal matrix nanocomposites*.
- [De Cicco 2009] De Cicco, M. P., Li, X., & Turng, L. S. (2009). Semi-solid casting (SSC) of zinc alloy nanocomposites. *Journal of Materials Processing Technology*, *209*(18-19), 5881-5885.
- [De Cicco 2011] De Cicco, M. P., Turng, L. S., Li, X., & Perepezko, J. H. (2011). Nucleation catalysis in aluminum alloy A356 using nanoscale inoculants. *Metallurgical and Materials Transactions A*, *42*(8), 2323-2330.
- [Dikici 2011] Dikici, B., Gavgali, M., & Bedir, F. (2011). Synthesis of in situ TiC nanoparticles in liquid aluminum: the effect of sintering temperature. *Journal of composite Materials*, *45*(8), 895-900.
- [Doi 1993] Doi, T., & Koster, J. N. (1993). Thermocapillary convection in two immiscible liquid layers with free surface. *Physics of Fluids A: Fluid Dynamics*, *5*(8), 1914-1927.
- [Easton 2005] Easton, M., & StJohn, D. (2005). An analysis of the relationship between grain size, solute content, and the potency and number density of nucleant particles. *Metallurgical and materials transactions A*, *36*(7), 1911-1920.
- [Easton 2008] Easton, M. A., & StJohn, D. H. (2008). Improved prediction of the grain size of aluminum alloys that includes the effect of cooling rate. *Materials Science and Engineering: A*, *486*(1-2), 8-13.
- [Easton 2016] Easton, M. A., Qian, M., Prasad, A., & StJohn, D. H. (2016). Recent advances in grain refinement of light metals and alloys. *Current Opinion in Solid State and Materials Science*, *20*(1), 13-24.

- [EStruga 2013] Estruga, M., Chen, L., Choi, H., Li, X., & Jin, S. (2013). Ultrasonic-assisted synthesis of surface-clean TiB2 nanoparticles and their improved dispersion and capture in Al-matrix nanocomposites. *ACS applied materials & interfaces*, *5*(17), 8813-8819.
- [Eustathopoulos 1999] Eustathopoulos, N., Nicholas, M. G., & Drevet, B. (Eds.). (1999). *Wettability at high temperatures* (Vol. 3). Elsevier.
- [Fan 2018] Fan, Z., Gao, F., Zhou, L., & Lu, S. Z. (2018). A new concept for growth restriction during solidification. *Acta Materialia*, *152*, 248-257.
- [Fathy 2013]Fathy, A., & El-Kady, O. (2013). Thermal expansion and thermal conductivity characteristics of Cu–Al2O3 nanocomposites. *Materials & Design*, *46*, 355-359.
- [Feyzullahoğlu 2010] Feyzullahoğlu, E., & Şakiroğlu, N. (2010). The wear of aluminium-based journal bearing materials under lubrication. *Materials & Design (1980-2015)*, *31*(5), 2532-2539.
- [Feyzullahoğlu 2010] Feyzullahoğlu, E., & Şakiroğlu, N. (2010). The wear of aluminium-based journal bearing materials under lubrication. *Materials & Design (1980-2015)*, *31*(5), 2532-2539.
- [Findik 2003] Findik, F., & Uzun, H. (2003). Microstructure, hardness and electrical properties of silver-based refractory contact materials. *Materials & design*, *24*(7), 489-492.
- [Frens 1973] Frens, G. (1973). Controlled nucleation for the regulation of the particle size in monodisperse gold suspensions. *Nature physical science*, *241*(105), 20.
- [Gelles 1978] Gelles, S. H., & Mark worth, A. J. (1978). Microgravity studies in the liquid-phase immiscible system: Aluminum-indium. *AIAA Journal*, *16*(5), 431-438.

- [Gianola 2006] Gianola, D. S., Van Petegem, S., Legros, M., Brandstetter, S., Van Swygenhoven, H., & Hemker, K. J. (2006). Stress-assisted discontinuous grain growth and its effect on the deformation behavior of nanocrystalline aluminum thin films. *Acta Materialia*, *54*(8), 2253-2263.
- [Goh 2008] Goh, C. S., Wei, J., Lee, L. C., & Gupta, M. (2008). Ductility improvement and fatigue studies in Mg-CNT nanocomposites. *Composites Science and Technology*, *68*(6), 1432-1439.
- [Gollas 2013] Gollas, B., Luegger, A., & Zidar, J. (2013). The Electrodeposition of Zinc-Bismuth Alloys. *ECS Transactions*, *50*(52), 123-133.
- [Greer 1994] Greer, A. L. (1994). Nanostructure by nucleation. *Nature*, 368, 688–689
- [Greer 2000] Greer, A. L., Bunn, A. M., Tronche, A., Evans, P. V., & Bristow, D. J. (2000). Modelling of inoculation of metallic melts: application to grain refinement of aluminium by Al–Ti–B. *Acta materialia*, *48*(11), 2823-2835.
- [Greer 2006] Greer, A. L., & Quested, T. E. (2006). Heterogeneous grain initiation in solidification. *Philosophical Magazine*, *86*(24), 3665-3680.
- [Greer 2016] Greer, A. L. (2016). Overview: Application of heterogeneous nucleation in grain-refining of metals. *The Journal of Chemical Physics*, *145*(21), 211704.
- [Gu 2014] Gu, D., Wang, H., Chang, F., Dai, D., Yuan, P., Hagedorn, Y. C., & Meiners, W. (2014). Selective laser melting additive manufacturing of TiC/AlSi10Mg bulk-form nanocomposites with tailored microstructures and properties. *Physics Procedia*, *56*, 108-116.

- [Guo 2009] Guo, M., Shen, K., & Wang, M. (2009). Relationship between microstructure, properties and reaction conditions for Cu–TiB2 alloys prepared by in situ reaction. *Acta Materialia*, *57*(15), 4568-4579.
- [Guo 2018] Guo, E., Shuai, S., Kazantsev, D., Karagadde, S., Phillion, A. B., Jing, T., & Lee, P. D. (2018). The influence of nanoparticles on dendritic grain growth in Mg alloys. *Acta Materialia*, *152*, 127-137.
- [Hantzsche 2010] Hantzsche, K., Bohlen, J., Wendt, J., Kainer, K. U., Yi, S. B., & Letzig, D. (2010). Effect of rare earth additions on microstructure and texture development of magnesium alloy sheets. *Scripta Materialia*, *63*(7), 725-730.
- [Hassan 2007] Hassan, S. F., & Gupta, M. (2007). Development of nano-Y2O3 containing magnesium nanocomposites using solidification processing. *Journal of Alloys and Compounds*, *429*(1-2), 176-183.
- [He 2008] He, F., Han, Q., & Jackson, M. J. (2008). Nanoparticulate reinforced metal matrix nanocomposites–a review. *International Journal of Nanoparticles*, *1*(4), 301-309.
- [Hull 2001] Hull, D., & Bacon, D. J. (2001). *Introduction to dislocations*. Butterworth-Heinemann.
- [Humphreys 1996] Humphreys, F. J., & Ardakani, M. G. (1996). Grain boundary migration and Zener pinning in particle-containing copper crystals. *Acta materialia*, *44*(7), 2717-2727.
- [Inoue 1987] Inoue, A., Yano, N., Matsuzaki, K., & Masumoto, T. (1987). Microstructure and superconducting properties of melt-quenched insoluble Al-Pb and Al-Pb-Bi alloys. *Journal of materials science*, *22*(1), 123-131.

- [Ishikawa 1990] Ishikawa, K. (1990). Fractals in dimple patterns of ductile fracture. *Journal of Materials Science Letters*, *9*(4), 400-402.
- [Israelachvili 2011] Israelachvili, J. N. (2011). *Intermolecular and surface forces*. Academic press.
- [Jamaati 2014] Jamaati, R., Toroghinejad, M. R., & Edris, H. (2014). Effect of SiC nanoparticles on the mechanical properties of steel-based nanocomposite produced by accumulative roll bonding process. *Materials & Design (1980-2015)*, *54*, 168-173.
- [Javadi 2017] Javadi, A., Cao, C., & Li, X. (2017). Manufacturing of Al-TiB2 Nanocomposites by Flux-Assisted Liquid State Processing. *Procedia Manufacturing*, *10*, 531-535.
- [Javadi 2018] Javadi, A., Pan, S., Cao, C., Yao, G., & Li, X. (2018). Facile Synthesis of 10 nm Surface Clean TiB 2 Nanoparticles. *Materials Letters*.
- [Jiang 2016] Jiang, L., Yang, H., Yee, J. K., Mo, X., Topping, T., Lavernia, E. J., & Schoenung, J. M. (2016). Toughening of aluminum matrix nanocomposites via spatial arrays of boron carbide spherical nanoparticles. *Acta Materialia*, *103*, 128-140.
- [Jiang 2017] Jiang, S., Wang, H., Wu, Y., Liu, X., Chen, H., Yao, M., & Lv, Z. (2017). Ultrastrong steel via minimal lattice misfit and high-density nanoprecipitation. *Nature*, *544*(7651), 460.
- [Johnson 1999] Johnson, W. L. (1999). Bulk glass-forming metallic alloys: Science and technology. *MRS bulletin*, *24*(10), 42-56.
- [Johnsson 1993] Johnsson, M., Backerud, L., & Sigworth, G. K. (1993). Study of the mechanism of grain refinement of aluminum after additions of Ti-and B-containing master alloys. *Metallurgical Transactions A*, *24*(2), 481-491.

- [Juhász 2012] Juhász, K. L., Baumli, P., & Kaptay, G. (2012). Fabrication of carbon fibre reinforced, aluminium matrix composite by potassium iodide (KI)–potassium hexafluoro-titanate (K2TiF6) flux. *Materialwissenschaft und Werkstofftechnik*, *43*(4), 310-314.
- [Kaban 2011] Kaban, I., Köhler, M., Ratke, L., Hoyer, W., Mattern, N., Eckert, J., & Greer, A. L. (2011). Interfacial tension, wetting and nucleation in Al–Bi and Al–Pb monotectic alloys. *Acta Materialia*, *59*(18), 6880-6889.
- [Kadkhodaee 2013] Kadkhodaee, M., Babaiee, M., Manesh, H. D., Pakshir, M., & Hashemi, B. (2013). Evaluation of corrosion properties of Al/nanosilica nanocomposite sheets produced by accumulative roll bonding (ARB) process. *Journal of Alloys and Compounds*, *576*, 66-71.
- [Karantzalis 2010] Karantzalis, A. E., Lekatou, A., Georgatis, M., Poulas, V., & Mavros, H. (2011). Casting-Based Production of Al-TiC-AlB2 Composite Material Through the Use of KBF4 Salt. *Journal of materials engineering and performance*, *20*(2), 198-202.
- [Karantzalis 2011] Karantzalis, A. E., Lekatou, A., Georgatis, M., Poulas, V., & Mavros, H. (2011). Casting-Based Production of Al-TiC-AlB 2 Composite Material Through the Use of KBF 4 Salt. *Journal of materials engineering and performance*, *20*(2), 198-202.
- [Kasavajjula 2007] Kasavajjula, U., Wang, C., & Appleby, A. J. (2007). Nano-and bulk-silicon-based insertion anodes for lithium-ion secondary cells. *Journal of Power Sources*, *163*(2), 1003-1039.
- [Keene 1993] Keene, B. J. (1993). Review of data for the surface tension of pure metals. *International Materials Reviews*, *38*(4), 157-192.

- [Kennedy 1999] Kennedy, A. R., & Karantzalis, A. E. (1999). The incorporation of ceramic particles in molten aluminium and the relationship to contact angle data. *Materials Science and Engineering: A*, *264*(1-2), 122-129.
- [Kennedy 1999']Kennedy, A. R., Karantzalis, A. E., & Wyatt, S. M. (1999). The microstructure and mechanical properties of TiC and TiB2-reinforced cast metal matrix composites. *Journal of materials science*, *34*(5), 933-940.
- [Kiesler 2015] Kiesler, D., Bastuck, T., Theissmann, R., & Kruis, F. E. (2015). Plasma synthesis of titanium nitride, carbide and carbonitride nanoparticles by means of reactive anodic arc evaporation from solid titanium. *Journal of Nanoparticle Research*, *17*(3), 152.
- [Kim 1991] Kim, W. T., Zhang, D. L., & Cantor, B. (1991). Microstructure of rapidly solidified aluminium-based immiscible alloys. *Materials Science and Engineering: A*, *134*, 1133-1138.
- [Kim 2007] Kim, K. T., Cha, S. I., & Hong, S. H. (2007). Hardness and wear resistance of carbon nanotube reinforced Cu matrix nanocomposites. *Materials Science and Engineering: A*, *449*, 46-50.
- [Kim 2015] Kim, S. H., Kim, H., & Kim, N. J. (2015). Brittle intermetallic compound makes ultrastrong low-density steel with large ductility. *Nature*, *518*(7537), 77.
- [Kirkby 2011] Kirkby, J., Curtius, J., Almeida, J., Dunne, E., Duplissy, J., Ehrhart, S., & Kupc, A. (2011). Role of sulphuric acid, ammonia and galactic cosmic rays in atmospheric aerosol nucleation. *Nature*, *476*(7361), 429.
- [Kiselev 2016] Kiselev, A., Bachmann, F., Pedevilla, P., Cox, S. J., Michaelides, A., Gerthsen, D., & Leisner, T. (2016). Active sites in heterogeneous ice nucleation—the example of K-rich feldspars. *Science*, aai8034.

- [Koch 1989] Koch, C. C. (1989). Materials synthesis by mechanical alloying. *Annual review of materials science*, *19*(1), 121-143.
- [Kopeliovich 2001] Kopeliovich, D., Shapiro, A., & Shagal, V. (2001). *U.S. Patent No. 6,273,970*. Washington, DC: U.S. Patent and Trademark Office.
- [Kumar 2015] Kumar, A., Jayasankar, K., Debata, M., & Mandal, A. (2015). Mechanical alloying and properties of immiscible Cu-20 wt.% Mo alloy. *Journal of Alloys and Compounds*, *647*, 1040-1047.
- [Kundan 2015] Kundan, A., Plawsky, J. L., & Wayner Jr, P. C. (2015). Effect of capillary and Marangoni forces on transport phenomena in microgravity. *Langmuir*, *31*(19), 5377-5386.
- [Labrecque 1998] Labrecque, C., & Gagne, M. (1998). Ductile iron: fifty years of continuous development. *Canadian Metallurgical Quarterly*, *37*(5), 343-378.
- [Lan 2004] Lan, J., Yang, Y., & Li, X. (2004). Microstructure and microhardness of SiC nanoparticles reinforced magnesium composites fabricated by ultrasonic method. *Materials Science and Engineering: A*, *386*(1-2), 284-290.
- [Lavernia 1986] Lavernia, E. J., GHANSHYAM, R., & Grant, N. J. Liquid dynamic compaction of a rapidly solidified high strength aluminum alloy. *The International journal of powder metallurgy & powder technology*, *22*(1), (1986) 9-16.
- [Lavernia 2010] Lavernia, E. J., & Srivatsan, T. S. (2010). The rapid solidification processing of materials: science, principles, technology, advances, and applications. *Journal of Materials Science*, *45*(2), 287.
- [Lee 2003] Lee, D. W., & Kim, B. K. (2003). Synthesis of nano-structured titanium carbide by Mg-thermal reduction. *Scripta materialia*, *48*(11), 1513-1518.

- [Lee 2003] Lee, H. T., Chen, M. H., Jao, H. M., & Liao, T. L. (2003). Influence of interfacial intermetallic compound on fracture behavior of solder joints. *Materials Science and Engineering: A*, *358*(1-2), 134-141.
- [Lee 2007] Lee, D. W., Yu, J. H., & Jang, T. S. (2007). Properties of TiC and TiCN nanoparticles fabricated by a magnesium thermal reduction process. In *Solid State Phenomena* (Vol. 124, pp. 1225-1228). Trans Tech Publications.
- [Lepper 1997] Lepper, K., James, M., Chashechkina, J., & Rigney, D. A. (1997). Sliding behavior of selected aluminum alloys. *Wear*, *203*, 46-56.
- [Li 2003] Li, J., Wang, Z. L., Zeng, H., Sun, S., & Ping Liu, J. (2003). Interface structures in FePt/Fe 3 Pt hard-soft exchange-coupled magnetic nanocomposites. *Applied physics letters*, *82*(21), 3743-3745.
- [Li 2003'] Li, J., Wei, P., Qiliang, H., Chen, J., & Zhang, Z. (2003). Mechanism of titanium deposition on AlN surface by molten salt reaction. *Materials letters*, *57*(8), 1369-1373.
- [Li 2004] Li, X., Yang, Y., & Cheng, X. (2004). Ultrasonic-assisted fabrication of metal matrix nanocomposites. *Journal of Materials Science*, *39*(9), 3211-3212.
- [Li 2005] Li, P., Kandalova, E. G., & Nikitin, V. I. (2005). In situ synthesis of Al–TiC in aluminum melt. *Materials Letters*, *59*(19-20), 2545-2548.
- [Li 2008] Li, J., Pan, W., Yuan, Z., & Chen, Y. (2008). Titanium metallization of alumina ceramics by molten salt reaction. *Applied Surface Science*, *254*(15), 4584-4590.
- [Li 2008'] Li, X., Dong, Z., Westwood, A., Brown, A., Zhang, S., Brydson, R., & Rand, B. (2008). Preparation of a titanium carbide coating on carbon fibre using a molten salt method. *Carbon*, *46*(2), 305-309.

- [Li 2011] Li, X., Dong, Z., Westwood, A., Brown, A., Brydson, R., Walton, A., & Cong, Y. (2011). Low-temperature preparation of single crystal titanium carbide nanofibers in molten salts. *Crystal Growth & Design*, *11*(7), 3122-3129.
- [Li 2017] Li, X. P., Ji, G., Chen, Z., Addad, A., Wu, Y., Wang, H. W., & Kruth, J. P. (2017). Selective laser melting of nano-TiB2 decorated AlSi10Mg alloy with high fracture strength and ductility. *Acta Materialia*, *129*, 183-193.
- [Li 2018] Li, Z., Wang, H., Guo, Q., Li, Z., Xiong, D. B., Su, Y., & Zhang, D. (2018). Regain strain-hardening in high-strength metals by nanofiller incorporation at grain boundaries. *Nano Letters*.
- [Liang 2008] Liang, Y., Dong, S., & Yang, T. (2008). Thermodynamic analysis of the formation of In-situ reinforced phases in cast Al-4.5 Cu alloy. *Journal of Wuhan University of Technology-Mater. Sci. Ed.*, *23*(3), 342.
- [Lin 2003] Lin, D. C., Liu, S., Guo, T. M., Wang, G. X., Srivatsan, T. S., & Petraroli, M. (2003). An investigation of nanoparticles addition on solidification kinetics and microstructure development of tin–lead solder. *Materials Science and Engineering: A*, *360*(1-2), 285-292.
- [Liu 2011] Liu, C., Wang, K., Luo, S., Tang, Y., & Chen, L. (2011). Direct Electrodeposition of Graphene Enabling the One-Step Synthesis of Graphene–Metal Nanocomposite Films. *small*, *7*(9), 1203-1206.
- [Liu 2013] Liu, G., Zhang, G. J., Jiang, F., Ding, X. D., Sun, Y. J., Sun, J., & Ma, E. (2013). Nanostructured high-strength molybdenum alloys with unprecedented tensile ductility. *Nature Mmaterials*, *12*(4), 344.

- [Liu 2016] Liu, W., Cao, C., Xu, J., Wang, X., & Li, X. (2016). Molten salt assisted solidification nanoprocessing of Al-TiC nanocomposites. *Materials Letters*, *185*, 392-395.
- [Liu 2018] Liu, J., Chen, Z., Zhang, F., Ji, G., Wang, M., Ma, Y., & Wang, H. (2018). Simultaneously increasing strength and ductility of nanoparticles reinforced Al composites via accumulative orthogonal extrusion process. *Materials Research Letters*, *6*(8), 406-412.
- [Lu 2004] Lu, L., Shen, Y., Chen, X., Qian, L., & Lu, K. (2004). Ultrahigh strength and high electrical conductivity in copper. *Science*, *304*(5669), 422-426.
- [Ma 2005] Ma, E. (2005). Alloys created between immiscible elements. *Progress in materials science*, *50*(4), 413-509.
- [Ma 2015] Ma, C., Chen, L., Cao, C., & Li, X. (2017). Nanoparticle-induced unusual melting and solidification behaviours of metals. *Nature communications*, *8*, 14178.
- [Ma 2016] Ma, C., Zhao, J., Cao, C., Lin, T. C., & Li, X. (2016). Fundamental study on laser interactions with nanoparticles-reinforced metals—Part I: Effect of nanoparticles on optical reflectivity, specific heat, and thermal conductivity. *Journal of Manufacturing Science and Engineering*, *138*(12), 121001.
- [Ma 2016'] Ma, C., Zhao, J., Cao, C., Lin, T. C., & Li, X. (2016). Fundamental Study on Laser Interactions With Nanoparticles-Reinforced Metals—Part II: Effect of Nanoparticles on Surface Tension, Viscosity, and Laser Melting. *Journal of Manufacturing Science and Engineering*, *138*(12), 121002.
- [Mackay 1977] MacKay, M. L. (1977). Innovation in Powder Metallurgy--an Engine Bearing Material. *Met. Prog.*, *111*(6), 32-35.
- [Malakhov 2000] Malakhov, D. V. (2000). Thermodynamic assessment of the Bi-Zn system. *Calphad*, *24*(1), 1-14.

- [Martin 2017] Martin, J. H., Yahata, B. D., Hundley, J. M., Mayer, J. A., Schaedler, T. A., & Pollock, T. M. (2017). 3D printing of high-strength aluminum alloys. *Nature*, *549*(7672), 365.
- [McKeown 2014] McKeown, J. T., Kulovits, A. K., Liu, C., Zweiacker, K., Reed, B. W., LaGrange, T., & Campbell, G. H. (2014). In situ transmission electron microscopy of crystal growth-mode transitions during rapid solidification of a hypoeutectic Al–Cu alloy. *Acta Materialia*, *65*, 56-68.
- [McKeown 2015] McKeown, J. T., Wu, Y., Fowlkes, J. D., Rack, P. D., & Campbell, G. H. (2015). Simultaneous In-Situ Synthesis and Characterization of Co&Cu Core-Shell Nanoparticle Arrays. *Advanced Materials*, *27*(6), 1060-1065.
- [Meenashisundaram 2015] Meenashisundaram, G. K., & Gupta, M. (2015). Synthesis and characterization of high performance low volume fraction TiC reinforced Mg nanocomposites targeting biocompatible/structural applications. *Materials Science and Engineering: A*, *627*, 306-315.
- [Meng 2005] Meng, S. G. Z. (2005). Progress in High-strength and High-conductivity Copper Alloys and Copper Base Composites [J]. *Special Casting & Nonferrous Alloys*, *9*, 008.
- [Miracle 1983] Nemati, N., Khosroshahi, R., Emamy, M., & Zolriasatein, A. (2011). Investigation of microstructure, hardness and wear properties of Al–4.5 wt.% Cu–TiC nanocomposites produced by mechanical milling. *Materials & Design*, *32*(7), 3718-3729. [Nemati 2011] Nemati, N., Khosroshahi, R., Emamy, M., & Zolriasatein, A. (2011). Investigation of microstructure, hardness and wear properties of Al–4.5 wt.% Cu–TiC nanocomposites produced by mechanical milling. *Materials & Design*, *32*(7), 3718-3729.

- [Mohammad 2016] Mohammad, K., & Saheb, N. (2016). Molecular level mixing: An approach for synthesis of homogenous hybrid ceramic nanocomposite powders. *Powder Technology*, *291*, 121-130.
- [Molina 2008] Molina, J. M., Narciso, J., Weber, L., Mortensen, A., & Louis, E. (2008). Thermal conductivity of Al–SiC composites with monomodal and bimodal particle size distribution. *Materials Science and Engineering: A*, *480*(1-2), 483-488.
- [Morris 1991] Morris, D. G., & Morris, M. A. (1991). Microstructure and strength of nanocrystalline copper alloy prepared by mechanical alloying. *Acta metallurgica et materialia*, *39*(8), 1763-1770.
- [Murty 2002] Murty, B. S., Kori, S. A., & Chakraborty, M. (2002). Grain refinement of aluminium and its alloys by heterogeneous nucleation and alloying. *International Materials Reviews*, *47*(1), 3-29.
- [Musil 2001] Musil, J., & Vlček, J. (2001). Magnetron sputtering of hard nanocomposite coatings and their properties. *Surface and Coatings Technology*, *142*, 557-566.
- [Nabawy 2015] Nabawy, A. M., & Chen, X. G. (2015). Fabrication of Al-TiB2 nanocomposites by flux-assisted melt stirring. *Metallurgical and Materials Transactions B*, *46*(4), 1596-1602.
- [Nardone 1986] Nardone, V. C., & Prewo, K. M. (1986). On the strength of discontinuous silicon carbide reinforced aluminum composites. *Scripta Metallurgica*, *20*(1), 43-48.
- [Nayeb 1985] Nayeb-Hashemi, A. A., & Clark, J. B. (1985). The Bi-Mg (bismuth-magnesium) system. *Bulletin of Alloy Phase Diagrams*, *6*(6), 528-533.
- [Nie 2003] Nie, J. F. (2003). Effects of precipitate shape and orientation on dispersion strengthening in magnesium alloys. *Scripta Materialia*, *48*(8), 1009-1015.

- [Nielsen 2014] Nielsen, M. H., Aloni, S., & De Yoreo, J. J. (2014). In situ TEM imaging of CaCO3 nucleation reveals coexistence of direct and indirect pathways. *Science*, *345*(6201), 1158-1162.
- [Oberg 1973] Oberg, K. E., Friedman, L. M., Boorstein, W. M., & Rapp, R. A. (1973). The diffusivity and solubility of oxygen in liquid copper and liquid silver from electrochemical measurements. *Metallurgical Transactions*, *4*(1), 61-67.
- [Ozawa 2004] Ozawa, S., & Motegi, T. (2004). Solidification of hyper-monotectic Al–Pb alloy under microgravity using a 1000-m drop shaft. *Materials Letters*, *58*(20), 2548-2552.
- [Pan 2016] Pan, F., Zhang, J., Chen, H. L., Su, Y. H., Kuo, C. L., Su, Y. H., & Hwang, W. S. (2016). Effects of rare earth metals on steel microstructures. *Materials*, *9*(6), 417.
- [Peker 1993] Peker, A., & Johnson, W. L. (1993). A highly processable metallic glass: Zr41. 2Ti13. 8Cu12. 5Ni10. 0Be22. 5. *Applied Physics Letters*, *63*(17), 2342-2344.
- [Poirier 2010] Poirier, D., Drew, R. A., Trudeau, M. L., & Gauvin, R. (2010). Fabrication and properties of mechanically milled alumina/aluminum nanocomposites. *Materials Science and Engineering: A*, *527*(29-30), 7605-7614.
- [Prasad 2013] Prasad, A., Yuan, L., Lee, P. D., & StJohn, D. H. (2013). The Interdependence model of grain nucleation: A numerical analysis of the Nucleation-Free Zone. *Acta Materialia*, *61*(16), 5914-5927.
- [Premkumar 2006] Premkumar, P. A., Dasgupta, A., Kuppusami, P., Parameswaran, P., Mallika, C., Nagaraja, K. S., & Raghunathan, V. S. (2006). Synthesis and Characterization of Ni and Ni/CrN Nanocomposite Coatings by Plasma Assisted Metal-Organic CVD. *Chemical Vapor Deposition*, *12*(1), 39-45.

- [Qian 2010] Qian, M., Cao, P., Easton, M. A., McDonald, S. D., & StJohn, D. H. (2010). An analytical model for constitutional supercooling-driven grain formation and grain size prediction. *Acta Materialia*, *58*(9), 3262-3270.
- [Qu 2011] Qu, X. H., Zhang, L., Mao, W. U., & Ren, S. B. (2011). Review of metal matrix composites with high thermal conductivity for thermal management applications. *Progress in Natural Science: Materials International*, *21*(3), 189-197.
- [Quang 2007] Quang, P., Jeong, Y. G., Yoon, S. C., Hong, S. H., & Kim, H. S. (2007). Consolidation of 1 vol.% carbon nanotube reinforced metal matrix nanocomposites via equal channel angular pressing. *Journal of materials processing Technology*, *187*, 318-320.
- [Rai 1998] Rai, U. S., & Rai, R. N. (1998). Physical chemistry of the organic analog of metal–metal eutectic and monotectic alloys. *Journal of crystal growth*, *191*(1-2), 234-242.
- [Rai 2016] Rai, R. N., Saha, S. C., Datta, G. L., & Chakraborty, M. (2016, March). Studies on synthesis of in-situ Al-TiC metal matrix composites. In *IOP Conference Series: Materials Science and Engineering* (Vol. 117, No. 1, p. 012042). IOP Publishing.
- [Ratke 1995] Ratke, L., & Diefenbach, S. (1995). Liquid immiscible alloys. *Materials Science and Engineering: R: Reports*, *15*(7-8), 263-347.
- [Ratke 2007] Ratke, L., Bruck, S., Mathiesen, R., Ludwig, A., Gruber-Pretzler, M., Tonn, B., & Agren, J. (2007). Lead-free bearing alloys for engine applications results of the ESA-MAP project MONOPHAS. *Transactions-Indian Institute of Metals*, *60*(2/3), 103.
- [Reardon 2011] Reardon, A. C. (Ed.). (2011). *Metallurgy for the Non-metallurgist*. ASM International.

- [Ren 2011] Ren, S., Shen, X., Guo, C., Liu, N., Zang, J., He, X., & Qu, X. (2011). Effect of coating on the microstructure and thermal conductivities of diamond–Cu composites prepared by powder metallurgy. *Composites Science and Technology*, *71*(13), 1550-1555.
- [Rohatgi 2007] Rohatgi, P., & Schultz, B. (2007). Lightweight metal matrix nanocomposites–stretching the boundaries of metals. *Material Matters*, *2*(4), 16-20.
- [Rosales 2014] Rosales, I., Gonzalez-Rodriguez, G., Gama, J. L., & Guardian, R. (2014). Bismuth Effect on the Mechanical Properties of Antifriction Al-Sn Alloys. *Materials Sciences and Applications*, *5*(05), 330.
- [Roy 1988] Roy, A. K., & Chhabra, R. P. (1988). Prediction of solute diffusion coefficients in liquid metals. *Metallurgical Transactions A*, *19*(2), 273-279.
- [Rudrakshi 2004] Rudrakshi, G. B., Srivastava, V. C., Pathak, J. P., & Ojha, S. N. (2004). Spray forming of Al–Si–Pb alloys and their wear characteristics. *Materials Science and Engineering: A*, *383*(1), 30-38.
- [Salehi 2012] Salehi, M., Saadatmand, M., & Mohandesi, J. A. (2012). Optimization of process parameters for producing AA6061/SiC nanocomposites by friction stir processing. *Transactions of Nonferrous Metals Society of China*, *22*(5), 1055-1063.
- [Sanaty 2012] Sanaty-Zadeh, A. (2012). Comparison between current models for the strength of particulate-reinforced metal matrix nanocomposites with emphasis on consideration of Hall–Petch effect. *Materials Science and Engineering: A*, *531*, 112-118.
- [Shi 2006] Shi, L., Sun, C., Gao, P., Zhou, F., & Liu, W. (2006). Mechanical properties and wear and corrosion resistance of electrodeposited Ni–Co/SiC nanocomposite coating. *Applied Surface Science*, *252*(10), 3591-3599.

- [Shi 2018] Shi, Q., Gu, D., Lin, K., Chen, W., Xia, M., & Dai, D. The Role of Reinforcing Particle Size in Tailoring Interfacial Microstructure and Wear Performance of Selective Laser Melting WC/Inconel 718 Composites. *Journal of Manufacturing Science and Engineering*.
- [Shin 2015] Shin, H., & Eun, J. H. (2015). Titanium carbide nanocrystals synthesized from a metatitanic acid-sucrose precursor via a carbothermal reduction. *Journal of Nanomaterials*, *16*(1), 217.
- [Stjohn 2005] StJohn, D. H., Qian, M. A., Easton, M. A., Cao, P., & Hildebrand, Z. (2005). Grain refinement of magnesium alloys. *Metallurgical and Materials Transactions A*, *36*(7), 1669-1679.
- [Stjohn 2011] StJohn, D. H., Qian, M., Easton, M. A., & Cao, P. (2011). The interdependence theory: the relationship between grain formation and nucleant selection. *Acta Materialia*, *59*(12), 4907-4921.
- [Stjohn 2015] StJohn, D. H., Prasad, A., Easton, M. A., & Qian, M. (2015). The contribution of constitutional supercooling to nucleation and grain formation. *Metallurgical and Materials Transactions A*, *46*(11), 4868-4885.
- [Straumal 2001] Straumal, B. B., Zięba, P., & Gust, W. (2001). Grain boundary phase transitions and phase diagrams. *International Journal of Inorganic Materials*, *3*(8), 1113-1115.
- [Straumal 2008] Straumal, B. B., Kogtenkova, O., & Zięba, P. (2008). Wetting transition of grain-boundary triple junctions. *Acta Materialia*, *56*(5), 925-933.

- [Straumal 2010] Straumal, B. B., Baretzky, B., Kogtenkova, O. A., Straumal, A. B., & Sidorenko, A. S. (2010). Wetting of grain boundaries in Al by the solid Al 3 Mg 2 phase. *Journal of materials science*, *45*(8), 2057-2061.
- [Strauss 2011] Strauss, H. W., Chromik, R. R., Hassani, S., & Klemberg-Sapieha, J. E. (2011). In situ tribology of nanocomposite Ti–Si–C–H coatings prepared by PE-CVD. *Wear*, *272*(1), 133-148.
- [Sun 2006] Sun, Z. B., Wang, Y. H., & Guo, J. (2006). Liquid phase separation of Cu-Cr alloys during rapid cooling. *Transactions of Nonferrous Metals Society of China*, *16*(5), 998-1002.
- [Sun 2017] Sun, Q., Jiang, H., Zhao, J., & He, J. (2017). Microstructure evolution during the liquid-liquid phase transformation of Al-Bi alloys under the effect of TiC particles. *Acta Materialia*, *129*, 321-330.
- [Suryanarayana 2001] Suryanarayana, C. (2001). Mechanical alloying and milling. *Progress in materials science*, *46*(1-2), 1-184.
- [Suryanarayana 2011] Suryanarayana, C. (2011). Synthesis of nanocomposites by mechanical alloying. *Journal of Alloys and Compounds*, *509*, S229-S234.
- [Suryanarayana 2013] Suryanarayana, C., & Al-Aqeeli, N. (2013). Mechanically alloyed nanocomposites. *Progress in Materials Science*, *58*(4), 383-502.
- [Tamirisakandala 2005] Tamirisakandala, S., Bhat, R. B., Tiley, J. S., & Miracle, D. B. (2005). Grain refinement of cast titanium alloys via trace boron addition. *Scripta materialia*, *53*(12), 1421-1426.

- [Tiller 1953] Tiller, W. A., Jackson, K. A., Rutter, J. W., & Chalmers, B. (1953). The redistribution of solute atoms during the solidification of metals. *Acta metallurgica*, *1*(4), 428-437.
- [Tjong 2000] Tjong, S. C., & Ma, Z. Y. (2000). Microstructural and mechanical characteristics of in situ metal matrix composites. *Materials Science and Engineering: R: Reports*, *29*(3-4), 49-113.
- [Tong 1998] Tong, X. C., & Fang, H. S. (1998). Al-TiC composites In Situ-processed by ingot metallurgy and rapid solidification technology: Part I. Microstructural evolution. *Metallurgical and Materials Transactions A*, *29*(3), 875-891.
- [Tschopp 2014] Tschopp, M. A., Murdoch, H. A., Kecskes, L. J., & Darling, K. A. (2014). "Bulk" nanocrystalline metals: review of the current state of the art and future opportunities for copper and copper alloys. *JOM*, *66*(6), 1000-1019.
- [Tyagi 2005] Tyagi, R. (2005). Synthesis and tribological characterization of in situ cast Al–TiC composites. *Wear*, *259*(1-6), 569-576.
- [Tyagi 2005] Tyagi, R. (2005). Synthesis and tribological characterization of in situ cast Al–TiC composites. *Wear*, *259*(1-6), 569-576.
- [Valiev 2004] Valiev, R. (2004). Nanostructuring of metals by severe plastic deformation for advanced properties. *Nature materials*, *3*(8), 511.
- [Valiev 2006] Valiev, R. Z., Estrin, Y., Horita, Z., Langdon, T. G., Zechetbauer, M. J., & Zhu, Y. T. (2006). Producing bulk ultrafine-grained materials by severe plastic deformation. *Jom*, *58*(4), 33-39.

- [Wang 1998] Wang, W., Zhu, F., Weng, J., Xiao, J., & Lai, W. (1998). Nanoparticle morphology in a granular Cu–Co alloy with giant magnetoresistance. *Applied physics letters*, *72*(9), 1118-1120.
- [Wang 2002] Wang, C. P., Liu, X. J., Ohnuma, I., Kainuma, R., & Ishida, K. (2002). Formation of immiscible alloy powders with egg-type microstructure. *Science*, *297*(5583), 990-993.
- [Wang 2010] Wang, F., Han, Y., Lim, C. S., Lu, Y., Wang, J., Xu, J., & Liu, X. (2010). Simultaneous phase and size control of upconversion nanocrystals through lanthanide doping. *Nature*, *463*(7284), 1061.
- [Wang 2014] Wang, B., Alam, M. T., & Haque, M. A. (2014). Grain growth in nanocrystalline nickel films at low temperature and stress. *Scripta Materialia*, *71*, 1-4.
- [Wang 2014] Wang, J., Li, D., & Wang, Y. (2014). Microstructure and properties of Ag–SnO2 materials with high SnO2 content. *Journal of Alloys and Compounds*, *582*, 1-5.
- [Wang 2015] Wang, L., Cui, Y., Li, B., Yang, S., Li, R., Liu, Z., & Fei, W. (2015). High apparent strengthening efficiency for reduced graphene oxide in copper matrix composites produced by molecule-lever mixing and high-shear mixing. *RSC Advances*, *5*(63), 51193-51200.
- [Wei 2011] Wei, S., Xu, B. Q., Bin, Y., Sun, H. Y., Song, J. X., Wan, H. L., & Dai, Y. N. (2011). Preparation of TiC powders by carbothermal reduction method in vacuum. *Transactions of Nonferrous Metals Society of China*, *21*(1), 185-190.
- [Wu 2008] Wu, Y., Han, W., Zhou, S. X., Lototsky, M. V., Solberg, J. K., & Yartys, V. A. (2008). Microstructure and hydrogenation behavior of ball-milled and melt-spun Mg–10Ni–2Mm alloys. *Journal of Alloys and Compounds*, *466*(1-2), 176-181.

- [Wu 2013] Wu, M., Cao, C. Z., He, X. B., & Qu, X. H. (2013). Brazing diamond/Cu composite to alumina using reactive Ag-Cu-Ti alloy. *Transactions of Nonferrous Metals Society of China*, *23*(6), 1701-1708.
- [Wu 2017] Wu, G., Chan, K. C., Zhu, L., Sun, L., & Lu, J. (2017). Dual-phase nanostructuring as a route to high-strength magnesium alloys. *Nature*, *545*(7652), 80.
- [Xu 2012] Xu, J. Q., Chen, L. Y., Choi, H., & Li, X. C. (2012). Theoretical study and pathways for nanoparticle capture during solidification of metal melt. *Journal of Physics: Condensed Matter*, *24*(25), 255304.
- [Xu 2013] Xu, J., Chen, L., Choi, H., Konish, H., & Li, X. (2013). Assembly of metals and nanoparticles into novel nanocomposite superstructures. *Scientific reports*, *3*, 1730.
- [Xu 2015] Xu, J., Cao, C., Das, S., Chen, L., Ma, C., Mishra, R. S., & Li, X. (2015). High performance Mg6Zn nanocomposites fabricated through friction stir processing. In *Magnesium Technology 2015* (pp. 383-386). Springer, Cham.
- [Xu 2015'] Xu, J. (2015). *Achieving Uniform Nanoparticle Dispersion in Metal Matrix Nanocomposites* (Doctoral dissertation, UCLA).
- [Yang 2007] Yang, Y., & Li, X. (2007). Ultrasonic cavitation based nanomanufacturing of bulk aluminum matrix nanocomposites. *Journal of manufacturing science and engineering*, *129*(3), 497-501.
- [Yang 2014] Yang, H., Topping, T. D., Wehage, K., Jiang, L., Lavernia, E. J., & Schoenung, J. M. (2014). Tensile behavior and strengthening mechanisms in a submicron B 4 C-reinforced Al trimodal composite. *Materials Science and Engineering: A*, *616*, 35-43.

- [Yi 2012] Sun, Y. (2012) Microstructure Modification by Nanoparticles in Aluminum and Magnesium Matrix Nanocomposites (Master dissertation, University of Wisconsin, Madison)
- [Yin 2004] Yin, Y., & Alivisatos, A. P. (2004). Colloidal nanocrystal synthesis and the organic–inorganic interface. *Nature*, *437*(7059), 664.
- [Yu 2010] Yu, C., Zhu, T. J., Xiao, K., Shen, J. J., Yang, S. H., & Zhao, X. B. (2010). Reduced grain size and improved thermoelectric properties of melt spun (Hf, Zr) NiSn half-Heusler alloys. *Journal of electronic materials*, *39*(9), 2008-2012.
- [Yuan 2015] Yuan, P., Gu, D., & Dai, D. (2015). Particulate migration behavior and its mechanism during selective laser melting of TiC reinforced Al matrix nanocomposites. *Materials & Design*, *82*, 46-55.
- [Zeng 2017] Zeng, W., Xie, J., Zhou, D., Fu, Z., Zhang, D., & Lavernia, E. J. (2017). In-situ formation of NbC in nanocrystalline Cu. *Journal of Alloys and Compounds*, *725*, 334-341.
- [Zhang 1999] Zhang, H. W., Sun, Z. G., Zhang, S. Y., Han, B. S., Shen, B. G., Tung, I. C., & Chin, T. S. (1999). Intergrain exchange coupling and coercivity mechanism of nanocrystalline Sm 2 Fe 15− x Cu x Si 2 C (x= 0 and 1) ribbons prepared by melt spinning. *Physical Review B*, *60*(1), 64.
- [Zhang 2006] Zhang, Z., & Chen, D. L. (2006). Consideration of Orowan strengthening effect in particulate-reinforced metal matrix nanocomposites: A model for predicting their yield strength. *Scripta Materialia*, *54*(7), 1321-1326.

- [Zhang 2008] Zhang, Z., & Chen, D. L. (2008). Contribution of Orowan strengthening effect in particulate-reinforced metal matrix nanocomposites. *Materials Science and Engineering: A*, *483*, 148-152.
- [Zhang 2008'] Zhang, H., Li, F., Jia, Q., & Ye, G. (2008). Preparation of titanium carbide powders by sol–gel and microwave carbothermal reduction methods at low temperature. *Journal of Sol-Gel Science and Technology*, *46*(2), 217-222.
- [Zhang 2014] Zhang, Y., Wang, H., Zhai, T., Yang, T., Qi, Y., & Zhao, D. (2014). Hydrogen storage characteristics of the nanocrystalline and amorphous Mg–Nd–Ni–Cu-based alloys prepared by melt spinning. *International Journal of Hydrogen Energy*, *39*(8), 3790-3798.
- [Zhang 2017] Zhang, H., Dasbiswas, K., Ludwig, N. B., Han, G., Lee, B., Vaikuntanathan, S., & Talapin, D. V. (2017). Stable colloids in molten inorganic salts. *Nature*, *542*(7641), 328.
- [Zhao 2006] Zhao, Y. H., Bingert, J. F., Liao, X. Z., Cui, B. Z., Han, K., Sergueeva, A. V., & Zhu, Y. T. (2006). Simultaneously increasing the ductility and strength of ultra-fine-grained pure copper. *Advanced Materials*, *18*(22), 2949-2953.
- [Zhou 2001] Zhou, F., Lee, J., Dallek, S., & Lavernia, E. J. (2001). High grain size stability of nanocrystalline Al prepared by mechanical attrition. *Journal of Materials Research*, *16*(12), 3451-3458.
- [Zhou 2014] Zhou, S., Dai, X., Xiong, Z., Wu, C., Zhang, T., & Zhang, Z. (2014). Influence of Al addition on microstructure and properties of Cu–Fe-based coatings by laser induction hybrid rapid cladding. *Journal of Materials Research*, *29*(7), 865-873.

- [Zhou 2016] Zhou, D., Zeng, W., & Zhang, D. (2016). A feasible ultrafine grained Cu matrix composite microstructure for achieving high strength and high electrical conductivity. *Journal of Alloys and Compounds*, *682*, 590-593.
- [Zhou 2017] Zhou, D., Geng, H., Zeng, W., Zhang, D., Kong, C., & Munroe, P. (2017). Suppressing Al2O3 nanoparticle coarsening and Cu nanograin growth of milled nanostructured Cu-5vol.% Al2O3 composite powder particles by doping with Ti. *Journal of materials science & technology*, *33*(11), 1323-1328.
- [Zhou 2018] Zhou, D., Wang, X., Muránsky, O., Wang, X., Xie, Y., Yang, C., & Zhang, D. (2018). Heterogeneous Microstructure of an Al23 Dispersion Strengthened Cu by Spark Plasma Sintering and Extrusion and Its Effect on Tensile Properties and Electrical Conductivity. *Materials Science and Engineering: A*.
- [Zhou 2018] Zhou, S., Dai, X., Wang, C., Xie, M., Yang, J., & Li, Z. (2018). Phase separated characteristics and soft magnetic properties of [Cu0. 6 (FeCrC) 0.4] 100− xSix immiscible composites by laser induction hybrid cladding. *Journal of Alloys and Compounds*, *732*, 740-747.
- [Zweben 1992] Zweben, C. (1992). Metal-matrix composites for electronic packaging. *Jom*, *44*(7), 15-23.
- [Zweben 1998] Zweben, C. (1998). Advances in composite materials for thermal management in electronic packaging. *Jom*, *50*(6), 47-51.